University College London

Computational study of the interactions of small molecules with the surfaces of iron-bearing minerals

Thesis submitted for the degree of Doctor of Philosophy (PhD) by

Nelson Yaw Dzade

Supervisor

Prof. Nora H. de Leeuw

University College London

Department of Chemistry

September, 2014

Declaration

I, Nelson Yaw Dzade, hereby declare that this thesis titled “Computational study of the interactions of small molecules with the surfaces of iron-bearing minerals” is my own work and that all materials from other sources have been properly and fully acknowledged.

Sign: ---

Date: ---

The problems of chemistry and biology can be greatly helped if our ability to see what we are doing, and to do things on an atomic level, is ultimately developed –a development which I think cannot be avoided.

Richard Feynman

Abstract

This thesis presents a comprehensive computational study of the bulk and surface properties of two major iron-bearing minerals: hematite (α-Fe_2O_3) and mackinawite (tetragonal FeS), and subsequently unravels the interactions of a number of environmentally important molecules with the low-Miller index surfaces of these iron-bearing minerals using a state-of-the-art methodology based on the density functional theory (DFT) techniques.

First, we have used the Hubbard corrected DFT (GGA+U) calculations to unravel the interactions of a single benzene molecule with the (0001) and $(01\bar{1}2)$ surfaces of α-Fe_2O_3 under vacuum conditions. α-Fe_2O_3 is correctly described as a charge-transfer insulator, in agreement with the spectroscopic evidence when the optimized value for $U = 5$ eV is employed. The benzene molecule is shown to interact relatively more strongly with the $(01\bar{1}2)$ surface *via* cation-π interactions between the π-electrons of benzene ring and the surface Fe *d*-orbitals than with the (0001) where van der Waals interactions are found to play important role in stabilizing the molecule at the surface.

In the second part of this thesis, DFT calculations with a correction for van der Waals interactions (DFT-D2 scheme of Grimme) have been used to simulate the bulk properties, surface structures and reactivity of layered mackinawite (FeS). We demonstrate that the inclusion of van der Waals dispersive interaction sensibly improves the prediction of interlayer separation distance in FeS, in good agreement with experimental data. The effect of interstitial impurity atoms in the interlayer sites on the structure and properties of FeS is also investigated, and it is found that these

contribute considerably to the mechanical stability of the FeS structure. From the geometry optimization of the low-Miller index surfaces of FeS, we have shown the (001) surface terminated by sulfur atoms is by far the most energetically stable surface of FeS. The calculated surface energies are used successfully to reproduce the observed crystal morphology of FeS.

As an extension to the surface studies, we have used the DFT-D2 method to model the adsorption mechanism of arsenious acid ($As(OH)_3$), methylamine (CH_3NH_2) and nitrogen oxides (NO and NO_2) molecules on the low-Miller index FeS surfaces under vacuum conditions. The $As(OH)_3$ molecule is demonstrated to preferentially form bidentate adsorption complexes on FeS surfaces *via* two O–Fe bonds. The calculated long As−Fe and As−S interatomic distances (> 3 Å) clearly suggest interactions *via* outer sphere surface complexes with respect to the As atom, in agreement with the experimental observations. The growth modifying properties of methylamine, the capping agent used in the synthesis of FeS, are modelled by surface adsorption. The strength of the interaction of CH_3NH_2 on the different FeS surfaces is shown to increase in the order: (001) < (011) < (100) < (111) and an analysis of the nature of bonding reveals that the CH_3NH_2 molecule interacts preferentially with the surface Fe *d*-orbitals *via* the lone-pair of electrons located on the N atom. Our simulated temperature programmed desorption process shows that methylamine is stable up to about 180 K on the most reactive (111) surface, which is comparable to the experimental desorption temperatures predicted at metallic surfaces. Finally, the catalytic properties of FeS as a nanocatalyst for the adsorption, activation and decomposition of environmentally important NO_x gases have been explored, where we consider the nature of binding of the NO_x species to the FeS surfaces and their dissociation reaction mechanisms.

Table of contents

Acknowledgements

First and foremost, I thank the Almighty God for His grace, favour, protection and provisions throughout my PhD studies in UCL.

Secondly, my heartfelt acknowledgement goes my supervisor Professor Nora de Leeuw, for her insightful directions and support throughout the last four years. I am also highly indebted to my second supervisor Professor C. R. A. Catlow for his support and helpful suggestions.

Special acknowledgements also go to the following people, who have enriched my experience at UCL immeasurably: Dr Alberto Roldan, Dr. Ricardo Grau-Crespo Dr. Zhimei Du, Dr. Devis di Tommaso, and all members of the group.

I also thank the University College London for funding my studies through the Overseas Students Scholarship. Gratitude also goes to the Industrial Doctorate Centre for Molecular Modelling & Materials Science for studentship.

I also acknowledge the use of HECToR, the UK’s national high-performance computing service, the UCL@Legion High Performance Computing Facility, the Iridis Compute Cluster -University of Southampton, and associated support services, in the completion of this work.

Finally, I would like to thank my family, especially my loving wife Godsway for all her support and encouragement throughout my studies.

Thanks to everyone!

List of publications

The work described in this thesis and other related works have been published in the following papers:

1. **N. Y. Dzade**, A. Roldan, and N.H. de Leeuw: “The surface chemistry of NO_x on mackinawite (FeS) surfaces: A DFT-D2 study”. *Phys. Chem. Chem. Phys.,* 16, 15444-15456 (2014)

2. **N. Y. Dzade**, A. Roldan, and N. H. de Leeuw: “A density functional theory study of the adsorption of benzene on hematite (α-Fe_2O_3) surfaces”, *Minerals, 4,* 89-115 (2014)

3. **N. Y. Dzade**, A. Roldan, and N. H. de Leeuw: “Adsorption of methylamine on mackinawite (FeS) surfaces: A density functional theory study”. *J. Chem. Phys.* 139, 124708 (2013)

4. S. S. Tafreshi, A. Roldan, **N. Y. Dzade**, N. H. de Leeuw: “Adsorption of hydrazine on the perfect and defective copper (111) surface: A dispersion-corrected DFT study”. *Surface Science* 622, 1-8 (2013)

5. **N. Y. Dzade**, A. Roldan, and N.H. de Leeuw; “Structure of $As(OH)_3$ adsorption complexes on mackinawite (FeS) surfaces: A DFT-D2 study”. *Manuscript in preparation* (2014)

6. **N. Y. Dzade**, A. J. Devey, A. Roldan, and N.H. de Leeuw: “A Density Functional Theory study of the effect of interstitial transition metal impurities on the structure and properties of mackinawite (FeS)”. *Manuscript in preparation* (2014)

Chapter 1

Introduction

Iron bearing minerals (oxides and sulfides) constitute one of the largest group of minerals on Earth. They are ubiquitous in nature and are present in soils and rocks, lakes and rivers, on the seafloor, and in organisms (Cornell & Schwertmann, 2000; Russell & Hall, 1997). Their importance in ores has long been, and continues to be, a major reason for the interest of mineralogists and geochemists in these materials (Vaughan & Craig, 1978). The diversity in the chemical structure and the excellent physical and chemical properties of iron oxides and iron sulfides provide many different applications at the research and industrial levels. This chapter introduces the family of iron oxide and sulfide minerals and their potential applications, with focus on the studied minerals in this thesis: hematite (α-Fe_2O_3) and mackinawite (tetragonal FeS). An overview of the subsequent chapters is also presented.

1.1 Iron oxide minerals

Iron oxides represent one of the most important transition metal oxides of technological importance. Altogether, sixteen different types of pure phases of iron oxides, *i.e.*, oxides, hydroxides or oxy-hydroxides have been reported in the literature, differing in composition, valence of Fe, and most importantly in crystal structure (Cornell & Schwertmann, 2003). In Table 1.1, the different types of iron oxides and hydroxides together with their chemical formula and magnetic properties are presented. Iron oxides have been extensively studied for their potential use in a wide range of important industrial applications such as pigments in ceramics glaze, catalysis, electrochemistry, magnetization, biomedical science, and environmental applications (Teja & Koh, 2009; Mahmoudi *et al*., 2010; Wang *et al*., 2011; Singh *et al*., 2011; Hassan *et al*., 2011; Gupta *et al.*, 2005; Wu *et al*., 2011; Feng *et al.*, 2013, Lai *et al.*, 2012). Shown in Figure 1.1 are the different scientific disciplines that are concerned with iron oxides applications. Hematite (α-Fe_2O_3), maghemite (γ-Fe_2O_3) and magnetite (Fe_3O_4), for example, are used as catalysts in the Fischer-Tropsch synthesis of hydrocarbons and ammonia (Twigg, 1989; Xu *et al.*, 1994; Max Appl, 2011; Jung & Thomson, 2011, Huang *et al*., 1993, Lei *et al.*, 2005), and in the synthesis of styrene through the dehydrogenation of ethylbenzene (Mimura *et al.*, 1998; Zscherpel *et al*., 1997; Chang *et al.*, 1997). Other industrial applications of iron oxides are in magnetic devices (Suber *et al*., 2005; Xiong *et al*., 2008), or semiconductors (Fujishiro *et al.* 1999), when the iron oxide can be incorporated into the interlayer of layered compounds as semiconductor pillars which show excellent photocatalytic activity (Sivula *et al*., 2012). In medical applications, nanoparticulate magnetic and super-paramagnetic iron oxides have been used for drug delivery in the treatment of cancer (Peng *et al.*, 2008; Yu *et al.*, 2010). Iron oxides are also important as pigments, where natural and synthetic pigments are used in the manufacture of red, brown, and black paints or as admixtures, for example in coloured glasses (Mendoza *et al.*, 1990; Morsi & El-Shennawi, 1993; Burkhard, 1997). The building materials industry is the biggest user of iron oxide pigments. They are extensively used in the manufacture of paving blocks, designer and roofing tiles, stamped concrete, etc. Iron oxide (α-Fe_2O_3) also serves as the main feedstock of the steel and iron industries, for example, they are used in the production of pure iron, steel, and many alloys (Greenwood & Earnshaw, 1997).

FIGURE 1.1: Scheme of the different scientific disciplines concerned with iron oxides. Reproduced with permission from Cornell & Schwertmann, 2003.

Iron oxide nanomaterials are also promising for removing toxic heavy metal ions and inorganic/organic pollutants from waste water, due to their low cost, natural abundance, strong adsorption capacity, easy separation, enhanced stability and environment-friendly properties: they are inert and non-toxic (Hu *et al.*, 2005; Carabante *et al.*, 2009; Fan *et al.*, 2012). Nanoparticles of iron (hydr)oxides including amorphous hydrous ferric oxide (FeOOH), goethite (α-FeOOH), hematite (α-Fe_2O_3), maghemite (γ-Fe_2O_3), and magnetite (Fe_3O_4) have been explored extensively for waste water and soil treatments, and there exist a number of excellent review works on this subject in the literature (Waychunas *et al.*, 2005; Nassar, 2012; Xu *et al.*, 2012). The current applications of iron oxide nanomaterials in contaminated water treatment can be largely divided into three groups: (a) Adsorbent for efficient removal of pollutants from the contaminated water (Nassar, 2010; Hu *et al.*, 2005, 2007, 2008); (b) Photocatalysts to break down or to convert contaminants into less toxic forms (Li *et al.*, 2007; Cao *et al.*, 2010, 2011; Liu *et al.*, 2012; Xu *et al.*, 2012); (c) Heterogeneous Fenton catalyst for the treatment of pollutants (Matta *et al.*, 2007; Hartmann *et al.*, 2010; Jessica *et al.*, 2013; Nidheesh *et al.*, 2014).

Type	**Chemical formula**	**Name**	**Crystal system**	**Type of magnetism**
Oxides	α-Fe_2O_3	Hematite	Rhombohedral hexagonal	AFM
	β-Fe_2O_3	Synthetic	Cubic face centered	-
	γ-Fe_2O_3	Maghemite	Cubic or tetragonal	FiM
	ε-Fe_2O_3	Synthetic	Orthorhombic	AFM
	Fe_3O_4	Magnetite	Cubic	FiM
	FeO	Wustite	Cubic	AFM
Oxide/hydroxide	α-FeOOH	Goethite	Orthorhombic	AFM
	β-FeOOH	Akaganeite	Monoclinic	AFM
	γ-FeOOH	Lepidocrocite	Orthorhombic	AFM
	δ-FeOOH	Synthetic	Hexagonal	FiM
	δ'-FeOOH	Feroxyhyte	Hexagonal	FiM
	High pressure FeOOH	Synthetic	Orthorhombic	AFM
	$Fe_{16}O_{16}(OH)_y(SO_4)_z.nH_2O$			
Hydroxides	$Fe_5HO_8.4H_2O$	Ferrihydrite	Hexagonal	SPM
	$Fe(OH)_3$	Bernalite	Orthorhombic	WFM
	$Fe(OH)_2$	–	Hexagonal	PFM

TABLE 1.1: Common types of iron oxides and hydroxides minerals (Cornell & Schwertmann, 2003). AFM = Antiferromagnetic; FiM = Ferrimagnetic; SPM = Speromagnetic; WFM = Weak ferromagnetic; PFM = Planar-ferromagnetic.

1.2 Hematite (α-Fe_2O_3)

Hematite (α-Fe_2O_3) is the thermodynamically most stable form of iron oxide under ambient conditions, and as such, it is also the most common form of crystalline iron oxide (Cornell & Schwertmann, 2003). As an important mineral in the Earth's crust, it is an active material in heterogeneous catalysis (Twigg, 1989; Xu *et al.*, 1994; Max Appl, 2011), and it is used as an electrode in photo-electrolysis (Sivula *et al.*, 2012) as well as in magnetic recording devices (Suber *et al.*, 2005; Xiong *et al.*, 2008). Hematite is isostructural with corundum α-Al_2O_3 and α-Cr_2O_3, (Catlow *et al.*, 1982; Rohr *et al.*, 1997; Mackrodt *et al.*, 1987; Ching *et al.*, 1994; Rohrbach *et al.*, 2004). The iron and oxygen atoms in hematite arrange in the corundum structure, which is trigonal-hexagonal scalenohedral (class $\bar{3}\,2/m$) with space group $R\bar{3}c$, lattice parameters $a = 5.034$ Å, $c = 13.749$ Å, and six formula units per unit cell (Figure 1.2a). The primitive cell is rhombohedral with lattice parameter $a = 5.034$ Å, with two formula units per unit cell (cell (Figure 1.2b), (Pauling & Hendricks, 1925; Finger and Hazen, 1980).

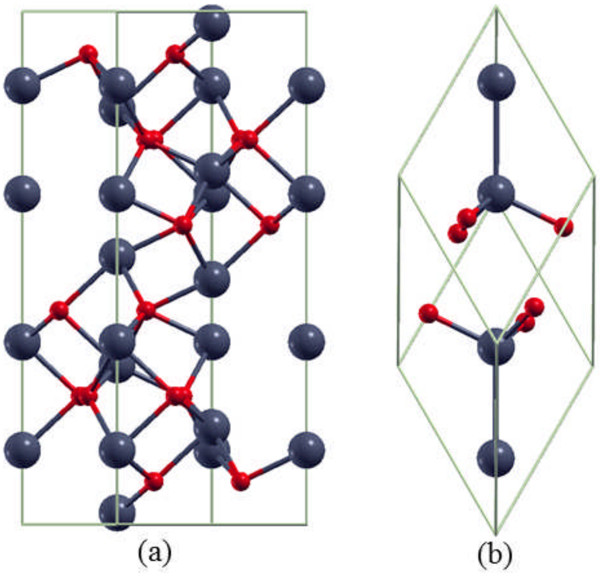

FIGURE 1.2: The corundum structure of hematite: (a) hexagonal unit cell, (b) the rhombohedral primitive cell. (Colour: Fe = grey and O = red).

In the hematite structure, the O^{2-} atoms are arranged in a hexagonal closed-packed lattice along the [001] direction with the cations (Fe^{3+}) occupying two-thirds of the octahedral sites between oxygens. The arrangement of the cations produces pairs of $Fe(O)_6$ octahedra. Each octahedron shares edges with three neighbouring octahedra in the same plane, and one face with an octahedron in an adjacent plane above or below in the [001] direction as shown in Figure 1.3.

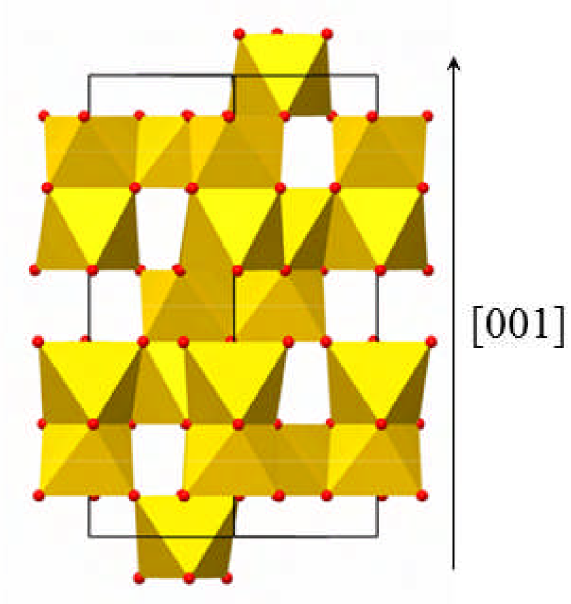

FIGURE 1.3: Polyhedral model showing the edge and face sharing octahedra in the hexagonal structure of hematite.

Pure hematite is anti-ferromagnetic below ~960 K (Freier *et al.*, 1962; Lielmezs *et al.*, 1965) and has a charge-transfer band gap of 2.2 eV (Sivula *et al.*, 2011). Shown in Figure 1.4 is the anti-ferromagnetic (AFM) structure of hematite, in which the iron atoms are coupled ferromagnetically within a single octahedral layer, and alternating layers are coupled anti-parallel along the [001] direction. However, as all iron atoms have an equivalent octahedral environment, the electronic and magnetic properties are the same at each iron site.

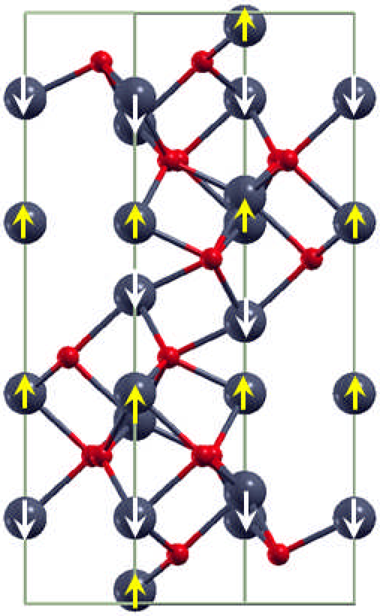

FIGURE 1.4: Hexagonal hematite lattice with the anti-ferromagnetic spin arrangements indicated by up (yellow) and down (white) arrows at the Fe sites.

The magnetic and electronic properties of hematite have been studied extensively using density functional theory calculations, notwithstanding the challenges it poses (Rohrbach *et al.*, 2004; Rollmann *et al.*, 2004; Punkkinen *et al.*, 1999). The Fe 3*d* electrons in α-Fe_2O_3 are strongly correlated, so methods beyond standard DFT are needed to correctly describe the system in terms of electronic and magnetic properties. Earlier standard DFT studies of bulk α-Fe_2O_3 have shown that these correlation effects cannot be treated appropriately within the local-spin density approximation (LSDA), even with the spin-polarized generalized-gradient approximation (SGGA), (Rollmann *et al.*, 2004; Punkkinen *et al.*, 1999; Sandratskii *et al.*, 1996). These standard DFT calculations predicted band gaps that were too small or non-existent, magnetic moments too small, and also incorrect positions of the iron 3*d* states in relation to the oxygen 2*p* states, characterizing α-Fe_2O_3 as a *d*-*d* Mott-Hubbard insulator, whereas spectroscopic evidence argues in favour of a charge-transfer insulator (Uozumi *et al.*, 1996; Fujimori *et al.*, 1989; Ciccacci *et al.*, 1991). Very recently, it has been shown that the problems inherent in standard DFT approaches can be largely overcome by adopting the DFT+U approach, where the effects of the strong intra-atomic electronic correlations are modelled by adding an on-site Coulomb repulsion U_{eff} term to the DFT Hamiltonian (Rohrbach *et al.*, 2004). This effect has led to satisfactory description of the structural, electronic, and magnetic properties of hematite (Rohrbach *et al.*, 2004). Similar approach has been used to investigate point defects (e.g. interstitials, vacancies and substitutional dopants) in hematite (Lee & Han, 2013; Rivera *et al.*, 2012; Meng *et al.*, 2011; Liao *et al.*, 2011). The DFT+U approach has also been used extensively to complement experimental efforts in elucidating our understanding of the surface structures of hematite (both clean and hydrated hematite surfaces), (Trainor *et al.*, 2004 and Wang *et al.*, 1998; de Leeuw & Cooper, 2007; Rustad *et al.*, 1999; Wasserman *et al.*, 1997; Jones *et al.*, 2000; Nguyen *et al.*, 2013; Yin *et al.*, 2007; Lo *et al.*, 2007).

1.3 Iron sulfide minerals

Iron sulfides constitute a diverse group of solids and dissolved complexes, many of which play important roles in hydrothermal systems and in biogeochemical processes (Rickard & Luther, 2007). Iron sulfide minerals exist in various intermediate forms depending on their structure and stoichiometry. At least seven different minerals consisting only of iron and sulfur are known to occur naturally (Rickard & Luther, 2007). Shown in Table 1.2 are the different iron sulfide phases, their composition, structure and properties. Volumetrically, pyrite (FeS_2) is the most abundant sulfide mineral on Earth, mainly due to its thermodynamic stability.

The economic importance of iron sulfides is not only limited to mining activities, where they are mined to satisfy the ever increasing world demand for non-ferrous metals. Iron sulfides have also attracted significant attention in the literature for potential applications in solar cells (Ennaoui *et al.*, 1984, 1985, 1986), photochemical technologies (Buker *et al.*, 1992; Yu et al. 2011), solid batteries (Yamaguchi *et al.* 2010; Paolella *et al.*, 2011), and heterogeneous catalysis (Cody, 2004a), owing to their unique and interesting physical, electronic, magnetic and chemical properties (Liu *et al.*, 2007; Akhter *et al.*, 2011; Abdelhady *et al.*, 2012, Joo *et al.*, 2003). For example, pyrite (FeS_2) has been considered as a possible material for photovoltaic solar cells owing to its semiconducting properties (Steinhagen *et al.*, 2012; Kirkeminde *et al.*, 2012). Pyrite was first explored as a photovoltaic (PV) semiconductor in the mid-1980s (Ennaoui, 1984, 1985, 1986), but there has been renewed interest in this material recently (Lin *et al.*, 2009; Puthussery *et al.*, 2011; Bi *et al.*, 2011; Wu *et al.*, 2011).

The diverse and interesting magnetic and electronic properties of iron sulfides have also been explored for potential applications in biomedicine, including protein immobilization and separation, magnetic targeting and drug delivery, and magnetic resonance imaging (Feng *et al.*, 2013, Lai *et al.*, 2012). Among the natural iron sulfide minerals, pyrrhotite ($Fe_{1-x}S$) and greigite (Fe_3S_4) are anti-ferromagnetic, pyrite (cubic FeS_2) and marcasite (orthorhombic FeS_2) are diamagnetic and troilite (hexagonal FeS) is anti-ferromagnetic (Rao *et al.*, 1976; Vaughan & Craig, 1978; Makovicky, 2006). Mössbauer studies on mackinawite (tetragonal FeS) shows no magnetic ordering down to very low temperatures (< 4.2 K) and these studies testifies to the absence of Fe magnetic moment (Vaughan & Ridout, 1971).

Another reason for even greater research interest in iron sulfide minerals arose from the discoveries of active hydrothermal systems in the deep oceans (Corliss *et al.*, 1979). The presence of life forms that have chemical rather than photosynthetic metabolisms, and that occur in association with newly-forming sulfides, has encouraged research on the potential of sulfide surfaces in catalysing the reactions leading to assembling of the complex molecules needed for life on Earth (Russell & Hall, 1997; Cody, 2004b; Martin *et al*., 2008; Martin & Russell, 2008). Pioneering research into an evolutionary biochemistry by Wächtershäuser and others have suggested that many of the prebiotic chemical reactions might be catalysed by iron sulfide (mackinawite, greigite, pyrite and violarite) surfaces at hydrothermal vents on the ocean floor during the Hadean and early Archean eras (Wächtershäuser, 1992; Blöchl *et al*., 1992; Cody, 2004b). In fact, acetic acid has been synthesized on sulfide surfaces in conditions simulating Earth before life (Huber & Wächtershäuser, 1997).

Iron sulfides have also attracted significant attention in environmental catalysis due to their ability to immobilize heavy metal atoms notably through processes involving either sorption (Watson *et al.,* 2000; Wolthers *et al.*, 2005) or oxidative dissolution (Livens *et al*., 2004 and Mullet *et al.*, 2004). Mackinawite, the studied iron sulfide phase in this thesis has been reported to have the capacity to immobilize pollutant metals such as chromium (Patterson *et al*., 1997), selenium (Scheinost *et al.*, 2008), arsenic (Moore *et al*., 1988; Farquhar *et al*., 2002; Bostick & Fendorf, 2003; Wolthers *et al*., 2005), thus playing important roles in the remediation of contaminated sites. Mackinawite is also an excellent mercury sorbent material from marine environments (Liu *et al.*, 2008, 2009; Burton *et al.*, 2009).

TABLE 1.2: The solid phases of iron sulfide minerals (Rickard and Luther, 2007)

1.4 Mackinawite (FeS)

Mackinawite (often referred to as tetragonal FeS) is considered the first iron sulfide phase formed from the reaction of Fe and S in low temperature aqueous environments (Rickard & Luther, 2007). It is also known to be the precursor to the formation of nearly all other iron sulfides in sedimentary and hydrothermal systems: including greigite and pyrite (Livens *et al.*, 2004; Rickard and Luther, 2007). This iron sulfide phase was first discovered in the Snohomish County, Washington, USA, within the Mackinaw mine, where it derived its name from (Evans *et al.*, 1962; Evans *et al.*, 1964).

The synthesis of mackinawite was first reported by Berner (1962, 1964) by immersing reagent grade of metallic iron wire in a saturated aqueous solution of H_2S, and tetragonal iron sulfide was precipitated. This solid phase was reported to possess a black colour when wet, to be soluble in concentrated HCl, to be unattracted by an ordinary magnet, and to oxidise rapidly in air to lepidocrocite (FeOOH) and orthorhombic sulphur (Berner, 1962). Two other approaches reported in the literature for the synthesis of mackinawite at low temperatures include: precipitation from the reaction of sulfide solution with ferrous iron solutions (Rickard, 1978) and *via* sulphate-reducing bacteria (Watson *et al.*, 2000). Mackinawite samples synthesised from the reaction of sulfide solution with metallic iron wire (Berner 1962, 1964) usually leads to more crystalline mackinawite (Lennie and Vaughan, 1996; Mullet *et al.*, 2002). In contrast, the other two methods lead to less crystalline phases that are more similar to those found in natural environments (Spadini *et al.*, 2003; Wolthers *et al.*, 2003).

A significant variation in the unit cell parameters, especially in the interlayer spacing distance has been reported in the literature (see Table 1.3). These variations suggest that the physicochemical properties of nanocrystalline mackinawite are strongly affected by preparation conditions. The expansion along the *c*-axis of crystalline mackinawite has been attributed to excess Fe uptake between S–S layers (Vaughan & Ridout, 1971). It was also suggested that water molecules can be intercalated between the tetrahedral sheets (Wolthers *et al*., 2003), and the observed expansion in the interlayer gap of nanocrystalline mackinawite samples may be caused by lattice relaxation due the water intercalation.

1.4.1 Structure of mackinawite

Mackinawite crystallises in the tetragonal structure (Figure 1.5) with space group *P4/nmm* (no. 29) and has lattice parameters $a = b = 3.674$ Å and $c = 5.033$ Å (Lennie *et al.,* 1995; Taylor & Finger, 1970). In the FeS structure, the iron atoms are in square-planar coordination and with an Fe–Fe distance of 2.597 Å (Lennie *et al.*, 1995), which is similar to the Fe–Fe distance in bcc Fe (2.482 Å), (Hung *et al.*, 2002). The iron atoms are linked in a tetrahedral coordination to four equidistant sulfur atoms on a square lattice to form edge-sharing tetrahedral layered sheets that are stacked along the c-axis and stabilized *via* van der Waals forces (see Figure 1.6). The relatively short Fe–Fe distance of 2.597 Å obviously suggests substantial metallic bonding in this material. Vaughan and Ridout originally suggested that the *d*–electrons in FeS are extremely delocalized in Fe–Fe plane forming metallic bonds (Vaughan & Ridout, 1971).

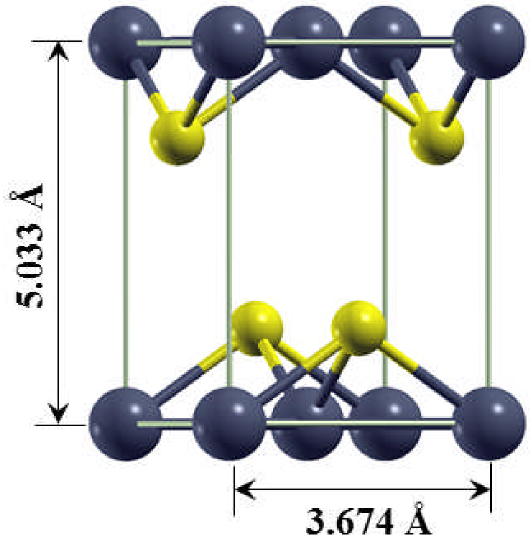

FIGURE 1.5: Tetragonal structure of mackinawite. Colour scheme: Fe = grey and S = yellow.

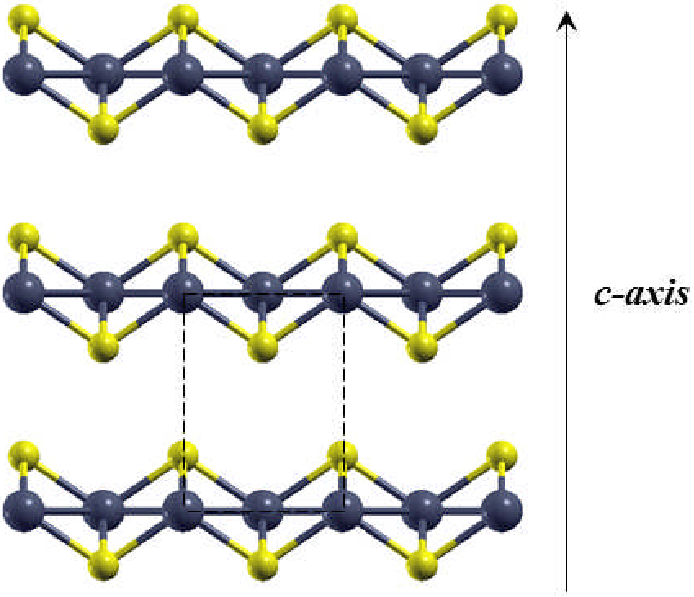

FIGURE 1.6: Multiple FeS unit cells showing its layered structure. A single unit is indicated with the dashed line.

Synthesis route	*a* (Å)	*c* (Å)	Reference	Fe^{2+} source	Methods of analysis
Metallic iron	3.674	5.033	Lennie *et al.*, (1995)	Iron wire	XRD
	3.665	4.997	Lennie *et al.*, (1997)	Iron wire	XRD
	3.670	5.059	Mullet *et al.*, (2002)	Iron wire	XRD, TEM, TMS, XPS
	3.679	5.047	Berner (1962)		
Ferrous solution	3.650	5.48–6.60	Wolthers *et al.*, (2003)	$(NH_4)_2Fe(SO_4)_2.6H_2O$	LAXRD,TEM, SAED
	3.685	5.030	Michel *et al.*, 2005	$(NH_4)_2Fe(SO_4)_2.6H_2O$	XRD (PDF), TEM
	–	5.050	Benning *et al.*, 2000	$(NH_4)_2Fe(SO_4)_2.6H_2O$	XRD,SEM
	–	5.08–5.19	Ohfuji & Rickard, 2006	$(NH_4)_2Fe(SO_4)_2.6H_2O$	LAXRD, SAED, HRTEM
	3.670	5.200	Jeong *et al.*, (2008)	$FeCl_2$	XRD, XAS, TEM
	3.674	5.035	Sines *et al.*, 2012	$FeCl_2$	XRD, TEM, SAED
Sulfate-reducing bacteria	–	5.700	Watson *et al.*, 2000	N/A	TEM, EXAFS, XANES
	–	~5.00	Herbert *et al.*, 1998	$FeSO_4$	XRD, SEM, XPS

TABLE 1.3: Unit cell parameters of mackinawite synthesized *via* three different routes. XRD: X-ray powder diffraction, TEM: transmission electron microscopy, TMS: transmission Mössbauer spectroscopy, XPS: X-ray photoelectron spectroscopy, PDF: pair distribution analysis, SEM: scanning electron microscopy, LAXRD: low-angle X-ray powder diffraction, HRTEM: high-resolution transmission electron microscopy, XAS: X-ray absorption spectroscopy, SAED: selected-area electron diffraction.

1.4.2 Composition of Mackinawite

Naturally occurring mackinawite has been reported to be non-stoichiometric, postulated to result from an S deficiency (Kostov, *et al.*, 1982). As such its formula is conventionally written FeS_{1-x} (typically $0 \leq x \leq 0.07$). Detailed Rietveld investigation of the structure of synthetic mackinawite by Lennie *et al.* (1995) however, showed that any sulfur vacancy or surplus iron occupancy was below the detection limit of the method, which suggests that the composition of synthetic mackinawite approaches stoichiometric FeS. The results are however, in contrast to previous reported analyses of synthetic mackinawite. Rickard (1997) found the composition $Fe_{1.04}S$, whereas Sweeney and Kaplan (1973) have reported compositions between $Fe_{1.06}S$ and $Fe_{1.15}S$, while Ward (1970) identified a range between $Fe_{0.99}S$ and $Fe_{1.023}S$, indicating the presence of excess Fe.

A recent Mössbauer spectroscopy and X-ray photoelectron study demonstrated the presence of up to 20 % excess Fe in the tetrahedral sites between the layers of mackinawite prepared from iron in sulfide solutions (Mullet *et al.*, 2002). Naturally occurring mackinawite samples have also been reported to contain substantial amounts of other transition metals impurities such as Ni (up to 20 %), Co (up to 20 %), Cu and Cr (up to 10 %) (Clark, 1969; Vaughan, 1969). As to the location of the excess Fe atoms in the mackinawite structure, Vaughan (1970) noted that the layered structure of mackinawite allows the incorporation of the additional interstitial Fe between the FeS layers. A recent DFT calculation validated Vaughan’s suggestion by predicting the tetrahedral site between the FeS layers as the energetically most favourable location for an interstitial Fe (Brgoch *et al.*, 2012). The excess metal impurities introduces non-stoichiometry in the FeS composition, thus the composition of mackinawite is commonly written as $Fe_{1+x}S$ but better written as $(Fe,M)_{1+x}S$, where M is another metal. When present, these metal impurity atoms have been reported to affect the stability, structure and properties of mackinawite (Takeno, 1965; Clark 1966; Takeno & Clark, 1967). For example, it has been reported that the presence of about 8–9 % weight of Ni and Co in the mackinawite structure increases its breakdown temperature from about 135 ^{o}C to 200-250 ^{o}C (Clark *et al.*, 1966). The Vickers micro-indentation hardness of mackinawite has also been reported to increase with impurity content (Clark, 1969; Vaughan, 1969). The expansion along the *c*-axis of crystalline mackinawite was explained by excess Fe uptake between S–S layers (Vaughan & Ridout, 1971).

1.4.3 Stability and transformation of mackinawite

A number of experimental studies on the stability of mackinawite have demonstrated that it converts to the more oxidised spinel phase greigite (Fe_3S_4), (Lennie *et al.*, 1997), although it has been shown that if mackinawite is kept in a reducing atmosphere devoid of any reactant other than H_2S, it is stable, and its transition to the greigite phase may be inhibited over a wide range of pH and temperature (Benning *et al.*, 2000). The transformation of mackinawite to other iron sulfides occurs through oxidation processes where it is generally considered that the following reaction sequence is involved in the formation of pyrite nuclei: mackinawite → greigite → pyrite (Berner, 1964; Lennie *et al.*, 1997). The first step of the conversion, mackinawite → greigite transformation occurs through the oxidation of some of the ferrous iron in the mackinawite structure into ferric iron. There are however, some uncertainties concerning the nature of the oxidant that drives the reaction, and the role of air in the mackinawite oxidation process is not completely understood. Berner (1964), in a study of iron sulfides formation from aqueous solutions at low temperatures and atmospheric pressures, reported that air was necessary to the oxidation process. The transformation of mackinawite, studied with heating experiments under vacuum conditions, showed that its phase transformation to hexagonal pyrrhotite occurs at approximately 270 ^{o}C (Kouvo *et al.*, 1963), while the transformation of mackinawite to greigite was observed already at 130 ^{o}C (Lennie *et al.*, 1997).

1.4.4 Electronic and magnetic properties of mackinawite

Mackinawite is believed to be metallic with highly delocalized Fe 3*d* electrons based on its short Fe−Fe distance (2.60 Å), which is close to that in elemental bcc iron (2.48 Å), (Vaughan & Ridout, 1971). Electronic structure calculations provide clear evidence of the metallic nature of mackinawite, its projected density of states reveal that the electronic states of Fe *d*-orbitals dominates the region around the Fermi level (Subedi *et al.*, 2008; Devey *et al.*, 2008). The fundamental magnetic property of mackinawite is however, still inconclusive *i.e.*, whether mackinawite has magnetic order or not. Both room temperature neutron diffraction (Bertaut *et al.*, 1965) and Mössbauer studies (Vaughan & Ridout, 1971) demonstrate no evidence of magnetic ordering down to temperatures as low as 1.7 K. These studies testify to the absence of an iron magnetic moment, indicating that mackinawite is comprised of low-spin Fe^{2+}. The effect has been attributed to strong covalency in the Fe–S bonding on the one hand (Bertaut *et al.*, 1965) and to extensive *d*-electron delocalisation within the sheets on the other hand (Vaughan & Ridout, 1971). A recently published superconducting quantum interference device (SQUID) data on the mackinawite, for both field cooled (FC) and zero field cooled (ZFC) conditions, also showed no evidence of magnetic ordering (Denholme *et al.*, 2014). A theoretical study using the linear muffin tin orbital approach of DFT have predicted a vanishing magnetic moment for the ferromagnetic structure of FeS, a consequence of the Fe–Fe interaction for edge-sharing FeS_4 tetrahedra which causes low density of states at the Fermi level (Welz & Rosenberg, 1987). From PAW calculations with PW91 functional, Devey *et al.* (2008), investigated the different magnetic phases of mackinawite and concluded that it is a non-magnetic material. On the contrary, Kwon *et al.*, (2011) using ultrasoft pseudopotential in association with the PBE functional concluded that the ground state of mackinawite is single-stripe antiferromagnetic and that the Fe atoms possess substantial magnetic moment, an observation that has been attributed to the existence of strong itinerant spin fluctuations in mackinawite.

1.5 Iron sulfides in hydrothermal vents

About three decades ago, scientists discovered active hydrothermal vents in the ocean floor of the Galapagos Islands (Corliss *et al.*, 1979). Like the findings of Charles Darwin over a century earlier, the discovery of hydrothermal vents on the Galapagos rift fundamentally altered our notions about life on Earth. The hydrothermal vents are formed as metal-rich, low pH (2–4), reduced, super-heated (350 ^{o}C–400 ^{o}C) fluids mix turbulently with oxygen-rich, cold (2 ^{o}C) seawater (Kelley *et al.*, 2002). The drastic temperature-chemical changes cause minerals such as anhydrite ($CaSO_4$), barite ($BaSO_4$), pyrite (FeS_2), chalcopyrite ($CuFeS_2$), mackinawite (tetragonal FeS), greigite (Fe_3S_4), and sphalerite (ZnS) to precipitate (Tivey *et al.*, 1986; Tivey, 1995). The fine-grained sulfide particles form chimney-like structures with heights up to 100–200 m as shown in Figure 1.7 (Lilley *et al.*, 1995). Because the precipitate sulfides and sulphates colour the surrounding waters black, the hydrothermal vents are often called “black smokers” (Jannasch & Wirsen, 1979). Effluents at black smokers’ are rich in dissolved transition metals, such as Fe, Mn, Zn, and Cu (Damm *et al.*, 1995). The black smoker fluids also commonly contain high concentrations of carbon dioxide (CO_2), hydrogen sulfide (H_2S), methane (CH_4), dihydrogen (H_2), and silicon dioxide (SO_2), (Damm *et al.*, 1995).

FIGURE 1.7: Black smokers showing chimney-like structures formed from fine-grained sulfide particles. *http://deepseamustangdiver.blogspot.co.uk/2012/04/geology-geography-formation-and.html*

Despite temperatures of the vent effluents can exceed 380 °C (Urabe *et al.* 1995; Schmidt *et al.*, 2007), mixing with cold (2 ^{o}C) seawater results in biologically habitable regimes which support extensive biological communities, demonstrating just how resilient life can be (Gaill *et al.*, 1997; Sarrazin & Juniper, 1999; Govenar *et al.*, 2005). Common vent living species include predatory crab, tubeworms, zoarcid fish, anemones and barnacles among others (see Figure 1.8). Although majority of vent species are heterotrophs, those that have nutritional symbioses with chemoautotrophic bacteria constitute as much as 96 % of the community biomass

(Sarrazin & Juniper, 1999). These chemoautotrophic symbionts harness energy *via* the oxidation of reduced chemical species and fix inorganic compounds for growth and biosynthesis. The co-availability of chemically reduced and oxidized compounds within vent mixing zones is ideal for chemoautotrophic activity.

Zoarcid fish *Predatory crab*

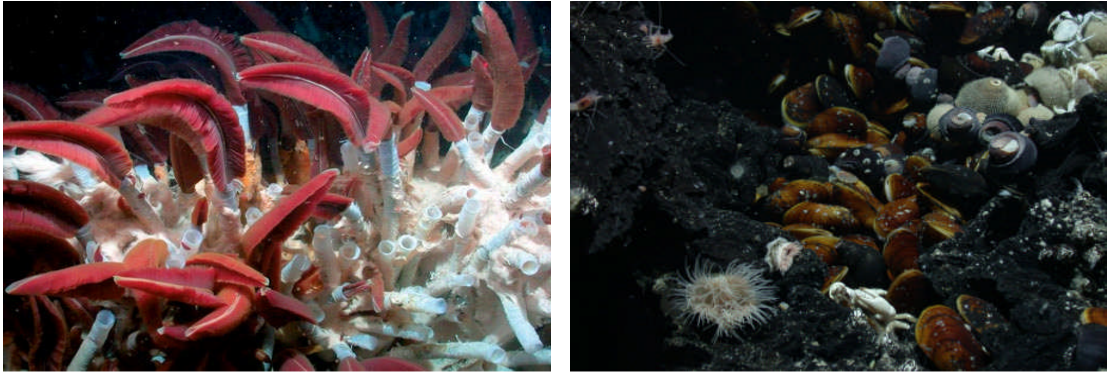

Tubeworms *Black snails*

Yeti Crabs *Anemones and Barnacles*

FIGURE 1.8: Diversity of life forms in the hydrothermal vent ecosystem. Pictures were taken from UK marine conservation society webpage. http://www.marine-conservation.org.uk/thermalventlife.html.

1.7 Overview of the thesis

Knowledge about the surface chemistry of minerals and its consequences on reactivity is vital for improving our understanding of the interesting and important chemical phenomena occurring on mineral surfaces. The chemical activity of minerals is directly related to the surface structure exposed to the environment and its composition, geometric and electronic properties. Although there exist several experimental techniques including X-ray Photoelectron Spectroscopy (XPS), X-ray Absorption Spectroscopy, Low Energy Electron Diffraction (LEED), Infra-red (IR) and Raman spectroscopy etc., that can be used to study surfaces, and to draw a chemical picture from a mineral surface, using just spectroscopic or electrochemical data is definitely not an easy task. However, the increase of computational power associated with the development of more accurate methodologies and efficient implementations make computational methods important tools for investigating mineral surfaces. Density Functional Theory (DFT) is especially important in this scenario, because it has a high accuracy and the computational cost for such calculations is affordable, and it has been used extensively in combination with spectroscopic data to improve our understanding of surface phenomena at the molecular level (de Leeuw & Cooper, 2007; Hinnemann *et al*., 2005; Moses *et al.*, 2007; Liu & Hu, 2012; Catlow *et al*., 1997; Trainor *et al.*, 2004 and Wang *et al*., 1998; Rustad *et al.*, 1999; Wasserman *et al.*, 1997; Nguyen *et al.*, 2013).

In this thesis, we have used computational methods based on DFT to model the bulk properties, surface structures and the chemical reactivity of hematite (α-Fe_2O_3) and mackinawite (FeS) surfaces towards a number of environmentally important molecules. The thesis is organized as follows:

The present chapter (chapter 1) has introduced the family of iron oxide and sulfide minerals and their potential applications, with focus on hematite and mackinawite, the studied minerals in this thesis, where both experimental studies and computer investigations were reported. Chapter 2 provides a description of the theoretical and practical information about the methodology and models applied in this work, and chapters 3 to 7 constitute the results of the different investigations carried out during the PhD study period.

The role of iron oxides in removing environmental pollutants from underground water and soil sediments due to their characteristically high surface areas and higher adsorption affinity makes it important to investigate the interactions of aromatic hydrocarbons with the major surfaces of hematite. The studies reported in chapter 3, have been carried out to unravel the interactions of a single benzene molecule with the (0001) and $(01\bar{1}2)$ surfaces of hematite under vacuum conditions using the Hubbard corrected density functional theory calculations (GGA+U).

Chapter 4 demonstrates a more detailed comparative study of the structural parameters and properties of stoichiometric FeS and non-stoichiometric $(Fe, M)_{1+x}S$ systems containing interstitial metal atoms (M = Cr, Mn, Fe, Co, Ni and Cu) using dispersion corrected DFT-D2 calculations to provide an accurate description of the interlayer interactions. The structures and stabilities of the low-index surfaces of the stoichiometric FeS have also been characterized, and the calculated surface energies are used to simulate the equilibrium morphology of the mackinawite crystal. As an extension to the FeS surface studies, the interactions and sorption mechanism of arsenious acid ($As(OH)_3$) on the low-index surfaces is presented in chapter 5. Here, the structures of the energetically most stable $As(OH)_3$ adsorption complexes are determined. The nature of bonding and the vibrational properties of the adsorption complexes are also presented.

The use of long chain amines, such as oleylamine, as capping agent in the synthesis of iron sulfide nanoparticles make it important to study the adsorption and desorption properties of amine functional groups on iron sulfide surfaces. The work presented in chapter 6 provides a molecular level insight into adsorption and desorption properties of methylamine (the simplest amine) on the low-index surfaces of mackinawite. The preferred adsorption geometries and their strength of binding as well as information on their electronic structures, vibrational properties and temperature programmed desorption temperatures (TPD) are also presented.

Finally, in chapter 7, the catalytic properties of mackinawite towards the adsorption, activation and decomposition of nitrogen oxides (nitrogen monoxide (NO) and nitrogen dioxide (NO_2) have been explored using DFT-D2 calculations, where we consider the nature of binding of the NO_x species to the FeS surfaces and their dissociation reaction mechanisms. A summary that discusses the results presented and an outline of possible future research direction concludes this work in chapter 8.

Bibliography

- Abdelhady A. L.; Malik M. A.; O’Brien P.; Tuna F.; *J. Phys. Chem. C*, **116**, 2253 (2012)
- Akhtar M.; Akhter J.; Malik M. A.; O’Brien P.; Tuna F.; Raftery J.; Helliwell M.; *J. Mater. Chem.*, **21**, 9737 (2011)
- Benning L. G.; Wilkin R. T.; Barnes H. L.; *Chemical Geology*, **167**, 25 (2000)

- Berner R. A.; *Science*, **137**, 669 (1962)
- Berner R. A.; *J. Geol*., **72**, 293 (1964)
- Bertaut E. F.; Burlet P.; Chappert J.; *Solid State Commun*. **3**, 335 (1965)
- Bi Y.; Yuan Y.; Exstrom C. L.; Darveau S. A.; Huang J.; *Nano Lett*., **11**, 4953 (2011)
- Binnig G.; Rohrer H.; *Reviews of Modern Physics*, *71*, S324, (1999)
- Blöchl E.; Keller M.; Wächtershäuser G.; Stetter K. O.; *Proc. Natl. Acad. Sci. U.S.A*. **89**, 8117 (1992)
- Bourdoiseau J.-A.; Jeannin M.; Sabot R.; Rémazeilles C.; Refait Ph.; *Corrosion Science*, **50**, 3247 (2008)
- Brgoch J.; Miller G. J.; *J. Phys. Chem. A*, **116**, 2234 (2012)
- Buker K.; Alonso-Vante N., Tributsch H.; *J. Appl. Phys*., **72**, 5721 (1992)
- Burkhard D. J. M.; *Solid State Communications*, **101**, 903 (1997)
- Burton E. D.; Bush R. T.; Sullivan L. A.; Hocking R. K.; Mitchell D. R. G.; Johnston S. G.; Fitzpatrick R.W.; Raven M.; McClure S.; Jang L. Y.; *Environ. Sci. Technol.*, **43**, 3128 (2009)
- Cao S. W.; Zhu Y. J.; Cheng G. F.; *J. Phys. Chem. Solids*, **71**, 1680 (2010)
- Cao S. W.; Zhu Y. J.; *Nanoscale Res. Lett*. **6**, 1 (2011)
- Carabante I.; Grahn M.; Holmgren A.; Kumpiene J.; Hedlund J.; *Colloids Surf A*. **346**, 106 (2009)
- Catlow C. R. A.; James R.; Mackrodt W. C.; Stewart R. F.; *Phys. Rev. B: Condens. Matter* **25**, 1006 (1982)
- Catlow C. R. A.; Ackermann L.; Bell R. G.; Gay D. H.; Holt S.; Lewis D. W.; Nygren M. A.; Sastre G.; Sayle D. C.; Sinclair P. E.; *J. Mol. Cat. A-Chem*. **115**, 431 (1997)
- Chang J. S.; Park S. E.; Park M. S.; *Chemistry Letters*, **26**, 1123 (1997)

- Chang R. H.; Wagner Jr J. B.; *J. Am. Ceramic Soc.*, **55**, 211 (1972)
- Chen G.; Zen J. M.; Fan F. R.; Bard A. J.; *J. Phys. Chem*., **95**, 3682 (1991)
- Ching W.Y.; Xu Y.-N.; *J. Am. Ceram. Soc*., **77**, 404 (1994)
- Ciccacci F.; Braicovich L.; Puppin E.; Vescovo E.; *Phys. Rev. B.*, **44**, 10444 (1991)
- Clark A. H.; Some comments on the composition and stability relations of mackinawite, *Neues Jahrb Mineral, Monatsh*., 300-304 (1966)
- Clark A. H., *Neues Jahrb. Mineral Monatsch*, **6**, 282 (1969)
- Cody G. D.; Boctor N. Z.; Filley T. R.; Hazen R. M.; Scott J. H.; Sharma A.; Yoder Jr. H. S.; *Science*, **289**, 1337 (2000)
- Cody G.; Boctor N.; Brandes J.; Filley T.; Hazen R.; Yoder H.; *Geochim. Cosmochim. Acta*, 68, 2185 (2004a)
- Cody G. D.; *Annu. Rev. Earth Planet Sci.* **32**, 569 (2004b)
- Corliss J. B.; Dymond J.; Gordon L. I.; Edmond J .M.; von Herzen R. P.; *Science*, *203*, 1073 (1979)
- Ching W. Y.; Xu Y-N.; *J. Am. Ceram. Soc*., **77**, 404 (1994)
- Cornell, R. M and Schwertmann, U.; The iron oxides: structure, properties, reactions, occurrences, and uses. *New York: Wiley-VCH, 2nd edition* (2003)
- Cornell R. M.; Schwertmann U.; Iron oxides in the laboratory: preparation and characterization. *New York: Wiley-VCH, 2nd edition* (2000)
- de Leeuw N. H.; Cooper T. G.; *Geochimica et Cosmochimica Acta*, **71**, 1655 (2007)
- Denholme S. J.; Demura S.; Okazaki H.; Hara H.; Deguchi K.; Fujioka M.; Ozaki T.; Yamaguchi T.; Takeya H.; Takano Y.; *Materials Chemistry and Physics* **147**, 50 (2014)

- Devey A. J.; Grau-Crespo R.; de Leeuw N. H.; *J. Phys, Chem C*, **112**, 10960 (2008)
- Ennaoui A.; Fiechter S.; Jaegermann W.; and Tributsch H.; *J. Electrochem. Soc*. **133**, 97 (1986)
- Ennaoui A.; Tributsch H.; *Sol. Cells*, **13**, 197 (1984)
- Ennaoui A.; Tributsch H.*; Sol. Energy Mater*. **14**, 461 (1986)
- Ennaoui A.; Fiechter S.; Pettenkofer C.; Alonso-Vante N.; Büker K.; Bronold M.; Höpfner C.; Tributsch H.; *Sol. Energy Mater. Sol. Cells*, **29**, 289 (1993)
- Evans H. T. Jr.; Berner R. A.; Milton C.; *Geol. Soc. Am. Prog*. **47a** (1962)
- Evans H. T. Jr.; Milton C.; Chao E. C. T.; Adler I.; Mead C.; Ingram B.; Berner R. A.; *USGS Professional Papers*, **475-D**, 64 (1964)
- Fan F. L.; Qin Z.; Bai J.; Rong W. D.; Fan F. Y.; Tian W. *et al*.; *J. Environ Radioact*; **106**, 40 (2012)
- Feng M.; Lu Y.; Yang Y.; Zhang M.; Xu Y.-J.; Gao H.-L.; Dong L.; Xu W.-P.; Yu S.-H.; *Scientific Reports*, **3**, 2994, (2013)
- Fujishiro Y.; Uchida S.; and Sato T.; *International Journal of Inorganic Materials*, **1**, 67 (1999)
- Fujimori A.; Saeki M.; Kimizuka N.; Taniguchi M.; Suga M.; *Phys. Rev. B.*, **34**, 7318 (1989)
- Girginova P. I.; Daniel-da-Silva A. L.; Lopes C. B.; Figueira P.; Otero M.; Amaral V. S.; *et al*.; *J. Colloid Interface Sci.,* **345**, 234 (2010)
- Gaill F. Shillito B.; Menard F.; Goffinet G.; Childress J. J.; *Mar. Ecol. Prog. Ser.* **148**,135 (1997
- Govenar B.; Le Bris N.; Gollner S.; Glanville J.; Aperghis A. B.; Hourdez S.; Fisher C. R.; Mar. *Ecol. Prog. Ser.* **305**, 67, (2005)
- Greenwood N. N.; Earnshaw A.; Chemistry of the Element (2nd ed.). Oxford: Butterworth-Heinemann. ISBN 0-7506-3365-4 (1997)

- Guevremont J.M.; Strongin D. R.; Schoonen M. A. A.; *American Mineralogist* **83**, 1246 (1998)
- Gupta A. K.; Gupta M.; *Biomaterials*, **26**, 3995 (2005)
- Hartmann M.; Kullmann S.; Keller H.; *J. Mater. Chem.*, **20** , 9002 (2010)
- Hassan M. F.; Guo, Z.; Chen, Z.; Lui, H.; *Mater. Res. Bull.*, **46**, 858 (2011)
- Henrich V. E.; Cox P. A.; The Surface Science of Metal Oxides, Cambridge: Cambridge University Press, (1994)
- Herbert Jr. R.B.; Benner S.G.; Pratt A.R.; Blowes D.W.; *Chemical Geology* **144**, 87 (1998)
- Hinnemann B.; Moses P. G.; Bonde J.; Jorgensen K. P.; Nielsen J. H.; Horch S.; Chorkendorff I.; Norskov J. K.; *J. Am. Chem. Soc*., 127, 5308 (2005)
- Hu J.; Chen G.; Lo I.; *Water Res.* **39**, 4528 (2005)
- Hu J.; Lo M.; Chen G.; *Sep. Purif. Technol*., **58**, 76 (2007)
- Hu J.; Zhong L.; Song W.; Wan L.; *Adv. Mater*., **20**, 2977 (2008)
- Huang C. S.; Xu L.; Davis B. H.; *Fuel Sci. & Tech. Int.*, **11**, 639 (1993)
- Huber C.; Wächtershäuser G.; *Science*, **276**, 245 (1997)
- Hung A.; Yarovsky I.; Russo S. P.*; J. Chem. Phys*. **118**, 6022 (2003)
- Hung A.; Yarovsky I.; Muscat J.; Russo S.; Snook I.; Watts R.O.; *Surf. Sci*., **501**, 261 (2002)
- Jannasch H. W.; Wirsen C. O.; *Bioscience*, **29**, 592 (1979)
- Jannasch H. W.; Chemosynthesis: The Nutritional Basis for Life at Deep-Sea Vents by *Oceanus*, vol. 27, no. 3, (1984)
- Jeong H. Y.; Lee J. H.; Hayes K. F.; *Geochim Cosmochim Acta*, **72**, 493 (2008)
- Jessica I.; Nieto J.; Tamar K.; *Photochem. Photobiol. Sci.*, **12**, 1596 (2013)

- Johnson M. K.; *In Encyclopedia of Inorganic Chemistry, ed. RB King, pp. 1896–915. Chichester, UK: Wiley* (1994)
- Jones F.; Rohl A. L.; Farrow J. B.; Bronswijk W.V.; *Phys. Chem. Chem. Phys*., **2**, 3209 (2000)
- Joo J.; Na H. B.; Yu T., Yu J. H.; Kim Y. W.; Wu F.; Zhang J. Z.; and Hyeon T.; *J. Am. Chem. Soc*. **125**, 11100 (2003)
- Jung H.; and Thomson W. J.; *Journal of Catalysis*, **139**, 375 (1993)
- Kelley D. S.; Baross J. A.; Delaney J. R.; *Annu. Rev. Earth Plan et Sci*., **30**, 385 (2002)
- Kiley P. J.; Beinert H.; *Curr. Opin. Microbiol*. **6**, 181 (2003)
- Kirkeminde A.; Scott R.; Ren S.; *Nanoscale*, **4**, 7649 (2012)
- Kostov I.; Minceva-Stefanova J.; Sulfide Minerals: Crystal Chemistry, Parageneses and Systematics, E. Bulgarian Acad. Sci. Inst. Geol. (1982)
- Kouvo O.; Vuorelainen Y.; Long J. V. P.; *Am Miner*. **48**, 511 (1963)
- Kwon K. D.; Refson K.; Bone S.; Qiao R.; Yang W.; Liu Z.; Sposito G.; *Phys. Rev*. **83**, 064402 (2011)
- Liao P.; Toroker M. C.; Carter E. A.; *Nano Lett*., **11**, 1775 (2011)
- Lai C.-H.; Lu M.-Y.; Chen L.-J.; *J. Mater. Chem*., **22**, 19 (2012)
- Lee J.; Han S.; *Phys. Chem. Chem. Phys*., **15**, 18906 (2013)
- Lei Y.; Cant N. W.; Trimm, D. L.; *Catalysis Letters*, **103**, 133 (2005)
- Lennie A. R.; Redfern S. A. T.; Schofield P. F.; Vaughan D. J.; *Mineral. Mag*., **59**, 677 (1995)
- Lennie A. R.; Redfern S. A. T.; Champness P. E.; Stoddart C. P.; Schofield P. F.; Vaughan D. J.; *Am. Mineralogist*, **82**, 302 (1997)
- Lin Y.-Y.; Wang D.-Y.; Yen H.-C.; Chen H.-L.; Chen C.-C.; Chen C.-M.; Tang C.-Y.; Chen C.-W.; *Nanotechnology*, **20**, 405207 (2009)

- Lilley M. D.; Landsteiner M. C.; McLaughlin E. A.; Parker C. B.; Cherkaoui A. S. M.; *Eos Trans. Am. Geophys. Union*, **76**, 420 (1995)
- Liu G.; Deng Q.; Wang H. Q.; Ng Dickon H. L.; Kong M. G.; Cai W. P; Wang G. Z.; *J. Mater. Chem.*, **22**, 9704 (2012)
- Li L. L.; Chu Y.; Liu Y.; Dong L.; *J. Phys. Chem. C*, **111**, 2123 (2007)
- Liu G. X.; Ma J.; and Du Q.; *Mater. Sci. Eng., B*, **145**, 17 (2007)
- Liu J.; Valsaraj K. T.; Devai I.; DeLaune R. D.; *J. Hazard. Mater.*, **157**, 432 (2008)
- Liu Z-P.; Hu P.; *J. Am. Chem. Sos.*, **124**, 14770 (2002)
- Liu J.; Valsaraj K. T.; Delaune R. D.; *Environ. Eng. Sci.*, **26**, 833 (2009)
- Livens F. R.; Jones M. J.; Hynes A. J.; Charnock J. M.; Mosselmans J F.; Hennig C.; Steele H.; Collison D.; Vaughan D. J.; Pattrick R. A.; Reed W. A.; Moyes L. N.; *J. Environ. Radioact.* **74**, 211 (2004)
- Lo, C. S.; Tanwar, K. S.; Chaka, A. M.; and Trainor, T. P.; *Phys. Rev. B.*, **75**, 075425 (2007)
- Mackrodt W. C.; Davey R. J.; Black S. N.; Docherty R.; *J. Cryst. Growth*, **80**, 441 (1987)
- Makovicky E.; *Rev. Mineral. Geochem*. **61**, 7 (2006)
- Martin W.; Baross J.; Kelley D.; Russell M. J.; Nature Reviews, *Microbiology*, **6**, 805 (2008)
- Martin W.; Russell M. J.; *Phil. Trans. R. Soc. B*, **362**, 1887 (2007)
- Matta R.; Hanna K.; Chiron S.; *Sci. Total Environ.*, **385**, 242 (2007)
- Max Appl “Ammonia, 2. Production Processes” in *Ullmann’s Encyclopedia of Industrial Chemistry, Wiley-VCH*, **3**, 227 (2011)
- Mahmoudi M.; Simchi I.; Imani M.; *J Iran Chem. Soc.*, **7**, S1-S27 (2010)

- Mendoza E. A.; Sunil D.; Wolkow E.; Gafney H. D.; Rafailovich M. H.; Sokolov J.; Long G. G.; Jemian P. R.; Schwartz S. A.; Wilkens B. J; *Appl. Phy. Lett.*, **57**, 209 (1990)
- Meng X. Y.; Qin G. W.; Li S.; Wen X. H.; Ren Y. P.; Pei W. L.; Zuo L.; *Appl. Phys. Lett.*, **98**, 112104 (2011)
- Michel F.M.; Antao S.M.; Chupas P.J.; Lee P.L.; Parise J.B.; Schoonen M.A.A.; *Chemistry of Materials* **17**, 6246 (2005)
- Mimura N.; Takahara I; Ando M.; Catal. Today, 45, 61 (1998)
- Morsi M. M.; and El-Shennawi A. W. A.; Ceramics International, 19, 333 (1993)
- Moses P. G.; Hinnemann B.; Topsøe H.; Nørskov J. K.; *Journal of Catalysis,* 248, 188 (2007)
- Moyes L. N.; Jones M. J.; Reed W. A.; Livens F. R.; Charnock J. M.; Mosselmans J.F. W.; Hennig C.; Vaughan D. J.; Pattrick R. A. D.; *Envir. Sci. Technol.*, **36**, 179 (2002)
- Mullet M.; Boursiquot S.; Ehrhardt J. J.; Colloids and Surfaces A: *Physicochem. Eng. Aspects*, 244, 77 (2004)
- Mullet M.; Boursiquot S.; Abdelmoula M.; Génin J.-M.; Ehrhardt J.-J; *Geochimica et Cosmochimica Acta* **66**, 829 (2002)
- Nassar N. N.; *J. Hazard. Mater. ,* **184** , 538 (2010)
- Nassar N. N.; Iron Oxide Nanoadsorbents for Removal of Various Pollutants from Wastewater: An Overview. *Application of Adsorbents for Water Pollution Control*, 81-118 (2012)
- Nguyen M-T.; Seriani N.; Gebauer R.; *J. Chem. Phys.*, **138**, 194709 (2013)
- Nidheesh P. V.; Gandhimathi R.; Velmathi S.; Sanjini N. S.; *RSC Adv.*, **4**, 5698 (2014)
- Ohfuji H.; Rickard D., *Earth Plan et Sci. Lett.*, **241**, 227 (2006)
- Parker S. C.; de Leeuw N. H.; Redfern S. E.; *Faraday Discuss.*, **114**, 381 (1999)

- Paolella A.; George C.; Povia M.; Zhang Y.; Krahne R.; Gich M.; Genovese A.; Falqui A.; Longobardi M.; Guardia P.; Pellegrino T.; Manna L.; *Chem. Mater.* **23**, 3762 (2011)
- Pauling L.; Hendricks S.; *J. Am. Chem. Soc.*, **47**, 781 (1925)
- Peng X.; Qian X; Maoh H.; Wang, A. Y.; Chen Z.; Nie S.; Shin D. M.; *International Journal of Nanomedicine*, **3**, 311 (2008)
- Punkkinen M. P. J.; Kokko K.; Hergert W.; Väyrynen I. J.; *J. Phys.: Condens. Matter*, **11**, 2341 (1999)
- Puthussery J.; Seefeld S.; Berry N.; Gibbs M.; Law M.; *J. Am. Chem. Soc.*, **133**, 716 (2011)
- Rohrbach A.; Hafner J.; Kresse G.; *Phys. Rev. B.*, **70**, 125426 (2004)
- Rao C. N. R.; Pisharody K. P. R.; *Prog. Solid State Chem.*, **10**, 207 (1976)
- Rickard D.; *Geochim. Cosmochim. Acta*, **61**, 115 (1997)
- Rickard D.; Luther G. W.; *Chem. Rev.*, **107**, 514 (2007)
- Rivera R.; Pinto H. P.; Stashans A.; Piedra L.; *Phys. Scr.*, **85**, 015602 (2012)
- Rodriguez J. A.; Abreu I. A.; *Journal of Phy. Chem. B* 109, 2754 (2005)
- Rohr F.; Baumer M.; Freund H. J.; Mejias J. A.; Staemmler V.; Muller S.; Hammer L.; Heinz K.; *Surf. Sci.*, **372**, L291 (1997)
- Russell M. J.; Hall A. J.; *J. Geog. Soc. London.*, **154**, 377 (1997)
- Rustad J. R.; Wasserman E.; Felmy A. R.; *Surface Science*, **424**, 28 (1999)
- Sandratskii L. M.; Uhl M.; Kübler J.; *J. Phys.: Condens. Matter*, **8**, 983 (1996)
- Sarrazin J.; Juniper S. K.; *Mar. Ecol. Prog. Ser.* **185**, 1 (1999)
- Scheinost A. C.; Charlet L.; *Environ. Sci. Technol.* **42**, 1984 (2008)
- Schmidt K.; Koschinsky A.; Garbe-Schoönberg D.; de Carvalho L. M.; Seifert R., *Chem. Geol.* **242**, 1 (2007)

- Shirane G.; Pickart S. J.; Nathans R.; Ishikawa Y.; J. *Phys, and Chem. of Solids*, **10**, 35 (1959)
- Singh J.; Srivastava M.; Dutta J., Dutta P. K.*; Int. J. Biol Macromol*. **48**, 170 (2011)
- Sines I.T. Vaughn D. D.; Misra R.; Popczun E. J.; Schaak R. E.; *Journal of Solid State Chemistry* **196** 17 (2012)
- Steinhagen C.; Harvey T. B.; Stolle C. J.; Harris J.; Korgel B. A.; *J. Phys. Chem. Lett.* **3**, 2352 (2012)
- Stirling A.; Bernasconi M.; Parrinello M.; *Journal of Chem. Phys*. 118, 8917 (2003)
- Subedi A.; Zhang L.; Singh D. J.; Du M. H.; Phys. Rev. B, 78, 134514 (2008)
- Suber L.; Imperatori P.; Ausanio G.; Fabbri F.; Hofmeister H.; *J. Phys. Chem, B*, **109**, 7103 (2005)
- Sweeney R. E.; Kaplan I. R.; *Econ. Geol*. **68**, 618 (1973)
- Teja A. S.; Koh P. Y.; *Prog crystal Growth Charact. Matt*., **55**, 22 (2009)
- Tivey M. K.; Delaney J .R.; *Earth Plan et Sci. Lett*. **77**, 303 (1986)
- Tivey M. K.; *Geochim. Cosmochim. Acta*, **59**, 1933 (1995)
- Twigg M. V.; *Catalyst Handbook Wolfe Publishing*, London (1989)
- Urabe T.; Baker E. T.; Ishibashi J.; Feely R. A.; Marumo K.; Massoth G. J.; Maruyama A.; Shitashima K.; Okamura K.; Lupton J. E.; *Science*, **269**, 1092 (1995)
- Uozumi T.; Okada K.; and Kotani A.; *J. Electron Spectrosc. Relat. Phenom*., **78**, 103 (1996)
- Vaughan D. J.; Ridout M. S.; *J Inorg Nucl. Chem*, **33**, 741 (1971)
- Vaughan D. J.; *Transvaal. Am. Mineral*. **54**, 1190 (1969)
- Vaughan D. J.; *Transvaal Am. Mineral*, **55**, 1807 (1970)

- Ward J. C.; *Rev. Pure Appl. Chem.*, **175**, 175 (1970)
- Vaughan D. J.; Craig J. R., *Mineral Chemistry of Metal Sulfides, Cambridge University Press, Cambridge*, UK, (1978)
- Venables J. A.; Introduction to Surface and Thin Film Processes. Cambridge University Press, (2000)
- Von Damm K. L.; *Controls on the Chemistry and Temporal Variability of Seafloor Hydrothermal Fluids*. (*American Geophysical Union, Washington DC,* 222–247 (1995)
- Wächtershäuser G.; *Biophys. Molec. Biol.*, **58**, 85 (1992)
- Wächtershäuser G.; *Science*, **289**, 1307, (2000)
- Wang S. S.; Seefurth R. N.; *J. Electrochem. Soc*, **134**, 530 (1987)
- Wang G.; Lui T.; Luo Y.; Zhao Y.; Ren. Z.; Bai J.; *Journal of Alloys and Compounds*, **509**, L216 (2011)
- Wasserman E.; Rustad J. R.; Felmy A. R.; Hay B. P.; Halley J. W.; *Surf. Sci.*, **385**, 217 (1997)
- Watson J. H. P.; Cressey B. A.; Roberts A. P.; Ellwood D.C.; Charnock J. M.; Soper A. K.; *J. Magnetism and Magnetic Materials*, **214**, 13 (2000)
- Waychunas G. A.; Kim C. S.; Banfield J. F.; J. Nanoparticle Res., 7, 409 (2005)
- Welz D.; Rosenberg M.; J. Phys. C: Solid State Phys. **20**, 3911 (1987)
- White B. R.; Stackhouse B. T.; Holcombe J. A.; *J Hazard Mater*;**161**, 848 (2009)
- Wolthers M.; Charlet L.; Linde P. R. V. D.; Rickard D.; Weuden C. H. V. D.; *Geochimica et Cosmochimica Acta*, 69, 3469 (2005)
- Wu B.; Song H.; Zhou J.; Chen X.; *Chem. Commun.*, **47**, 8653 (2011)
- Xu L.; Bao S.; O’brien R. J.; Houpt, D. J; Davis, B. H.; *Fuel Sci. & Tech. International*, **12**, 1323 (1994)

- Xiong Y.; Ye J.; Gu, X.; Chen Q.; Journal of Magnetism and Magnetic Materials, 320, 107 (2008)
- Yamaguchi Y.; Takeuchi T.; Sakaebe H.; Kageyama H.; Senoh H.; Sakai T.; Tatsumi K.; *J. Electrochem. Soc*, **157**, A630 (2010)
- Yu L.; Lany S.; Kykyneshi R.; Jieratum V.; Ravichandran R.; Pelatt B.; Altsehul E.; Platt H. A. S.; Wager J. F.; Keszler D. A.; Zunger A.; *Adv. Energy Matter*, **1**, 748 (2011)
- Yu M.; Park J.; Jeong Y. Y.; Moon W. K.; Jon S.; *Nanotechnology*, **21**, 415102 (2010)
- Xu P.; Zeng G.M.; Huang D. L; Feng C. L.; Hu S.; Zhao M .H.; Lai C.; Wei Z.; Huang C.; Xie G. X.; Liu Z. F.; *Sci. Total Environ*., **424**, 1 (2012)
- Yin S.; Ma X.; Ellis D. E.; *Surf. Sci.*, **601**, 2426 (2007)
- Zscherpel D.; Weiss W; Schlogl R.; *Surf. Sci*., **382**, 326 (1997)

Chapter 2

Computational methods

Abstract

Density functional theory (DFT) methods for calculating the quantum mechanical ground states of condensed matter systems are now a common and significant component of materials research. DFT has been highly successful (for example, the Nobel Prize in chemistry, 1998) because for many classes of systems, approximate functionals, such as LDA, GGA, and hybrids, give reasonably accurate results. The growing importance of DFT reflects the development of sufficiently accurate functionals, efficient algorithms and continuing improvements in computing capabilities. This chapter presents an overview of the fundamental theoretical background of the *ab initio* DFT electronic structure method. Description of the fundamental concepts employed in this work for modelling and analysing the systems investigated are also covered.

2.1 Introduction

The properties of materials are ultimately determined by the interactions of electrons and nuclei, and the fundamental description of those interactions requires quantum mechanics. In 1929, shortly after the Schrödinger equation (SE) was formulated, Dirac famously observed that, the general theory of quantum mechanics is now almost complete by stating that...

"*The underlying physical laws necessary for the mathematical theory of a large part of physics and the whole of chemistry are thus completely known, and the difficulty is only that the exact application of these laws leads to equations much too complicated to be soluble*" (Dirac, 1929).

While the Schrödinger equation is hardly solvable analytically, numerical approaches to obtaining approximate solutions for electronic structure have become invaluable to chemistry and materials science. These computational efforts received a critical boost in 1964 when Hohenberg and Kohn (1964), and Kohn and Sham (1964), reformulated the Schrödinger equation, which involves all the *3N* spatial coordinates of *N* interacting electrons, into density functional theory (DFT), a theory based on the electron density, a function of only three spatial coordinates. The resulting Kohn–Sham (KS) equations reconstructed the intractable complexity of the detailed many-body interactions into a computationally manageable single-particle effective potential *via* the exchange-correlation functional. While the 'divine functional' (Mattsson, 2002) that would make this reformulation exact is still been pursued, approximate functionals have proven highly successful in describing many properties of materials. DFT methods have therefore become a backbone of materials science and DFT calculations are a common, important component of many materials research efforts.

Efficient algorithms devised to implement the KS equations have been built into increasingly sophisticated general purpose production codes. These resourceful codes combined with ever-expanding computer power, have greatly increased the size and scope of problems that can be studied with DFT. Some of the commonly used DFT based electronic structure codes that uses plane waves and related methods include: Vienna Ab-initio Simulation Package (VASP), (the code used in this work) (Kresse & Hafner, 1993, 1994, 1996), Cambridge Serial Total Energy Package (CASTEP) (Clark *et al.*, 2005), Quantum-Espresso (opEn Source Package for Research in Electronic Structure, Simulation, and Optimization) (Giannozzi *et al.*, 2009). A more comprehensive and extensive list can be found at the link (http://dft.sandia.gov/codes.html).

2.2 Fundamental concepts

There exist numerous descriptions of DFT ranging from brief introductory summaries to extensive and comprehensive texts in the literature (Martin, 2004; Argaman & Makov, 2000; Capelle, 2006; Kohn *et al.*, 1996; Perdew *et al.*, 2009). With such extensive literature already in place, this section will focus only on the fundamental principles and concepts that are relevant to this work.

2.2.1 Schrödinger equation

The properties of matter at the nanoscale are described by the laws of quantum mechanics. The behaviour of atoms and electrons in a system evolving with time is governed according to the time-dependent Schrödinger equation (Schrödinger, (1926) which has the general form:

$$i\hbar\frac{\partial}{\partial t}\Psi = \hat{H}\Psi \tag{2.1}$$

where i is the imaginary unit, $\hbar$ is the Planck's constant divided by 2π, Ψ is the wave-function of the quantum system, and $\hat{H}$ is the Hamiltonian operator (which characterizes the total energy of any given wave-function and takes different forms depending on the situation). The symbol *"∂/∂t"* indicates a partial derivative with respect to time *t*. When considering a stationary situation, the Hamiltonian is independent of time and the time-independent Schrödinger equation simply takes the form:

$$E\Psi = \hat{H}\Psi \tag{2.2}$$

In words, the equation states: when the Hamiltonian operator acts on a certain wave function Ψ, and the result is proportional to the same wave function Ψ, then Ψ is in a stationary state, and the proportionality constant, E, is the energy of the state Ψ.

The Hamiltonian $(\hat{H})$ of interacting electrons and nuclei within a condensed matter system can be described by the following equation:

$$\hat{H} = -\sum_i \frac{\hbar^2}{2m_e}\nabla_i^2 - \sum_I \frac{\hbar^2}{2M_I}\nabla_I^2 - \sum_{i,I}\frac{Z_I e^2}{\left|r_i - R_I\right|} + \frac{1}{2}\sum_{i\neq j}\frac{e^2}{\left|r_i - r_j\right|} + \frac{1}{2}\sum_{I\neq J}\frac{Z_I Z_J e^2}{\left|R_I - R_J\right|} \tag{2.3}$$

The electrons are denoted by lower subscripts and nuclei denoted by upper case subscripts. M_I and Z_I are the masses and charge of the nuclei and m_e is the mass of an electron. R_I and r_i are positions of the I^{th} nucleus and i^{th} electron respectively. The first two terms describe the kinetic energy of the electrons and nuclei. The other three terms represent the attractive electrostatic interaction between the electrons and the nuclei and repulsive potential due to the electron-electron and nucleus-nucleus interactions. The solution to this many-body problem within the exact quantum mechanical framework is practically impossible. Certain physically meaningful approximations are thus necessary, to make the problem tractable. Some of these meaningful approximations are described as follows.

2.2.2 Born-Oppenheimer approximation

The adiabatic or Born-Oppenheimer (B-O) approximation is based on the fact that the nuclei are much heavier than the electrons; hence the velocities of electrons are much higher than that of the nuclei (Born & Oppenheimer, 1927). Thus, the nuclear kinetic energy in the Hamiltonian expression (equation 2.3) can be neglected to a first approximation. Using B-O approximation and atomic units: $m_e = e = \hbar = 1$, equation 2.3 is modified to give B-O Hamiltonian for electrons of a fixed nuclear configuration *R*:

$$\hat{H}_{B-O}(R) = -\frac{1}{2}\sum_i \nabla_i^2 - \sum_{i,I} \frac{Z_I}{|r_i - R_I|} + \frac{1}{2}\sum_{i \neq j} \frac{1}{|r_i - r_j|} \tag{2.4}$$

where the first, second and third terms are respectively, the kinetic energy of the electrons, the electron-nucleus Coulomb interaction and the electron-electron Coulomb interaction. The nucleus-nucleus Coulomb interaction $\frac{1}{2}\sum_{I \neq J} \frac{Z_I Z_J}{|R_I - R_J|}$ is not included because it is a constant for a fixed ionic configuration *R*, and hence results in only a simple shift of the B-O energy eigenstates. The many-body equation (2.4) contains two-body Coulomb terms and the exchange correlation (in the third term) and thus requires further simplification. Density Functional Theory (DFT) provides an enormous simplification to this problem.

2.2.3 Density Functional Theory

Density Functional Theory (DFT), based on Hohenberg-Kohn (H-K) theorems (Hohenberg & Kohn, 1964) and Kohn-Sham (K-S) equations (Kohn & Sham, 1965), is presently the most widely used method to compute the total energy and electronic structure of matter, where the basic variable used is the ground state electron density $n(r)$ of the system, rather than the many electrons wave-functions. The huge computational cost associated with the large number of slater determinants for a many-body system is thus saved in this approach. The two Hohenberg-Kohn theorems described next, show that the spatially dependent electron density $n(r)$ is sufficient to determine the ground state energy and properties of the system.

2.2.4 Hohenberg-Kohn Formalism

The many-electron wave-function is a function of $3N$ variables and it is too complicated to deal with. In order to provide an exact theory for many-body systems, Hohenberg and Kohn together in 1964 proposed and proved two important theorems that enable the electron density to be used instead. The proofs of these theorems are outside the scope of this thesis. Interested readers are referred to review papers and several textbooks that provide mathematical proofs of these theorems (Martin, 2004; Hohenberg & Kohn, 2006; Capelle, 2006; Kohn *et al.*, 1996; Argaman & Makov, 2000).

***Theorem 1**: For any system of interacting particles in an external potential* $v_{ext}(r)$*, the potential* $v_{ext}(r)$*, is determined uniquely, except for a constant, by the ground state particle density* $n_o(r)$*.*

***Theorem 2**: A universal functional for the energy* $E[n(r)]$ *in terms of the density* $n(r)$ *can be defined valid for any external potential* $v_{ext}(r)$*, and for any particular* $v_{ext}(r)$*, the ground state energy of the system is the global minimum value of this functional, and the density* $n(r)$ *that minimizes the functional is the exact ground state density* $n_o(r)$.

For an electronic system with a given Hamiltonian, considering the fact that the ground state electron density determines the number of electrons, it follows that the density determines the wave-function and thereby all the ground state properties of the system. The total ground state energy, the ground state kinetic energy, the energy of the electrons in the external potential $v_{ext}(r)$ and the electron-electron interaction energies are all functions of the density $n(r)$. Thus the total energy functional $E[n(r)]$ in the second Hohenberg and Kohn theorem can be written in terms of the given external potential $v_{ext}(r)$ as follows;

$$E[n(r)] = \int v_{ext}(r)n(r)dr + F[n(r)] \tag{2.5}$$

where $F[n(r)]$ is an unknown functional (*i.e.*, the exact analytical solution is not known), but otherwise it is a universal functional of the electron density $n(r)$ only. The functional $F[n(r)]$ is the electronic part of the Hamiltonian, consisting of the kinetic energy, $T[n(r)]$, of the electrons and the electron-electron interaction (v_{e-e}). Thus, $F[n(r)]$ can be written as,

$$F[n(r)] = \langle \Psi | n | T + v_{e-e} | \Psi | n \rangle \tag{2.6}$$

The two Hohenberg-Kohn theorems provide the formal justification of effectively reducing the $3N$ dimensional minimization problem into determining the ground state electronic density. However, the two theorems do not offer a way of computing $F[n(r)]$, and thus no practical way out for determining the ground state energy of the system. Kohn and Sham (1965) thus came out with a derivation to give the form of $F[n(r)]$ a year after the seminal DFT paper by Hohenberg and Kohn.

2.2.5 The Kohn-Sham equations

In 1965, Kohn and Sham proposed a new reformulation of the energy functional, equation (2.5), in order to find an analytical solution for it. The functional $F[n(r)]$ was separated into three distinct parts:

$$F[n(r)] = T[n(r)] + E_H[n(r)] + E_{xc}[n(r)] \tag{2.7}$$

The first term, $T[n(r)]$, is the kinetic energy functional for a fictitious system of non-interacting electrons producing the same density as $n(r)$.

$$T[n(r)] = -\frac{1}{2}\sum_{i=1}^{N}\int \psi_i^*(r)\nabla^2\psi_i(r)dr \tag{2.8}$$

The second term, $E_H[n(r)]$, is the so called Hartree energy, arising classically from the mutual Coulomb repulsion of all electrons:

$$E_H[n(r)] = \frac{1}{2}\iint \frac{n(r)n(r')}{|r-r'|}drdr' \tag{2.9}$$

The last term, $E_{xc}[n(r)]$, called the exchange-correlation functional, is a correction term, which accounts for all the many-body effects in $F[n(r)]$. The functional form of the correction term $E_{xc}[n(r)]$ is unknown and must be approximated. Practical applications of DFT are therefore classified according to the approximations taken for the exchange-correlation functional $E_{xc}[n(r)]$.

2.2.6 Exchange-correlation functional

The exchange-correlation term (E_{xc}) is the energy contribution from the quantum effects not included in the Coulomb repulsion and the single-particle kinetic energy. The exact form of this expression is unknown. The commonly used approximations to determine the exchange-correlation energy include the local density approximation (LDA), generalized gradient approximation (GGA), and hybrid functionals. These approximations are discussed below.

2.2.6.1 Local Density Approximation (LDA)

The local density approximation, the LDA, uses only the electron density, *n(**r**)*, at a spatial point ***r*** to determine the exchange-correlation energy at that point. The exchange-correlation energy density is taken to be that of the uniform electron gas of the same density. The exchange part of the functional is defined as the exact expression derived for a homogeneous electron gas (Kohn & Sham, 1964).

$$E_{xc}^{LDA}[n(r)] = \int n(r)\varepsilon_{xc}^{\hom} n(r)dr \tag{2.10}$$

For the homogeneous electron gas, the exchange energy is given by;

$$\varepsilon_{xc}^{\hom} = \frac{-e^2}{4\pi\varepsilon}\frac{3}{4}\left(\frac{3n}{\pi}\right)^{1/3} \tag{2.11}$$

The available versions of LDA differ only in their representation of the correlation. All modern LDA correlation functionals are based on Ceperley and Alder’s (CA’s) 1980, Monte Carlo calculation of the total energy of the uniform electron gas. The Perdew-Zunger (PZ) (Perdew and Zunger, 1981), Perdew–Wang (PW) (Perdew and

Wang, 1992) and Vosko-Wilk-Nusair (VWN) (Vosko *et al.*, 1980) are different fits to the CA data.

2.2.6.2 The generalized gradient approximation (GGA)

The generalized gradient approximation, the GGA, adds the gradient of the density, |∇*n(r)*|, as an independent variable.

$$E_{xc}^{GGA} = \int n(r)\varepsilon_{xc}(n,|\nabla n|)dr \tag{2.12}$$

The gradient introduces non-locality into the description of the exchange and correlation. This can improve the functional's performance greatly by helping to account for fast varying changes in the electron density that are not well described by the local density approximation. Several approximations of the gradient have been implemented, and all of them give better results for geometries, vibrational frequencies, charge densities, and binding energies than LDA. Some existing GGA functionals are:

- Perdew-Wang 86 (PW86), (Perdew, 1986)
- Lee-Yang-Parr (LYP), (Lee *et al.*, 1988)
- Perdew-Wang 91 (PW91), (Perdew *et al.*, 1992)
- Perdew-Burke-Enzerhof (PBE), (Perdew *et al.*, 1996, 1997)
- Revised Perdew-Burke-Enzerhof (RPBE), (Hammer *et al.*, 1999)

In this thesis, all the calculations are carried out with the PW91 functional, which tends to be a good functional for the description of chemical bonds. In some cases, other functionals have been tested for comparison.

2.2.6.3 Hybrid Functionals

The well-known standard density functionals (LDA and GGA) underestimate band gaps especially for small gap systems, and structural properties related to the band gap are difficult to predict. In quantum chemistry this has long been realized, and hybrid functionals which incorporate a portion of the exact exchange from Hartree–Fock theory with the exchange and correlation from other sources (*ab initio* or empirical) have been introduced (Becke, 1993), and they are generally preferred over purely LDA and GGA functionals. Such functionals usually predict a much larger band gap than purely standard density functionals and they also provide a simple scheme for improving many molecular properties, such as atomization energies, bond lengths and vibration frequencies (Perdew *et al.*, 1996). One of the most commonly used versions of hybrid functional among quantum chemists is B3LYP, which stands for Becke, 3-parameter, Lee-Yang-Parr (Becke, 1988).

$$E_{xc}^{B3LYP} = E_x^{LDA} + a_0\left(E_x^{HF} - E_x^{LDA}\right) + a_x\left(E_x^{GGA} - E_x^{LDA}\right) + E_c^{LDA} + a_c\left(E_c^{GGA} - E_c^{LDA}\right) \qquad (2.13)$$

Where a_0 = 0.20, a_x = 0.72, and a_c = 0.81. E_x^{GGA} and E_x^{LDA} E_x^{B3LYP} are generalized gradient approximations: the Becke 88 exchange functional (Becke 1988) and the correlation functional of Lee, Yang and Parr (1988) for B3LYP, and E_c^{LDA} is the VWN local-density approximation to the correlation functional (Vosko *et al.*, 1980).

Another popular version is the PBE0 functional (Perdew *et al.*, 1996) which includes 25 % of Hartree-Fock exchange is defined as:

$$E_{xc}^{PBE0} = 0.25E_x^{HF} + 0.75E_x^{PBE} + \Delta E_c^{PBE} \qquad (2.\ 14)$$

where E_x^{PBE} and E_c^{PBE} respectively denote the exchange and correlation parts of the PBE density functional.

2.2.7 Basis sets

To solve the single-particle Kohn-Sham equations, the single-electron wave-functions must be expanded in terms of a basis. This transforms the series of integro-differential single-particle Schrödinger equations, into a matrix equation which can be solved computationally in an efficient fashion. Modern electronic structure methods fall into two broad classes, depending on the choice of the basis set used for the expansion of the valence orbitals and charge densities. These include localized atomic orbitals (AOs) and plane-waves (PWs) basis sets. When molecular calculations are performed, it is common to use a basis composed of a finite number of atomic orbitals, centered at each atomic nucleus within the molecule. Plane-wave basis sets, on the other hand, are not localized on an atom; instead they are popular in calculations involving periodic boundary conditions. PWs have been a huge success for a number of reasons. They enable the use of fast Fourier transforms to move between real space and k-space, making some operations much faster. As the PWs do not depend on the position of the atoms, the Hellmann-Feynman theorem can be used to calculate the forces directly (Hellmann, 1937; Feynman, 1939). Basis superposition errors are also avoided as PW are orthogonal across the system. In principle, the basis set should be complete enough to represent any wave-function but this requires an infinite number of PWs or AOs and, in practice; the functions are truncated at the kinetic energy that sufficiently converges the total energy calculation. The results presented in thesis are carried using the VASP code which employs plane-wave basis set.

2.2.8 Periodicity

Simulating an isolated system containing few atoms is straightforward. But often it is required to simulate a bulk solid material, which would require a great many atoms. However, this can be avoided by simulating a unit-cell of the solid and periodically repeating it in all 3 spatial dimensions. Surfaces can be simulated in a similar way, by leaving a vacuum gap in one of the dimensions. As well as enabling the simulation of bulk solids and surfaces, periodic boundaries also have some computational benefits. When a periodic system is being treated, Blöch's theorem can be applied. Blöch's theorem states that, the wavefunction of an electron within a perfectly periodic potential may be written as:

$$\psi_{n,k} = u_{n,k} e^{ik.r} \tag{2.15}$$

where $u_{n,k}$ is a function that has the periodicity of the underlying lattice, and k is a wavevector confined to the first Brillouin Zone. Since $u_{n,k}$ is a periodic function, we may expand it in terms of a Fourier series:

$$u_{n,k} = \sum_{G} c_{j,G} e^{iG.r} \tag{2.16}$$

where the *G* are reciprocal lattice vectors defined through $G \cdot R = 2\pi m$, where *m* is an integer, *R* is a real space lattice vector and the $c_{j,G}$ are plane-wave expansion coefficients. The electron wavefunctions may therefore be written as a linear combination of plane-waves as:

$$\psi_{n,k} = \sum_{G} c_{j,k+G} e^{i(k+G).r} \tag{2.17}$$

In principle, the series in equation 2.16 should be infinite; but in practice, the series is truncated in order that it may be handled computationally. The coefficients for the plane-waves have a kinetic energy $\frac{\hbar}{2m}|k+G|^2$, and plane-waves with high kinetic energy are typically less important than those of low kinetic energy. One may thus introduce a kinetic energy cut-off E_{cut} in order to achieve a finite basis set. The kinetic energy cut-off is defined through $E_{cut} = \frac{\hbar}{2m}|k+G|^2$, and thus this fixes the highest reciprocal lattice vector *G* used in the plane-wave expansion, resulting in a finite basis set.

Given that each electron occupies a state of definite *k*, the infinite number of electrons within the solid gives rise to an infinite number of *k*-points. At each *k*-point, only a finite number of the available energy levels will be occupied. Thus one only needs to consider a finite number of electrons at an infinite number of *k*-points. This may seem to be replacing one infinity (number of electrons) with another one (number of k-points) to little discernible advantage. However, one does not need to consider all of these *k*-points; rather, since the electron wavefunctions will be almost identical for all values of *k* that are sufficiently close, one can represent the wavefunctions over a region of reciprocal space by considering the wavefunction at a single *k*-point. It is therefore sufficient to consider the electronic states at a finite number of *k*-points in order to determine the ground-state density of the solid. The net effect of Blöch’s theorem therefore has been able to change the problem of an infinite number of electrons to one of considering only the number of electrons in the unit cell at a finite number of *k*-points chosen so as to appropriately sample the Brillouin zone.

2.2.8 Pseudopotentials

Although the Kohn-Sham equations have been shown to be tractable when plane-wave basis sets are used to expand the electron wavefunctions, an all-electron calculation including both the core and valence electrons, along with the full Coulombic potential of the nuclei would still be prohibitively expensive using a plane-wave basis set. This is because the tightly bound core orbitals, and the highly oscillatory nature of the valence electrons, demand that a high value of E_{cut}, and hence the number of plane-waves to be used in order to accurately describe the electronic wavefunctions (Payne *et al.*, 1992). However, it is possible to partition the electrons between core and valence states; such a partition is possible because majority of the physical/chemical properties of solids depend upon the valence electrons; in contrast, the core electrons are almost environment independent. It is for this reason that the pseudopotential approximation was introduced (Phillips *et al.*, 1958, 1959; Cohen & Heine, 1970). The core electrons and ionic potential are removed and replaced with a pseudopotential that acts on a set of pseudo wave functions, reducing the computational cost significantly. The pseudopotential is constructed such that the pseudo wave-function has no radial nodes within the core region and that the pseudo wave-functions and potential agree with the *true* wave-function and potential outside some cut-off radius E_{cut}. Further, the pseudopotential must preserve the atomic properties of the element, including phase shifts on scattering across the core; as these phase shifts will in general be dependent upon the angular momentum state. In general, a pseudopotential must be non-local, *i.e.*, it must have projectors for the different angular momentum states.

The main drawback of using a pseudopotential in contrast to an all-electron method is that it compromises the universality of the method. A pseudopotential must do its best to accurately reflect the interaction between core and valence electrons, in all the different possible environments into which an atom could be placed. This is known as the transferability of the pseudopotential. There are different kinds of pseudopotentials. Norm-conserving pseudopotentials (Hamalm *et al.*, 1979) ensure that the charge within the cut-off region is equal to the charge of the core electrons. In essence, the core region of the atom is not greatly affected by the surrounding environment and so aids transferability. There are also ultra-soft pseudopotentials (Kresse *et al.*, 1999), which result in smoother Kohn-Sham wave-functions and thus require fewer plane-waves. The ultrasoft pseudopotentials have the merit to make calculations for first-row elements and for systems with *d*− or *f*−electrons feasible at tractable effort. The criterion for the quality of a pseudopotential is not how well it matches experiment, but how well it reproduces the results of accurate all-electron calculations. Due to the non-linearity of the exchange interaction between the valence and core electrons, pseudopotential calculations have some drawback for all systems where the overlap between valence- and core-electron densities is not completely negligible. This deficiency may be removed by using the projector-augmented wave method.

The projector-augmented wave (PAW) method, originally introduced by Blöchl (1994) uses plane-waves in the interstitial region between atoms and a localized basis close to the atoms. This means that the PAW method has access to the full all-electron wave-function and can therefore, be a more transferable method than a pure plane-wave implementation. As the PAW method contains all the electrons in the system, it has at least some variational freedom in the core region that enables it to produce more accurate results than a frozen core approximation. However, retaining the plane-waves for most of the system helps keep the computational cost down and retains the attractiveness of a single convergence parameter, namely the PW cut-off.

2.3 The DFT+U Method

Standard DFT methods often perform poorly in describing the electronic and magnetic properties of strongly correlated materials, *i.e.*, materials containing *d*- and *f*-electrons. Many transition metal oxides belong to this class (Maekawa *et al.*, 2010). Standard DFT methods predict band gaps that are too small or non-existent, magnetic moments too small for the semiconducting transition metal oxides (Rohrbach *et al.*, 2004). Theoretical models of the electronic structure of strongly correlated materials must therefore include electronic correlation to be accurate. One method of correcting the strong intra-atomic electronic correlations is by adopting the DFT+U approach, which adds an on-site Coulomb repulsion to the DFT Hamiltonian. Different formulations of the DFT+U approximation have been devised (Anisimov *et al.*, 1991; Ebert *et al.*, 2003; Dudarev *et al.*, 1998), but whichever form is taken, the main concept is to correct the LDA or GGA with a mean-field Hubbard-like term (Hubbard, 1963), designed to improve the description of the electron correlations relating to the on-site Coulomb repulsions. In this work, we have used the DFT+U approach proposed Dudarev *et al.*, (1998), which takes the form:

$$E_U = \frac{U - J}{2} \sum_{\sigma} \left(n_{m,\sigma} - n_{m,\sigma^2} \right) \tag{2.18}$$

where U and J are the effective Coulomb and exchange parameters, respectively, and n is the occupation number of a *d*-orbital of number m with spin σ. U and J can in principle, be computed from first principles. In reality, however, the theoretical values of U and J give poor results, and therefore, these parameters are adjusted by fitting to experimental data, such as the oxide band gap or the lattice parameters. Because equation 2.18 depends on only the difference, $U-J$, can be replaced with one variable $U_{eff} = U-J$ for the sake of brevity.

2.4 The van der Waals DFT

While today's standard DFT approaches, such as the LDA and GGA are particularly successful for describing materials with strong local atomic bonds, they fail to accurately describe the weak non-local long-range dispersion forces between atoms separated by empty space (Rydberg *et al.*, 2003). Dispersive van der Waals interactions (vdW) are common in sparse systems (systems with vast regions having very low electron density) including layered materials like graphite, BN, MoS_2, PbO, and tetragonal FeS. They are also ubiquitous in interacting systems, like in adsorption systems and in biostructures like DNA, protein structure and protein folding. To understand and accurately describe these sparse systems, there is the need to account for both the strong local atomic bonds and the weak non-local van der Waals forces between atoms separated by empty space.

The basic requirement for any DFT-based dispersion scheme should be that it yields reasonable $-1/r^6$ asymptotic behaviour for the interaction of particles in the gas phase, where r is the distance between the particles. Several schemes within DFT have now been proposed to account for dispersion in one way or another (Dobson & Dinte, 1996; Andersson *et al.*, 1996; Hult *et al.*, 1996; Adamson *et al.*, 1999; Rydberg *et al.*, 2003; Dion *et al.*, 2004; Becke & Johnson, 2005; Tkatchenko *et al.*, 2009; Harl *et al.*, 2009; Antony *et al.*, 2010). Currently, there are two commonly used approaches to include dispersive forces in DFT: (1) the design of new functionals derived in a fully *ab* initio fashion as recommend by Dion *et al*. 2004, (2) an empirical correction to the standard DFT energy and gradient on the basis of the empirical London formula as re-proposed by Grimme 2004, 2006, and later improved by Tkatchenko and co-workers (Tkatchenko *et al.*, 2009). The scheme used in this thesis is the Grimme's correction scheme, which is hereafter, termed the DFT-D2 method (Grimme, 2006). In this scheme, an additional energy term is added to the Kohn-Sham DFT energy to account for the missing long-range attraction as follows:

$$\mathrm{E}_{\text{DFT-D}} = \mathrm{E}_{\text{KS-DFT}} + \mathrm{E}_{\text{disp}} \tag{2.19}$$

where

$$E_{disp} = -s_6 \sum_{i=1}^{N-1} \sum_{j=i+1}^{N} \frac{C_6^{ij}}{R_{ij}^6} f_{damp}(R_{ij}) \tag{2.20a}$$

Here, N is the number of atoms in the system, C_6^{ij} denotes the dispersion coefficient for atom pair ij, $s_6 = 0.75$ is a global scaling factor that is a functional dependent scaling factor, and R_{ij} is the interatomic distance between atoms *i* in the reference cell and *j* in the neighbouring cells (Grimme, 2006). All pairs farther than 30 Å are disregarded in the summations because of their negligible contribution. In order to avoid double counting for small interatomic distances, a damping function f_{damp} must be used, which is given by:

$$f_{damp}(R_{ij}) = \frac{1}{1 + e^{-d\left(\frac{R_{ij}}{R_{vdW}} - 1\right)}} \tag{2.20b}$$

where R_{vdW} is the atomic van der Walls' radii and *d* is the damping function steepness (*d* = 20), (Grimme, 2006). In the Grimme's approach, R_{vdW} is set as the atomic van der Waals radii, which are 1.562, 1.342, 1.683, 1.760, 1.397, 1.452, and 1.001 Å for Fe, O, S, As, N, C, and H respectively (the elements that constitute the systems investigated in this thesis). The definition of the C_6^{ij} coefficients in equation 2.21a follows the well-known geometrical mean:

$$C_6^{ij} = \sqrt{C_6^i C_6^j} \tag{2.21a}$$

$$C_6^i = 0.05 N I_p^i \alpha^i \tag{2.21b}$$

In equation 2.21b, N is the number of the shell electrons and has values of 2, 10, 18, 36, 54, and 72 for atoms from rows 1−6 in the periodic table. In the DFT-D2 scheme the C_6^i parameters were derived from the atomic polarizabilities, α^i, and ionization energies, I_p^i, leading to 10.80, 0.70, 5.57, 16.370, 1.230, 1.750, and 0.140 Jnm^6/mol Fe, O, S, As, N, C, and H respectively (Grimme, 2004, 2006). Data for all elements up to Xe are available, and this scheme is probably the most widely used method for accounting for dispersion in DFT at present.

2.5 Calculation of forces

Forces acting on individual atoms are very important to determine the optimized or relaxed geometry of the system, bond strengths, etc. Forces can directly be obtained from the first derivative of the total energy with respect to atomic displacements. This however, needs calculation of self-consistent energies at many different configurations; thus it gets cumbersome to extract the force constants for different bonds in the system. This problem can be overcome if the forces are calculated by following the description by Hellmann-Feynman theorem (Hellmann, 1937; Feynman, 1939) which states that the first derivative of the eigenvalues of a

Hamiltonian, $\hat{H}_\lambda$, that depends on a parameter λ is given by the expectation value of the derivative of the Hamiltonian:

$$\frac{\partial E_\lambda}{\partial \lambda} = \left\langle \psi_\lambda \middle| \frac{\partial \hat{H}_\lambda}{\partial \lambda} \middle| \psi_\lambda \right\rangle \tag{2.22}$$

Where ψ_λ is the eigenfunction of $\hat{H}_\lambda$ corresponding to the E_λ eigenvalue: $H_\lambda \psi_\lambda = E_\lambda \psi_\lambda$. In the Born-Oppenheimer approximation, nuclear coordinates act as parameters in the electronic Hamiltonian. The force (F_I) acting on the I^{th} nucleus in the electronic ground state is thus;

$$F_I = -\frac{\partial E_{B-O}(R)}{\partial R_I} = -\left\langle \psi(R) \middle| \frac{\partial \hat{H}_{B-O}(R)}{\partial R_I} \middle| \psi(R) \right\rangle \tag{2.23}$$

where $\psi(R)$ is the electronic ground-state wave-function of the Born-Oppenheimer Hamiltonian and E_{B-O} is the Born-Oppenheimer energy surface. This Hamiltonian depends on R *via* the electron-ion interaction that couples to the electronic degrees of freedom only through the electron charge density. The equilibrium geometry of the system is given by the condition that the forces acting on individual nuclei vanish.

$$F_I = -\frac{\partial E(R)}{\partial R_I} = 0 \tag{2.24}$$

2.6 Electronic structure analysis

In addition to the optimized structure and the ground state energy that are calculated for the system under investigation, all observables that can be derived from the electronic structure are also available.

2.6.1 Density of states

One of the principal aims of computational chemistry is to understand how chemical bonds are created and how the molecules interact with solid surfaces. Density of states (DOS) is the representation of the number of states in a specified energy. Inside the Brillouin zone, each k-point defines energy levels that form energy bands which can be represented by means of a band diagram plot. A high DOS at a specific energy level means that there are many states available for occupation. A DOS of zero means that no states can be occupied at that energy level. The energy level within the material's DOS that is very useful for characterizing the electrical behaviour of the material is known as the Fermi level (E_F). In an insulator, E_F lies within a large band gap, far away from any states that are able to carry current. In an intrinsic or lightly doped semiconductor, E_F is close enough to a band edge that there are a dilute number of thermally excited carriers residing near that band edge. In a metal or semimetal, E_F lies within a delocalized band. A large number of states nearby E_F in a metal or semimetal are thermally active and readily carry current.

The DOS can also be projected onto each ion in a given system using the volume that it occupies. Further projections onto the *s*, *p*, and *d* bands can enable interpretation of the relative energies of different bands and their interactions in bonds. For adsorption systems, charge transfers, ionic interactions and covalent interactions can also be analyzed by inspecting the displacements and intensity changes of the interacting bands.

2.6.2 Charge density analysis

Decomposing the charge of a material into contributions from individual atoms can provide new information for material properties. The decomposed charged can be interpreted as to indicate charge transfer process in adsorption systems and thus enables the characterization of the different kind of bonding between an adsorbate and a substrate. In covalent bonds, significant charge transfer is often calculated, whereas in physisorbed interactions, small or negligible charge transfer occurs between adsorbates and a substrate. A number of methods exist for charge segregation into atomic charges which can give quite varied results (Guerra *et al.*, 2004). The method used in this thesis is the Bader charge analysis method (Bader, 1990) as implemented in the VASP code using the Henkelman algorithm (Henkelman *et al.*, 2006, Tang *et. al.*, 2009). The Bader method determines the zero flux surface in the charge density around an atom. The volume enclosed by this surface is termed the Bader basin, inside of which the electron density is summed in order to find the Bader charge for that atom. Due to electron delocalization in DFT, the Bader method commonly underestimates ionic charges, as is clearly shown even in the highly ionic NaCl and MgO systems, where the charges are severely underestimated, by 12−14 %, compared to the formal oxidation state of +1 and +2 for Na and Mg, respectively (Henkelman *et al.*, 2006). However, the method is reliable in identifying trends between similar systems.

2.6.3 Transition states

One of the common and important problems in theoretical chemistry and in condensed matter physics is the identification of a lowest energy path for the rearrangement of a group of atoms from one stable configuration to another. Such a path is often referred to as the ‘minimum energy path’ (MEP). It is frequently used to define a ‘reaction coordinate’ (Marcus, 1996) for transitions, such as chemical reactions, changes in conformation of molecules, or diffusion processes in solids. The potential energy maximum along the MEP is the saddle point energy which gives the activation energy barrier. Many different methods have been developed for finding the reaction path and saddle points (see McKee & Page, 1993 for a review). The method implemented in this thesis is the climbing image nudged elastic band method (CI-NEB) (Henkelman *et al.*, 2000). The CI-NEB method represents a small modification to the direct NEB method, as the highest energy image is driven up to the saddle point. This image does not feel the spring forces along the band; instead, the true force at this image along the tangent is inverted. In this way, the image tries to maximize its energy along the band, and minimize in all other directions. When this image converges, it will be at the exact saddle point. The direct NEB method works by optimizing a number of intermediate images along the reaction path where each image finds the lowest energy possible while maintaining equal spacing to neighbouring images. This constrained optimization is done by adding spring forces along the band between images and by projecting out the component of the force due to the potential perpendicular to the band. An identified transition state is further confirmed through vibrational frequency calculations, in which only one imaginary frequency is obtained corresponding to the reaction coordinate. The reaction energy (ΔE) is calculated as the total energy difference between the final state and the initial state and the reaction barrier (E_a) is defined as the total energy differences between the initial state and the saddle point.

2.6.4 Vibrational frequencies

Vibrational frequency calculations are necessary for several reasons: for example, vibrational frequencies help to locate the steady state on the hypersurface and ensure that the optimized stationary point is a minimum on the potential energy surface (or a transition state). They are also important for simulating the infrared (IR) or Raman spectra which can be compared directly with experimental data. Vibrational frequencies also enable calculation of the molecular partition function and thus prediction of thermodynamic functions at temperatures other than 0 K and finite pressure.

Vibrational frequencies are related directly with the force constants, which are the second derivatives of the total energy with respect to atomic displacements. The vibrational frequencies ω are determined by the eigenvalues of the Hessian of the Born-Oppenheimer energy, scaled by the nuclear masses:

$$\det\left|\frac{1}{\sqrt{M_I M_J}}\frac{\partial^2 E(R)}{\partial R_I \partial R_J} - \omega^2\right| = 0. \tag{2.25}$$

To calculate the Hessian matrix, finite differences are used, *i.e.*, each ion is displaced in the direction of each Cartesian coordinate, and from the forces, the Hessian matrix is determined by equation 2.26. A stationary point is confirmed as a local minimum if all second derivatives are positive *i.e.*, the vibrational frequencies are all real, whereas if one imaginary frequency is found then, the stationary point can be assigned to be saddle point.

$$H(f)=\begin{bmatrix} \frac{\partial^2 f}{\partial r_1{}^2} & \frac{\partial^2 f}{\partial r_1 \partial r_2} & \cdots & \frac{\partial^2 f}{\partial r_1 \partial r_n} \\ \frac{\partial^2 f}{\partial r_2 \partial r_1} & \frac{\partial^2 f}{\partial r_2{}^2} & \cdots & \frac{\partial^2 f}{\partial r_2 \partial r_n} \\ \vdots & \vdots & \ddots & \vdots \\ \frac{\partial^2 f}{\partial r_n \partial r_1} & \frac{\partial^2 f}{\partial r_n \partial r_2} & \cdots & \frac{\partial^2 f}{\partial r_n \partial r_n} \end{bmatrix} \tag{2.26}$$

2.6.5 Temperature programmed desorption (TPD)

Temperature-programmed desorption (TPD) techniques are important methods for the determination of kinetic and thermodynamic parameters of desorption processes of molecules from a surface when the surface temperature is increased (Wang *et al.*, 2013). TPD was first proposed in 1963 by Amenomiya and Cvetanovic, which is also known as thermal desorption spectroscopy (TDS), although the technique has nothing to do with spectroscopy. When molecules or atoms come in contact with a surface, they adsorb onto it, minimizing their energy by forming a bond with the surface. If the surface is heated, the energy transferred to the adsorbed species due to increase in temperature will cause some particular adsorbed species to desorb from the surface, resulting in a pressure increase. As the temperature continues to rise further, the amount of the species on the surface will reduce, causing the pressure to decrease again. This results in a peak in the pressure versus temperature plot. The temperature of the peak maximum provides information on the binding energy of the bound species.

In TPD experiments, the peak temperature is directly related with the desorption energy (E_{des}) of the sample gas, and the Polanyi−Wigner equation relates the rate of desorption (r_{des}) to the desorption energy. The desorption rate of n$^{\mathrm{th}}$ order Polanyi−Wigner equation can be written as (Laidler & King, 1983):

$$r_{des}(t) = -\frac{d\theta_{A*}}{dt} = \upsilon_n \theta_{A*}^{n} \exp\left(-\frac{E_{des}}{RT}\right) \tag{2.27}$$

Where θ_{A*} denotes the surface coverage of the adsorbate A in monolayers (ML), t the time (s), υ_n the pre-exponential factor, R the gas constant, and T the temperature.

The desorption process can be represented as follows:

$$\text{A*} \rightarrow \text{A} + * \tag{2.28}$$

where A*, A, and * denote the adsorbed molecule, free molecular, and the free site on the surface, respectively. From micro-kinetic model, the rate of desorption (r_{des}) can be defined by equation 2.29, where k_{des} (s^{-1}) is the rate constant.

$$r_{des}(t) = k_{des}\theta_{A*} \tag{2.29}$$

For the first-order Polanyi−Wigner equation, the definition of the desorption rate from equation (2.27) is analogous to equation (2.29), and it generates

$$\upsilon_n = k_{des} \exp\left(\frac{E_{des}}{RT}\right) \tag{2.30}$$

The rate constant for a given elementary step can be derived from the conventional classical harmonic transition state theory of Evans-Polanyi-Eyring (Laidler & King, 1983) as in equation 2.31,

$$k_{des} = \left(\frac{k_b T}{h}\right)\left(\frac{q^{\#}}{q}\right)\exp\left(-\frac{\Delta E}{k_B T}\right) \tag{2.31}$$

Where h is the Planck constant, $q^{\#}$ is the partition function of the transition state, and q is the partition function of the reactants. Partitions functions include translational, rotational, vibrational, and electronic contributions which are summarized as follows:

Translational partition function: $$q_{trans} = \left(\frac{2\pi m k_B T}{h^2}\right)^{3/2} \tag{2.32}$$

Rotational partition function (Linear): $q_{rot}^{linear} = \frac{1}{\sigma}\left(\frac{k_B T}{hB}\right)$ (2.33)

Rotational partition function (Nonlinear): $q_{rot}^{nonlinear} = \frac{1}{\sigma}\left(\frac{k_B T}{hB}\right)^{3/2}\sqrt{\frac{\pi}{ABC}}$ (2.34)

Vibrational partition function: $q_{vib} = \prod_{i}^{DF}\left(\frac{1}{1-e^{-hv_i/k_B T}}\right)$ (2.35)

Electronic partition function: $q_{elec} = (2S+1)e^{-E_g/k_B T}$ (2.36)

Total partition function: $q = q_{tran} \times q_{rot} \times q_{vib} \times q_{elec}$ (2.37)

Where σ is the symmetry factor, A, B, and C are rotational constants, v_i is the vibrational frequency of the i^{th} mode, DF is the degree of freedom (3N−5 for linear molecules and 3N−6 for nonlinear molecules), S is the total spin angular momentum, and E_g is the electronic energy from the ground state.

In this work, the TPD spectra were assumed to be recorded in a batch-type reactor, and the adsorbates were pre-adsorbed on the surface. We assume that the pump rate of the system is indefinitely large, thus no gasses will absorb during the desorption. In this microkinetic simulation, the TPD intensity is equal to the desorption rate of the adsorbate, and the relationship between surface coverage of A (θ_A) and time (t) in the desorption process could be obtained by solving the ordinary differential equation (ODE) of equation 2.27. All ODEs in this work were solved by numerical method using Maple software (URL: www.maplesoft.com/products/maple/).

2.6.6 Determination of elastic constants

The elastic tensors were derived using the standard finite difference technique, where the calculation of the second order elastic constants (C_{ij}) is achieved through the description of a linear elastic strain response of the material as it opposes to a certain stress. Each C_{ij} was derived *via* the second-order Taylor expansion of the total energy with respect to the applied distortion, equation (2.38):

$$C_{ij} = \frac{1}{V_o} \frac{\partial^2 E}{\partial \varepsilon_i \partial \varepsilon_j} \tag{2.38}$$

where E is the total energy of the strained cell, ε is the component of the applied strain, and V_o is the equilibrium unit cell volume. The tensor of elastic constants for anisotropic material takes the form:

$$C_{ij} = \begin{bmatrix} C_{11} & C_{21} & C_{31} & C_{41} & C_{51} & C_{61} \\ C_{12} & C_{22} & C_{32} & C_{42} & C_{52} & C_{62} \\ C_{13} & C_{23} & C_{33} & C_{43} & C_{53} & C_{63} \\ C_{14} & C_{24} & C_{34} & C_{44} & C_{54} & C_{64} \\ C_{15} & C_{25} & C_{35} & C_{45} & C_{55} & C_{65} \\ C_{16} & C_{26} & C_{36} & C_{46} & C_{56} & C_{66} \end{bmatrix} \tag{2.39}$$

Tetragonal crystal structures have higher symmetry than a completely anisotropic single-crystal; and therefore, for a complete description of its constitutive behaviour, only six independent parameters are needed. The elasticity matrix for tetragonal crystal structures can be written in terms of the six independent parameters as:

$$C_{ij} = \begin{bmatrix} C_{11} & C_{12} & C_{13} & & & \\ C_{12} & C_{11} & C_{13} & & & \\ C_{13} & C_{13} & C_{33} & & & \\ & & & C_{44} & & \\ & & & & C_{44} & \\ & & & & & C_{66} \end{bmatrix} \tag{2.40}$$

Since the strain tensor is symmetric ($\alpha_{ij} = \alpha_{ji}$), the designations *xx* = 1, *yy* = 2, *zz* = 3, *xy* = *yx* = 6, *xz* = *zx* = 5, and *yz* = *zy* = 4, are introduce (Landau & Lifshitz, 1970). The distortion (strain) matrix in the general case has the following form:

$$\varepsilon = \begin{bmatrix} 1+\delta_{xx} & \delta_{xy} & \delta_{xz} \\ \delta_{yx} & 1+\delta_{yy} & \delta_{yz} \\ \delta_{zx} & \delta_{zy} & 1+\delta_{zz} \end{bmatrix} \tag{2.41}$$

In order to determine the independent elastic constants for the tetragonal FeS, different strains (distortions) must be applied. To determine C_{11}, the distortion matrix takes the form:

$$\varepsilon = \begin{bmatrix} 1+\delta & 0 & 0 \\ 0 & 1 & 0 \\ 0 & 0 & 1 \end{bmatrix} \tag{2.42}$$

Where $\delta = \frac{a'}{a}$ is the dimensionless strain ratio, a' is the deformed and a is the undeformed lattice parameter. This distortion changes the size of the basal plane in the *x* axis, while keeping the *y* and *z* axes constant. The expression for the internal energy of the unit cell as a function of this strain is given by a Taylor expansion about E(0):

$$E(\varepsilon_1) = E(0) + \frac{1}{2}\left.\frac{\partial^2 E}{\partial \varepsilon_1^2}\right|_0 \delta^2 + \cdots \tag{2.43}$$

This can be written in terms of the elastic constant as

$$\begin{aligned} E(\varepsilon_1) &= E(0) + \frac{1}{2} V_o C_{11} \delta^2 + \cdots \\ &= a + b\delta^2 + \cdots \end{aligned} \tag{2.44}$$

Where a and b are the coefficient of a polynomial fit of E versus δ. Thus from equation (2.38), C$_{11}$ can be written as:

$$C_{11} = \frac{1}{V_o}\frac{\partial^2 E}{\partial\varepsilon_i \partial\varepsilon_j} = \frac{2b}{V_o} \tag{2.45}$$

Similarly, the C$_{12}$ elastic constant can be calculated by applying the following deformation matrix.

$$\varepsilon = \begin{bmatrix} 1+\delta & 0 & 0 \\ 0 & 1+\delta & 0 \\ 0 & 0 & 1 \end{bmatrix} \tag{2.46}$$

In this distortion, the strain is applied in both the *a* and *b* directions simultaneously while keeping *c* axes constant. The energy associated with this distortion is given by:

$$E(\varepsilon_1,\varepsilon_2) = E(0,0) + V\left(\frac{1}{2}C_{11} + \frac{1}{2}C_{22} + \frac{1}{2}C_{12} + \frac{1}{2}C_{21}\right)\delta^2 + \cdots \tag{2.47}$$

From the symmetry considerations, C$_{11}$ = C$_{22}$ and C$_{12}$ = C$_{21}$, this expression becomes;

$$E(\varepsilon_1,\varepsilon_2) = E(0,0) + V\left(C_{11} + C_{12}\right)\delta^2 + \cdots \tag{2.48}$$

$$= a + b\delta^2 + \cdots$$

Thus $C_{11} + C_{12} = \frac{b}{V_o}$. Therefore C$_{12}$ may be found once C$_{11}$ has been determined.

A summary of the other distortion matrices and the corresponding relationship between their elastic constants and the second order coefficient of fit are provided in Table 2.1. For tetragonal crystals structures, the six independent elastic coefficients are positive and obey the well-known Born criterion for a mechanically stable system: $C_{11} > 0$, $C_{33} > 0$, $C_{44} > 0$, $C_{66} > 0$, $C_{11}-C_{12} > 0$, $C_{11}+C_{33}-2C_{13} > 0$ and

2(C$_{11}$+C$_{12}$)+4C$_{13}$ > 0 (Born, 1954). The bulk compression moduli (B) and shear moduli (G) of single crystals were determined in the Voigt (V) approximation (Shein & Ivanovskii, 2008; Voigt, 1928) using equations 2.49 and 2.50 respectively.

$$B_V = \frac{1}{9}\left(2C_{11} + 2C_{12} + C_{33} + 4C_{13}\right) \tag{2.49}$$

$$G_V = \frac{1}{30}\left(4C_{11} - 2C_{12} + 2C_{33} - 4C_{13} + 12C_{44} + 6C_{66}\right) \tag{2.50}$$

The elastic moduli are useful in predicting the structural stability of materials: the B$_V$ measures the material's resistance to uniform compression, whereas the G$_V$ measures the material's response to shearing strain.

Distortion matrix	Relationship between the elastic constant and the second order of fit
$\varepsilon_{11} = \begin{bmatrix} 1+\delta & 0 & 0 \\ 0 & 1 & 0 \\ 0 & 0 & 1 \end{bmatrix}$	$\frac{2b}{V_o}$
$\varepsilon_{33} = \begin{bmatrix} 1 & 0 & 0 \\ 0 & 1 & 0 \\ 0 & 0 & 1+\delta \end{bmatrix}$	$\frac{2b}{V_o}$
$\varepsilon_{44} = \begin{bmatrix} 1 & 0 & 0 \\ 0 & 1 & \delta \\ 0 & \delta & 1 \end{bmatrix}$	$\frac{b}{2V_o}$
$\varepsilon_{66} = \begin{bmatrix} 1 & \delta & 0 \\ \delta & 1 & 0 \\ 0 & 0 & 1 \end{bmatrix}$	$\frac{b}{2V_o}$
$\varepsilon_{12} = \begin{bmatrix} 1+\delta & 0 & 0 \\ 0 & 1+\delta & 0 \\ 0 & 0 & 1 \end{bmatrix}$	$C_{11} + C_{12} = \frac{b}{V_o}$
$\varepsilon_{13} = \begin{bmatrix} 1+\delta & 0 & 0 \\ 0 & 1 & 0 \\ 0 & 0 & 1+\delta \end{bmatrix}$	$C_{11} + C_{33} + 2C_{13} = \frac{2b}{V_o}$

TABLE 2. 1: Relationship between the elastic constant and the second order of fit from a given distortion matrix of a tetragonal crystal ($a = b \neq c\,;\alpha = \beta = \gamma = 90^o$).

2.6.7 Surface modelling

Different surfaces can be created when a bulk crystal is cleaved along different crystallographic planes commonly referred at as Miller indices. A family of lattice planes is determined by three integers: h, k, and l, the Miller indices. They are written as (h k l), and each index denotes a plane orthogonal to a direction (h, k, l) in the basis of the reciprocal lattice vectors. For example, Miller index (100) represents a plane orthogonal to direction h; index 010 represents a plane orthogonal to direction k, and index 001 represents a plane orthogonal to l. If the plane cuts an axis on the negative side of the origin, the corresponding index is negative and by convention it is denoted with an over bar, e.g. $(h\bar{k}l)$ indicates the plane cuts the y-axis on the negative side of the origin. For hexagonal and rhombohedral lattice systems, it is possible to use the Bravais-Miller index which has 4 numbers (h k i l), $i = -(h + k)$. Here h, k and l are identical to the Miller index, and i is a redundant index.

The created surface is the place where molecules from the gas phase or a liquid come into contact with the material. Atoms at the surface commonly tend to have lower coordination than those in the bulk. Due to changes in the coordination of surface atoms and the presence of dangling bonds in some cases, the surface geometry will relax or possibly even reconstruct, to let the surface atoms find their new equilibrium positions. Two common models used in surface simulations include the cluster model and the periodic slab model. The cluster model treat the surface as a small isolated cluster of atoms, one facet of which has the same symmetry and atomic arrangement as the crystal surface intended to study. In a periodic slab model, periodicity in two lateral directions generates exposed surfaces with vacuum on either side of the slab (see Figure 2.1). Two important things should be kept in mind when using the periodic slab model. The vacuum thickness should be large enough to avoid surfaces of consecutive slabs from interacting with each other, and the thickness of the slab should also be thick enough to avoid interaction between the two surfaces of one slab. One could “freeze” one end of the slab usually at the bottom to mimic the bulk; whiles the atoms at the topmost layers are allowed to relax unconstrainedly. This is denoted by relaxed and fixed atoms in Figure 2.1. This approach permits the simulation of a single surface and allows more choice in complex surfaces.

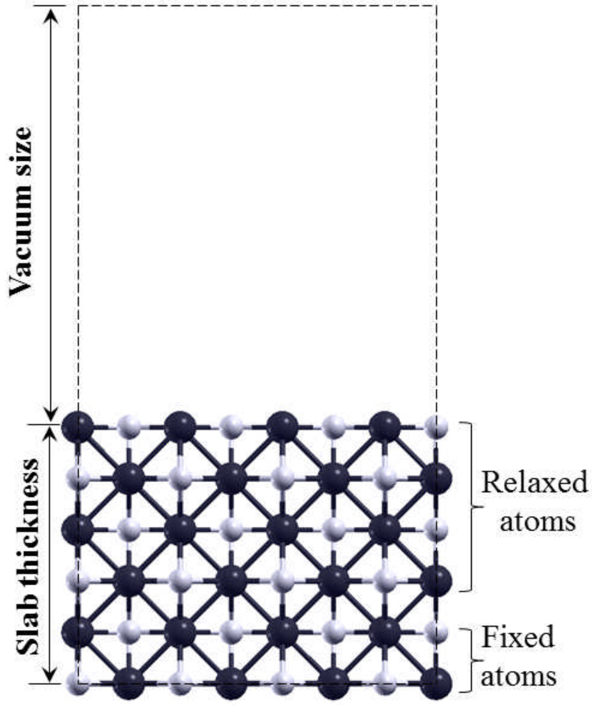

FIGURE 2.1: Representation of a periodic slab model showing a slab constructed with six atomic layers thickness and a vacuum region.

The different low-index surfaces investigated in this thesis were created from the optimized bulk materials, using the METADISE code (Watson *et al.*, 1996), which does not only consider periodicity in the plane direction but also provides the different atomic layer stacking resulting in a zero dipole moment perpendicular to the surface plane, as is required for reliable and realistic surface calculations (Tasker, 1979). The dipole method, pioneered by Tasker, considers the crystal as a stack of planes, where three possibilities can arise as depicted in Figure 2.2 (Tasker, 1979). In type I, each plane has overall zero charge because it is composed of anions and cations in stoichiometric ratio which makes it non-dipolar, whereas in type II, the stacking of three symmetrically charged planes cancels out the dipole moment perpendicular to the surface. In type I and II, no reconstruction of the surface is needed because the repeat unit is non-dipolar perpendicular to the surface. However, in type III surfaces, alternating charged planes stack in a sequence that produces a dipole moment perpendicular to the surface, but the surface can be reconstructed to have zero dipole moment perpendicular to surface by moving half of the ions with the same charge from the top to the bottom of the slab.

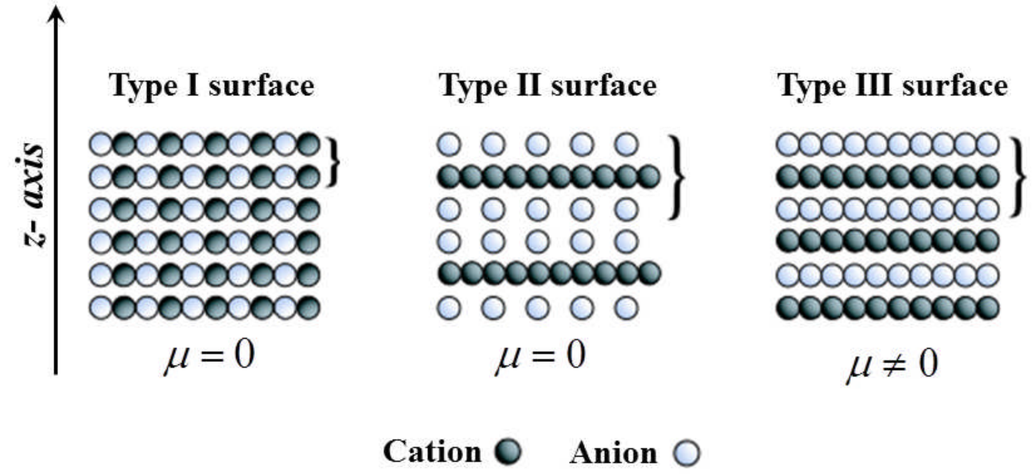

FIGURE 2.2: Surfaces classification according to Tasker (1979): (a) Type I, each plane contains an equal number of cations and anions (the net dipole moment is zero; $\mu = 0$); (b) Type II, each plane is charged, but there is no net dipole moment perpendicular to the surface ($\mu = 0$); (c) Type III, charged planes and dipole moment normal to the surface ($\mu \neq 0$).

2.2.7.1 Surface stabilities

The surface stability is an important property of the surface, because it influences the reactivity. Generally, the less stable surfaces tend to be more reactive towards adsorbing species than the more stable ones (de Leeuw *et al.*, 2007). The free surface energy of a given plane is a measure of the stability of that particular surface, where a small, positive value indicates a stable surface. Using the periodic slab model containing slabs with two surfaces, the surface energy, which is the energy required to create a given Miller index surface from the bulk material, can be calculated from the combination of the surface energy of the relaxed and the unrelaxed surfaces as:

$$\gamma_u + \gamma_r = \frac{E_{slab} - nE_{bulk}}{A} \tag{2.51}$$

where γ_u and γ_r denote the unrelaxed and relaxed surface energies, respectively, E_{slab} is the energy of the slab, nE_{bulk} is the energy an equal number, (*n*), of the bulk FeS atoms, and *A* is the area of one side of the slab.

Before geometry relaxation of the constructed surface in the slab model, the slab contains two unrelaxed surfaces both of which have equal surface energies ($\gamma_u = \gamma_r$). Thus the unrelaxed surface energy (γ_u) may be obtained from a single point calculation as:

$$\gamma_u = \frac{E_{slab}^{unrelaxed} - nE_{bulk}}{2A} \tag{2.52}$$

where $E_{slab}^{unrelaxed}$ is the energy of the unrelaxed slab. When only one side of the slab (the topmost layer atoms) is allowed to relax unconstrainedly, keeping the bottom layer atoms fixed at the bulk parameters as implemented in this thesis, the additional energy due to the relaxed surface at the top of the slab must be separated from the energy of the unrelaxed surface at the bottom, as the two differ ($\gamma_u \neq \gamma_r$). From equation (2.51), the relaxed surface energy (γ_r) can thus be calculated from the total energy of the relaxed slab as

$$\gamma_r = \frac{E_{slab}^{relaxed} - nE_{bulk}}{A} - \gamma_u \tag{2.53}$$

By substituting γ_u from equation (2.52) into equation (2.53), the expression for calculating the relaxed surface energy (γ_r) is obtained as:

$$\gamma_r = \frac{E_{slab}^{relaxed} - nE_{bulk}}{A} - \frac{E_{slab}^{unrelaxed} - nE_{bulk}}{2A} \tag{2.54}$$

2.2.7.2 Equilibrium crystal morphology

The morphology of a crystal is the macroscopic shape that it adopts. The thermodynamic crystal morphology of a crystal can be constructed using Wulff's method (Wulff, 1901). According to Wulff's theorem, the equilibrium shape of a crystal is determined by the surface energies of its various surfaces, in such a way that the equilibrium morphology is the shape of the crystal with minimum total surface free energy. When a crystal is in its equilibrium shape, the height of a face is directly proportional to its specific free energy and this ratio is constant. If σ_i is the specific free energy of the i^{th} plane, and h_i is the distance from the centre of the crystal to the i^{th} plane, this can be expressed as:

$$\frac{\sigma_1}{h_1} = \frac{\sigma_2}{h_2} = \cdots = \frac{\sigma_n}{h_n} \tag{2.55}$$

According to Gibbs (1928), the equilibrium morphology of a crystal structure is the morphology that minimises the surface free energy for a given volume. If two faces have the same specific surface energy, they will have the same area. When the faces have different surface energies, the surface with the highest surface energy will grow faster, resulting in a small surface area with a longer distance from the centre, whereas the surface with a lower surface energy will grow more slowly, resulting in a larger surface area with a short distance from the centre, and this surface will be expressed more in the crystal morphology. In this work the equilibrium crystal morphology of mackinawite was generated using the GDIS (Graphical Display Interface for Structures) program, (*http://gdis.sourceforge.net/*).

2.2.7.3 Surface adsorption

Atoms and molecules interact with surfaces with forces originating either from the “physical” van der Waals interactions or from the “chemical” hybridization of their orbitals with those of the atoms of the substrate (Chorkendorff & Niemantsverdriet, 2003). Depending on which contribution dominates, we speak of physisorption or of chemisorption. These are limiting cases since hybridization is always present at small enough adsorption distances, even for adsorbed rare gases. Physisorption is based on the van der Waals interactions between the adsorbate and the substrate and also between the adsorbed molecules. The binding energy depends on the number of atoms involved and varies between few meV (light gases) and few eV (large organic molecules). It is completely non-specific, *i.e.* almost all gases can physisorb under the correct conditions to almost all surfaces. The geometrical structure and electronic characteristics of the physisorbed molecule or atom, and also of the surface are essentially preserved. At the most a slight deformation takes place. A physisorbed molecule can spontaneously leave the surface after a certain time. Chemisorption on the other hand occurs when there is the formation of a chemical (often covalent) linkage between adsorbate and substrate. Binding energies are typically of several eV. Compared to physisorption, the geometrical structure and electronic characteristics of the chemisorbed molecule or atom are strongly perturbed. The hybridized orbitals formed are often characterized by charge transfer from the substrate to adsorbate and vice versa. The surface structure is also typically not preserved in chemisorption, as the surface atoms usually undergo relaxation in order to minimize their energy. Catalytic activity depends on how rapidly chemisorption occurs and the strength (energy) of the chemisorption bond. If the bond is too weak, the molecule may desorb prior to reacting; if too strong, the release of the product and regeneration of the site may be retarded.

When atoms or molecules adsorb at surfaces, created bonds with the surface will release energy. The total energy component of this formation energy is called adsorption or binding energy, E_{ads}, which is a function of coverage and distribution of the adsorbates at the surface. Considering a molecule, *M*, adsorbed on a given surface, the adsorption energy is calculated using the expression:

$$E_{ads} = E_{surface+M} - (E_{surface} + E_M) \tag{2.56}$$

where $E_{surface+M}$ represents the total energy of the adsorbate-substrate system, $E_{surface}$ represents the energy of a clean surface, and E_M represents the energy of the molecule in the gas phase. By this definition, a negative adsorption energy indicates exothermicity and favourable adsorption. The total energy of an isolated molecule can be obtained in cubic box of size large enough (> 10 Å) to minimize lateral interactions in neighbouring cells.

Bibliography

- Adamson R. D.; Dombroski J. P.; Gill P. M. W.; *J. Comput. Chem.* **20**, 921 (1999)
- Amenomiya Y.; Cvetanovic R.J.; *J. Phys. Chem.*, **67**, 144 (1963)
- Andersson Y.; Langreth D. C.; Lundqvist B. I.; *Phys. Rev. Lett.* **76**, 102 (1996)
- Anisimov V. I.; Zaanen J.; Andersen O. K.; *Phys. Rev. B*, **44**, 943 (1991)
- Antony J.; Ehrlich S.; Grimme S.; Krieg H.; *J. Chem. Phys.* **132**, 154104 (2010)
- Argaman N.; Makov G.; *American Journal of Physics*, **68**, 69 (2000)
- Bader R.F.W.; *Atoms in Molecules –A quantum theory, Oxford University Press, New York*, (1990)
- Becke A. D.; *J. Chem. Phys*. **98**, 1372 (1993)
- Becke A. D.; *Phys. Rev. A.*, **38**, 3098 (1988)
- Becke A. D.; Johnson E. R.; *J. Chem. Phys*. **122**, 154104 (2005)
- Becke A. D.; *Phys. Rev. A*, **38**, 3098 (1988)
- Bengone O.; Alouani M.; Blöchl P.; Hugel J.; *Phys. Rev. B.* **62**, 392 (2000)
- Blaylock D. W.; Ogura T.; Green W. H.; Beran G. J. O.; *J. Phys. Chem. C*, **113**, 4898 (2009)
- Blöchl P. E.; *Physical Review B*, **50**, 17953 (1994)
- Born M.; Oppenheimer J. R.; *Ann. Physik*, **84**, 457 (1927)
- Born M.; Huang K.; Dynamical Theory of Crystal Lattices, Oxford University Press, 1954
- Capelle K.; A bird's-eye view of density functional theory of electronic structure. *Brazilian Journal of Physics*, **36**, 1318, 2006
- Cao X.-M.; Burch R.; Hardacre C.; Hu P.; *Catal. Today*, **165**, 71 (2011)

- Clark S. J.; Segall M.D.; Pickard C.J.; Hasnip P.J.; Probert M.J.; Refson K.; Payne M.C.; *Z. Kristallogr*. **220**, 567 (2005)
- Ceperley D. M. Alder B. J.; *Phys. Rev. Lett*. **45**, 566 (1980)
- Chorkendorff I.; Niemantsverdriet J. W.; Concepts of Modern Catalysis and Kinetics, Weinheim: Wiley–VCH, (2003)
- Cohen M. L. Heine V.; *Solid State Physics*, **24**, 37 (1970)
- Cortright R. D. Dumesic, J. A.; *Adv. Catal*., **46**, 161 (2001)
- de Leeuw N. H.; Rabone J. A. L.; *CrystEngComm*, **9**, 1178 (2007)
- Dion M.; Rydberg H.; Schröder E.; Langreth D. C.; Lundqvist B. I.; *Phys. Rev. Lett.* **92** 246401 (2004)
- Dirac P. A. M.; *Proc. R. Soc. Lond. A* **123**, 714 (1929)
- Dobson J. F.; Dinte B. P.; *Phys. Rev. Lett*. **76**, 1780 (1996)
- Dudarev S. L.; Liechtenstein A. I.; Castell M. R.; Briggs G. A. D.; Sutton A. P.; *Phys. Rev. B* **56**, 4900 (1997)
- Dudarev S. L.; Botton G. A.; Savrasov S. Y.; Humphreys C. J.; Sutton A. P.; *Phys. Rev. B*. **57**, 1505 (1998)
- Ebert H., Perlov A.; Mankovsky S.; *Solid State Comm*., **127**, 443 (2003)
- Feynman R.P.; *Phys. Rev. B*. **56**, 340, (1939)
- Giannozzi P.*et al*.; *J. Phys.: Condens. Matter*, **21**, 395502 (2009)
- Grimme S.; *J. Comput. Chem.* **27**, 1787 (2006)
- Gibbs J. W.; Collected Works, Longman: New York, (1928)
- Gokhale A. A.; Kandoi S.; Greeley J. P.; Mavrikakis M.; Dumesic J. A.; *Chem. Eng. Sci*., **59**, 4679 (2004)
- Gokhale A. A.; Dumesic J. A.; Mavrikakis M.; *J. Am. Chem. Soc*. **130**, 1402 (2008)

- Guerra C.F.; Handgraaf J.-W.; Baerends E.J.; Bickelhaupt F.M.; *J. Comput. Chem.*, **25**, 189 (2004)
- Harl J.; Kresse G.; *Phys. Rev. Lett.* **103**, 056401 (2009)
- Hellmann H.; *Einfuhrung in die Quantumchemie*, Franz Deutsche, 1937
- Hamann D. R.; Schlüter M.; Chiang C.; *Phys. Rev. Lett.* **43**, 1494 (1979)
- Hammer B.; Hansen L. B.; Nørskov J. K.; *Phys. Rev. B.*, **59**, 7413 (1999)
- Henkelman G.; Arnaldsson A.; Jonsson H.; *Comput. Mater. Sci*., **36**, 354 (2006)
- Hohenberg P.; Kohn W.; *Phys. Rev. B.* **136**, B864 (1964)
- Hubbard J.; *Proc. Roy. Soc. A*, **276**, 238 (1963)
- Hult E.; Andersson Y.; Lundqvist B. I.; Langreth D. C.; *Phys. Rev. Lett*. **77**, 2029 (1996)
- Jonsson H.; Mills G.; and Jacobsen K. W.; “Nudged Elastic Band Method for Finding Minimum Energy Paths of Transitions”, in ‘Classical and Quantum Dynamics in Condensed Phase Simulations’, ed. B. J. Berne, G. Ciccotti and D. F. Coker, World Scientific, (1998)
- Kandoi S.; Greeley J.; Sanchez-Castillo M. A.; Evans S. T.; Gokhale A. A.; Dumesic J. A.; Mavrikakis M.; *Top. Catal.*, **37**, 17 (2006)
- Kresse, G.; Hafner J.; Physical Review B, **48**, 13115 (1993)
- Kresse, G.; Hafner J.; Physical Review B, **49**, 14251 (1994)
- Kresse, G.; Furthmüller J.; *J. Physical Review B: Condensed Matter*, **54**, 11169 (1996)
- Kresse, G.; Joubert D.; *Phys. Rev. B.* **59**, 1758, (1999)
- Kohn W.; Sham L. J.; *Phys. Rev. B.* **140**, A1133 (1965)
- Kohn. W.; Becke A. D.; Parr R. G.; *J. Phys. Chem*., **100**, 12974 (1996)
- Laidler K. J.; King M. C.; *J. Phys. Chem*. **87**, 2657 (1983).

- Laidler K. J.; Glasstone S.; Eyring H.; *J. Chem. Phys*. **8**, 659 (1940)
- Landau L. D.; Lifshitz E. M.; Course of Theoretical Physics, Vol. 7: Theory of Elasticity (Nauka, Moscow, 1966; Pergamon, Oxford, 1970).
- Lee C.; Yang W.; Parr R. G.; *Phys. Rev. B*, **37**, 785 (1988)
- Madon R. J.; Braden D.; Kandoi S.; Nagel P.; Mavrikakis M.; Dumesic J. A.; *J. Catal*., **281**, 1 (2011)
- Maekawa S.; Tohyama T.; Barnes S. E.; Ishihara S.; Koshibae W.; Khaliullin G.; Physics of Transition Metal Oxides; ISBN: 3642059635, (2010)
- Marcus R.; *J. Chem. Phys*. **45**, 4493 (1966)
- Mattsson A. E.; In pursuit of the ‘Divine’ functional; *Science*, **298**, 759 (2002)
- Martin R.; Electronic Structure: Basic Theory and Practical Methods. Cambridge University Press, *ISBN 0521782856* (2004)
- McKee M.L.; Page M.; Reviews in Computational Chemistry Vol. IV, K.B. Lipkowitz and D.B. Boyd, Eds., VCH Publishers Inc., New York, (1993)
- Novell-Leruth G.; Ricart J. M.; Perez-Ramirez J.; *J. Phys. Chem. C*, **112**, 13554 (2008)
- Perdew J. P.; Ruzsinszky A.; Constantin L. A.; Sun J.; Csonka G. I.; *Journal of Chemical Theory and Computation*; **5**, 902 (2009)
- Perdew J. P.; *Phys. Rev. B*, **33**, 8822 (1986)
- Perdew J. P; Zunger A.; *Phys. Rev. B*. **23**, 5048 (1981)
- Perdew J. P. Wang Y.; *Phys. Rev. B*. **45**, 13244 (1992)
- Perdew J. P.; Burke K.; Ernzerhof M.; *Phys. Rev. Lett*. **77**, 3865 (1996)
- Perdew J.; Ernzerhof M.; Burke K.; *J. Chem. Phys*. **105**, 9982 (1996)
- Perdew J. P.; Burke K.; Ernzerhof M.; *Phys. Rev. Lett*. **78**, 1396 (1997)

- Perdew J. P.; Chevary J. A.; Vosko S. H.; Jackson K. A.; Pederson M. R., Singh D. J.; Fiolhais C., *Phys. Rev. B.* **46**, 6671 (1992)
- Payne M. C.; Teter M. P.; Allan D. C.; Arias T. A.; Joannopoulos J. D.; *Rev. Mod. Phys*. **64**, 1045 (1992)
- Phillips J. C.; *Phys. Rev*. **112**, 685 (1958)
- Phillips J. C; Kleinman L.; *Phys. Rev.* **116**, 287 (1959)
- Redhead P. A.; Thermal Desorption of Gases. *Vacuum*, **12**, 203 (1962)
- Rohrbach A.; Hafner J.; Kresse G.; *Phys. Rev. B.* **70**, 125426 (2004)
- Rohrbach A.; Hafner J.; Kresse G.; *J. Phys. Condens. Matter*, **15**, 979 (2003)
- Rydberg H.; Dion M.; Jacobson N.; Schröder E.; Hyldgaard P.; Simak S. I.; Langreth D. C.; Lundqvist B. I.; *Phys. Rev. Lett*. **91**, 126402 (2003)
- Schrödinger, E. *Physical Review*, **28**, 1049 (1926)
- Shein I. R.; Ivanovskii A. L.; *Scripta Materialia*, **59**, 1099 (2008)
- Tang W.; Sanville E.; Henkelman G.; *J. Phys.: Condens. Matter*, **21**, 084204 (2009)
- Tasker P. W.; *J. Phys. C: Solid State Physics*, **12**, 4977 (1979)
- Tkatchenko A.; Scheffler M.; *Phys. Rev. Lett.* **102**, 073005 (2009)
- Voigt, W.; Lehrbuch der Kristallphysik, Teubner, Leipzig, 1928
- Vosko S. H.; Wilk L.; Nusiar M.; *J. Phys.* **58**, 1200 (1980)
- Wang C-C.; Wu J-Y.; Jiang J-C.; *J. Phys. Chem. C*, **117**, 6136 (2013)
- Watson G. W.; Kelsey E. T.; de Leeuw N. H.; Harris D. J.; Parker S. C.; *J. Chem. Soc., Faraday Trans*., **92**, 433 (1996)
- Wulff G..; *Zeitschrift für Kristallographie Kristallgeometrie*, **39**, 449 (190)

Chapter 3

Adsorption of benzene on iron oxide (α-Fe_2O_3) surfaces

Abstract

Iron oxide minerals contribute crucially to the retention of aromatic hydrocarbons in subsurface environments. In this study, Hubbard corrected DFT (GGA+U) calculations were employed to unravel the interactions of a single benzene with the (0001) and $(01\bar{1}2)$ surfaces of hematite (α-Fe_2O_3) under vacuum conditions. Hematite is correctly described as a charge-transfer insulator, in agreement with the spectroscopic evidence, when the optimized value for U = 5 eV is employed. The results of our energy minimization calculations of the benzene-hematite surface adsorption complexes show that the benzene molecule is preferentially adsorbed to the hematite surfaces such that its molecular plane is practically parallel to the surface plane. The benzene molecule is demonstrated to interact more strongly with the $(01\bar{1}2)$ surface *via* cation-π interactions between the π-electrons of the benzene ring and *d*-orbitals of the surface Fe. Instead on the (0001) surface, van der Waals interactions are found to play important role in stabilizing the benzene molecule.

3.1. Introduction

The oxides and hydroxides of iron constitute a broad class of minerals that play important roles in removing environmental pollutants from underground water and soil sediments due to their characteristically high surface areas, higher adsorption affinity and capacity (Cornell & Schwertmann, 2003; Waychunas *et al.*, 2005; Nassar, 2012; Xu *et al.*, 2012). The sorption of inorganic and organic pollutants on iron mineral surfaces can substantially influence the transport, bioavailability, and fate of these contaminants in soils, sediments, and water, and thus help in the design and implementation of effective schemes for remediation of contaminated soils and water (Luthy *et al.*, 1997; Weber *et al.*, 2001; Knezovich *et al.*, 1987; Rebhun *et al.*, 1992; Lijestrand *et al.*, 1992). Nanoparticles of iron (hydr)oxides including amorphous hydrous ferric oxide (FeOOH), goethite (α-FeOOH), hematite (α-Fe_2O_3), maghemite (γ-Fe_2O_3), and magnetite (Fe_3O_4) have been explored extensively for wastewater and soil treatments and there exist a number of excellent review works on this subject in the literature (Waychunas *et al.*, 2005; Nassar, 2012; Xu *et al.*, 2012).

The sorption of hydrophobic organic contaminants (HOC), including benzene and polycyclic aromatic hydrocarbons (PAHs) on iron oxide mineral surfaces and soil components have attracted significant attention in the literature (Stauffer *et al.*, 1986; Means *et al.*, 1980; Amellal *et al.* 2006; Ping *et al.*, 2006). Aromatic hydrocarbons (mono and polycyclic), produced during coal gasification, petroleum cracking, crude oil refinement, organic biosynthesis and volcanic eruptions (Neff, 1979), are among the most widespread pollutants that pose serious risks for ecosystems and human health. They are also target components for study due to their carcinogenic, mutagenic, and toxic properties (Wilson & Jones 1993; Carmichael *et al.*, 1997). The adsorption of aromatic hydrocarbons on iron oxide mineral surfaces is therefore an important environmental chemical process and has been investigated extensively in the literature (Means *et al.*, 1980; Stauffer & MacIntyre, 1986; Weber & Miller, 1988; Piatt *et al.*, 1996; Xia & Ball, 1999; Allen-King *et al.*, 2002). Different competing mechanisms have been proposed to explain the sorption of PAHs to iron oxide mineral surfaces. For non-polar hydrophobic species containing an aromatic ring structure, a charge-induced dipole-dipole interaction between the positively charged sorption domain and the electron-rich π-system of the aromatic ring has been suggested (Mader *et al.*, 1997). Another suggestion based on cation-π interactions between the π-electrons of aromatic rings and cations was recently identified in a wide range of natural systems, including the sorption of the mono-aromatic ring of benzene and benzene substitutes to specific soil organic matter domains or to mineral surfaces (Ma & Dougherty, 1997; Zaric, 2003; Zhu *et al.*, 2003, 2004).

Despite these proposed explanations, the detailed nature of the interactions of aromatic hydrocarbons with iron oxide mineral surfaces at the molecular level is still limited. It was only recently that the interaction of benzene with the mineral goethite (FeOOH) surface was studied by means of quantum mechanical calculations based on density functional theory (Aquino *et al*., 2007). Similarly, a systematic DFT study of the interactions between a set of mono- and polycyclic aromatic hydrocarbons and the (110) goethite surface have shown that these species form relatively weak surface complexes having their molecular plane parallel to the surface plane (Tunega *et al.*, 2009). The source of the mineral-adsorbate interactions was attributed to the polarization of the π-system by polar OH groups and to the formation of weak hydrogen-bonds where the π-system acts as a proton acceptor.

Despite the large number of studies of the interactions of mono- and poly-aromatic hydrocarbons with goethite surfaces, there is still no reported molecular level study of the sorption mechanism of benzene on hematite surfaces in the literature to the best of our knowledge. Benzene represents the smallest aromatic hydrocarbon and it is also the building unit of PAHs, it therefore provides an excellent starting point for probing the molecular-level interactions of aromatic molecules with hematite surfaces. In this chapter, we have used the Hubbard-corrected DFT energy functional (GGA+U) with a correction for the long-range interactions (DFT-D2) to study the bulk and surface structures of hematite, and subsequently the adsorption structures of a single benzene molecule on the (0001) and $(01\bar{1}2)$ surfaces under vacuum conditions. Energy minimization calculations show that the benzene molecule is preferentially adsorbed to the hematite surfaces such that their molecular plane is practically parallel to the surface plane.

3.2 Computational details

Geometry optimizations were carried out with the Vienna Ab-initio Simulation Package (VASP) code (Kresse *et al*., 1993, 1994, 996) which employs a basis set of plane-waves to solve the Kohn-Sham (KS) equations of the density functional theory (DFT) in a periodic system. All geometry optimizations have been done starting from the X-ray data of the hexagonal α-Fe_2O_3 structure ($R\bar{3}c$) presented in Figure 3.1and Table 3.1 (Finger & Hazen, 1980). We note that there are two types of pairs of Fe atoms, which are characterized by a short Fe–Fe distance (type A) and by a larger distance (type B), along the hexagonal axis as shown in Figure 3.1. All calculations were spin-polarised, but spin-orbit coupling was not considered. The anti-ferromagnetic arrangement shown in Figure 3.1, where the iron atoms coupled ferromagnetically within a single octahedral layer, and alternating layers are coupled anti-parallel along the [001] direction was imposed on all calculations. This spin order was demonstrated to be the energetically most favourable one when compared to alternative magnetic orders, and in agreement with previous simulations (Catti &Valerio, 1995; Huda *et al.*, 2010).

In order to describe the electronic and magnetic behaviour properly, an accurate treatment of the electron correlation in the localized *d*-Fe orbitals is crucial. To improve the description of the localized 3*d*-electrons, we have used the GGA+U approach in the form proposed by Dudarev and Liechtenstein *et al.*, (1997, 1998). Different U_{eff} values have been tested and their implications for the description unit cell parameters, electronic band-gap and Fe magnetic moment have been checked. The generalized gradient approximation (GGA) was employed with the PW91 functional, (Perdew *et al.*, 1992) and long-range dispersion interactions were modelled *via* the semiempirical method of Grimme (Grimme, 2006). The core electrons, up to and including the *3p* levels of Fe and the *1s* of O, were frozen and their interaction with the valence electrons was described by the projector augmented wave (PAW) method (Blöchl, 1994; Kresse & Joubert 1999). The KS valence states were expanded in a plane-wave basis set with a cut-off of 500 eV for the kinetic energy. An energy threshold-defining self-consistency of the electron density was set to 10^{-5} eV and the optimization of the structures was conducted *via* a conjugate gradients technique, which stops when the Hellmann–Feynman forces on relaxed atoms are less than 0.01 eV/Å. Sampling of the Brillouin zone was performed using a Monkhorst–Pack grid of 11 x 11 x 7 gamma-centred k-points which ensured electronic and ionic convergence (Monkhorst & Pack, 1976). Test calculations with a higher number of k-points led to an energy difference smaller than 1 meV per cell.

The different low-index hematite surfaces were created from the optimized bulk using the dipole method implemented in METADISE code (Watson *et al.*, 1996), which does not only consider periodicity in the plane direction but also provides the different atomic layer stacking resulting in a zero dipole moment perpendicular to the surface plane (dipolar surfaces), as is required for reliable and realistic surface energy calculations (Tasker, 1979). The different low-index surfaces of hematite were constructed of 9−13 atomic layers. In every simulation cell, a vacuum region of 15 Å was added perpendicular to the surface to avoid interaction between the periodic slabs. Different slab and vacuum thicknesses as well as numbers of relaxed layers were tested until convergence within 1 meV per cell was achieved.

The adsorption calculations were carried using a (2 x 2) and (2 x 1) supercells of the (0001) and ($01\bar{1}2$) surfaces, ensuring that the minimum distance between the benzene molecule and its images in the neighbouring cells is larger than 5 Å. The atoms of the adsorbate and the four topmost layers of the slab were allowed to relax unconstrained until residual forces on all atoms reached 0.01 eV/Å. Symmetry constraints were not included in the structural optimization; in particular, the benzene molecule was free to move away laterally and vertically from the initial site or reorient itself to find the minimum energy adsorption structure. For the isolated benzene molecule, we used a cell with lattice constants of 15 Å, sampling only the Γ-point of the Brillouin zone. To characterize the strength of the adsorbate/surface interactions, the adsorption energy (E_{ads}) was calculated using equation 4.1.

$$E_{ads} = E_{surface+C_6H_6} - (E_{surface} + E_{C_6H_6}) \tag{4.1}$$

where $E_{surface+C_6H_6}$ represents the total energy of the adsorbate-substrate system, $E_{surface}$ represents the energy of a clean surface, and $E_{C_6H_6}$ represents the energy of the benzene molecule in the gas phase. A negative adsorption energy indicates a favourable adsorption. Bader charge analysis was carried out for all the adsorbate-substrate systems, using the Henkelman algorithm (Henkelman, 2006) in order to quantify any charge transfer between the α-Fe_2O_3 surfaces and adsorbed benzene molecule.

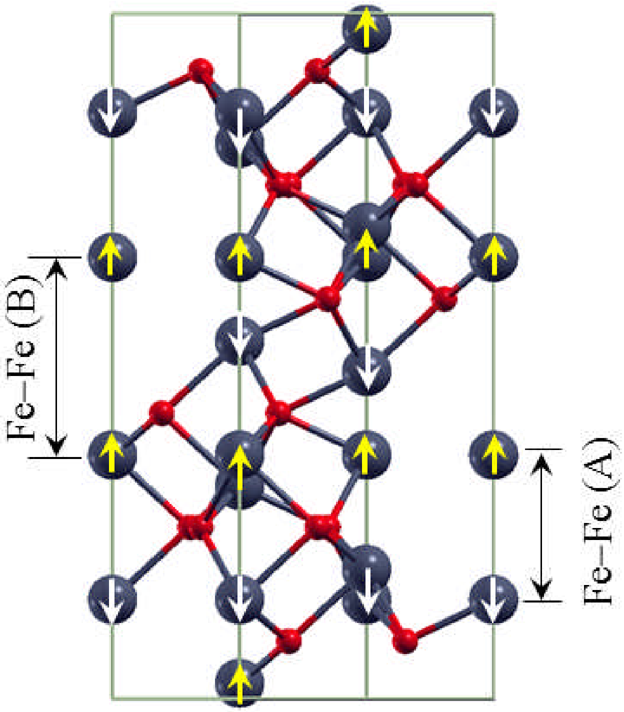

FIGURE 3.1: Hexagonal unit cell of α-Fe_2O_3 showing the anti-ferromagnetic spin arrangements indicated by up (yellow) and down (white) arrows at the Fe sites. Along the [001] direction, there are two sorts of pairs of Fe atoms, one (denoted as type A) with a short and one (type B) with a larger Fe–Fe distance.

3.3 Results and discussions

3.3.1 Structure, electronic and magnetic properties hematite (α-Fe_2O_3)

Shown in Table 3.1 are the optimized lattice parameters, Fe−Fe bond lengths, electronic band gap and Fe magnetic moments obtained from full geometry relaxation of the hexagonal unit cell at different U-values. By increasing the U value, the unit cell parameters, as well as the electronic band gap and Fe magnetic moment increases towards the reported experimental values (Table 3.1). This observation can be explained by considering the increasing repulsion on the Fe-sites as the U value increases, and similar results have been reported for DFT+U calculations on, α-Cr_2O_3, (Mosey &Carter, 2007). The best agreement with experimental data and earlier theoretical is obtained at a U value of 5 eV. The fully relaxed unit cell parameters at U = 5 eV are predicted at a = 5.024 Å and c = 13.712 Å, Table 3.1, in close agreement with experimental data (Pauling & Hendricks, 1925; Finger & Hazen, 1980) and are consistent with the results obtained by Rohrbach *et al.*, 2004, with the PW91+U = 5 eV functional (Table 3.1). It is also worth noting that as the U-value gets larger; it causes an elongation of the Fe–Fe (B) in contrast to the Fe–Fe (A) distance which is calculated to decrease with increasing U-value (Figure 3.2).

In Figure 3.3, we show how the electronic band-gap of α-Fe_2O_3 increases with increasing U value; the shaded area denotes the experimental range. The agreement with the experimental range of 1.9–2.2 eV, Sivula *et al.*, 2011, is best for U = 5 eV, at which the band-gap is predicted at 2.1 eV. Without considering the +U correction term (*i.e.* U = 0 eV), the band gap is dramatically underestimated at 0.38 eV. The total and projected density of states (pDOS) of α-Fe_2O_3 plotted at U = 0, 1, 3, and 5 eV are displayed in Figure 3.4). U values of 0 and 1 eV, incorrectly predict the positions of the iron 3*d*-orbitals in relation to the oxygen 2*p* states, characterizing the α-Fe_2O_3 as a *d*-*d* Mott insulator. The valence-band edge is predicted to be dominated by is Fe (3*d*), when it should have been characterized by O(2*p*). At higher U values, 3 and 5 eV, the valence-band edge is composed mainly of the O 2*p* states with a small contribution of the Fe 3*d* states, in agreement with experimental measurements that show that hematite has the valence band edge dominated by the O 2*p* states (Uozumi *et al.*, 1996; Fujimori *et al.*, 1989; Ciccacci *et al.*, 1991). The conduction band is dominated by Fe 3*d* states, indicating that α-Fe_2O_3 is an O 2*p* → Fe 3*d* charge transfer insulator in good agreement with the experimental evidence.

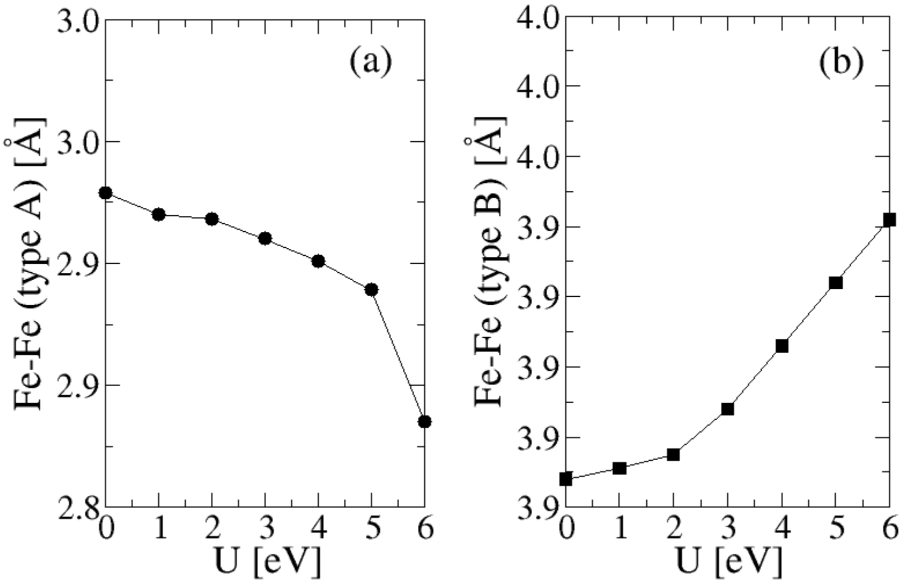

FIGURE 3.2: PW91-D2 Fe–Fe bond length (type A) and (type B) plotted against different U values. Bond lengths are expressed in Å, while U in eV.

The dependence of the Fe magnetic moment on U value is depicted in Figure 3.5. By increasing the values of U, the magnetic moment increases, however, the experimental values of 4.6–4.9 μ_B/Fe, (Coey *et al.*, 1971; Kren *et al.*, 1965) are still underestimated even for U = 6 eV. The observed increase in the Fe magnetic moments when the U correction is introduced can be attributed to the improved localization of the Fe *d* electrons. At U values of 5 and 6 eV, the average magnetic moment is calculated at 4.23 and 4.32 μ_B/Fe respectively, both of which represent an underestimation relative to the experimental data of 4.6–4.9 μ_B/Fe. These results are consistent with an earlier DFT+U = 5 eV calculation of Rohrbach *et al.*, 2004 which predicted the band gap and magnetic moment of hematite at 2.00 eV and 4.11 μ_B/Fe respectively. Without the inclusion of the onsite U term, the Fe magnetic moment is significantly underestimated by at least 1.23 μ_B/Fe, when compared to the experimental values of 4.6–4.9 μ_B/Fe (see Table 3.1).

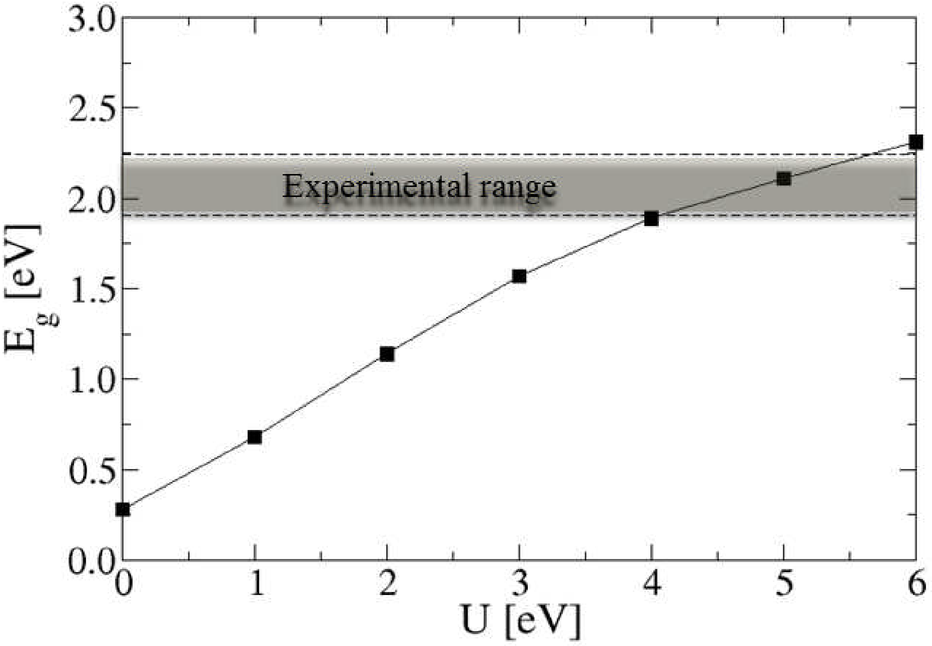

FIGURE 3.3: Plot of the electronic band-gap (E_g, in eV) of α-Fe_2O_3 as a function of the U parameter, in eV. The experimental band-gap range (Sivula *et al.*, 2011) is indicated by the shaded area.

Functional	U /eV	a /Å	c /Å	c/a	Fe−Fe(A) /Å	Fe−Fe(B) /Å	μ / μ_B Fe^{-1}	E_g /eV
PW91-D2	0	4.940	13.632	2.759	2.929	3.868	3.37	0.38
PW91-D2	1	4.981	13.645	2.739	2.920	3.871	3.71	0.78
PW91-D2	2	5.001	13.668	2.733	2.918	3.875	3.89	1.24
PW91-D2	3	5.009	13.691	2.731	2.910	3.888	4.02	1.67
PW91-D2	4	5.013	13.708	2.734	2.901	3.906	4.13	1.98
PW91-D2	5	5.024	13.712	2.729	2.889	3.924	4.25	2.10
PW91-D2	6	5.037	13.723	2.724	2.835	3.942	4.32	2.41
PW91[a]	4	4.997	13.847	---	---	---	4.14	1.82
PW91[b]	5	5.067	13.882	2.739	2.896	4.044	4.11	2.0
Expt.[c]	---	5.029	13.730	2.730	2.883	3.982	4.6–4.9 [e, f]	---
Expt.[d]	---	5.035	13.747	2.730	2.896	3.977	---	1.9−2.2 [g]

TABLE 3.1: Lattice constants a and c, axial ratio c/a, bond lengths (Fe–Fe(A), Fe–Fe(B)), magnetic moments μ, and band gap E_g of antiferromagnetic α-Fe_2O_3. [a]Kiejna *et al.*, 2012; [b]Rohrbach *et al.*, 2004; [c]Pauling & Hendricks, 1925; [d]Finger & Hazen, 1980; [e]Coey & Sawatzky 1971; [f]Kren *et al.*, 1965; [g]Sivula *et al.*, 2011.

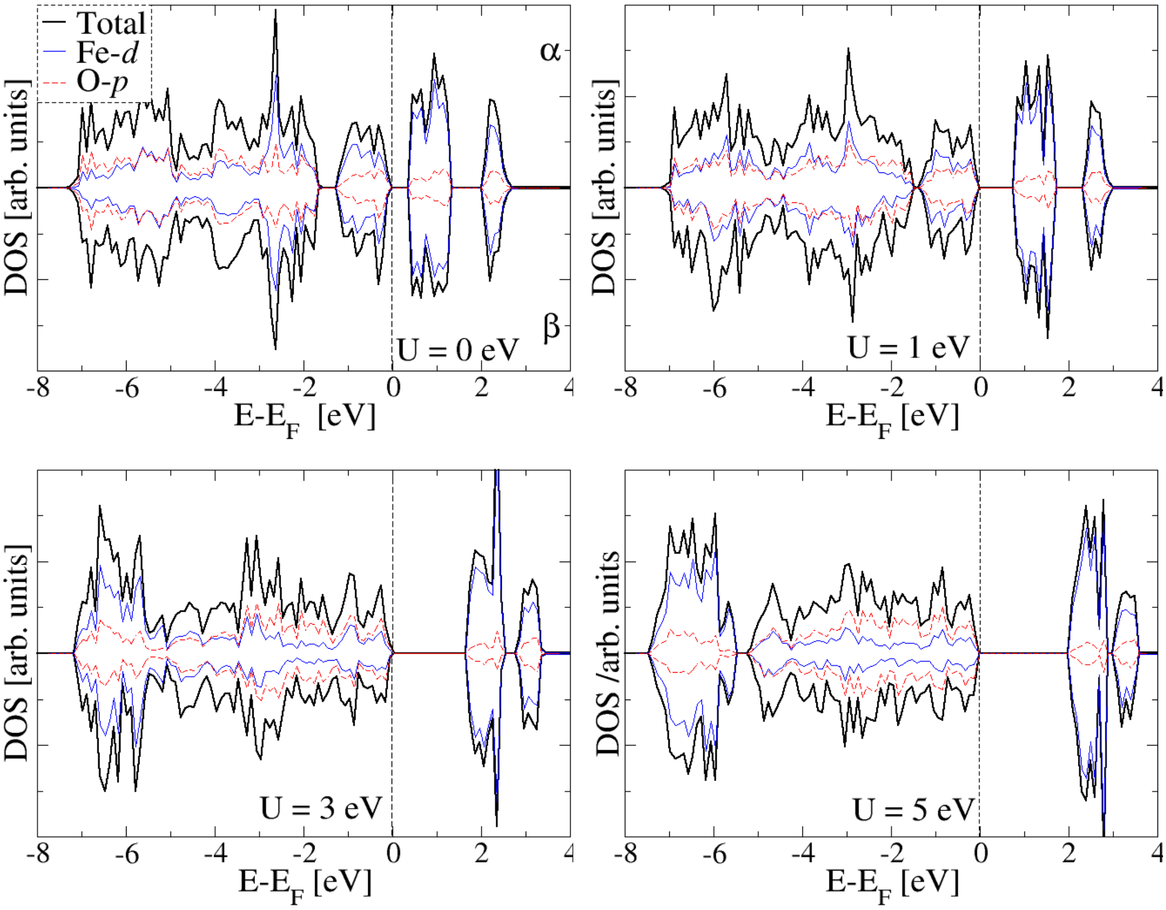

FIGURE 3.4: Total and projected DOS of α-Fe_2O_3 at U = 0 eV (top left), U = 1 eV (top right), U = 3 eV (bottom left) and U = 5 eV (bottom right). The Fermi level is set to zero as shown by the dashed vertical line.

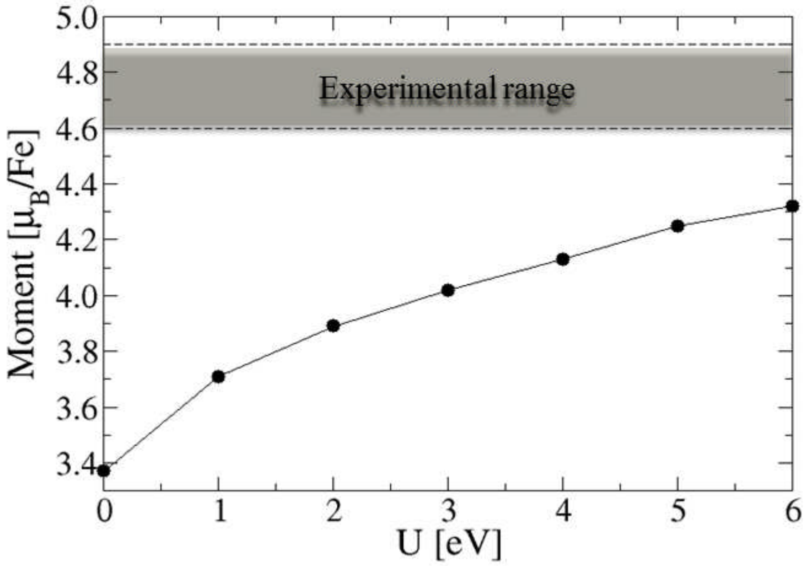

FIGURE 3.5: Plot of the calculated Fe magnetic moment (μ) for α-Fe_2O_3 as a function of the U parameter. The experimental Fe moment range (Coey & Sawatzky 1971) is indicated by the shaded area.

3.3.2 The structure of hematite surfaces

Unravelling the relationship between the atomic surface structure and other physical and chemical properties of metal oxides is challenging due to the mixed ionic and covalent bonding often found in metal oxide systems (Barteau, 1993). Theoretical calculations have, however, proven to be an indispensable complementary tool to experiments in elucidating our understanding of the surface structures of metal oxides and they have been used extensively to study the structure of the clean and hydrated hematite surfaces in the literature (Trainor *et al.*, 2004; Wang *et al.*, 1998; de Leeuw *et al.*, 2007; Wasserman *et al.*, 1997; Jones *et al.*, 2000; Yin *et al.*, 2007; Lo *et al.*, 2007; Parker *et al.*, 1999; Lado-Touriňo *et al.*, 2000; Kiejna *et al.*, 2012). The (0001) and ($01\bar{1}2$) surfaces planes of hematite are the dominant growth faces (Cornell & Schwertmann, 2003) and these planes are therefore the ones studied in this work. Earlier theoretical calculations, Trainor *et al.*, (2004) and Wang *et al.*, (1998) have showed that the (0001) surface can be terminated by either a single or double Fe layer or by oxygen ions, although the unreconstructed double Fe–termination and oxygen–terminated surface are dipolar, possessing a dipole moment perpendicular to the surface. We have therefore, considered only the non-dipolar single Fe-termination in this study. The side and top views of the single Fe-terminated (0001) surface is schematically shown Figure 3.6. The top view shows the topmost cations in three-fold coordinated with oxygen, in agreement with the cations coordination predicted by Kiejna and Pabisiak, (2013) when they modelled the mixed termination of hematite (0001) surface.

Geometry optimization of the single-iron terminated (0001) surface shows that it undergoes strong relaxations within its surface layers and interlayer spacings, a characteristic that is common to most metal oxide surfaces. The relaxed surface energy of the single-iron terminated (0001) is calculated at 1.66 J m^{-2} (Table 3.2), which is in close agreement with the studies of Wasserman *et al*. 1997, de Leeuw *et at*. 2007, and Mackrodt *et al.* 1988, who predicted 1.65, 1.78, and 1.53 J m^{-2} respectively. The optimized interlayer spacings compared with previous theoretically predicted values and experimentally measured interlayer spacings (Thevuthasan *et al*., 1999) using X-ray photoelectron diffraction are summarize in Table 3.3. Generally, the calculated inward relaxation of the layer spacings of the single-Fe terminated α-Fe_2O_3(0001) surface in this study are consistent with the X-ray photoelectron diffraction results and with earlier theoretical calculations (Wang *et al*., 1998; Wasserman *et al*., 1997; de Leeuw *et al*., 2007) but the magnitude of the relaxation differs.

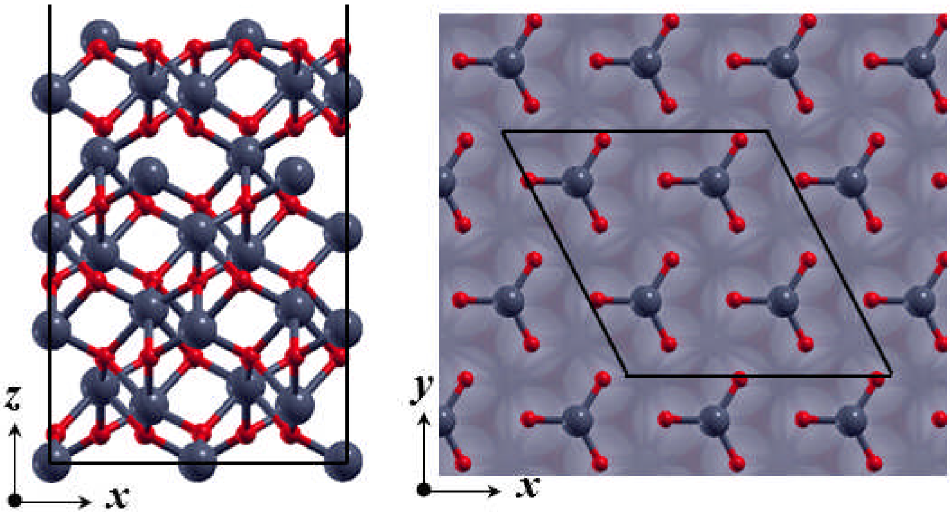

FIGURE 3.6: The side (left) and top (right) views of the relaxed structure of the single Fe–terminated α-Fe_2O_3(001)–(2 x 2) surface. Only the topmost atoms are shown in the top view for clarity of the cation coordination.

Surface	γ_u (J m^{-2})	γ_r (J m^{-2})	Relaxation (%)
(0001) Fe-termination	2.31	1.66	28.10
$(01\bar{1}2)$ termination A	2.14	1.92	10.28
$(01\bar{1}2)$ termination B	3.84	2.25	41.40

TABLE 3.2: Calculated surface energies before (γ_u) and after (γ_r) relaxation for the two major low-Miller index surfaces of α-Fe_2O_3.

Investigations	L1-L2 (bulk = 0.85)	L2-L3 (bulk = 0.85)	L3-L4 (bulk = 0.61)	L4-L5 (bulk = 0.85)
This work	0.40 (−52 %)	0.91 (+8 %)	0.45 (−26 %)	1.05 (+23 %)
Wang *et al.*, 1998	0.36 (−57 %)	0.90 (+7 %)	0.46 (−23 %)	0.97 (+15 %)
Wasserman *et al.*, 1997	0.43 (−49 %)	0.82 (−3 %)	0.36 (−40 %)	1.02 (+21 %)
de Leeuw *et al.*, 2007	0.21 (−76 %)	0.90 (+7 %)	0.42 (−31 %)	0.97 (+15 %)
Thevuthasan *et al.*, 1999	0.50 (−41 %)	1.0 (+18 %)	0.55 (−9 %)	1.24 (+47 %)

TABLE 3.3: Optimized interlayer spacing (in Å) and percent relaxations (in bracket) at the single-iron terminated α-Fe_2O_3(0001) surfaces.

The average magnetic moment of the terminating Fe atoms are slightly reduced (3.97 μ_B/Fe) compared with that of the bulk Fe atoms (4.23 μ_B/Fe). The change in the coordination of the surface atoms compared to those in the bulk modifies the shape of the bands of the O 2*p* and Fe 3*d* hybridization, which consequently affect the local magnetic moments. The electronic density of states for the relaxed single Fe-terminated α-Fe_2O_3 (0001) surface, shown in Figure 3.7, reveals that the surface remains semi-conducting but with a reduced gap width (~1.7 eV) compared to the bulk hematite (2.1 eV). The valence bands due to the oxygen 2*p* states lies below the Fermi level and the conduction band is dominated by the Fe 3*d* states. The work function, calculated as the difference between the electrostatic potential in the vacuum region and the Fermi energy of single Fe-terminated (0001) surface, is 4.4 eV, in agreement with earlier results of Jin *et al*. 2007 who obtained 4.0 eV and Wang *et al.* (1998) who obtained 4.3 eV.

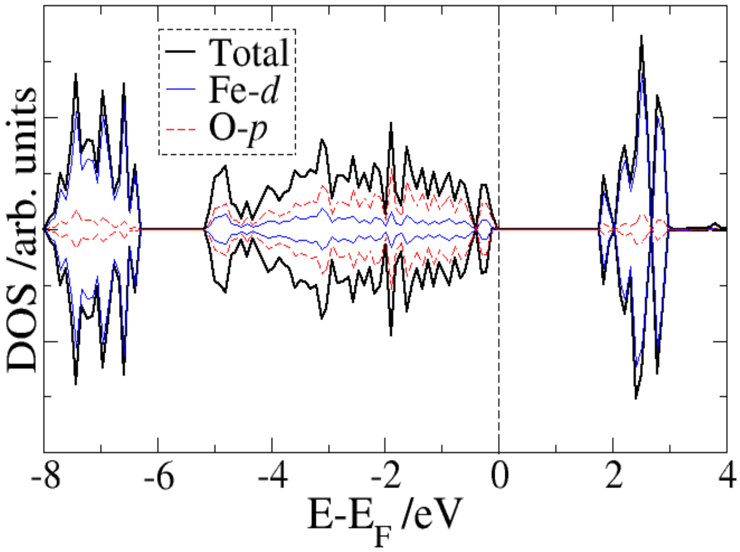

FIGURE 3.7: Total and projected density of states of the α-Fe_2O_3 (0001) surface.

The other surface structure studied in this work is the $(01\bar{1}2)$ surface, which is also commonly written in the literature as $(1\bar{1}02)$ or simply (012), (Lo *et al*., 2007). It is one of the dominant growth faces exposed on α-Fe_2O_3, and has been investigated in the past by both experimental (Henderson *et al.*, 1998; Henderson, 2007; Chatman *et al.*, 2013) and theoretical methods (de Leeuw *et al*., 2007; Lo *et al*., 2007; Tanwar *et al*., 2007). The $(01\bar{1}2)$ surface has two non-dipolar terminations, both of which have been considered, but we have used only the most stable termination to investigate the adsorption properties of benzene. The topography of the most stable termination (termination-A) of the $(01\bar{1}2)$ surface is characterized by raised undulating rows of oxygen parallel to the *y*-direction and valleys perpendicular to the *x*-direction as shown in Figure 3.8. The relaxed surface energy of the $(01\bar{1}2)$ is calculated at 1.92 J

m^{-2}, which compares well with the results obtained by de Leeuw *et al.*, 2007, (1.88 J m^{-2}), and Reeves & Mann, 1991 (1.96 J m^{-2}). Geometry optimization calculations show that this termination undergoes small relaxation relative the bulk interlayer spacings, where the topmost three percentage relaxations of the interlayer spacings are respectively calculated to be +22 %, −20 %, and +6 %, similar to the percentage relaxations (+37 %, −26 %, and +7 %) predicted by Lo *et al.* 2007 for this termination of the α-$Fe_2O_3(01\bar{1}2)$ surface.

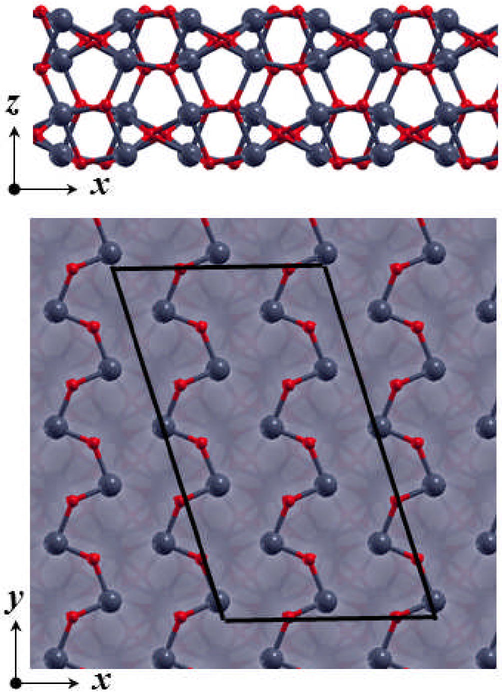
$(01\bar{1}2)$-termination-A

FIGURE 3.8: The side (top) and top (bottom) views of the relaxed structures of the most stable termination of α-Fe_2O_3 $(01\bar{1}2)$ surface, (termination-A).

The unrelaxed and relaxed structures of the second non-dipolar termination of the α-$Fe_2O_3(01\bar{1}2)$ surface (termination-B) are shown in Figure 3.9. During energy minimization, the protruding Fe ions in the unrelaxed surface move 0.98 Å towards the bulk, thereby compressing the surface layer atoms underneath which move horizontally to accommodate this relaxation, leaving the surface to be terminated by rows of oxygen atoms. The unrelaxed surface energy of this termination is calculated at 3.84 J m^{-2}, whereas the relaxed surface energy is calculated to be 2.25 J m^{-2}, representing a percentage relaxation of 41.4 % relative to the unrelaxed surface energy. This significant relaxation in the surface energy is consistent with the downward movement of the protruding Fe ions in the unrelaxed surface towards the bulk. The percentage relaxations in the topmost three interlayer vertical spacings of this termination are calculated to be −32 %, −11 %, and +8 %.

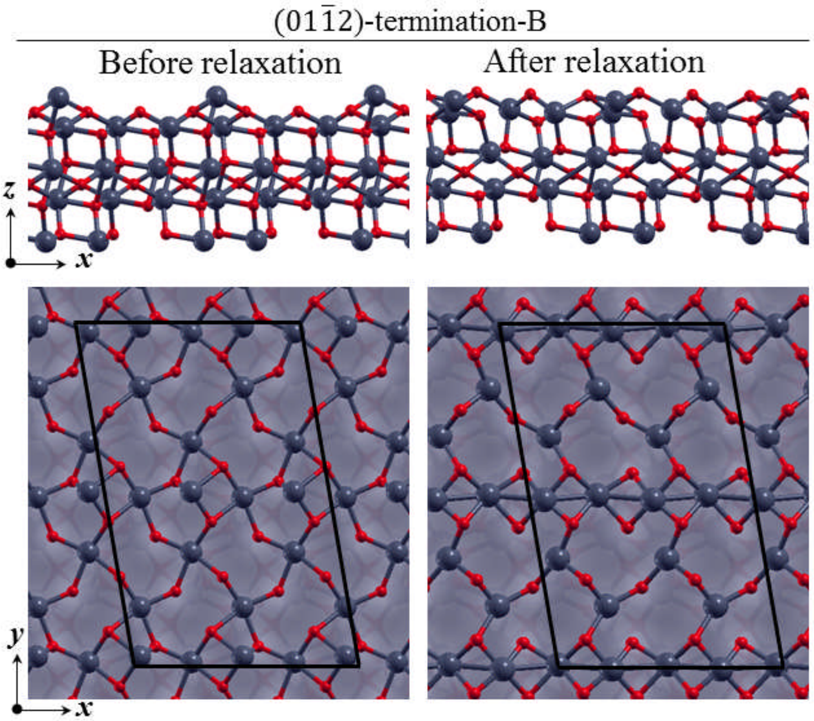

FIGURE 3.9: The side (top) and top (bottom) views of the unrelaxed and relaxed structures of termination-B of α-Fe_2O_3 $(01\bar{1}2)$ surface before and after relaxation.

The electronic density of states of the two terminations of the α-Fe_2O_3 $(01\bar{1}2)$ surface are shown in Figure 3.10. Both surface remained semi-conducting but their gap width is considerably reduced, calculated respectively at ~1.0 eV and ~0.5 eV for terminations A and B. The work function of terminations A and B are to be 4.1 and 3.9 eV respectively. The average magnetic moments of the surface Fe atoms at in terminations A and B are calculated 4.01 and 4.03 μ_B/Fe, both of which are smaller when compared with bulk Fe magnetic moment of (4.23 μ_B/Fe). The change in the surface Fe magnetic moments can be attributed the less coordination of the terminating surface Fe atoms compared to the bulk. The change in the Fe coordination modifies the hybridization of the O 2*p* and Fe 3*d* bands and thus affects the local magnetic moments.

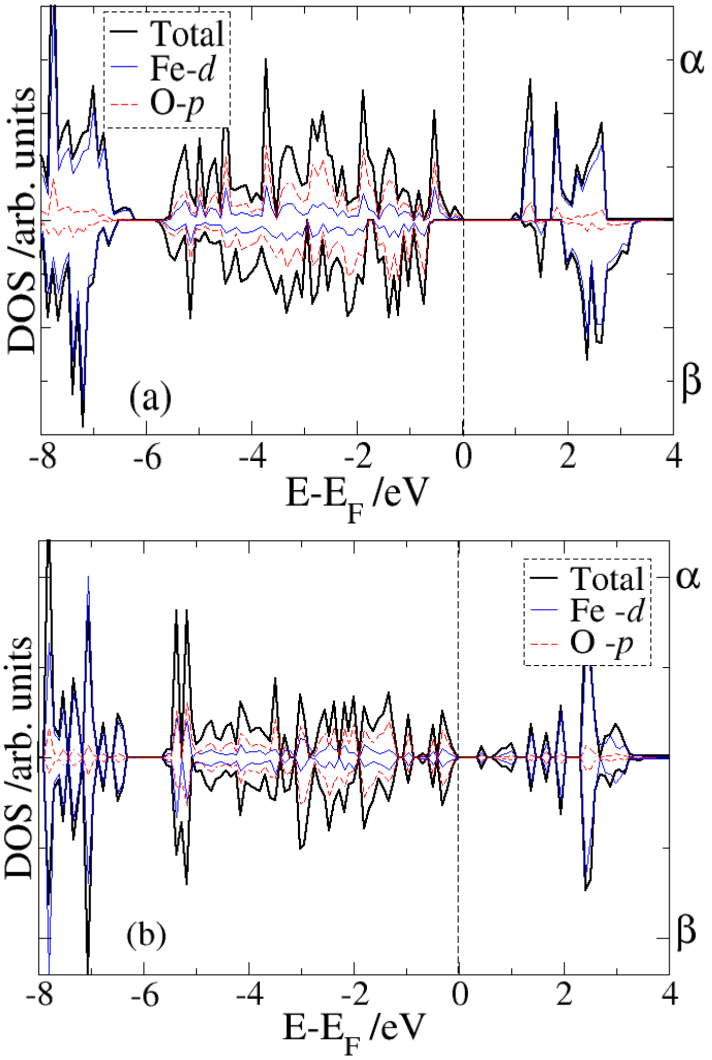

FIGURE 3.10: Total and projected density of states of the α-Fe_2O_3 (01$\bar{1}$2) surface: (a) termination A, and (b) termination B. The Fermi level is set to zero as shown by the vertical dashed line.

3.3.3 Benzene molecule

Prior to the adsorption of the benzene molecule on the (0001) and $(01\bar{1}2)$ hematite surfaces, we have calculated its structural parameters in the gas phase and compared them with available experimental data to ensure that our calculations are accurate and reliable. The calculated bond distances and angles are summarized in Table 3.4 showing excellent agreement with experiment (Lide, 2010).

Parameter	Expt. (Lide, 2010)	This work
d(C–H) /Å	1.101	1.091
d(C–C) /Å	1.399	1.400
<C–C–C /°	120.0	119.9
<C–C–H /°	120.0	120.0

TABLE 3.4: The equilibrium bond distances and angles in benzene calculated in this work and compared with experiment.

3.3.4 Benzene adsorption on (0001) surface

The optimized adsorption geometries of benzene on the (0001) surface are shown in Figure 3.11 and the adsorption parameters (binding energy, bond distances and bond angles) are summarized in Table 3.5. The interaction of the benzene molecule in all three adsorption geometries at the (0001) surface does not involve direct chemical bond formation with atoms of the oxide substrate, suggesting that van der Waals interactions (vdW) play an important role in stabilizing the adsorbed benzene molecule. The energetically most stable adsorption geometry is calculated to be the parallel adsorption geometry which releases an adsorption energy of 1.17 eV (contribution of the van der Waals interactions: E_{vdW} = 0.44 eV). In the parallel adsorption geometry, the benzene ring lies symmetrically around the interacting surface Fe atom at an almost equivalent C–Fe distance (2.301 Å); see the top view of Figure 3.11(a). The delocalization of electrons within the aromatic ring favours this adsorption geometry, where the benzene molecule interacts with the surface Fe atom through π-bonding. The adsorbed benzene molecule remains planar without any significant changes in the internal conformations. The C–H bonds are slightly bent towards the oxide surface and the interacting surface Fe atom is displaced upwards in the z-direction by 0.123 Å relative to its position on the naked surface.

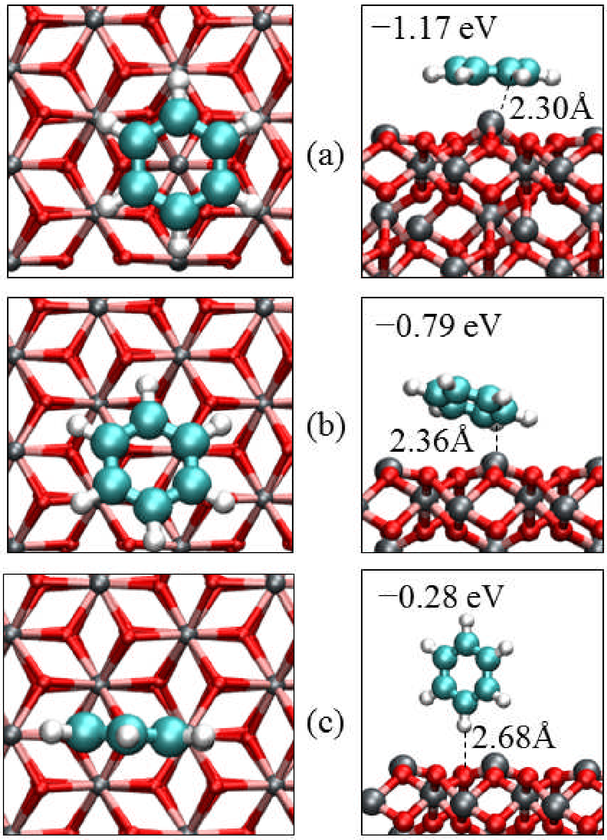

FIGURE 3.11: Top (left) and side (right) views of the relaxed adsorption geometries of benzene on α-Fe_2O_3 (0001) surface. The parallel and vertical geometries are shown in (a) and (b) respectively. Color scheme: Fe = grey; O = red; C = green and H = white.

We have also identified two other stable adsorption geometries, namely slant and vertical adsorption geometries as schematically displayed in Figure 3.11 (b & c). In the slant adsorption geometry (Figure 3.11(b)), the benzene molecule lies at an angle of ~45 ° to the surface normal interacting through one carbon-iron π-bond (2.361 Å) and released an adsorption energy of 0.79 eV (E_{vdW} = 0.26 eV). The benzene molecule remained planar in the adsorbed state without significant changes in its internal bond distance and angles. The weakest interaction is predicted in the vertical adsorption geometry (Figure 3.11(c)) where the benzene molecule only interacts with the surface oxygen atoms *via* weak hydrogen bonding between the hydrogen and the surface anions. The adsorption energy of the vertical geometry is calculated to be −0.28 eV ($E_{\mathrm{vdW}} = -0.17$ eV) suggesting that the vertical adsorption geometry is stabilized mainly by the weak van der Waals forces. The closest O–H bond distance is calculated to be 2.682 Å.

Parameters	α-$Fe_2O_3(0001)$			α-$Fe_2O_3(01\bar{1}2)$	
	Parallel	Slant	Vertical	Parallel	Vertical
E_{ads} /eV	−1.17	−0.79	−0.28	−1.52	−0.41
Q_{mol} /e$^-$	−0.07	−0.05	0.00	−0.23	−0.00
d(Fe–C) /Å	2.301	2.363	–	1.952	–
d(O–C) /Å	3.001	3.065	–	1.631	–
d(O–H) /Å	3.106	2.701	2.682	3.001	2.300
d(C–H) /Å	1.093	1.091	1.090	1.104	1.091
d(C–C) /Å	1.421	1.411	1.401	1.503	1.401
<C–C–C /°	119.9	119.8	120.0	116.9	120.0
<C–C–H /°	120.3	120.2	120.0	117.4	119.9

TABLE 3.5: Adsorption energies and structure parameters of benzene adsorbed on the (0001) and $(01\bar{1}2)$ α-Fe_2O_3 surfaces. E_{ads} and Q_{mol} denote respectively the adsorption energy and charge on the adsorbed benzene molecule.

3.3.5 Benzene adsorption on ($01\bar{1}2$) surface

The benzene molecule is found to adsorb relatively stronger on the ($01\bar{1}2$) surface than on the (0001) surface. Compared to the (0001) surface, the parallel adsorption geometry on the ($01\bar{1}2$) surface involves direct chemical bond formation between the carbon atoms of the benzene molecule (Figure 3.12(a)) and the surface atoms, giving a stronger interaction with an adsorption energy of −1.52 eV ($E_{\mathrm{vdW}} = -0.48$ eV). The C–Fe and C–O bond distances are respectively calculated to be 1.952 Å and 1.631 Å. The stronger interactions at the ($01\bar{1}2$) surface results in small distortion of the benzene ring with the hydrogen atoms around the bound region slightly displaced upwards, causing the C–H bonds to elongate (1.091 → 1.104 Å). The C–C bond distance around the bound region is also slightly elongated (1.400 → 1.503 Å).

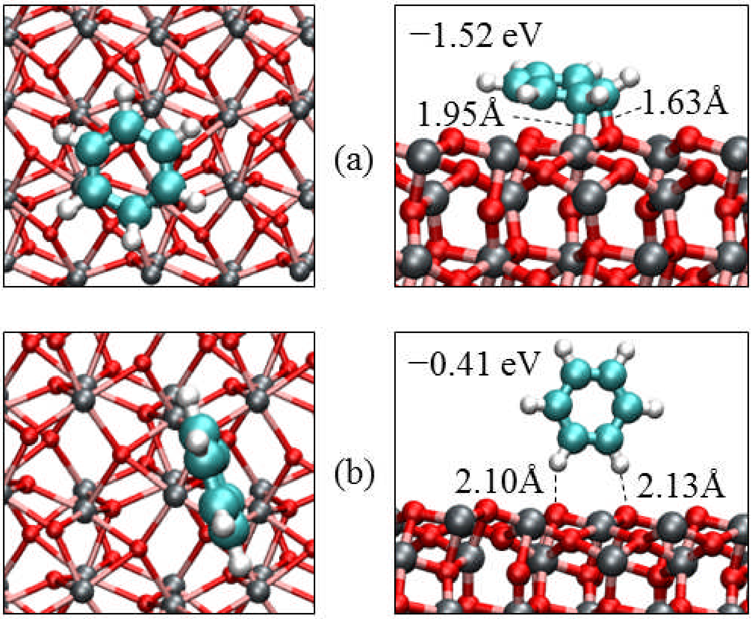

FIGURE 3.12: Top (left) and side (right) views of the relaxed adsorption geometries of benzene on α-Fe_2O_3 ($01\bar{1}2$) surface. The parallel and vertical geometries are shown in (a) and (b) respectively.

The vertical adsorption geometry (Figure 3.12(b)) gave a weak interaction with an adsorption energy of −0.41 eV (E_{vdW} = −0.23 eV). In the vertical geometry, the benzene molecule only interacts through weak hydrogen bonds with the surface oxygen atoms as shown in Figure 3.10(b) and is further stabilized by van der Waals interactions. The molecule remained planar with no significant changes in the internal bond distances and angles as shown in Table 3.5.

3.3.6 Electronic structures

In order to gain insight into the interactions of the benzene molecule with the hematite (0001) and ($01\bar{1}2$) surfaces, we have plotted the electronic density of states (DOS) of the lowest energy structures, projected on orbitals of C and H species and of the interacting surface Fe and O substrate. At the (0001) surface, we see mixing between the C *p*-orbitals with the surface Fe *d*-orbitals at around −4.0 eV, which is consistent with π-bonding between the two (Figure 3.13a). A much stronger hybridization is observed between the C *p*-orbitals and the surface Fe *d*-orbitals at the ($01\bar{1}2$) surface within the energy range of −2.0 to −5.0 eV (Figure 3.13b). We have also noticed small mixing of H *s*-orbitals with the O *p*-orbitals around −5.0 eV, indicative of some hydrogen bonded interactions between the two species at the ($01\bar{1}2$) surface. The stronger interaction of the benzene molecule with the ($01\bar{1}2$) surface, resulted in a considerable shifted of conduction band edge towards the valence bands upon benzene adsorption, reducing the band gap significantly (from 1.0 eV to 0.4 eV). The effect could favour an easier electron transfer across the gap and thus the stronger interaction of the benzene molecule calculated the ($01\bar{1}2$) surface. The band gap at the (0001) is reduced from 1.7 eV to 1.2 eV upon benzene adsorption. From Bader population analyses, the net charge transfer from the hematite surfaces to the adsorbed benzene molecule is however calculated to be very small. The charge transfer from the (0001) surface is <0.1 e^{-}, whereas at the $(01\bar{1}2)$ surface, where the benzene molecule is chemisorbed in the parallel mode, a charge of 0.23 e^{-} is transferred from the interacting surface species.

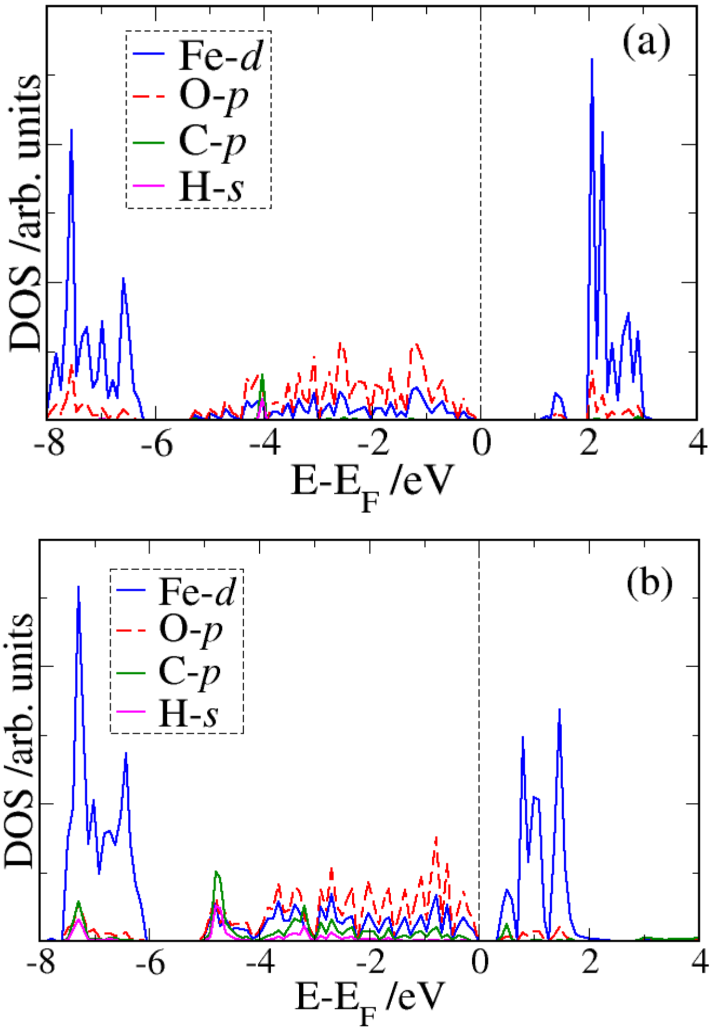

FIGURE 3.13: Electronic density of states of benzene adsorbed on hematite surfaces: (a) (0001), and (b) $(01\bar{1}2)$, projected on the interacting surface Fe *d*-states and O *p*-states, and on the C *p*-states and H *s*-states of the benzene molecule.

3.4 Summary and conclusions

We have presented a systematic DFT+U calculations of the interactions of a single benzene molecule with the (0001) and $(01\bar{1}2)$ hematite surfaces under vacuum conditions. The inclusion of the on-site Coulomb repulsion (U) to the DFT Hamiltonian is found to provide an accurate description of the structural parameters, electronic and magnetic properties of bulk hematite and its surface structures. Whereas low U values (0 and 1 eV) incorrectly predicts the positions of the iron 3*d*-orbitals in relation to the oxygen 2*p* states, characterizing the α-Fe_2O_3 as a *d-d* Mott-Hubbard insulator, U values greater than 3 eV (here U =5 eV which provides the best agreement with experiment) correctly described α-Fe_2O_3 is as a charge-transfer insulator.

Energy minimization calculations of the benzene-hematite surface adsorption complexes show that the benzene molecule is preferentially adsorbed to the hematite surfaces such that their molecular plane is practically parallel to the surface plane. The benzene molecule forms stronger surface complexes with the $(01\bar{1}2)$ surface than the (0001). The nature of the interactions is mainly characterized by cation-π interactions between the π-electrons of benzene ring and *d*-orbitals, and van der Waals interactions are found to play important role in stabilizing the benzene molecule at the hematite surfaces. The calculated binding energies in the range of 0.28−1.52 eV is significant, indicating that the hematite surfaces play important role in the retention of aromatic hydrocarbons in soils and sediments.

Comparing the interations of benzene with the hematite surfaces to those obtained with goethite (FeOOH) surfaces (Tunega *et al.*, 2009; Aquino *et al.*, 2007), we note that for the later, the benzene molecule forms relatively weak surface complexes due the presence of surface OH groups in this mineral. The origin of the interactions at the goethite surface is in the polarization of the π-system by the polar OH groups and in the formation of weak hydrogen-bonds where the π-system acts as a proton acceptor. The stronger interaction of the isolated benzene molecule with the hematite surfaces under vacuum conditions arises from the direct cation-π interactions between the π-electrons of the aromatic ring and surface cations. If an aqueous condition is considered, the benzene molecule will have to compete with water or hydroxyl molecules for the cationic sorption sites on the hematite surface and as it is often the case; the water molecules bind more strongly to the active surface sites, and thereby, will prevent the benzene from having direct access to these active sites. This effect will result in the benzene molecule forming relatively weak outer-sphere surface complexes *via* long hydrogen-bonds, where the π-system will act as a proton acceptors, as was observed on the goethite surface. We therefore expect that the presence of water or hydroxyl molecules on the hematite surfaces will weaken the strength of interaction, as the direct cation-π interactions will replaced with weak hydrogen-bonds and van der Waals interactions. Future calculations should incorporate the effect of water, as sorption of organic pollutants normally occurs in aqueous environments. Our calculated interatomic distances for the adsorption of isolated benzene molecule on the hematite surface under vacuum conditions could, however, serve towards the development of reliable forcefields that can be employed in classical MD simulations to simulate complex systems, including single benzene and poly-aromatic molecules and the effect of water, which will provide a more realistic description of the hematite-water-benzene system.

Bibliography

- Allen-King R. M.; Grathwohl P.; Ball W. P.; *Advances in Water Research*, **25**, 985 (2002)
- Amellal S.; Boivin A.; Ganier C. P.; Schiavon M.; *Agron. Sustain. Dev.*, **26**, 99 (2006)
- Aquino A. J. A.; Tunega D.; Haberhauer G.; Gerzabek M. H.; Lischka H.; *J. Phys. Chem. C*, **111**, 877 (2007)
- Barteau M. A.; *J. Vac. Technol. A*, **11**, 2162 (1993)
- Bengone O.; Alouani M.; Blöchl P.; Hugel J.; *Phys. Rev. B*. **62**, 392 (2000)
- Blöchl P. E.; *Phys. Rev. B*. **50**, 17953 (1994)
- Błoński P.; Kiejna A.; Hafner J.; *Surf. Sci.*, **590**, 88 (2005)
- Carmichael L. M.; Christman R. F.; Pfaender F. K.; *Environmental Science & Technology*, **31**, 126, (1997)
- Catti M.; Valerio G.; *Phys. Rev. B*. **51**, 7441 (1995)
- Chatman S.; Zarzyckib P.; Rosso K. M.; *Phys. Chem. Chem. Phys*., **15**, 13911 (2013)
- Ciccacci F.; Braicovich L.; Puppin E.; Vescovo E.; *Phys. Rev. B*, **44**, 10444 (1991)
- Coey J.; Sawatzky G.; *J. Phys. C*, **4**, 2386 (1971)
- Cornell, R.M.; Schwertmann, U. The Iron Oxides: Structure, Properties, Reactions, Occurrences, and Uses, 2nd ed.; Wiley-VCH: New York, NY, USA, 2003.
- De Leeuw N. H.; Cooper T. G.; *Geochim. Cosmochim. Acta*, **71**, 1655 (2007)
- Dudarev S. L.; Botton G. A.; Savrasov S. Y.; Humphreys C. J.; Sutton A. P.; *Phys. Rev. B*. **57**, 1505 (1998)

- Dudarev S. L.; Liechtenstein A. I.; Castell M. R.; Briggs G. A. D.; Sutton A. P.; Phys. Rev. B 56, 4900 (1997)
- Farquhar M. L.; Charnock J. M.; Livens F. R.; Vaughan D. J. *Environ. Sci. Technol.*, **36**, 1757 (2002)
- Finger L.; Hazen R.; *J. Appl. Phys.*, **51**, 5362 (1980)
- Freier S.; Greenshpan P.; Hillman P.; Shechter H.; *Phys. Lett.*, **2**, 191 (1962)
- Fujimori A.; Saeki M.; Kimizuka N.; Taniguchi M.; Suga M.; *Phys. Rev. B*, **34**, 7318 (1989)
- Fetzer J.C.; The Chemistry and Analysis of the Large Polycyclic Aromatic Hydrocarbons, Wiley, New York, 2000.
- Grimme S., *Journal of Computational Chemistry*, **27**, 1787 (2006)
- Henderson M. A.; *Surf. Sci*., **515**, 253 (2002)
- Henderson M. A.; Joyce S. A.; Rustad J. R.; *Surf. Sci.*, **417**, 66 (1998)
- Huda M. N.; Walsh Y.; Yan Y.; Wei S.-H.; Al-Jassim M. N.; *J. Appl. Phys*., **107**, (2010)
- Jin J.; Ma X.; Kim C.-Y.; Ellis D. E.; Bedzyk M. J.; *Surf. Sci.*, **601**, 3082 (2007)
- Jones F.; Rohl, A. L.; Farrow J. B.; Bronswijk W. V.; *Phys. Chem. Chem. Phys.*, **2**, 3209 (2000)
- Kiejna A.; Pabisiak T.; *J. Phys. Condens. Matter*, **24**, 095003 (2012)
- Kiejna A.; Pabisiak T.; *J. Phys. Chem. C*, **117**, 24339 (2013)
- Knickelbein M. B.; *J. Chem. Phys.*, **116**, 9703 (2002)
- Kren E.; Szabo P.; Konczos G.; *Phys. Lett.*, **19**, 103 (1965)
- Kresse G.; Furthmuller J.; *Phys. Rev. B*, **54**, 11169 (1996)
- Kresse G.; Hafner J.; *Phys. Rev. B*, **48**, 13115 (1993)

- Kresse G.; Hafner J.; *J. Phys. Condens. Matter*, **6**, 8245 (1994)
- Kresse G.; Joubert D.; *Phys. Rev. B*, **59**, 1758 (1999)
- Lado-Touriňo I.; Tsobnang F.; *Comp. Mater. Sci.*, **17**, 243 (2000)
- Lielmezs J.; Chaklader A. C. D.; *J. Appl. Phys.*, **36**, 866 (1965)
- Lo C. S.; Tanwar K. S.; Chaka A. M.; Trainor T. P.; *Phys. Rev. B*, **75**, 075425 (2007)
- Luthy R. G; Aiken G. R.; Brussau M. L; Cunningham S.D.; Gschwend P. M.; Pignatello J. J.; Reinhard M.; Traina S. J; Weber W.J.; Westall J. C.; *Environmental Science & Technology*, **31**, 3341 (1997)
- Ma J. C.; Dougherty D. A.; *Chemical Reviews*, **97**, 1303 (1997)
- Mackrodt W. C.; *Phys. Chem. Miner.*, **15**, 228 (1988)
- Mader B. T.; Goss K. U.; Eisenreich S. J.; *Environmental Science and Technology*, **31**, 1079 (1997)
- Means J. C.; Wood S. G.; Hassett J. J.; Banwart W. L.; *Environmental Science and Technology*, **14**, 1524 (1980)
- Monkhorst H. J.; Pack J. D. *Phys. Rev. B*, **13**, 5188 (1976)
- Nassar, N.N. Iron Oxide Nanoadsorbents for Removal of Various Pollutants from Wastewater: An Overview. In Application of Adsorbents for Water Pollution Control; Bentham Science Publishers: *Sharjah, United Arab Emirates*, pp. 81 (2012).
- Neff J. M.; Polycyclic aromatic hydrocarbons in the aquatic environment: sources, fates, and biological effects, ISBN 0853348324, 9780853348320, Applied Science Publishers (1979)
- Nguyen M.-T.; Seriani N.; Gebauer R.; *J. Chem. Phys.*, **138**, 194709 (2013)
- Parker S. C.; de Leeuw N. H.; Redfern S. E.; *Faraday Discuss.*, **114**, 381 (1999)

- Reeves N. J.; Mann S.; *J. Chem. Soc. Faraday Trans.*, **87**, 3875 (1991)
- Pauling L.; Hendricks S.; *J. Am. Chem. Soc*., **47**, 781 (1925)
- Perdew J. P.; Chevary J. A.; Vosko S. H.; Jackson K. A.; Pederson M. R.; Singh D. J.; Fiolhais C.; *Phys. Rev. B.* **46**, 6671 (1992)
- Piatt J. J.; Backhus D. A.; Capel P. D.; Eisenreich S. J.; *Environmental Science and Technology*, **30**, 751 (1996)
- Stauffer T. B.; MacIntyre W. G.; *Environmental Toxicology and Chemistry*, **5**, 949 (1986)
- Sherman D. M.; Randall S. R.; *Geochim. Cosmochim. Acta*, **67**, 4223 (2003)
- Sivula K.; Le Formal F.; Grätzel M.; *ChemSusChem*, *4*, 432 (2011)
- Tanwar K. S.; Lo C. S.; Eng P. J.; Catalano J. G.; Walko D. A.; Brown G. E., Jr.; Waychunas G. A.; Chaka A. M.; Trainor T. P.; *Surf. Sci*., **601**, 460 (2007)
- Tasker P. W.; *J. Phys. C: Solid State Physics*, **12**, 4977 (1979)
- Trainor T. P.; Chaka A. M.; Eng P. J. Newville M.; Waychunas C. A.; Catalano J. C.; Brown Jr. G. E.; *Surf. Sci.*, **573**, 204 (2004)
- Tunega D.; Gerzabek M. H.; Haberhauer G.; Totsched K. U.; Lischka H.; *J. Colloid Interface Sci*., **330**, 244 (2009)
- Uozumi T.; Okada K.; Kotani A.; *J. Electron. Spectrosc. Relat. Phenom*., **78**, 103 (1996)
- Wang X. G.; Weiss W.; Shaikhutdinov S. K.; Ritter M.; Petersen M.; Wagner F.; Schlögl R.; Scheffler M.; *Phys. Rev. Lett*., **81**, 1038 (1998)
- Wasserman E.; Rustad, J. R.; Felmy A. R.; Hay B. P.; Halley J. W.; *Surf. Sci*., **385**, 217 (1997)
- Watson G. W.; Kelsey E. T.; de Leeuw N. H.; Harris D. J.; Parker S. C.; *J. Chem. Soc., Faraday Trans*., **92**, 433 (1996)
- Waychunas G. A.; Kim C. S.; Banfield J. F.; *J. Nanopart. Res.* **7**, 409 (2005)

- Weber W. J.; Leboeuf E. J.; Young T. M.; Huang W. L.; *Water Research*, **35**, 853 (2001)
- Weber W.J. Jr; Miller C. T.; *Water Research*, **22**, 457 (1988)
- Wilson S. C; Jones K.C.; *Environmental Pollution*, **81**, 229 (1993)
- Xia G.; Ball W. P.; *Environmental Science and Technology*, **33**, 262 (1999)
- Xu P.; Zeng G. M.; Huang D. L.; Feng C. L.; Hu S.; Zhao M. H.; Lai C.; Wei Z.; Huang C.; Xie G. X.; Lui Z. F.; *Sci. Total Environ.*, **424**, 1 (2012)
- Yin S.; Ma X.; Ellis D. E.; *Surf. Sci.*, **601**, 2426 (2007)
- Zaric S. D.; *European Journal of Inorganic Chemistry,* **12**, 2197 (2003)
- Zhu D.; Herbert B. E.; Schlautman M. A.; Journal of Environmental Quality, **32**, 232 (2003)
- Zhu D.; Herbert B. E.; Schlautman M. A.; Carraway, E. R.; Hur J.; *Journal of Environmental Quality*, **33**, 1322 (2004)

Chapter 4

Bulk and surface structures of mackinawite (tetragonal FeS)

Abstract

Density Functional Theory calculations with a correction for the van der Waals interactions (DFT-D2 scheme of Grimme) have been used to model the bulk and surface structures of mackinawite (FeS). We demonstrate that the inclusion of van der Waals dispersive interaction sensibly improves the prediction of interlayer separation distance in FeS, in good agreement with experimental data. The effect of interstitial impurity atoms in the interlayer sites on the structure and properties of FeS is also investigated, and it is found that these contribute considerably to the mechanical stability of the FeS structure by replacing the weak dispersive forces between layers with chemically bonded interactions between the interstitial metal dopants and the S and Fe_{net} atoms. The (001) surface terminated by sulfur atoms is predicted as most energetically stable surface of FeS from geometry relaxation of its low-Miller index surfaces. Our simulated crystal morphology which is based on the calculated surface energies, show that FeS crystals grow in thin and tabular forms, in excellent agreement with experimental observation (Ohfuji & Rickard, 2006).

4.1 Introduction

Mackinawite, tetragonal iron (II) sulfide, is an important iron sulfide mineral considered to be the first iron sulfide phase formed from the reaction of Fe and S in low temperature aqueous environments (Rickard & Luther, 2007). It is also known to be the precursor to the formation of nearly all other iron sulfides in sedimentary and hydrothermal systems including greigite and pyrite (Livens *et al.,* 2004; Rickard and Luther, 2007). Mackinawite crystallises in the tetragonal structure (Figure 4.1) with space group P4/nmm (no. 29) and has lattice parameters $a = b = 3.674$ Å and $c = 5.033$ Å (Lennie *et al.,* 1995; Taylor & Finger, 1970). In the FeS structure, the iron atoms are in square-planar coordination, with an Fe–Fe distance of (2.597 Å) (Lennie *et al.,* 1995), which is similar to the Fe–Fe distance in bcc Fe (2.482 Å) (Hung *et al.,* 2002). The iron atoms are linked in a tetrahedral coordination to four equidistant sulfur atoms on a square lattice to form edge-sharing tetrahedral layered sheets that are stacked along the c-axis (Figure 4.1) and stabilized via van der Waals forces. The relatively short Fe–Fe distance of 2.597 Å obviously suggests substantial metallic bonding in this material (Vaughan & Ridout, 1971).

This FeS compound is of growing interest among the large family of iron sulfide phases that span a diverse range of electronic, magnetic, and optical properties with applications that include solar cells (Ennaoui *et al*., 1986; Hu *et al*., 2008; Yuhas *et al*., 2012; Kirkeminde *et al.*, 2012) and lithium ion batteries (Yamaguchi *et al.* 2010; Paolella *et al*., 2011). Mackinawite has also been explored as a material for microbial fuel cells (Nakamura *et al*., 2010) and as a substrate for the removal of toxic trace metals from water (Jeong *et al*., 2007). Due to its chalcophilic nature and reducing capability, mackinawite exhibits high reactivity towards a range of chemical species, where for example, it is known to be an effective sorbent for divalent metals (Morse & Arakaki, 1993; Wharton *et al.*, 2000; Jeong *et al.*, 2007). It has also been found that mackinawite can immobilize Cr(VI) through its reduction to the less mobile Cr(III) species (Patterson *et al.*, 1997; Mullet *et al.*, 2004).

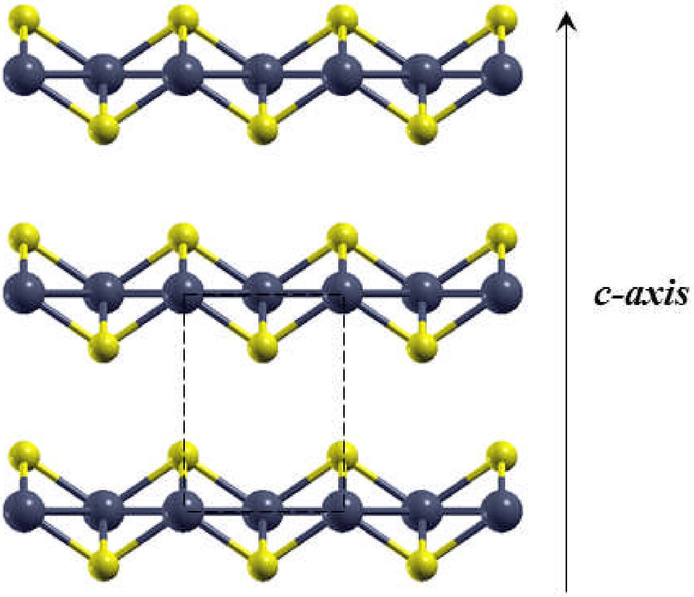

FIGURE 4.1: Multiple FeS unit cells showing its layered nature. A single unit is indicated with the dashed line.

Also, FeS is isostructural to super-conducting FeSe and $FeSe_{1-x}Te_x$, and while superconductivity has not yet been reported in this tetragonal FeS phase, it is attracting significant attention because of its structural, compositional, and electronic similarities to the known iron chalcogenide superconductors (Subedi *et al.*, 2008; Kwon *et al.*, 2011; Brgoch & Miller, 2012). Mackinawite-type FeS is also of interest because of its biogeochemical relevance: it is produced by sulfate-reducing bacteria (Livens *et al.*, 2004; Pósfai *et al.*, 1998; Gramp *et al.*, 2010), it occurs in sedimentary mineral deposits (Berner, 1962; Rickard & Luther, 2007), and it is implicated in the origin of life theories (Wächtershäuser, 1992; Huber & Wächtershäuser, 1997; Russell & Hall, 1997; Cody, 2004).

The successful synthesis of mackinawite has generated empirical information on its structure (Berner, 1962; Lennie *et al.*, 1995; Mullet *et al.*, 2002), oxidation with possible transformation to more stable iron sulfide phases (Benning *et al.*, 2000; Cahill *et al.*, 2000; Rickard & Morse, 2005; Lennie *et al.*, 1997), and magnetic behaviour (Denholme *et al.*, 2014; Vaughan & Ridout, 1971). Although mackinawite is often reported to contain significant amount of interstitial impurity metals between the S−S layers, information regarding their effect on the structure and properties of mackinawite is limited in the literature. It has been reported that the presence of about 8–9 % weight Ni and Co in the mackinawite structure increases its breakdown temperature from about 135 ^{o}C to 200-250 ^{o}C (Clark *et al.*, 1966). Also, the Vickers micro-indentation hardness of mackinawite is reported to increase with impurity content (Clark, 1969; Vaughan, 1969).

Information regarding the structures and the relative stabilities of the low-index surfaces of mackinawite is also scarce in the literature. The chemical activity of mackinawite and in particular its potential for catalytic applications, has also not been investigated so thoroughly. This information is however, crucial to improve our understanding of the surface chemistry of this mineral and its consequence on the reactivity towards different chemical species. Using an interatomic potential based theoretical calculations, (Devey *et al.*, 2008), predicted the (001) surface to be by far the most stable surface of mackinawite in agreement with experimental observations using selected area electron diffraction (SAED) analyses on FeS nanocrystals (both freeze-dried and precipitated samples), (Ohfuji & Rickard, 2006).

Like other layered materials such as β-MoS_2 and $NbSe_2$ (Bucko *et al.*, 2010), standard DFT-based methods fail to account for dispersive forces acting between S−S layers, and thus often result in poor description of the interlayer interactions in FeS (Devey *et al.*, 2008). As a result of this, the lattice *c* parameter of FeS was simply fixed at the experimental value in earlier standard DFT investigations (Subedi *et al.*, 2008; Kwon *et al.*, 2011), but this approach could introduce unrealistic strain in the surface calculations. Also this protocol is not suitable when considering defects, as mackinawite often contains significant amount of interstitial impurity metals in the tetrahedral sites between layers and therefore requires the potential to expand or compress freely to accommodate these defects.

The aim of the present chapter is therefore to carry out dispersion corrected density functional theory calculations within the scheme proposed by Grimme, 2006 (DFT-D2), to describe the bulk properties of stoichiometric FeS and non-stoichiometric $(Fe,M)_{1+x}S$, which contains interstitial metal atoms (M = Cr, Mn, Fe, Co, Ni, and Cu). The structures and the relative stabilities of the low-Miller index surfaces of the stoichiometric FeS are also systematically characterised. Using the calculated surface energies, we have simulated the equilibrium crystal morphology of FeS which shows excellent agreement with experimental observation of Ohfuji & Rickard, 2006 using high resolution transmission electron microscope (HRTEM).

4.2 Computational details

Geometry optimizations were carried out using the Vienna Ab-initio Simulation Package (VASP) code (Kresse *et al.*, 1993, 1994, 1996), which employs a basis set of plane-waves to solve the Kohn-Sham (KS) equations of the density functional theory (DFT) in a periodic system. Dispersion forces were accounted for using the Grimme DFT-D2 method, which is essential for a proper description of the interlayer interactions in layered structures. Detailed description of the Grimme scheme is provided in chapter 2, under section 2.4. All calculations are performed within the generalized gradient approximation (GGA), with the exchange-correlation functional (PW91) developed by Perdew *et al*., 1992. The PBE and LDA exchange correlation functionals have also been tested for comparison. The interaction between the valence electrons and the core was described with the projected augmented wave (PAW) method (Blöchl, 1994) in the implementation of Kresse and Joubert (1999). The KS valence states were expanded in a plane-wave basis set with a cut-off of 400 eV for the kinetic energy. An energy threshold-defining self-consistency of the electron density was set to 10^{-5} eV and the optimization of the structures was conducted *via* a conjugate gradient technique, which stops when the Hellmann–Feynman forces on all relaxed atoms are less than 0.01 eV/Å.

Integrations in the reciprocal space for the bulk calculations were performed using a Monkhorst-Pack grid of 11 x 11 x 11 gamma-centred k-points, which ensured electronic and ionic convergence (Monkhorst & Pack, 1976). Test calculations with a higher number of k-points led to an energy difference smaller than 1 meV per cell. The k-point grids for the surface calculations were chosen in such a way that a similar spacing of points in the reciprocal space was maintained. To improve the convergence of the Brillouin-zone integrations, the partial occupancies were determined using the tetrahedron method with Blöchl corrections, with a set width for all calculations of 0.02 eV. The on-site potential, GGA+U, was not considered for these calculations as previous DFT studies have shown that considering the +U correction term provides inadequate structural optimizations (Devey *et. al*., 2008).

In view of the still ongoing controversial debate as to the precise nature of the magnetic order of mackinawite (Devey *et al.*, 2008; Kwon *et al.*, 2011), and reflecting the fact that superconducting quantum interference device (SQUID) data (Denholme *et al.*, 2014) as well neutron diffraction (Bertaut *et al.*, 1965) and Mössbauer studies (Vaughan & Ridout, 1971) demonstrates no evidence of magnetic ordering down to temperatures as low as 4 K, in this work, we have decided to investigate the non-magnetic state for simplicity which provides, in addition, best agreement of the lattice constants with respect to the experimental data according to Devey *et al.*, 2008. The stoichiometric FeS was modelled using the tetragonal unit cell (Figure 4.2a) containing four atoms and the non-stoichiometric ($(\mathrm{Fe, M})_{1+x}\mathrm{S}$) structures were modelled by introducing one metal atom per unit cell in the tetrahedral site (Figure 4.2b) giving the composition $\mathrm{FeM_{0.5}S}$. To characterize the unit cell parameters and interatomic bond distance and angles, full geometry optimization calculations were performed on all model systems.

To characterization the surface structures and stabilities of mackinawite, different low-Miller index FeS surfaces were created from the optimized bulk using the METADISE code (Watson *et al.*, 1996), which does not only consider periodicity in the plane direction but also provides the different atomic layer stacking resulting in a zero dipole moment perpendicular to the surface plane (dipolar surfaces), as is required for reliable and realistic surface energy calculations (Tasker, 1979). Different slab and vacuum thicknesses, as well as numbers of relaxed layers were tested until convergence within 1 meV per cell was achieved. We have carried out energy minimisations of the different low-index FeS surfaces slabs to obtain their surface energies following the procedure describes in chapter 2, section 2.2.7.1. The equilibrium morphology of the FeS crystal which is based on the calculated surface energies was constructed according to Wulff's theorem (Wulff, 1901), where the distance from the centre of the particle to the surface is proportional to the surface energy. It is based on the Gibbs approach (Gibbs, 1928), who proposed that under thermodynamic control, the equilibrium morphology of a crystal should possess minimal total surface free energy for a given volume.

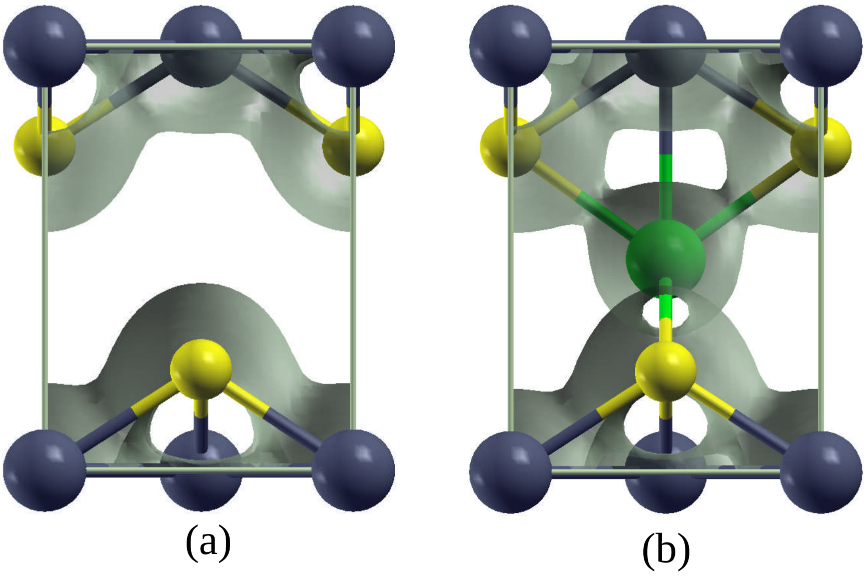

FIGURE 4.2: Schematic representation of the tetragonal structure: stoichiometric FeS (a) and TM-doped $FeTM_{0.5}S$ (b). Colour scheme (square-net Fe = grey, interstitial Fe = green and S = yellow). The isoelectronic surfaces at $\rho = 0.05$ e/Å^3 are also shown.

4.3 Results and discussions

4.3.1 Stoichiometric FeS

The lattice parameters a = 3.674 Å, c = 5.033 Å with c/a = 1.370, and the atomic positions originally reported by Lennie *et al*, (1995) were used as the starting point for our VASP geometry relaxation calculations. Structural optimization of the stoichiometric FeS was first conducted without accounting for van der Waals forces (i.e. standard DFT) using the LDA, PBE and the PW91 functionals. Table 4.1 summarizes the structural parameters obtained after a full structural relaxation. Whereas the lattice *a* and *b* parameters predicted by the LDA, PBE and the PW91 functionals remain consistent with the experimental values to within 2%, the lattice *c* parameter is significantly overestimated to within 11 % of the experimental value, reflecting the fact that, standard DFT-based methods can result in poor description of the interlayer interactions in layered structures. The LDA, PBE and the PW91 functional predict the lattice *c* parameter at 5.570 Å, 5.580 Å, and 5.584 Å respectively, compared to the experimental value of 5.033 Å (Lennie *et al*, 1995). Similar results have been reported for other layers materials, where for instance, the lattice *c* parameter in β-MoS_2, $NbSe_2$ and FeSe were overestimated, respectively by 20 %, 10 % and 14 % of their experimental values (Bucko *et al.*, 2010, Ricci & Profeta, 2013). In an earlier standard DFT full geometry optimization of FeS using PW91, the lattice *c* parameter was predicted at 5.625 Å, 12% larger than the experimental value of 5.033 Å (Devey *et. al.*, PhD thesis, University College London, 2009). Due to the poor description of the interlayer interactions, earlier electronic structure calculations on FeS of have simply fixed the lattice *c* parameter at the experimental value (Subedi *et al.*, 2008; Kwon *et al.*, 2011).

The dramatic increase of the lattice *c* parameter in the stoichiometric FeS structure, suggests that an improved calculation with a correction for van der Waals interactions is required to provide a better description of the interlayer interactions in FeS. By taking into account the van der Waals interactions in the formalism proposed by Grimme (DFT-D2 approach), there is a sensible improvement. The LDA-D2, PBE-D2 and PW91-D2 values are corrected within 2−4% with respect to experiments. The LDA-D2 slightly over binds the FeS layers (3.5 %), compared to the PBE-D2 (2.6 %) and PW91-D2 (2.5 %). The interatomic bond distances as reported in Table 4.1 show that the PBE-D2 and PW91-D2 functional reproduces with better accuracy the experimental interatomic bond distances than the LDA-D2. The z-coordinate of the S atoms along the c-axis (Z_S) are also reproduced in close agreement with experimental data using vdW corrections. For instance, the PW91-D2 predicts Z_S at 0.248 in close agreement with the experimental value 0.260 (Lennie *et al.*, 1995), while the standard PW91 predicted it at 0.226.

	LDA		PBE		PW91		
Parameter	DFT	DFT-D2	DFT	DFT-D2	DFT	DFT-D2	Expt.[a]
$a = b$ /Å	3.573	3.560	3.582	3.576	3.588	3.587	3.674
c /Å	5.570	4.858	5.580	4.901	5.584	4.908	5.033
c/a	1.558	1.365	1.558	1.370	1.556	1.368	1.369
V /Å^3	71.10	61.56	71.59	62.67	71.89	63.14	67.93
Z_S	0.213	0.233	0.220	0.242	0.226	0.248	0.260
d(Fe−S) /Å	2.186	2.182	2.189	2.200	2.192	2.202	2.256
d(Fe–Fe) /Å	2.535	2.537	2.538	2.547	2.537	2.549	2.598

TABLE 4.1: Optimized structural parameters for stoichiometric FeS. [a]*After Lennie et al., 1995 and* [b]*After Berner, 1962*

Hereafter, we adopt the GGA-PW91 functional which generally reproduces the FeS lattice parameters, interatomic distances and *z*-coordinate of the S atoms along the c-axis with and without vdW correction, to keep consistency throughout this work. It shall be used in the subsequent sections to evaluate the effect of interstitial transition metals on the structure and properties of non-stoichiometric (Fe, M)$_{1+x}$S systems.

4.3.2 Non-stoichiometric (Fe, M)$_{1+x}$S

Naturally occurring mackinawite, such as those located in lake sediments are often found to contain substantial concentrations of excess Fe and other impurity metals in the structure (Clark, 1969; Vaughan, 1969). Mössbauer spectroscopy and X-ray photoelectron study on synthetic mackinawite prepared from iron in sulfide solutions have also shown the presence of up to 20 % Fe in the tetrahedral sites between the FeS layers (Mullet *et al*., 2002). Significant amounts of up to 20 % of Ni, Co, Cr and Cu impurity atoms have been reported in naturally occurring mackinawite samples (Clark, 1969; Vaughan, 1969). The presence of the excess impurity metal atoms introduces non-stoichiometry in the FeS composition, thus the composition of mackinawite is commonly written as Fe$_{1+x}$S, but better written as (Fe, M)$_{1+x}$S, where M denote another interstitial impurity metal. As to the location of the excess Fe atoms in the mackinawite structure, Vaughan (1970) noted that the layered structure of mackinawite allows the incorporation of additional interstitial Fe between the FeS layers. A recent DFT calculation validated Vaughan’s suggestion by predicting the tetrahedral site between the FeS layers as the energetically most favourable location for an interstitial Fe (Brgoch *et al*., 2012).

To simulate the scenario of 20 % interstitial metal atoms in the mackinawite structure, a single metal atom was introduced at the centre of the tetragonal unit cell (*i.e*., composition FeM$_{0.5}$S), located at the tetrahedral site between layers in the FeS structure (see Figure 4.1b), following the prediction of Brgoch *et al*., 2012. Full structural relaxation calculations were performed on all metal-doped FeS systems as it offers them the potential to freely expand or compress to accommodate the interstitial defect atoms. The fully relaxed unit cell parameters and interatomic bond distances within of the $FeM_{0.5}S$ systems: M = Cr, Mn, Fe, Co, Ni and Cu are summarized in Table 4.2. Compared to the pure stoichiometric FeS, the lattice *c* parameters predicted with and without vdW correction for the different $FeM_{0.5}S$ systems do not differ significantly from each other and there is sensible improvement: the theoretical value is corrected within 1-2% with respect to experiments. The close agreement between the predicted lattice *c* parameters using the PW91 and PW91-D2 can be rationalized by considering the fact that, the inclusion of additional interstitial metal atoms in the van der Waals gap introduces attractive Fe_{int}–S and Fe_{int}–Fe_{net} forces that diminish the repulsive forces between adjacent sulfide layers.

For the $Fe_{1.5}S$, which contains additional interstitial Fe atom, the standard PW91 predicts the lattice *c* parameter at 5.127 Å, similar to the value of 5.116 Å predicted using PBE in earlier study (Brgoch *et al*., 2012). The dispersion corrected PW91-D2 yields a lattice *c* parameter of 5.024 Å, in close agreement with the experimental value of 5.047 Å reported by Berner, 1962, who originally noted the presence of excess iron in mackinawite. The lattice *a* and *b* parameters are also improved as they are predicted to within 1 % of the experimental values, with and without vdW correction. Similar results are obtained for the other interstitial metal impurities. The Co and Ni interstitial atoms demonstrate the most attractive forces between the FeS layers as is reflected in their shorter lattice *c* parameters calculated for $FeCo_{0.5}S$ and $FeNi_{0.5}S$ (see Table 4.2). Cr interstitial introduced the least attractive force between layers; the lattice *c* parameter of the $FeCr_{0.5}S$ system was calculated at 5.307 Å using PW91, and 5.204 Å using PW91-D2.

	$FeCr_{0.5}S$		$FeMn_{0.5}S$		$Fe_{1.5}S$		$FeCo_{0.5}S$		$FeNi_{0.5}S$		$FeCu_{0.5}S$	
Parameter	PW91	PW91-D2	PW91	PW91-D2	PW91	PW91-D2	PW91	PW91-D2	PW91	PW91-D2	PW91	PW91-D2
$a = b$ /Å	3.686	3.662	3.666	3.658	3.639	3.625	3.602	3.597	3.656	3.598	3.641	3.600
c /Å	5.307	5.204	5.238	5.155	5.127	5.024	5.000	4.944	5.047	4.992	5.155	5.103
c/a	1.439	1.421	1.429	1.409	1.409	1.386	1.381	1.374	1.380	1.387	1.415	1.418
Z_S	0.223	0.229	0.237	0.238	0.253	0.254	0.247	0.249	0.237	0.242	0.224	0.230
V_o /Å^3	72.10	69.79	70.39	68.97	67.89	66.01	65.52	63.97	67.46	64.62	68.34	66.13
d(Fe−S) /Å	2.186	2.172	2.213	2.175	2.200	2.193	2.188	2.169	2.186	2.165	2.172	2.173
d(Fe−Fe) /Å	2.606	2.568	2.592	2.545	2.543	2.551	2.558	2.551	2.584	2.553	2.572	2.575
d(M_{int}−S) /Å	2.359	2.302	2.293	2.252	2.195	2.201	2.204	2.200	2.269	2.218	2.293	2.291
d(M_{int}−Fe) /Å	2.653	2.602	2.620	2.576	2.563	2.512	2.499	2.472	2.524	2.496	5.577	2.552

TABLE 4.2: Optimized structural parameters of non-stoichiometric $FeM_{0.5}S$ structures. The interstitial impurity metal atom is designated as M_{int}.

Comparing the lattice volumes of the non-stoichiometric $FeM_{0.5}S$ systems with that of the stoichiometric FeS, we note that the inclusion of the interstitial metal atoms resulted in expansion of the lattice volumes. The extent of volume expansion resulting from the incorporation of the interstitial metal atoms decrease in the order: Cr > Mn > Cu > Fe > Ni > Co, with and without vdW correction. The variations in the extent of lattice volume expansion could be explained by considering the different covalent radii of atoms and the different bond lengths between bonding atoms. The larger volume expansion induced by the Cr and Mn interstitials in the FeS lattice volume is consistent with their larger covalent radii (1.39 Å), compared to that of Fe (1.32 Å), Co (1.26 Å), Ni (1.24 Å) and Cu (1.32 Å), (Cordero *et al.*, 2008). The electronic effects which could also contribute to the observed differences in the unit cell volume expansions are discussed next.

4.3.3. Electronic properties of mackinawite

Information regarding the electronic structure of the stoichiometric FeS is provided by the electronic total and projected density of states (PDOS). The total and PDOS of the stoichiometric FeS and the non-stoichiometric $Fe_{1.5}S$ as displayed in Figure 4.3 using the PW91-D2 method, show metallic character with the electronic states of the square-net Fe_{net} *d*-orbitals dominating the regions around the Fermi level in agreement with the metallic nature deduced by Vaughan and Ridout (1971). The projection on the interstitial Fe atom (Fe_{int}) shows that, it provides accessible bands at the Fermi level in the non-stoichiometric $Fe_{1.5}S$, whereas the contribution from the S atoms is negligible. These features are consistent with earlier DFT results on mackinawite (Subedi *et al.*, 2008; Devey *et al.*, 2008; Brgoch *et al.*, 2012).

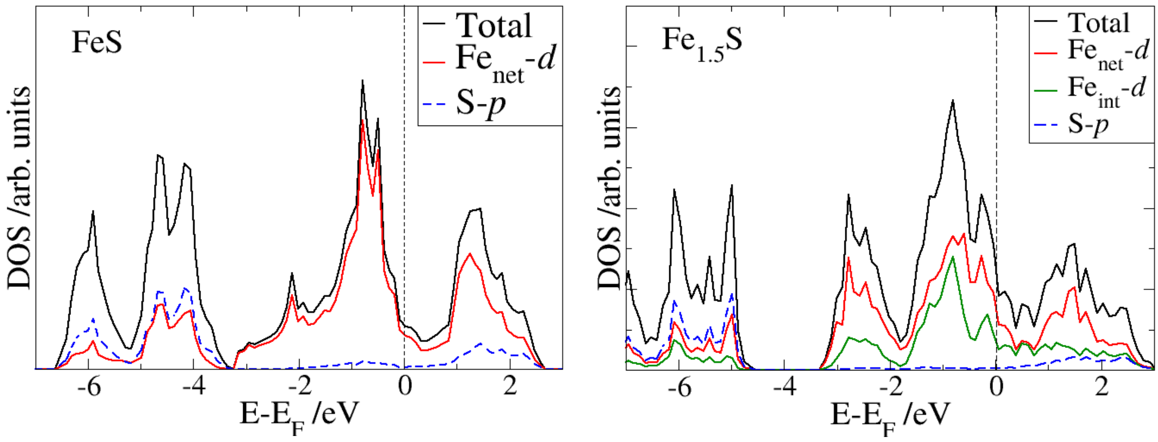

FIGURE 4.3: Electronic density of states (DOS) of stoichiometric FeS and stoichiometric $Fe_{1.5}S$ showing the total, and projection on the Fe-*d* and S-*p* orbitals.

Shown in Figure 4.4 are the total DOS of all the other interstitial metal doped FeS systems and their projected DOS on the Fe_{net} *d*, M_{int} *d* and sulfur *p* orbitals. All the doped FeS systems have very similar DOS features and remained metallic in nature as in the stoichiometric FeS. From the projection on each atom, it is evident that the interstitial metal atoms (M_{int}) provide accessible bands at the Fermi level; similar to the square-net Fe_{net} atoms. The contribution from the S atoms remained negligible at the Fermi level in all doped FeS systems. Cr, Mn, and Co interstitial atoms present the most densities at the Fermi level when compared to the Ni− and Cu−doped FeS systems. The contribution from the Cu *d*-states is negligible at the Fermi level. Similar to the stoichiometric FeS, the contribution from S *p*-states remains negligible at the Fermi level for all the non-stoichiometric $FeM_{0.5}S$ systems. These results suggest that the inclusion of the interstitial metals convert the two-dimensional electronic conductivity of the stoichiometric FeS within layers into three-dimensional conductive systems, within and across layers *via* the bridging interstitial metal atoms.

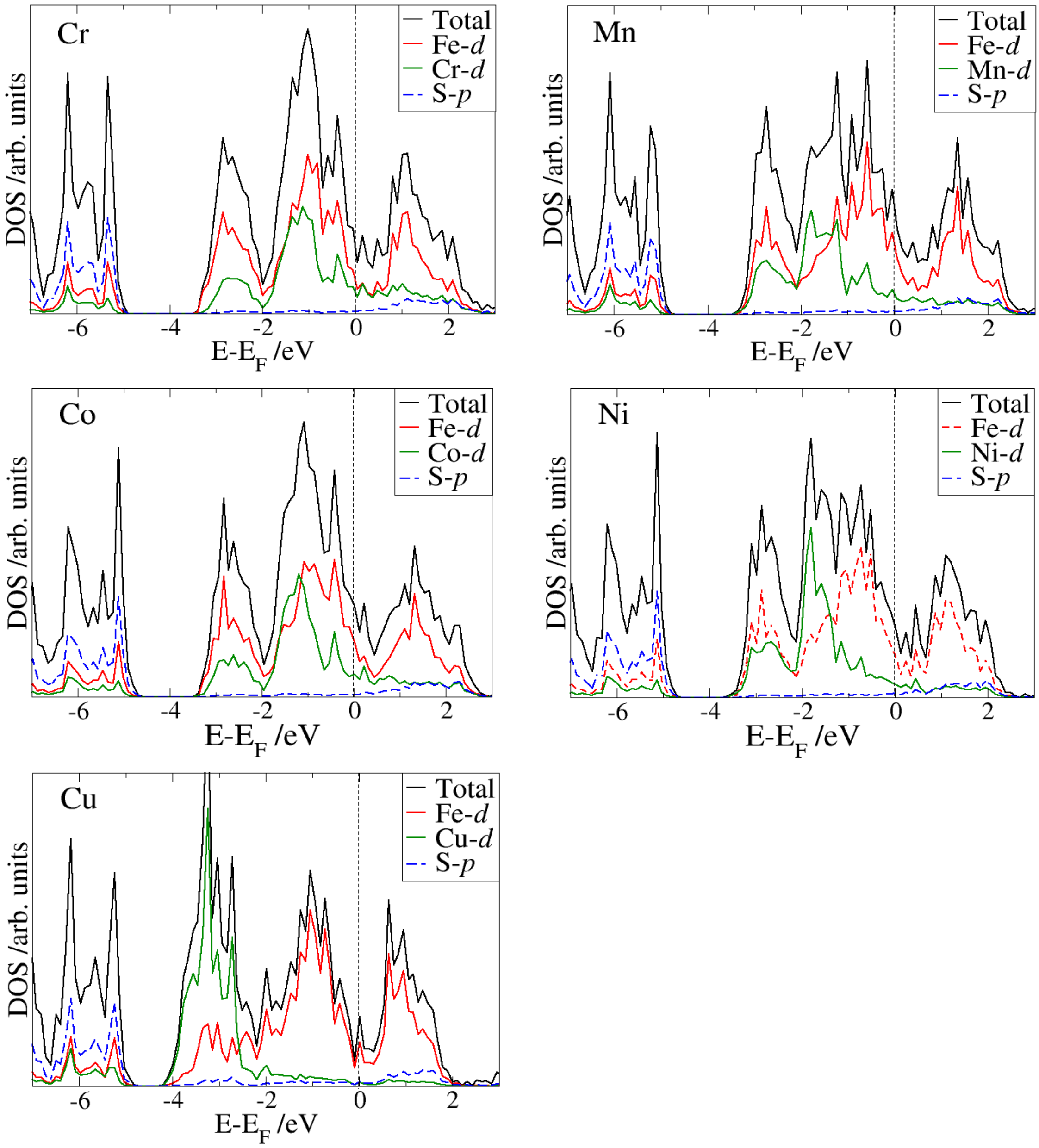

FIGURE 4.4: Electronic densities of states of non-stoichiometric $FeM_{0.5}S$ systems.

Further information regarding the electronic structures is provided by Bader charge population analyses in the implementation of Henkelman and co-workers (Henkelman, 2006; Sanville *et al.*, 2007; Tang *et al.*, 2009). The charge on each atomic species was determined for the non-stoichiometric $FeM_{0.5}S$ systems and compared with the stoichiometric FeS in order to ascertain the level of oxidation of each interstitial metal atom. Listed in Table 4.3 are the results of the Bader charge analyses based on the optimized crystal structures. The mean charges on Fe and S ions in the stoichiometric FeS are calculated at +0.83 e^{-} and −0.83 e^{-}, both of which fall short of the formal oxidation states (±2) of these atoms in this coordination. This can be expected as the Bader method commonly underestimates of ionic charges, as is clearly shown even in NaCl and MgO systems, where the charges are severely underestimated, by 12−14%, compared to the formal oxidation state of +1 and +2 for Na and Mg, respectively (Henkelman *et al.*, 2006). However, the method is reliable in identifying trends between similar systems, as is the case for the metal doped FeS systems studied here. The relative magnitude of the ionic charges, can be used be used to assess the level of oxidation or reduction of a given atomic specie in the $FeM_{0.5}S$ systems.

The Bader charge analyses of the $FeM_{0.5}S$ systems as shown in Table 4.3 indicate that when present, the interstitial metal atoms provide electrons to the FeS system that ultimately occupy Fe_{net}–Fe_{net} and Fe_{net}–S antibonding states. The interstitial Fe_{int} atom in the $Fe_{1.5}S$ system has a Bader charge of +0.78 e^{-}, representing an appreciable level of oxidation. The charge of the two square-net Fe_{net} ions are calculated to be +0.76 e^{-} and +0.69 e^{-}, representing a small reduction compared to the charge Fenet charge (+0.83 e^{-}) in the stoichiometric FeS. The S ions are reduced significantly in order to accommodate the excess electrons provided by the Fe_{int} ion. The charge on each S ion in the $Fe_{1.5}S$ was calculated at −1.11 e^{-} compared to the 0.83 e^{-} calculated in the stoichiometric FeS. The Co, Ni and Cu interstitial atoms show lesser extent of oxidation compared to the interstitial Fe_{int} atom. The Ni atom has a Bader charge of +0.55 e^{-}; indicating an appreciable level of oxidation and it is comparable to that found by Wang *et al.* (2007) when they modelled a range of Ni-S materials (0.41–

0.62 e^{-}). The Co and Cu impurity atoms are found to be oxidized to a similar extent as the Ni interstitial, providing 0.53 e^{-} and 0.50 e^{-} to the FeS system. The highest level of oxidation was predicted for the Cr and Mn interstitial impurity atoms which provide +1.22 e^{-} and +1.20 e^{-} respectively to the FeS system. Most of these electrons are transferred to the S ions, as they are appreciably reduced relative to the S ions in the stoichiometric FeS (Table 4.3).

Atom	FeS	Fe $Cr_{0.5}S$	$FeMn_{0.5}S$	$Fe_{1.5}S$	$FeCo_{0.5}S$	$FeNi_{0.5}S$	$FeCu_{0.5}S$
M_{int}	---	+1.22	+1.20	+0.78	+0.55	+0.53	+0.50
Fe_{net}^{1}	+0.83	+0.74	+0.71	+0.76	+0.76	+0.83	+0.78
Fe_{net}^{2}	+0.83	+0.62	+0.62	+0.69	+0.71	+0.72	+0.72
S^{1}	−0.83	−1.29	−1.27	−1.11	−1.01	−1.07	−1.01
S^{2}	−0.83	−1.29	−1.26	−1.10	−1.01	−1.01	−0.99

TABLE 4.3: Average charge (e^{-}) determined using Bader's analysis. M_{int} denotes the interstitial transition metals; Fe_{net} denote square-net Fe ions.

4.3.4 Vibrational frequencies of mackinawite

To determine the stability of the stoichiometric FeS and non-stoichiometric $FeM_{0.5}S$ systems, we have calculated the Gamma point phonon frequencies of all the PW91-D2 optimized structures using density functional perturbation theory (DFPT) within the standard Born-Oppenheimer approximation. Since the stoichiometric FeS unit cell contains four atoms, it supports 3 x 4 = 12 modes of vibrational, out of which nine are optical modes and the remaining three, are acoustic modes and corresponds to the displacement of the entire FeS lattice. Similarly, the non-stoichiometric $FeM_{0.5}S$ systems containing five atoms support 3 x 5 = 15 modes of vibration, out of which 12 are optical modes and the remaining three are acoustic modes. Shown in Table 4.4 are the frequencies of normal modes stoichiometric FeS and non-stoichiometric $FeM_{0.5}S$ system. No imaginary frequencies are observed, indicating that the FeS and $FeM_{0.5}S$ structures are dynamically stable. The eigenvectors showing the atomic displacement patterns of selected normal modes in the stoichiometric FeS and the non-stoichiometric $Fe_{1.5}S$ are shown in Figures 4.5 and 4.6 respectively. It is evident from the plot of the eigenvectors that the highest vibrational modes are associated with the displacement of S atoms. The eigenvectors of the other interstitial doped systems show similar displacement pattern as the excess Fe containing system.

Compared to the stoichiometric FeS, the incorporation of the interstitial metal atoms in the FeS structure resulted in a general increase in the vibrational frequencies of the $FeM_{0.5}S$ systems. The highest vibrational modes are calculated for the Co– and Ni–doped FeS systems, consistent with the shorter M_{int}–Fe_{net} and M_{int}–S interatomic bonds calculated for these systems compared to the other doped systems investigated. The increased vibrational frequencies suggest hardening of the interatomic bond distances in the FeS structures containing the interstitial metal atoms, and therefore indicate that when present the interstitial metal atoms could improve the mechanical stability of the FeS structure. The effects of the interstitial metal atoms on the mechanical properties of FeS are discussed in the next section.

Frequency	FeS	FeCr$_{0.5}$S	FeMn$_{0.5}$S	Fe$_{1.5}$S	FeCo$_{0.5}$S	FeNi$_{0.5}$S	FeCu$_{0.5}$S
υ_1 /cm^{-1}	418.4	436.0	432.7	451.7	456.4	453.3	424.7
υ_2 /cm^{-1}	414.3	435.6	432.3	449.9	441.6	435.2	423.0
υ_3 /cm^{-1}	404.5	387.3	378.4	404.0	411.2	412.6	406.7
υ_4 /cm^{-1}	395.6	381.9	373.9	396.5	398.4	392.1	384.8
υ_5 /cm^{-1}	388.6	379.5	373.8	384.9	397.7	391.6	383.7
υ_6 /cm^{-1}	387.2	377.9	309.9	377.9	396.6	391.0	379.4
υ_7 /cm^{-1}	263.5	286.2	303.2	336.8	335.9	319.4	263.6
υ_8 /cm^{-1}	257.2	239.8	244.5	268.0	265.0	258.4	244.4
υ_9 /cm^{-1}	255.8	238.4	244.4	266.0	264.3	257.9	243.3
υ_{10} /cm^{-1}	–	119.9	128.7	169.0	173.7	190.1	188.8
υ_{11} /cm^{-1}	–	119.4	123.4	158.6	159.6	142.8	108.5
υ_{12} /cm^{-1}	–	94.7	123.3	152.2	159.4	142.7	106.7

TABLE 4.4: Gamma point vibrational frequencies of stoichiometric FeS and non-stoichiometric FeM$_{0.5}$S systems containing interstitial metal atoms between layers.

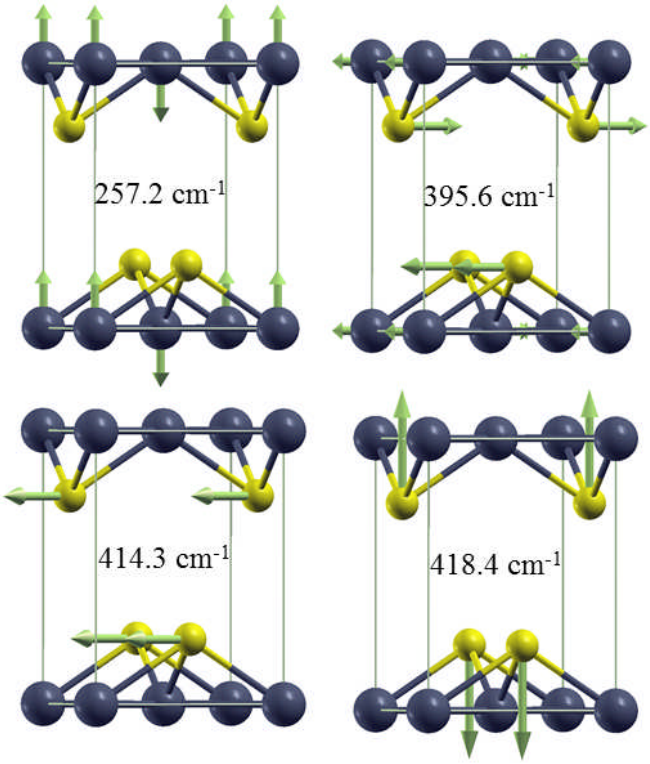

FIGURE 4.5: Selected normal modes of stoichiometric FeS.

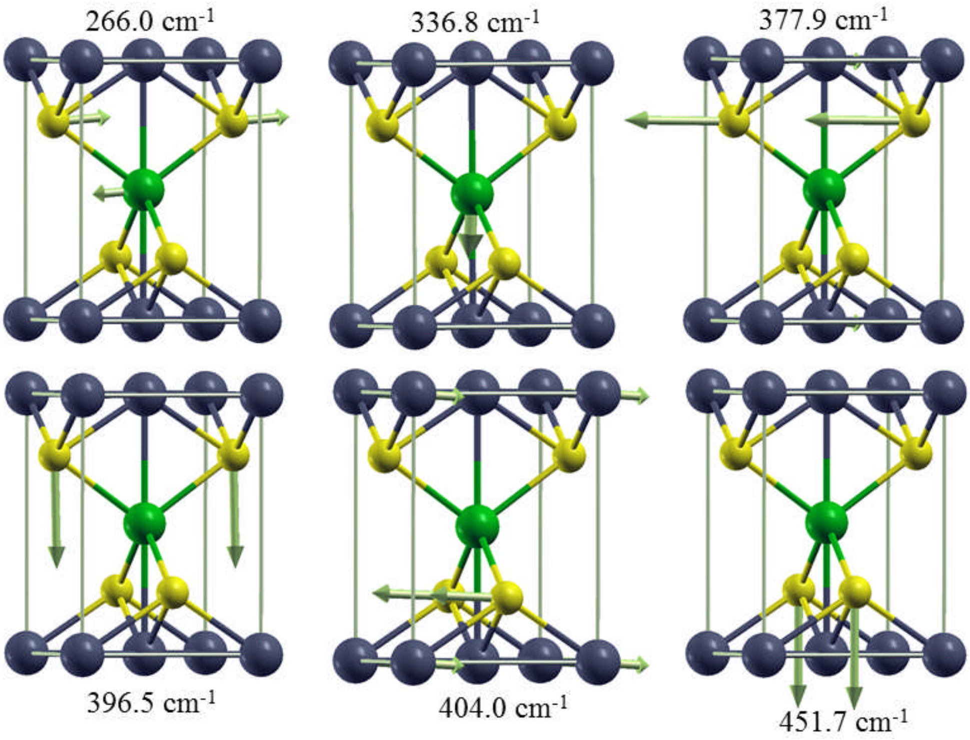

FIGURE 4.6: Selected normal modes of non-stoichiometric $Fe_{1.5}S$. Colour scheme (square-net Fe_{net} = grey, interstitial Fe_{int} = green and S = yellow).

4.3.5 Mechanical properties of mackinawite

Empirical information regarding the mechanical properties of mackinawite is scarcely reported in the literature, because it easily gets oxidized when exposed to air, making it difficult to characterize. Mackinawite is therefore an ideal system to investigate using first-principles DFT calculations. The only reported study on the mechanical property of mackinawite was done Ehm *et al.*, 2009, who predicted the bulk modulus of nanocrystalline FeS to be in the range of 27−39 GPa from their high pressure experiments. In this section, we have derived the elastic constants of stoichiometric FeS and non-stoichiometric $FeM_{0.5}S$ systems using DFT-D2 calculations. The elastic constants (C_{ij}) are derived *via* the second-order Taylor expansion of the total energy with respect to the applied distortion:

$$C_{ij} = \frac{1}{V_o} \frac{\partial^2 E}{\partial \varepsilon_i \partial \varepsilon_j} \tag{4.3}$$

where E is the total energy of the stressed cell, ε is the component of the applied strain, and V_o is the equilibrium stoichiometric FeS unit cell volume. In order to find the minimum of this relation a fitting procedure is used, which fits a parabola to a set of strains and the resultant increase or decrease in the internal energy for each discrete value of the applied strain allowing only electronic relaxations. The calculated elastic constants depend on the direction of the applied strain tensor. A given one-dimensional strain, represented by a dimensionless quantity and denoted by δ, is the ratio of any strained lattice parameter to the equilibrium value. For the C_{11} elastic constant, the distortion matrix takes the form:

$$\varepsilon = \begin{bmatrix} 1+\delta & 0 & 0 \\ 0 & 1 & 0 \\ 0 & 0 & 1 \end{bmatrix} \tag{4.4}$$

This distortion changes the size of the basal plane in the *x* axis, while keeping the *y* and *z* axes constant. Figure 4.7 shows the fit to the internal energy versus applied strain for the above deformation for the stoichiometric FeS. With this fit, the C_{11} is determined according to equation 2.45 (chapter 2):

$$C_{11} = \frac{1}{V_o} \frac{\partial^2 E}{\partial \varepsilon_i \partial \varepsilon_j} = \frac{2b}{V_o} \tag{4.5}$$

where *b* is the second order coefficient. From Figure 4.7, the second order coefficient is estimated at 8.952, thus $C_{11} = \frac{2 \times 8.952}{63.502} \frac{eV}{\dot{A}^3} = 45.19\,\text{GPa}$.

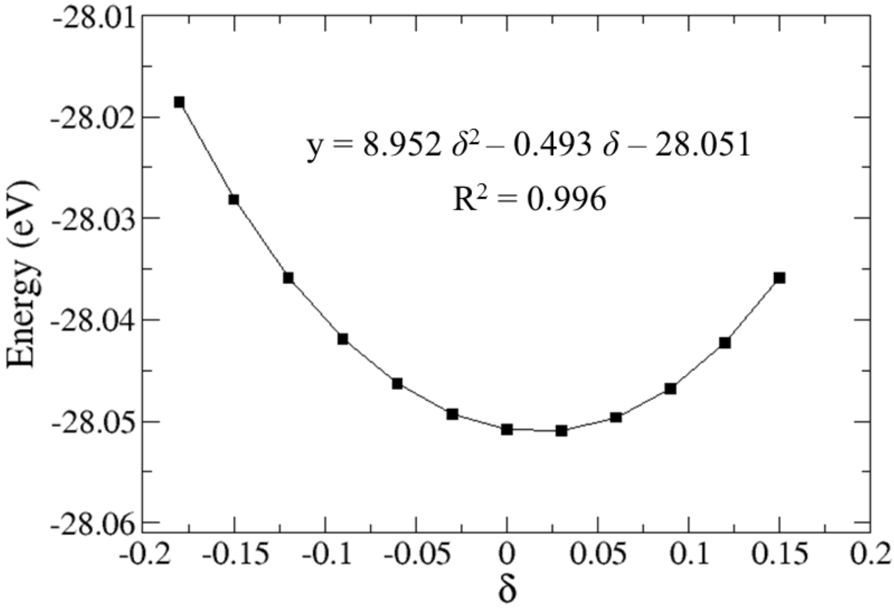

FIGURE 4.7: Graph of the fitting of the C_{11} elastic constant to the internal energy of the stoichiometric mackinawite unit cell versus applied strain.

Following the same procedure and applying the appropriate deformation tensors as presented in Table 2.1 (chapter two, section 2.6.6) the other elastic constants were determined and summarized in Table 4.5. The calculated elastic constants all satisfied the Born criteria for a tetragonal crystal: $C_{11} > 0$, $C_{33} > 0$, $C_{44} > 0$, $C_{66} > 0$, $(C_{11} - C_{12}) > 0$, $(C_{11} + C_{33} - 2C_{13}) > 0$ and $(2(C_{11} + C_{12}) + C_{33} + 4C_{13}) > 0$ (Born & Huang, 1954). For the pristine stoichiometric FeS, $C_{11} = C_{22}$ (45.19 GPa) is larger than C_{33} (16.3 GPa) suggesting that the distortion along the [001] direction is easier (Table 4.5), which agrees with the layered structure. The incorporation of the interstitial impurity metal atoms between the FeS layers is however, found to increase FeS's resistance to distortion along the [001] direction. This is reflected in the general increase of the calculated C_{33} for the non-stoichiometric $FeM_{0.5}S$ systems, an affect that can be attributed the replacement of weak dispersive forces between layers with chemically bonded interactions.

From the calculated elastic constants, the macroscopic bulk moduli (B_V) and shear moduli (G_V) were determined, using equations 4.6 and 4.7 respectively within the Voigt (V) approximation (Shein *et al.*, 2008).

$$B_V = \frac{1}{9}\left(2C_{11} + 2C_{12} + C_{33} + 4C_{13}\right) \tag{4.6}$$

$$G_V = \frac{1}{30}\left(4C_{11} - 2C_{12} + 2C_{33} - 4C_{13} + 12C_{44} + 6C_{66}\right) \tag{4.7}$$

The elastic moduli are useful in predicting the structural stability of materials: the B_V measures the material's resistance to uniform compression, whereas the G_V measures the material's response to shearing strains. The B_V and G_V of the stoichiometric FeS were calculated to be 31.37 GPa and 16.86 GPa respectively, confirming the soft nature of FeS. Our calculated B_V for the stoichiometric FeS falls within the range of bulk modulus (27−39 GPa) predicted from high pressure experiments on nanocrystalline FeS (Ehm *et al.*, 2009), and thus gives us confidence that the values predicted for the non-stoichiometric $FeM_{0.5}S$ counterparts are also reliable, where there are no available experimental data at ambient pressure to compare with. When we compare the bulk and shear moduli the stoichiometric FeS with those predicted for greigite (Fe_3S_4), we note that greigite's bulk and shear moduli are larger by almost a factor of two (B_V = 62.8 GPa and G_V = 36.0 GPa), (Roldan *et al.*, 2013), indicating that the mackinawite is prone to mechanical deformation than greigite.

In general, we found that when present, the interstitial metal atoms improve mackinawite's resistance to uniform compression and shear strain. The bulk moduli for Cr–, Mn–, Fe–, Co–, Ni– and Cu–doped mackinawite systems are calculated at 40.0 GPa, 41.1 GPa, 42.2 GPa, 45.5 GPa, 43.5 GPa, and 42.1 GPa respectively, all of which indicate an increase relative to the pristine stoichiometric FeS bulk modulus of 31.37 GPa. The highest bulk modulus predicted for the Co interstitial is consistent with the characteristic shorter M_{int}−S and M_{int}−Fe calculated in the $FeCo_{0.5}S$ compared to the other metal doped systems (Table 4.2). The incorporation of the interstitial metal atoms was also found to improve mackinawite's resistance to shear deformation as shown in Table 4.5. The predicted increase in the mechanical stability of FeS structures containing the interstitial metal atoms between its layers can be rationalized by considering the fact that, the addition of the interstitial metal atom (M_{int}) introduces attractive M_{int}−S and M_{int}−Fe_{net} forces that diminish the repulsive forces between adjacent sulfide layers. These results provide a quantitative agreement with earlier reports that suggested that the presence of Ni and Co impurities improvement in the mechanical hardness of mackinawite (*i.e.*, micro-indentation hardness), (Clarke *et al.*, 1969, 1970, Vaughan *et al.*, 1969); Blain, 1978).

Parameter	FeS	$FeCr_{0.5}S$	$FeMn_{0.5}S$	$Fe_{1.5}S$	$FeCo_{0.5}S$	$FeNi_{0.5}S$	$FeCu_{0.5}S$
C_{11} /GPa	45.19	55.74	55.56	61.85	65.79	64.43	63.15
C_{12} /GPa	32.98	42.98	41.91	41.89	44.87	42.67	40.78
C_{13} /GPa	28.19	34.87	35.81	36.82	39.43	37.51	36.32
C_{33} /GPa	13.21	23.21	24.08	25.94	29.38	27.33	26.01
C_{44} /GPa	21.19	29.21	30.74	31.32	33.21	32.19	30.49
C_{66} /GPa	37.19	41.19	41.74	41.98	42.65	41.78	41.82
B_V /GPa	31.37	40.01	41.14	42.30	45.49	43.50	42.12
G_V /GPa	16.86	22.38	22.62	23.20	24.36	23.79	23.15

TABLE 4.5: Elastic constants (C_{ij}), bulk (B_V) and shear moduli (G_V) for stoichiometric FeS and non-stoichiometric $Fe_{1.5}S$. The experimental B_V for the stoichiometric FeS was measured to be (27−39 GPa), Ehm *et al.*, 2009.

4.3.6 Structures and stabilities of FeS surfaces

We now discuss the surface structures and stabilities of the low-Miller index surfaces of the stoichiometric FeS. The different low-Miller index surfaces of stoichiometric mackinawite have been modelled by taking advantage of the crystal symmetry in the *a* and *b* directions to reduce the number of surfaces to (001), (100) (equivalent to (010)), (011) (equivalent to (101)), the (110) and the (111) surfaces planes. The (001) surface possesses two distinct terminations where the (001)–S surface corresponds to a termination of the complete FeS layer, leaving a typical type–II terminated (Tasker, 1979) surface of S atoms (Figure 4.8a), whereas the (001)–Fe surface is a reconstructed formally dipolar type–III surface leaving a partially vacant layer of Fe atoms at the surface (Figure 4.8b). The other low-index surfaces possess only a single termination each. Different slab and vacuum thicknesses as well as numbers of relaxed layers were tested for the different surfaces until convergence within 1 meV per cell was achieved. The converged slab thickness used to model the (001)–S, (001)–Fe (011), (100), (110) and (111) surfaces were constructed of 9, 7, 9, 6, 9, and 12 atomic layers respectively, and in every simulation cell, a vacuum region of 15 Å perpendicular to the each surface was tested to be sufficient avoid interactions between periodic slabs. Table 4.6 summarises the surface energies before and after energy minimization. Before relaxation, the order of increasing surface energies, and therefore decreasing stability, is (001)−S < (011) < (100) < (111) < (110) < (001)−Fe, which remains the same after relaxation.

The most stable surface is by far calculated to be the (001)–S termination, with a relaxed surface energy of 0.19 J m^{-2}. This is in good agreement with an earlier prediction using interatomic potential methods (Devey *et al*., 2008) and experimental data using selected areas electron diffraction (SAED) analyses on the FeS nanocrystals (Ohfuji & Rickard, 2006). The creation of the (001)–S terminated surface only involves breaking the weak vdW interactions between the sulfide layers which results in negligible relaxation of the surface species. The reconstructed (001)−Fe terminated surface, on the other hand, has a high surface energy calculated to be 2.67 J m^{-2}, reflecting the fact that its creation requires breaking of the most number of Fe−S bonds. No appreciable changes are observed in the average bond distances and angles at the topmost layers of the (001)−S and (001)−Fe surfaces upon relaxation (see Table 4.7) when compared to the bulk.

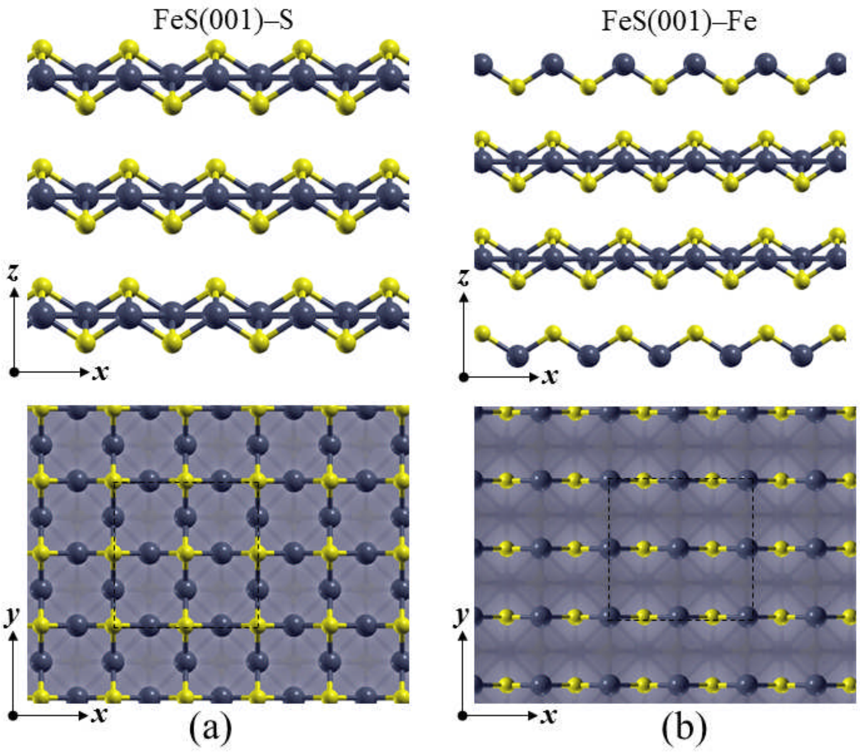

FIGURE 4.8: Schematic of the relaxed structures of the side (top) and top (bottom) view of the FeS(001). The sulfur termination is shown in (a) and iron termination is shown in (b). A (2 x 2) unit cell size is highlighted by dashed line in the top views.

Surface	γ_u (J m^{-2})	γ_r (J m^{-2})	Relaxation (%)
(001)−S	0.21	0.19	9.52
(001)−Fe	3.53	2.67	24.4
(011)	1.12	0.95	15.2
(100)	1.26	1.04	17.5
(111)	1.85	1.51	18.4
(110)	2.41	1.72	28.6

TABLE 4.6: Calculated surface energies before (γ_u) and after (γ_r) relaxation of the low-Miller index surfaces of stoichiometric FeS.

Surfaces	*d*(Fe−S)		*d*(Fe−Fe)	
	d	Δ*d*	*d*	Δ*d*
(001)–S	2.198	0.027	2.554	–0.005
(001)–Fe	2.129	0.073	–	–
(011)	2.189	0.013	2.554	–0.005
(100)	2.183	0.019	2.553	–0.004
(111)	2.110	0.092	2.589	–0.040
(110)	2.144	0.058	2.409	0.140

TABLE 4.7: The average bond distances (*d*, in Å) in the topmost surface layers after the slab optimization of the low-index surfaces and the relative bond distances compared to the relaxed bulk FeS (Δ*d*, in Å).

The (011) surface, which is identical to the (101) surface is terminated by Fe atoms in the topmost layer (Figure 4.9a) and has a relaxed surface energy of 0.95 Jm^{-2} (Table 4.6). During energy minimization, the topmost Fe atoms moved downwards by 0.131 Å towards the bulk, decreasing the interlayer spacing between atomic layers 1 and 2 by 5.1% relative to the unrelaxed interlayer spacing. The (011) surface undergoes minimal relaxation as reflected in their topmost layer interatomic bond distances (Table 4.7), which are similar to those in the bulk.

The (100) surface which is equivalent the (010) surface is calculated to be the next stable surface after the (011) surface. These surface planes are terminated by both S and Fe atoms at the topmost surface layer as shown in Figure 4.9b and their unrelaxed and relaxed surface energy were calculated to be 1.26 J m^{-2} and 1.04 J m^{-2} respectively, representing a percentage relaxation of 17.5 % (Table 4.6). During energy minimization, the terminating S atoms are moved downwards marginally by 0.05 Å. No appreciable changes are however, observed in the average bond distances and angles at the topmost layers of the (100) surface upon relaxation (Table 4.7).

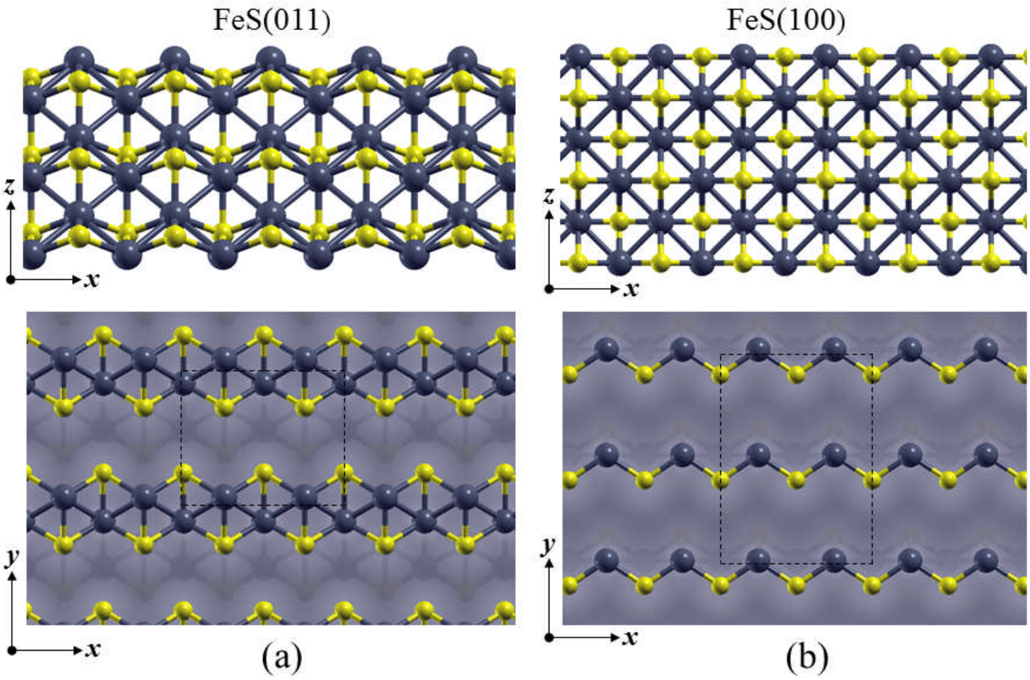

FIGURE 4.9: Schematic illustration of the side (top) and top (bottom) views of the relaxed structures of the (011)–(a) and (100) –(b) surfaces of FeS. A (2 x 2) unit cell size is highlighted by dashed line in the top view.

The (111) surface of FeS, terminated by S atoms in the topmost layer as shown in Figure 4.10(a), is found to undergo relaxation to some extent in the topmost layers. The unrelaxed and relaxed surface energies of the (111) surface plane were calculated at 1.85 J m^{-2} and 1.51 J m^{-2} respectively, representing a percentage relaxation of 18.4 % in the surface energy (Table 4.6). During energy minimisation, the terminating S moved 0.212 Å downwards toward the second layer thereby decreasing the interlayer separation between the topmost S–layer and the second Fe–layer by 2.1%. The least stable surface among the low-index FeS surfaces investigated was calculated to be the (110) surface. It is also the surface plane that exhibits the largest relaxation upon energy minimisation. The (110) surface is terminated by Fe atoms that are less coordinated in the topmost layer than in the bulk. Each topmost layer Fe atom is coordinated by two S atoms compared to the four S coordinated Fe atoms in the bulk (Figure 4.10b). The unrelaxed and relaxed surface energies of the (110) surface are calculated to be 2.41 J m^{-2} and 1.72 J m^{-2} respectively, representing a percentage relaxation of 28.6 %. During geometry relaxation the topmost Fe atoms move downwards by 0.331 Å towards the bulk, thereby reducing the vertical Fe–Fe bond distance from 2.549 Å to 2.409 Å, an indication of inward relaxation between the topmost Fe atoms and the second layer Fe atoms. Similarly, a shorter Fe–S bond distance of 2.144 Å was calculated between the topmost Fe atom and S in the second layer (see Table 4.7).

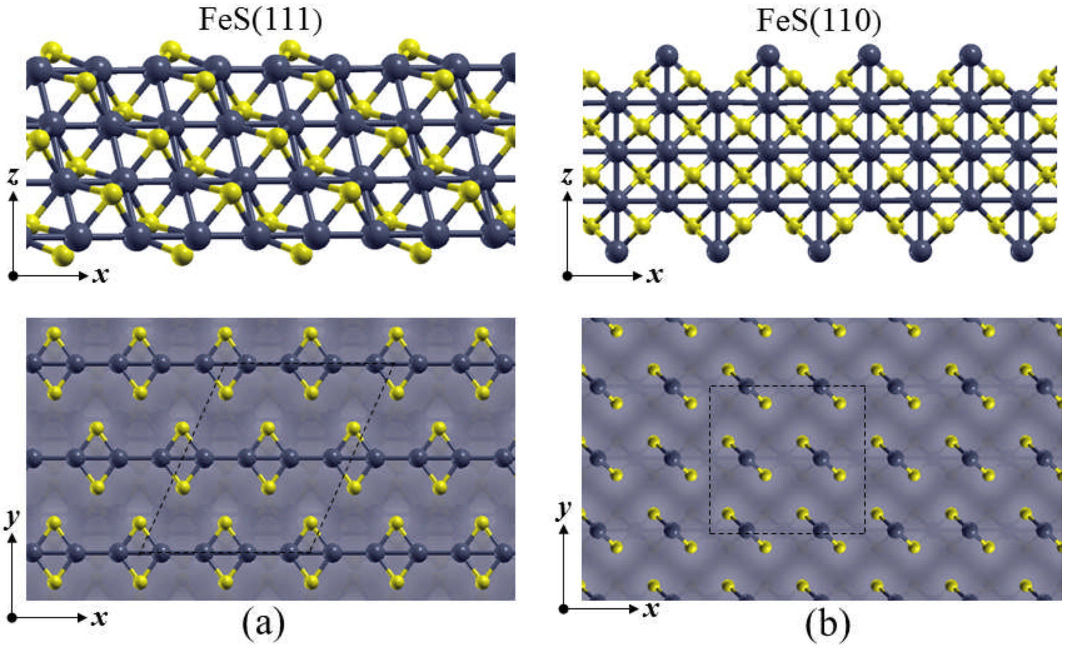

FIGURE 4.10: Schematic illustration of the side (top) and top (bottom) views of the relaxed structures of the (011)–(a) and (100) –(b) surfaces of FeS. A (2 x 2) unit cell size is highlighted by dashed line in the top view.

4.3.7 Surface electronic structures

To identify any changes in the electronic total and projected density of states (PDOS) of the low-index surfaces compared to the bulk material, the PDOS of the various relaxed surfaces are plotted and displayed in Figure 4.11. The plots show that the bulk-like metallic nature is retained at all the low-index surfaces, with the dominant contribution to the states at the Fermi level coming from Fe 3*d* states. The results also indicate that the slab thickness used in modelling the different surfaces is sufficient enough to retain the bulk-like electronic properties. Bader charge analyses have also been carried out on the relaxed FeS surfaces to identify any changes in charges of the surface species compared to the bulk material. The average charges of the surface ions as summarized in Table 4.8 show no appreciable changes when compared to the bulk Fe and S ions.

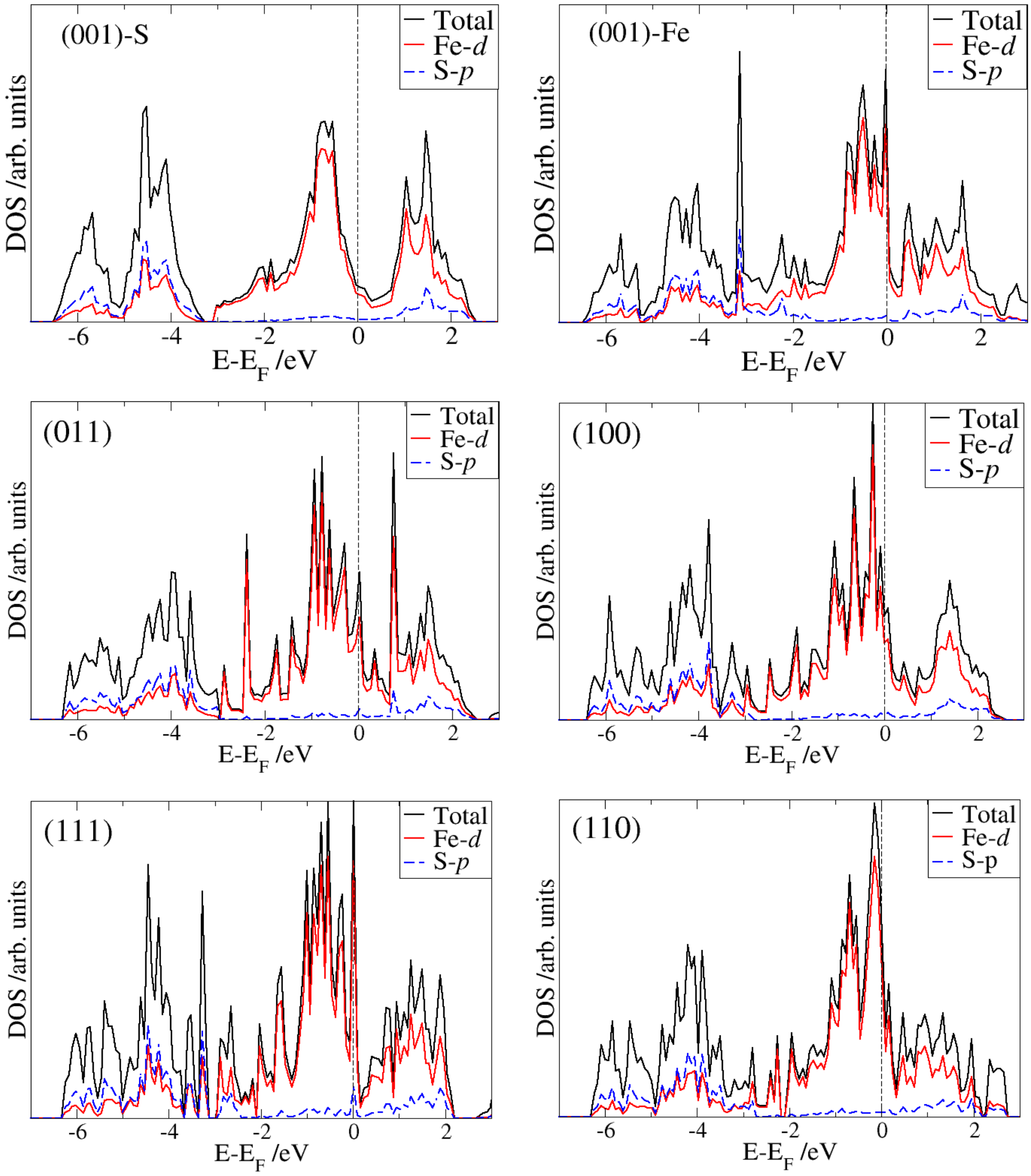

FIGURE 4.11: Electronic DOS of the low-Miler index surfaces of mackinawite

	Fe		S	
	q /e$^-$	Δq /e$^-$	q /e$^-$	Δq /e$^-$
Bulk	0.83	--	–0.83	--
(001)–S	0.83	0.00	–0.83	0.00
(001)–Fe	0.66	0.17	–0.71	–0.12
(011)	0.79	0.04	–0.80	–0.03
(100)	0.80	0.03	–0.80	–0.03
(111)	0.72	0.11	–0.73	–0.10
(110)	0.71	0.12	–0.77	–0.06

TABLE 4.8: Average charge (q) of relaxed topmost surface Fe and S ions and variance with respect to the bulk ions (Δq).

4.3.8 Crystal morphology of mackinawite

Based on the calculated surface energies, the thermodynamic crystal morphology of FeS was calculated using Wulff's method (Wulff, 1901). The simulated crystal morphology of mackinawite as presented in Figure 4.12, which shows that FeS crystals grow as thin and tabular crystals, in excellent agreement with the crystal morphologies observed by Ohfuji and Rickard, from their high resolution transmission electron microscope (HRTEM) examination of FeS aggregates. Their complementary selected area electron diffraction (SAED) analyses on the FeS nanocrystals (both freeze-dried and precipitated mackinawite) show clearly the (001) as the most stable surface, followed in decreasing stability by the (101), (200) (equivalent to the (100) surface), and (111) planes (Ohfuji & Rickard, 2006). These findings show good agreement with the surface energies predicted from our DFT-D2 calculations. The non-existence of the (110) surface reflections in the SAED patterns and its lack of appearance in the simulated morphology of the FeS crystal can be attributed to its relatively high surface energy.

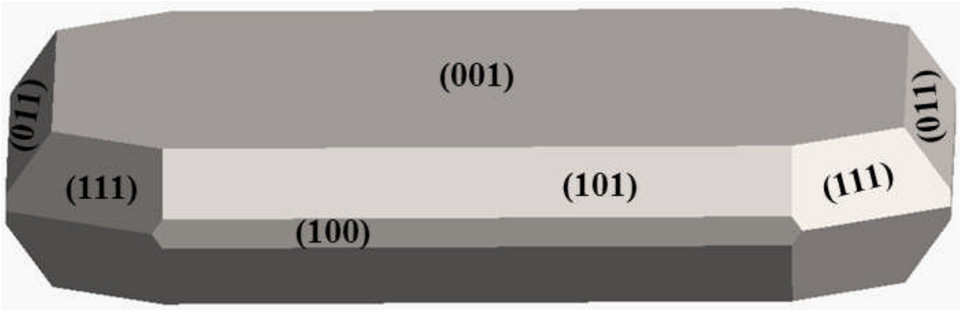

FIGURE 4.12: Calculated crystal morphology of mackinawite. The crystals grow in thin and tabular forms, with the (001) surface highly prominent.

4.4 Summary and conclusions

Ab initio DFT-D2 calculations have been used to model the structural, electronic, vibrational, and mechanical properties of stoichiometric FeS and non-stoichiometric $FeM_{0.5}S$ systems containing interstitial metal atoms between FeS layers. We have shown from our calculations that the dispersion corrected DFT-D2 method which explicitly accounts for the dispersive forces acting between FeS layers, sensibly improves the prediction of interlayer separation distance in FeS in good agreement with experimental data. The incorporation of interstitial metal atoms in the van der Waals gap is shown to introduce attractive Fe_{int}–S and Fe_{int}–Fe_{net} forces that diminish the repulsive forces between adjacent sulfide layers. As a result of this, both the DFT and DFT-D2 methods were found to reproduce interlayer separation gaps that do not differ significantly and in close agreement with experiment.

Calculated PDOS of the stoichiometric FeS and non-stoichiometric $FeM_{0.5}S$ systems show metallic features, with the electronic states of the Fe *d*-orbitals dominating the regions around the Fermi level, in agreement with the metallic nature deduced by Vaughan and Ridout (1971) and consistent with theoretical results reported in the literature. Bader charge analyses of the non-stoichiometric $FeM_{0.5}S$ systems indicate that when present, the interstitial metal atoms provide electrons to the FeS system that ultimately occupy Fe_{net}−Fe_{net} and Fe_{net}−S antibonding states. Cr and Mn impurities are found to be oxidised to a larger extent, providing almost three times more electrons to the FeS system than Co, Ni and Cu. The presence of the interstitial metal atoms in the tetrahedral site between FeS layers was also demonstrated to improve the mechanical stability of mackinawite, *via* the formation of M_{int}–S and M_{int}–Fe_{net} covalent bonds. Consistent with the shorter M_{int}–S and M_{int}–Fe_{net} bonds calculated for Co and Ni impurity atoms, compared to the interstitial metal atoms studied, the FeS systems containing these impurity interstitials atoms were predicted to highest bulk and shear moduli.

From geometry optimization of the low-index surfaces of stoichiometric FeS, we have shown the (001) surface terminated by sulfur is by far the most stable surface, consistent with diffraction SAED analyses results on the FeS nanocrystals (Ohfuji & Rickard, 2006). Compared to the other relaxed low-index surfaces, the order of increasing surface energies, and therefore decreasing stability is as follows: (001)−S < (011) < (100) < (111) < (110) < (001)−Fe. The calculated surface energies and resulting equilibrium morphology of FeS show excellent agreement with the crystals grown by Ohfuji and Rickard, who described thin and tabular crystals using high resolution transmission electron microscope (HRTEM), Ohfuji & Rickard, 2006.

Bibliography

- Benning L.G.; Wilkin R.T.; Barnes H.L.; *Chemical Geology* **167**, 25 (2000)
- Berner R. A.; Science, **137**, 669 (1962)
- Bertaut E. F.; Burlet P.; Chappert J.; *Solid State Commun*. **3**, 335 (1965)
- Blain C. F.; *Mineralogical Magazine*, **42**, 284 (1978)
- Blöchl P. E.; *Phys. Rev. B*. **50**, 17953 (1994)
- Born M.; Huang K.; Dynamical Theory of Crystal Lattices, Oxford University Press, 1954
- Bourdoiseau J.-A.; Jeannin M.; Sabot R.; Rémazeilles C.; Refait Ph.; *Corrosion Science*, **50**, 3247 (2008)
- Brgoch J.; Miller G. J.; *J. Phys. Chem. A*, **116**, 2234 (2012)
- Bucko T.; Hafner J.; Lebegue S.; Angyan J. G.; *J. Phys. Chem. A*, **114**, 11814 (2010)
- Cahill C.L.; Benning L.G.; Barnes H.L.; Parise J.B.; *Chemical Geology* **167**, 53 (2000)
- Clark A. H.; *Neues Jahrb. Mineral Monatsch*, **6**, 282 (1969)
- Clark A. H.; *Amer. Mineral*., **55**, 1802 (1970)
- Clark A. H.; *Neues Jahrb. Mineral Monatsch*, **6**, 282 (1969)
- Clark A. H.; Some comments on the composition and stability relations of mackinawite, *Neues Jahrb Mineral, Monatsh*. 300-304 (1966)
- Cody G. D.; *Annu. Rev. Earth Planet. Sci.*, **32**, 569 (2004)
- Cordero B.; Gómez V.; Platero-Prats A. E.; Revés M.; Echeverría J.; Cremades E.; Barragán F.; Alvarez S.; *Dalton Trans.* **21**, 2832 (2008)

- Devey A. J.; Grau-Crespo R.; de Leeuw N. H.; *J. Phys, Chem C*, **112**, 10960 (2008)
- Dobbek H.; Svetlitchnyi V.; Gremer L.; Huber R.; Meyer O.; *Science*, **293**, 1281 (2001)
- Denholme S. J.; Demura S.; Okazaki H.; Hara H.; Deguchi K.; Fujioka M.; Ozaki T.; Yamaguchi T.; Takeya H.; Takano Y.; *Materials Chemistry and Physics* **147**, 50 (2014)
- Ehm L., Michel F. M.; Antao S. M.; Martin C. D.; Leem P. L.; Shastri S. D.; Chupas P. J.; Parise J. B.; *J. Appl. Cryst.*, **42**, 15 (2009)
- Gibbs J. W.; Collected Works, Longman, New York, (1928)
- Gramp J. P.; Bigham J. M.; Jones F. S.; Tuovinen O. H.; *J. Hazard. Mater*. **175** 1062 (2010)
- Grimme S., *Journal of Computational Chemistry*, **27**, 1787 (2006)
- Henkelman G.; Arnaldsson A.; Jónsson H.; *Comput. Mater. Sci*., **36**, 345 (2006)
- Hunger S.; Benning L.G.; *Geochemical Transactions* **8**, 1 (2007)
- Huber C.; Wächtershäuser G.; *Science*, **276**, 245 (1997)
- Hu Y.; Zheng Z.; Jia H.; Tang Y.; Zhang L.; *J. Phys. Chem. C* **112**, 13037 (2008)
- Ishibashi S.; Terakura K.; Hoson H.; *J. Phys. Soc. Jpn*. **77**, 053709 (2008)
- Jeong H. Y.; Klaue B.; Blum J. D.; Hayes K. F.; *Environ. Sci. Tech*. **41** 7699 (2007)
- Kirkeminde A.; Ruzicka B.A.; Wang R.; Puna S.; Zhao H.; Ren S.; *ACS Appl. Mater. Interfaces* **4**, 1174 (2012)
- Kresse G.; Hafner J.; *Phys. Rev. B*, **48**, 13115 (1993)
- Kresse G.; Hafner J.; *J. Phys. Condens. Matter*, 6, 8245 (1994)

- Kresse G.; Furthmuller J.; *Phys. Rev. B*, **54**, 11169 (1996)
- Kresse G.; Joubert D.; *Phys. Rev. B*, **59**, 1758 (1999)
- Kwon K. D.; Refson K.; Bone S.; Qiao R.; Yang W.; Liu Z.; Sposito G.; *Phys. Rev*. **83**, 064402 (2011)
- Livens F. R.; Jones M. J.; Hynes A. J.; Charnock J. M.; Mosselmans J F.; Hennig C.; Steele H.; Collison D.; Vaughan D. J.; Pattrick R. A.; Reed W. A.; Moyes L. N.; *J. Environ. Radioact.* **74**, 211 (2004)
- Lennie A. R.; Redfern S. A. T.; Champness P. E.; Stoddart, Schofield P. F.; Vaughan D. J.; *Am. Mineral*. **82**, 302 (1997)
- Lennie A. R.; Redfern S. A. T.; Schofield P. F.; Vaughan D. J.; *Min. Mag.*, **59**, 677 (1995)
- Li Y. F.; Zhu L. F.; Guo S. D.; Xu Y. C.; Liu B. G.; *J. Phys. Condens. Matter* **21**, 115701 (2009)
- Monkhorst H. J.; Pack J. D.; *Phys. Rev. B.* **13**, 5188 (1976)
- Morse J. W.; Arakaki T.; Geochim. Cosmochim. Acta 57, 3635 (1993)
- Mullet M.; Boursiquot S.; Ehrhardt J.-J.; *Colloids Surf. A* **244**, 77 (2004)
- Mullet M.; Boursiquot S.; Abdelmoula M.; Génin J.-M.; Ehrhardt J.-J.; *Geochimica et Cosmochimica Acta*, **66**, 829 (2002)
- Nakamura R.; Okamoto A.; Tajima N.; Newton G.J.; Kai F.; Takashina T.; Hashimoto K.; *ChemBioChem* 11, 643 (2010)
- Ohfuji H.; Rickard D., *Earth Plan et Sci. Lett.*, **241**, 227 (2006)
- Paolella A.; George C.; Povia M.; Zhang Y.; Krahne R.; Gich M.; Genovese A.; Falqui A.; Longobardi M.; Guardia P.; Pellegrino T.; Manna L.; *Chem. Mater*. **23**, 3762 (2011)
- Patterson R. R.; Fendorf S.; Fendorf M.; *Environ. Sci. Technol*. **31**, 2039 (1997)

- Paolella A.; George C.; Povia M.; Zhang Y.; Krahne R.; Gich M.; Genovese A.; Falqui A.; Longobardi M.; Guardia P.; Pellegrino T.; Manna L.; *Chem. Mater.* **23**, 3762 (2011)

- Pósfai M.; Buseck P. R; Bazylinski D. A.; Frankel R. B.; *Am. Mineral*. **83**, 1469 (1998)

- Rickard D.; Luther G. W.; *Chem. Rev.*, **107**, 514 (2007)
- Rickard D.; *Geochim. Cosmochim. Acta*, **61**, 115 (1997)
- Rickard D.; Morse J.W.; *Marine Chemistry* **97**, 141 (2005)
- Roldan A.; Santos-Carballal D.; de Leeuw N. H.; *J. Chem. Phys*., **138**, 204712 (2013)

- Russell M. J.; Hall A. J.; *J. Geog. Soc. Lond.*, **154**, 377 (1997)
- Sanville E.; Kenny S. D; Smith R.; Henkelman G.; *J. Comput. Chem*., **28**, 899 (2007)

- Shein I. R.; Ivanovskii A. L.; *Scripta Materialia*, 59, 1099 (2008)
- Singh D. J.; Du M. H.; *Phys. Rev. Lett*. **100**, 237003 (2008).
- Subedi A.; Zhang L. J.; Singh D. J.; Du M. H.; *Phys. Rev. B*, **78**, 134514 (2008)

- Tang W.; Sanville E.; Henkelman G.; *J. Phys.: Condens. Matter*, **21**, 084204 (2009)

- Tasker P. W.; *J. Phys. C: Solid State Physics*, **12**, 4977 (1979)
- Vaughan D. J.; Craig J. R.; Mineral Chemistry of Metal Sulfides, Cambridge University Press, New York, (1978)

- Vaughan D. J.; Ridout M. S.; *J Inorg Nucl. Chem*, **33**, 741 (1971)
- Vaughan D. J.; *Transvaal. Am. Mineral*., **54**, 1190 (1969)
- Wang J. H.; Cheng Z.; Brédas J.-L.; Liu M.; *J. Chem. Phys.*, **127**, 214705 (2007)

- Watson G. W.; Kelsey E. T.; de Leeuw N. H.; Harris D. J.; Parker S. C.; *J. Chem. Soc., Faraday Trans.*, **92**, 433 (1996)
- Welz D.; Rosenberg M.; *J. Phys. C: Solid State Phys*. **20**, 3911 (1987)
- Wittekindt C.; Marx D.; *J. Chem. Phys*. **137**, 054710 (2012)
- Wolthers M.; van der Gaast S. J; Rickard D.; *Am. Mineral*, **88**, 2007 (2003)
- Wulff G.; Z. Kristallogr. Mineral., **34**, 449 (1901)
- Yamaguchi Y.; Takeuchi T.; Sakaebe H.; Kageyama H.; Senoh H.; Sakai T.; Tatsumi K.; *J. Electrochem. Soc*, **157**, A630 (2010)
- Yuhas B. D.; Smeigh A.L.; Samuel A.P.S.; Shim Y.; Bag S.; Douvalis A.P.; Wasielewski M.R.; Kanatzidis M.G.; *J. Am. Chem. Soc.* **133**,7252 (2011)

Chapter 5

Structure of $As(OH)_3$ adsorption complexes on FeS surfaces

Abstract

The sorption of arsenic on mineral surfaces is an important environmental chemical process because the sorption process influences the transportation, bioavailability and biodegradability of arsenic in water, soils and sediments (Gallegos-Garcia *et al.*, 2012). Interestingly, the interactions between $As(OH)_3$ complex (the most toxic and mobile form of As in aqueous solutions) and the surfaces of mackinawite, have not been clearly established. In this work, density functional theory calculations with a correction for the long-range interactions (DFT-D2) have been used to determine the energetically most stable adsorption complexes of $As(OH)_3$ on the low-index (001), (011), (100), and (111) surfaces of mackinawite under vacuum conditions. Geometry optimization calculations reveal that the $As(OH)_3$ molecule has preference for the formation of bidentate adsorption complexes over monodentate adsorption complexes. Our calculated long As−Fe and As−S interatomic distances clearly suggest interactions *via* outer sphere surface complexes with respect to the As atom, in agreement with the experimental observations of Farquhar *et al.*, (2002).

5.1 Introduction

Arsenic is recognized as one of the most serious inorganic contaminants in drinking water worldwide (Ferguson & Gavis, 1972). Arsenic often makes its way into water courses by the natural processes of weathering and dissolution of minerals such as arsenian pyrite, $Fe(As,S)_2$, and arsenopyrite, FeAsS (Welch *et al.*, 2000). Anthropogenic activities, particularly minerals extraction and processing can also introduce arsenic rich effluents into the environment if not carefully monitored and controlled (Nordstrom, 2002). The effects of arsenic on human health can be very detrimental, including arsenic poisoning being linked to neurological disorders, dermatological and gastrointestinal problems (Hughes, 2002) as well as being a known carcinogen (U.S. Environmental Protection Agency report, 1999).

Arsenic can exist in a range of oxidation states from –3 to +5, though it is most commonly found as As(III) or As(V) oxyacids in aqueous solutions. It is however, known that As(III) is both more toxic (Ferguson & Gavis, 1972) and more mobile (may travel five to six times faster than As(V)), (Amin *et al.*, 2006; Gulens *et al.*, 1979). Analyses of hydrothermal fluids show that As is transported mainly as As(III) (Ballantine & Moore, 1988), and the uptake of As(III) from aqueous solutions is reported to occur *via* channels of neutral molecules, suggesting that $As(OH)_3$ or related species could be the common form of arsenic in contaminated waters (Liu *et al.*, 2002; Sanders *et al.*, 1997). An understanding of the geochemistry of arsenite in low temperature anoxic sedimentary environments is therefore crucial to the development of safe drinking water and food supplies in many countries (Smedley *et al.*, 2002; Williams *et al.*, 2005). Of the processes influencing arsenite mobility, adsorption onto mineral surfaces is thought to strongly influence its concentrations in water environments (Gallegos-Garcia *et al.*, 2012). In anoxic sulfidic settings, arsenite mobility is thought to be controlled by its interaction with iron sulfides (Bostick *et al.,* 2003, Sadiq, 1997 and O'Day *et al.*, 2004). A number of experimental studies on the uptake of arsenite by iron sulfide minerals have been reported on troilite (hexagonal FeS), pyrite (FeS_2) and mackinawite (tetragonal FeS), (Moore *et al*., 1988; Farquhar *et al*., 2002; Bostick & Fendorf, 2003; Wolthers *et al*., 2005; Gallegos *et al.*, 2007).

Mackinawite's particle size and surface area, two properties that may impact As(III) uptake, have also been studied by Wolthers *et al.*, (2003) who reported 4 nm as the average primary particle size with 350 m^2/g of specific surface area (SSA). This large surface area suggests a potential high reactivity of mackinawite, and this has been demonstrated by Farquhar *et al*. (2002) who showed that mackinawite has higher As(III) removing efficiency from solution than pyrite, goethite and lepidocrocite. Other studies have also shown that mackinawite can influence the mobility and bioavailability of environmentally important trace elements, notably through processes involving either sorption (Watson *et al.*, 2000; Wolthers *et al.*, 2005) or oxidative dissolution (Scheinost *et al.*, 2008, Livens *et al*., 2004; Mullet *et al.*, 2004).

Mechanistic understanding of the adsorption processes of arsenite on iron sulfide mineral surfaces requires molecular level knowledge of the binding geometry of arsenite surface complexes, which is also critical to the quantification of the arsenite adsorption on the mineral surfaces. Compared to the extensive studies of the surface complexation of arsenite and arsenate on iron oxides and hydroxides using theoretical calculations (Blanchard *et al.*, 2012; Sherman & Randall, 2003) and X-ray absorption and vibrational spectroscopic techniques (Catalano *et at.*, 2007, 2008;

Fendorf *et al.*, 1997; Waychunas *et al.*, 1993, 1995; Manceau *et al.*, 1995; Lumsdon *et al.*, 1984), the registries of arsenite adsorption complexes on iron sulfide mineral surfaces are still not clearly established. Using DFT calculations, Blanchard *et al.* (2007) recently predicted a bidentate adsorption complex for $As(OH)_3$ on the (001) surface of pyrite (FeS_2). The structure of $As(OH)_3$ adsorption complexes on mackinawite surfaces is however, still not thoroughly investigated.

In this chapter, we have investigated the structure of $As(OH)_3$ adsorption complexes on the low-index surfaces of mackinawite and within the internal layers of the bulk mineral under vacuum conditions using DFT calculations with a correction for dispersion interactions using the proposed by Grimme (Grimme, 2006). We have considered both molecular and dissociative adsorption configurations, and information regarding vibrational and electronic properties of the adsorbed complexes is presented.

5.2. Computational details

Energy minimization calculations were carried out using the Vienna Ab-initio Simulation Package (VASP) code (Kresse *et al.*, 1993, 996) which employs a basis set of plane-waves to solve the Kohn-Sham (KS) equations of the density functional theory (DFT) in a periodic system. Dispersion forces were accounted for in our calculations using the Grimme DFT-D2 method (Grimme, 2006) which is essential for a proper description of the layered structure of mackinawite and the adsorption systems. We have used the generalized gradient approximation (GGA), with the PW91 functional (Perdew *et al.*, 1992) to calculate the total free energies. The interaction between the valence electrons and the core was described with the projected augmented wave (PAW) method (Blöchl, 1994) in the implementation of Kresse and Joubert (1999). The KS valence states were expanded in a plane-wave basis set with a cut off at 400 eV, which is high enough to ensure that no Pulay stresses occurred within the cell during relaxations. An energy threshold defining self-consistency of the electron density was set to 10^{-5} eV and the interatomic forces are minimized up to 0.01 eV/Å for structural relaxations. A 5 x 5 x 1 Monkhorst-pack grid (Monkhorst and Pack, 1976) were used to sample the reciprocal space of the substrate-adsorbate system, which ensures electronic and ionic convergence.

A (3x3) supercell was used for the FeS(001) surface adsorption calculations, whereas a (4x2) supercell was used for the (011), (100), and (111) FeS surfaces as shown in Figure 5.1. To determine the relaxed adsorption complexes, the atoms of the $As(OH)_3$ molecule and the topmost three atomic layers of the surface slabs were allowed to relax without constrains until the residual forces on each atom reach 0.01 eV/Å. The adsorption energy of $As(OH)_3$ was calculated using the expression:

$$E_{ads} = E_{surface+As(OH)_3} - (E_{surface} + E_{As(OH)_3}) \tag{5.1}$$

where $E_{surface+As(OH)_3}$ represents the total energy of the adsorbate-substrate system, $E_{surface}$ represents the energy of a clean surface, and $E_{As(OH)_3}$ represents the energy of the $As(OH)_3$ molecule in the gas phase. A negative adsorption energy indicates exothermicity and favourable adsorption.

Bader charge analysis was carried out for all the adsorbate-substrate systems, using the Henkelman algorithm (Henkelman, 2006) in order to quantify charge transfer between the FeS surfaces and adsorbed $As(OH)_3$ molecule. The climbing image nudged elastic band (CI-NEB) method was used for finding transition states and calculating reaction barriers for the dissociative adsorption of $As(OH)_3$ as implemented in the VASP code (Mills *et al.*, 1995; Ulitsky and Elber, 1990). Transition states were further confirmed through frequency calculations, in which only one imaginary frequency is obtained corresponding to the reaction coordinate. The reaction energy (ΔE) is calculated as the total energy difference between the final state and the initial state and the activation barrier (E_a) is defined as the total energy differences between the initial state and the saddle point.

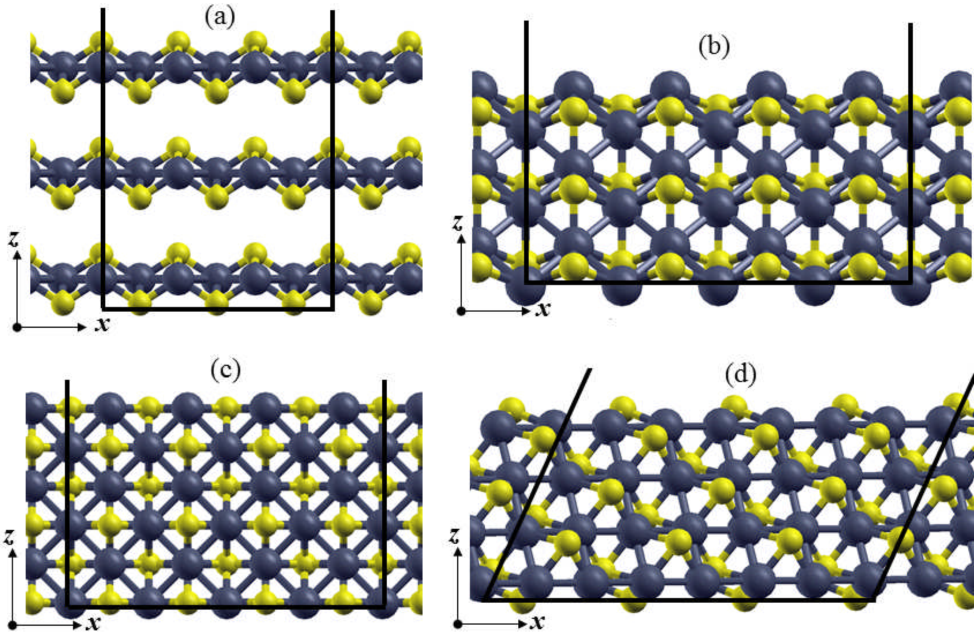

FIGURE 5.1: FeS surface terminations and simulation cells used for As(OH)3 adsorption calculations: (a) (001)−3 x 3; (b) (011)−4 x 2; (c) (100)−4 x 2; and (d) (111)−4x2.

5.3 Results and discussions

5.3.1 As(OH)$_3$ structural conformations

As(OH)$_3$ exhibits two stable conformations with either C_1 or C_3 symmetry. The optimized geometries of the C_1 and C_3 conformations are shown in Figure 5.2 (a & b) and the calculated interatomic bond distances and angles are listed in Table 5.1.

From geometry optimization calculations, the C_1 conformer is found to be only 0.03 eV more stable than the C_3 conformer, in agreement with earlier theoretical results of Ramirez-Solis *et al.* (2006) and Tossel (1997).

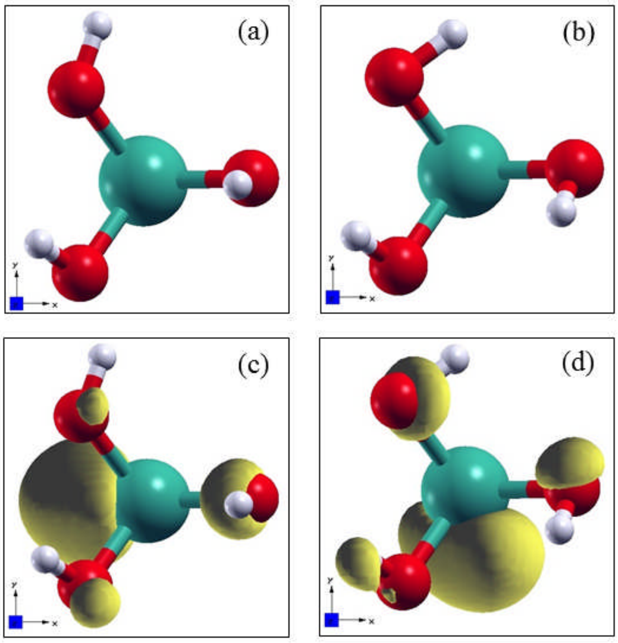

FIGURE 5.2: Optimized structures of C_1 and C_3 symmetry of As(OH)$_3$ shown respectively in (a) and (b). The corresponding highest occupied molecular orbital (HOMO) for the C_1 and C_3 conformations are shown (c) and (d) respectively. (Colour scheme: As = green, O = red and H = white).

The three As−O bond distances of the C_1 and the C_3 conformers were found not to differ significantly, they are calculated to be 1.798, 1.801, and 1.811 Å for the C_1 symmetry and 1.810, 1.811 and 1.813 Å for the C_3 symmetry. The calculated As–O bond distances show good agreement with earlier theoretical results (Ramirez-Solis *et al.* 2006; Tossel 1997; Blanchard *et al.*, 2007) as well with the experimental measured As–O bond distance of 1.77 Å (Ramírez-Solís *et al.*, 2004). The highest occupied molecular orbitals (HOMO) of the C_1 and C_3 conformers as shown in Figure 5.2 (c & d) reveal a dominant contribution from the As lone-pair orbitals which are expected to play important role in the sorption of $As(OH)_3$ onto the FeS mineral surfaces.

	C_1 Symmetry			C_3 Symmetry		
Parameter	This Work	PBE[a]	B3LYP[b]	This work	PBE[a]	B3LYP[b]
d(As–O) /Å	1.798	1.811	1.796	1.810	1.829	1.813
	1.801	1.818	1.800	1.811	1.829	1.813
	1.806	1.841	1.826	1.813	1.829	1.813
d(O–H) /Å	0.975	0.977	0.967	0.975	0.982	0.970
	0.978	0.980	0.969	0.978	0.982	0.970
	0.978	0.983	0.970	0.978	0.982	0.970
α(As-O-H) /°	108.6	105.3	110.2	108.6	104.9	109.9
	110.9	109.8	112.8	110.8	105.0	109.9
	111.2	111.8	112.8	111.0	105.0	109.9

TABLE 5.1: Interatomic bond distance and angles of $As(OH)_3$ calculated using the GGA-PW91 functional. PBE[a] results after Blanchard *et al.*, (2007) whereas the B3LYP[b] are after Ramírez-Solís *et al*, (2006).

5.3.2 Adsorption of $As(OH)_3$ between FeS layers

Prior to the adsorption of $As(OH)_3$ on the various low-index FeS surfaces, we have attempted to adsorb it between the internal layers of the bulk mineral in order to ascertain if segregation with respect to the bulk or surface of the mineral is expected. A (3 x 3 x 3) supercell of the tetragonal unit cell, which is large enough to minimize lateral interactions between the $As(OH)_3$ molecules within the FeS layers was used to simulate the interlayer adsorption. A full unit cell relaxation was carried out in order to allow the FeS lattice the potential to expand or compress freely to accommodate the $As(OH)_3$ molecule. The optimized structure of the mackinawite−$As(OH)_3$ system as shown in Figure 5.3 revealed a large lattice expansion in the interlayer spacing within which the $As(OH)_3$ molecule was adsorbed. The interlayer spacing between the two FeS layer where the $As(OH)_3$ is adsorbed was calculated to be 7.439 Å, whereas that of the nearest neighbouring FeS layer gap is calculated to be 4.957 Å.

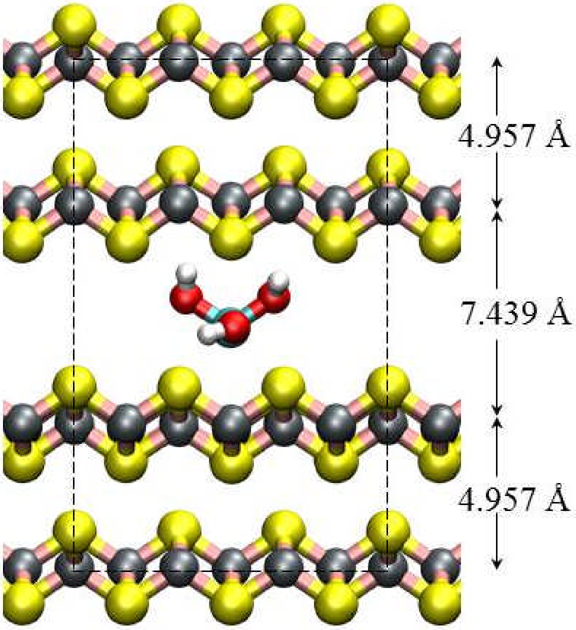

FIGURE 5.3: Optimized structure of $As(OH)_3$ adsorbed between the internal layers of bulk mackinawite.

The binding energy of the $As(OH)_3$ molecule when adsorbed between the internal layers of the bulk mackinawite, was obtained by subtracting from the total energy of the mackinawite−$As(OH)_3$ system, the sum of the energies of the free $As(OH)_3$ molecule in the gas phase C_1 conformation and the pristine mackinawite supercell. A positive binding energy of +2.09 eV was obtained, indicative of an endothermic process, and therefore suggests that it is thermodynamically unfavourable to adsorb $As(OH)_3$ between the internal layers of the bulk mineral. The unfavourable $As(OH)_3$ adsorption within the internal layers of the bulk mackinawite is reflected in the significant expansion observed in the interlayer spacing. The interatomic As−S and

As−Fe interatomic distance are calculated at 2.905 Å and 3.517 Å respectively. The internal As–O and O–H bond distances of the adsorbed $As(OH)_3$ molecule within the internal layers of the bulk mineral are reported in Table 5.2.

Parameter	Bulk interlayer adsorption	(001) surface As−down	(001) surface As−up
E_{ads} /eV	+2.09	–0.74	–0.61
∑q /e⁻	0.00	0.01	0.00
d(As–O) /Å	1.839	1.836	1.828
	1.828	1.810	1.814
	1.816	1.810	1.817
d(O–H) /Å	0.979	0.978	0.983
	0.981	0.978	0.979
	0.971	0.978	0.979
d(As–Fe) /Å	3.517	4.065	5.100
d(As–S) /Å	2.905	3.275	4.281

TABLE 5.2: Adsorption energies (E_{ads}) and relevant bond distances of $As(OH)_3$ adsorbed between the internal layer of bulk mackinawite and on FeS(001) surface. ∑q denotes the net charge gained by the $As(OH)_3$ molecule upon adsorption.

5.3.3 Adsorption of $As(OH)_3$ on FeS(001) surface

The adsorption of $As(OH)_3$ on the (001) surface was carried using a (3 x 3) supercell constructed with three FeS layers slab thickness, similar to the bulk interlayer adsorption calculation set up. No symmetry constraints were included in the structural optimization of the surface–$As(OH)_3$ system, in particular, the $As(OH)_3$ was free to move away laterally and vertically from the initial binding site or re-orient itself to find the minimum energy adsorption structure. The relaxed adsorption complexes of $As(OH)_3$ on the (001) surface are shown in Figure 5.4 (a & b), with the

As atom either point toward (denoted as As–down) or away (denoted As–up) from the surface atoms. Contrast to the bulk internal layer adsorption, the adsorption energies of both the As–down and As–up complexes are negative, calculated at –0.74 eV and –0.61 eV respectively. The negative adsorption energies indicate an exothermic process and therefore suggests that it is energetically more favourable for As(OH)$_3$ to be adsorbed at the mineral's surface rather than between the internal layers of the bulk mineral.

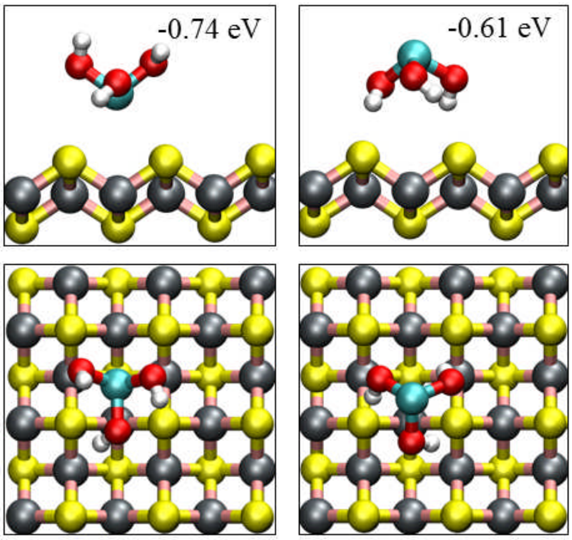

(a) As–down (b) As–up

FIGURE 5.4: Side (top) and top (bottom) views of the optimized adsorption complexes of As(OH)$_3$ on FeS(001) surface.

In the As–down surface complex (Figure 5.4a), the As atom interacts weakly with four sulfur atoms at equivalent As–S interatomic distance of 3.275 Å (Table 5.2) which is larger than the As–S interatomic distance calculated within the bulk interlayer adsorption (2.906 Å), both indicative of outer sphere complexation with respect to the As atom. The calculated As–S interatomic distance at the (001) surface shows good agreement with those obtained from spectroscopic data (As–S = 3.1 Å) for arsenite interaction on mackinawite surface in aqueous solution (Farquhar *et al.*, 2002). When adsorbed with the As atom pointing upwards (*i.e.*, As–up complex, Figure 5.4b), the three OH groups are oriented toward the surface sulfur atoms such the H–S bond distances are calculated at 2.343 Å, 2.751 Å and 2.732 Å, suggesting weak hydrogen bonded interactions between the H and surface S atoms. The internal As–O and O–H bond distances of the adsorbed $As(OH)_3$ are reported in Table 5.2.

Insight into election density rearrangement within the $As(OH)_3$/(001)-surface system can be gained from the electron density difference plot, obtained by subtracting from the electron density of the total adsorbate system, the sum of the electron densities of the molecule and the clean surface, calculated using the same geometry as the adsorbate system. The isosurfaces of the electron density differences due to adsorption of $As(OH)_3$ on the (001) surface are displayed in Figure 5.5.

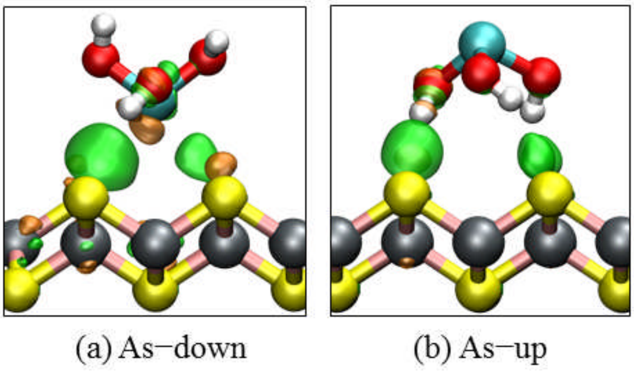
(a) As−down (b) As−up

FIGURE 5.5: Electron density difference plot relative to adsorbed $As(OH)_3$ on FeS(001) surface, showing electron density rearrangement in the regions between the $As(OH)_3$ and the surface atoms upon adsorption. Green and orange contours respectively denote electron density increase and decrease by 0.02 electrons/Å^3.

A small electron density depletion is noted to occur from the As surface S atoms in the As-down configuration, but accumulate within the interaction regions. There is however, no overlap between the charge density of the molecule and the surface species, consistent with physisorption and an outer sphere complexation with respect

As atom. We also see electron density accumulation between the hydrogen atoms of the As-up configuration and the surface S atoms, indicative of the hydrogen-bonded interaction between the two. Consistent with the physisorption, we observe only small charge transfers from the surface species to the adsorbed $As(OH)_3$, *i.e.*, 0.01 e^- in the As-down configuration and none in the As-up configuration.

Having shown that it is energetically more favourable for the $As(OH)_3$ to be adsorbed at the (001) surface of mackinawite rather than between the internal layers of the bulk, we went further to determine the structures of the energetically most stable adsorption complexes of $As(OH)_3$ on the (011), (100) and (111) FeS surfaces as well. The results are discussed in the following sections.

5.3.4 Adsorption of $As(OH)_3$ on FeS(011) surface

From geometry optimization calculations, we have identified four stable adsorption complexes of $As(OH)_3$ on the (011) surface, and these are shown in Figure 5.6. The lowest energy structure is calculated to be the bidentate Fe−AsO−Fe structure (Figure 5.6a), releasing an adsorption energy of 1.61 eV, with the As–Fe and O–Fe bond distances calculated at 2.246 Å and 2.062 Å respectively. The strong interaction of the $As(OH)_3$ in the Fe−AsO−Fe configuration causes elongation of the As−O bond lengths particularly the surface-bound As–O bond which is calculated at 1.916 Å, compared with the free unperturbed C_1 average As–O bond length of 1.802 Å. The other two non-interacting As−O bond lengths are calculated at 1.812 Å and 1.816 Å (Table 5.3). The stretched surface-bound As–OH bond of the bidentate Fe−AsO−Fe complex suggests that this bond might break away from the adsorbed $As(OH)_3$ molecule to produce $As(OH)_2$ and OH fragments, but an attempt to cleave the stretched As−OH bond was found to be thermodynamically less favoured by 0.23 eV relative to the molecularly adsorbed state. CI-NEB calculations reveal that the molecularly adsorbed $As(OH)_3$ has to overcome an activation barrier of 1.84 eV to produce the dissociated $As(OH)_2$ and OH fragments, and therefore suggests that the $As(OH)_3$ will preferentially remain molecular adsorbed on the (011) surface. Figure 5.7 shows the reaction profile for dissociation reaction of $As(OH)_3$ on the (011) surface.

The second most stable bidentate adsorption complex was calculated to be the complex in which the $As(OH)_3$ molecule interacts with (011) surface *via* two Fe–O bonds (denoted by Fe−OO−Fe) as shown in Figure 5.6(b). The Fe−OO−Fe complex released an adsorption energy of 1.29 eV, *i.e.*, 0.31 eV less favourable than the most stable bidentate Fe−AsO−Fe complex. The two Fe−O bond distances are calculated at 2.131 Å and 2.133 Å and the three As−O internal bond distances of the adsorbed $As(OH)_3$ molecule are calculated at 1.836, 1.855, and 1.834 Å respectively, all of which indicate an elongation relative to the gas phase free molecule's average As−O bond length of 1.802 Å.

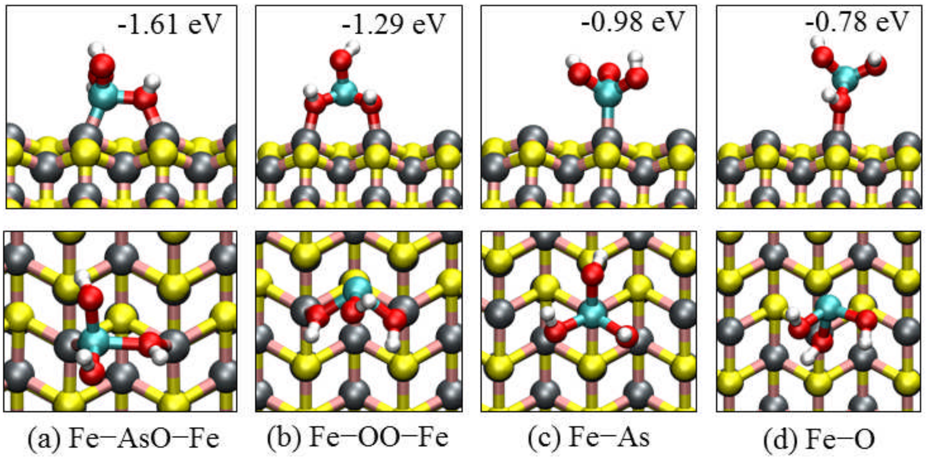

FIGURE 5.6: Side (top) and top (bottom) views of the optimized adsorption complexes of $As(OH)_3$ on FeS(011) surface.

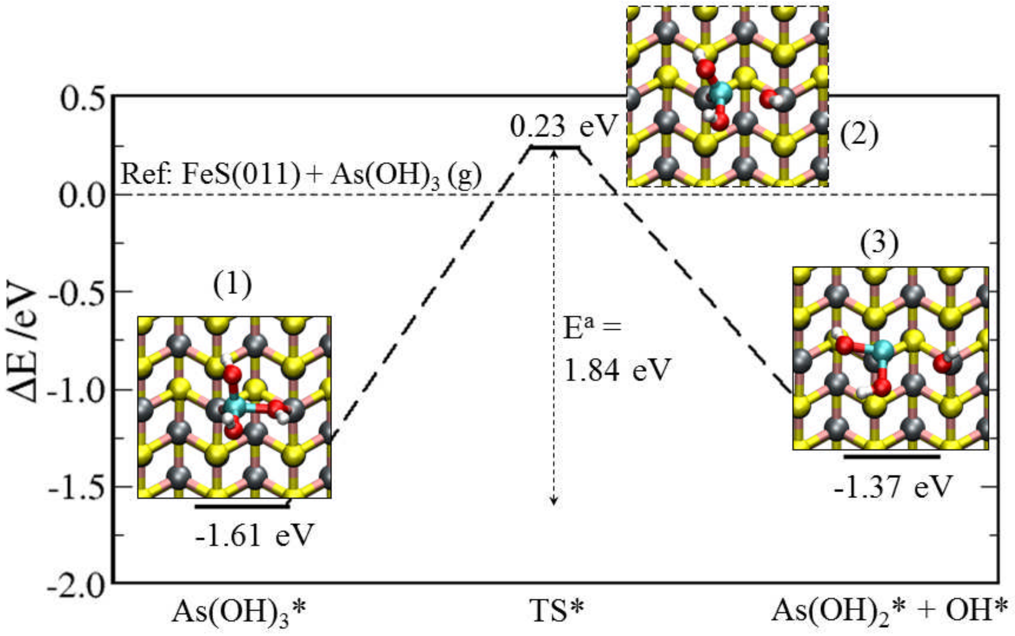

FIGURE 5.7: Reaction profile for the dissociation of $As(OH)_3$ surface-bound As–OH bond on FeS(011) surface. The insets show schematic representation of the steady states, numbered in accordance with the relevant stage in the overall reaction. The asterisks (*) denote the adsorbed species.

Parameter	Fe−AsO−Fe	Fe−OO−Fe	Fe−As	Fe−O
E_{ads} /eV	–1.61	–1.29	–0.98	–0.78
$\sum q$ /e^-	0.10	0.07	0.03	0.02
d(As–O) /Å	1.916	1.855	1.828	1.852
	1.812	1.834	1.812	1.827
	1.816	1.836	1.805	1.796
d(O–H) /Å	0.978	0.979	0.977	0.979
	0.978	0.979	0.976	0.975
	0.977	0.976	0.978	0.978
d(O–Fe) /Å	2.062	2.131	−	2.112
d(As–Fe) /Å	2.246	3.269	2.308	3.456
d(As–S) /Å	3.140	3.397	3.625	4.233

TABLE 5.3: Adsorption energies (E_{ads}) and relevant bond distances of $As(OH)_3$ adsorbed on FeS (011) surface. $\sum q$ denotes the net charge gained by the $As(OH)_3$ molecule upon adsorption.

We have also identified stable monodentate adsorption complexes of $As(OH)_3$ on the (011) surface, wherein the $As(OH)_3$ interacts with either a single Fe–As (Figure 5.6c) or single Fe–O (Figure 5.6d) bond. The monodentate Fe–As and Fe–O configurations are calculated to be less favourable by up to 0.63 eV and 0.82 eV respectively, relative to the lowest energy bidentate Fe−AsO−Fe adsorption complex. The single Fe–As and Fe–O bond distances in the monodentate adsorption complexes are calculated at 2.308 Å and 2.112 Å. Bader population analyses reveal that the adsorption process is characterised by only a small charge transfer from the surface species to the $As(OH)_3$ molecule (see Table 5.3), and therefore suggests that the nature of bonding between the $As(OH)_3$ and the FeS(011) surface is mainly physisorption. All relevant interatomic distances of the four adsorption complexes on the (011) surface are list in Table 5.3. The interatomic distances between the As atom and surface Fe and S species in the most stable bidentate Fe−AsO−Fe complex are calculated at As−S = 3.140 Å and As−Fe = 2.246 Å whereas in the bidentate Fe−OO−Fe complex, they are calculated at As−S = 3.397 Å and As−Fe = 3.268 Å. Similar interatomic bond distances have been calculated for the bidentate Fe−OO−Fe complex at pyrite (001) surface using DFT slab calculations (Blanchard *et al.*, 2007).

The isosurface plot of the electron density rearrangements within the $As(OH)_3$-FeS(011) systems are shown in Figure 5.8. An inspection of the isosurfaces reveal electron density depletion occurs from the molecules As and O atoms as well from the interacting surface Fe atoms (orange isosurfaces) but accumulate in the bonding regions between $As(OH)_3$ and the surface-bound atoms (green contours), which is consistent with the formation of a chemical bonds. The net charge transfer from the FeS(011) surface species to the adsorbed $As(OH)_3$ molecule as estimated from the Bader partition scheme is found to be very small. The $As(OH)_3$ molecule gained a charge of 0.18 e^-, 0.05 e^-, 0.02 e^- and 0.01 e^- when adsorbed in the Fe−AsO−Fe, Fe−OO−Fe, Fe−As and Fe−O adsorption complexes respectively.

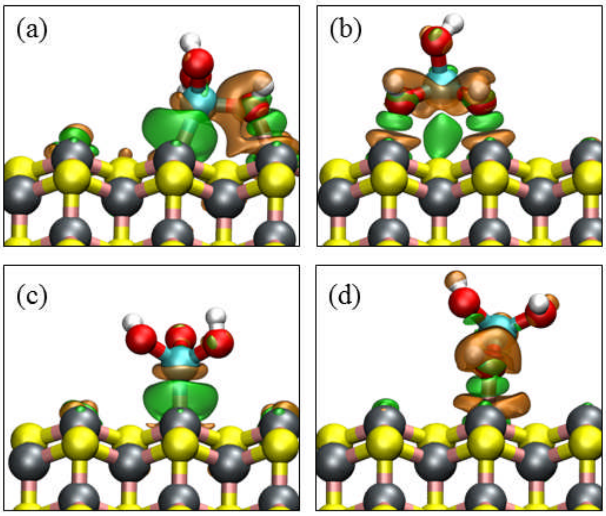

FIGURE 5.8: Electron density difference plot relative to adsorbed $As(OH)_3$ on FeS(011) surface, showing electron density rearrangement in the regions between the $As(OH)_3$ and the surface atoms upon adsorption in the (a) Fe−AsO−Fe, (b) Fe−OO−Fe, (c) Fe−As and (d) Fe−O adsorption complexes. Green and orange contours respectively denote electron density increase and decrease by 0.02 electrons/Å^3.

5.3.5 Adsorption of $As(OH)_3$ on FeS(100) surface

The relaxed adsorption structures of $As(OH)_3$ on the (100) surface are shown in Figure 5.9 (a-d). Compared to the (011) surface, the lowest energy configuration is calculated to be a bidentate complex with two Fe−O bonds, Fe−OO−Fe (Figure 5.9a), which releases an adsorption energy of 1.82 eV, *i.e.*, 0.22 eV more favourable than the lowest energy bidentate Fe−AsO−Fe complex on the (011) surface. The two Fe−O bond distances in the Fe−OO−Fe adsorption complex on the (100) surface are calculated at 2.102 Å and 2.120 Å (average value reported in Table 5.4) whereas the interatomic As−S and As−Fe bond distances are calculated at 3.433 Å and 3.213 Å respectively, in agreement with experimental data (Farquhar *et al.*, 2002). The three internal As–O bond distances of the adsorbed $As(OH)_3$ in the Fe−OO−Fe complex are calculated at 1.860 Å, 1.834 Å, and 1.813 Å, all of which represent an elongation relative to the free molecule's average As−O bond length of 1.802 Å.

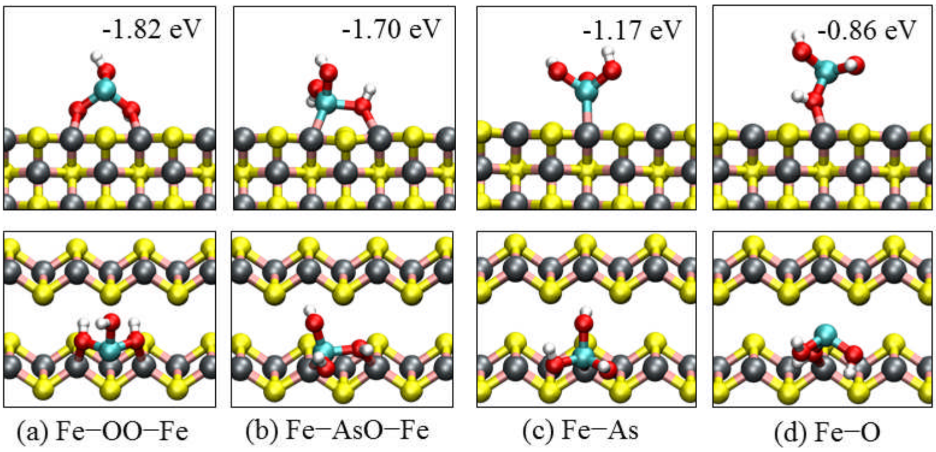

(a) Fe−OO−Fe (b) Fe−AsO−Fe (c) Fe−As (d) Fe−O

FIGURE 5.9: Side (top) and top (bottom) views of the optimized adsorption complexes of $As(OH)_3$ on FeS(100) surface.

Parameter	Fe−OO−Fe	Fe−AsO−Fe	Fe−As	Fe−O
E_{ads} /eV	–1.82	–1.70	–1.17	–0.86
$\sum q$ /e^-	0.11	0.06	0.04	0.02
d(As–O) /Å	1.860	1.922	1.811	1.856
	1.834	1.806	1.811	1.825
	1.813	1.802	1.794	1.800
d(O–H) /Å	0.990	0.979	0.978	0.983
	0.993	0.979	0.978	0.978
	0.976	0.985	0.983	0.975
d(O–Fe) /Å	2.111	2.097	–	2.105
d(As–Fe) /Å	3.322	2.259	2.296	3.782
d(As–S) /Å	3.432	3.110	3.354	4.342

TABLE 5.4: Adsorption energies (E_{ads}) and relevant bond distances of $As(OH)_3$ adsorbed on the FeS (100) surface. $\sum q$ denotes the net charge gained by the $As(OH)_3$ molecule upon adsorption.

The second most stable $As(OH)_3$ adsorption complex on the (100) surface was calculated to be a bidentate Fe−AsO−Fe complex (Figure 5.9b), releasing an adsorption energy of 1.70 eV, *i.e.*, 0.12 eV less favoured than the lowest energy Fe−OO−Fe adsorption complex. The interacting As−Fe and O−Fe bond distances in the Fe−AsO−Fe complex are calculated at 2.259 Å and 2.097 Å respectively, whereas the interatomic distance between the As and S (As−S) is calculated at 3.110 Å. The internal As−O bond lengths of the bidentate Fe−AsO−Fe complex reported in Table 5.4 show that upon adsorption these bond lengths are elongated, in particular the surface-bound As–O bond (1.992 Å) relative to the gas phase molecule's As−O bond lengths. Dissociation of the surface-bound As−OH bond produced $As(OH)_2$ and OH fragments adsorbed at top Fe sites *via* the As and O atom respectively. The dissociated state was found to thermodynamically less favoured by 0.22 eV relative to the molecular adsorbed Fe−AsO−Fe complex, and an energy barrier of 1.76 eV has to be overcome (Figure 5.10), indicative of preference for molecular adsorption over dissociative adsorption on the FeS(100) surface.

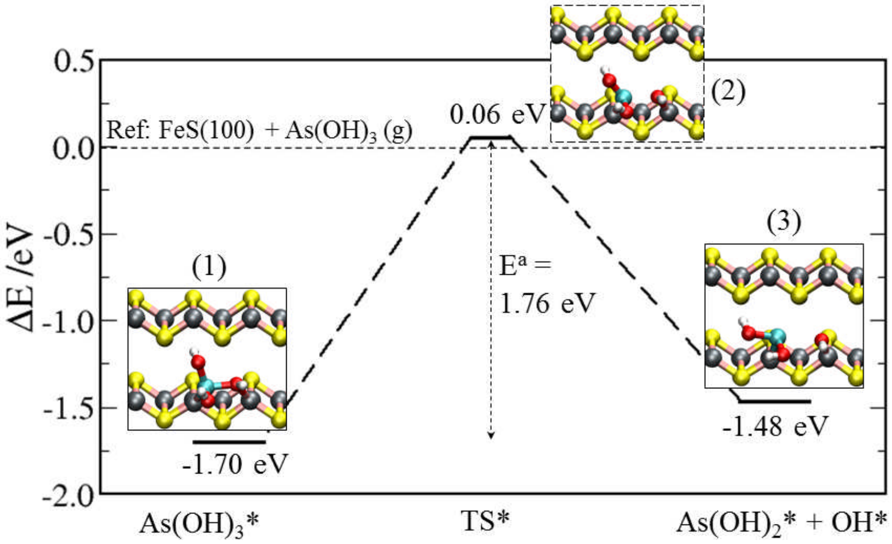

FIGURE 5.10: Reaction profile for the dissociation of $As(OH)_3$ surface-bound As–OH bond on FeS(100) surface. The insets show schematic representation of the steady states, numbered in accordance with the relevant stage in the overall reaction. The asterisks (*) denote the adsorbed species.

The monodentate adsorption complexes wherein the $As(OH)_3$ molecule interacts with the surface *via* either a single Fe–As (Figure 5.9c) or single Fe–O (Figure 5.9d) bond are calculated to be less favourable than the bidentate complexes on the (100) surface. The binding energy of the stable monodentate Fe–As and Fe–O complexes are calculated at 1.17 eV and 0.86 eV respectively, and the corresponding optimized As−Fe and O−Fe bond distances are calculated at 2.296 Å and 2.105Å respectively. We have also attempted calculating a monodentate S–As adsorption complex but found it to be unstable as the molecules always moves away from the sulfur site to the reactive iron sites. Bader population analyses for the four adsorption complexes at the (100) surface reveal only small charge transfer (Table 5.4) from the interacting surface species to the adsorbed $As(OH)_3$ molecules. The nature of the electron density accumulation within the Fe–O bond regions is consistent with chemisorption (Figure 5.11).

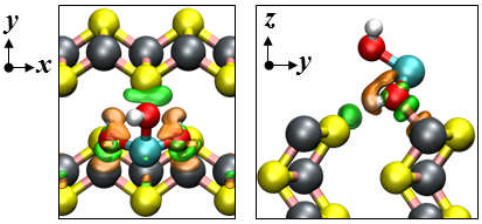

(a) Fe−OO−Fe

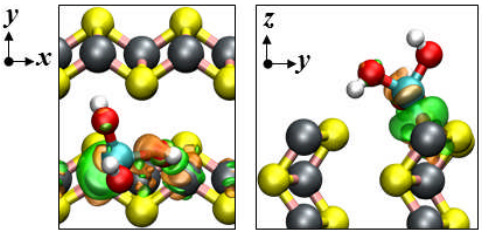

(b) Fe−AsO−Fe

FIGURE 5.11: Electron density difference plot relative to $As(OH)_3$ adsorbed in the (a) Fe−OO−Fe, and (b) Fe−OO−Fe configurations on the (100) surface, showing charge electron rearrangement in the regions between the $As(OH)_3$ and the surface atoms upon adsorption. Green and orange contours respectively denote electron density increase and decrease by 0.02 electrons/Å^3.

The isosurfaces also reveal electron density accumulation between the hydrogen atoms and the surface sulfur atoms in the Fe−OO−Fe complex (Figure 11a), suggestive of hydrogen bonded interactions between these species. This observation is in agreement with the short S–H distance calculated at 2.372 Å in this adsorption complex.

5.3.6 Adsorption of $As(OH)_3$ on FeS(111) surface

The strongest surface–$As(OH)_3$ interaction is calculated on the (111) surface. The lowest energy adsorption complex is calculated to be a bidentate Fe−OO−Fe (Figure 5.12a), wherein the $As(OH)_3$ molecule interacts with the surface *via* two O–Fe bonds releasing an adsorption of 1.91 eV, *i.e.*, 0.31 eV and only 0.09 eV more favourable than the lowest energy adsorption complexes calculated on the (011) and (100) surfaces respectively. The two O–Fe bond distances are calculated at 2.100 Å and 2.103 Å and the closest the As–S and As–Fe interatomic distances are calculated at 3.752 Å and 3.031 Å respectively. The long interatomic distances obviously suggest ab outer-sphere complexation with respect to the As atom in agreement with earlier experimental observations (Farquhar *et al.*, 2002). The internal As−OH bond lengths of the adsorbed $As(OH)_3$ molecule are calculated at 1.839 Å, 1.833 Å and 1.813 Å (Table 5.5).

The other bidentate complex adsorption complex wherein the $As(OH)_3$ interacts *via* one As–Fe and one O–Fe bond, Fe−AsO−Fe (Figure 12b), released an adsorption energy of 1.73 eV, *i.e.*, 0.18 eV less than the lowest energy Fe−OO−Fe adsorption complex. The As–Fe and O–Fe bond distances are calculated at 2.215 Å and 2.075 Å respectively and the interatomic As–S distance is calculated at 3.217 Å. In this configuration the surface-bound As−O bond (1.912 Å) is significantly elongated compared to the unbound ones (1.803 Å and 1.798 Å), (Table 5.5). Contrast to the endothermic dissociative adsorption calculated on the (011) and (100) surfaces, the cleavage of surface-bound As–OH bond to produce $As(OH)_2$ and OH on the (111) surface is found to be exothermic by 1.25 eV. The favourable thermochemical energy suggests that the surface-bound As−OH bond could readily break away from the adsorbed $As(OH)_3$ on the (111) surface, but will have to overcome a higher energy barrier of 2.22 eV, as shown Figure 5.13. The higher activation barrier for the dissociation of the As−OH bond on the (111) compared to the (011) and (100) surfaces can be attributed to the additional energy required to move the dissociated products from the top–Fe site to the most stable bridging–Fe sites.

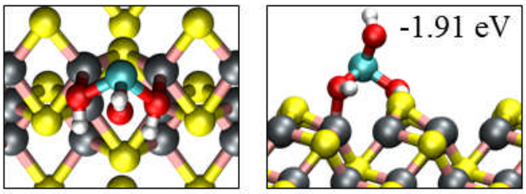

(a) Fe−OO−Fe

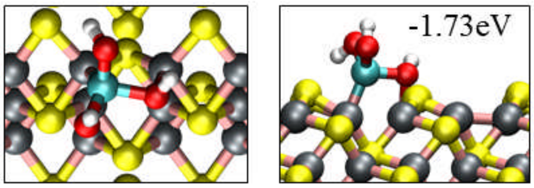

(b) Fe−AsO−Fe

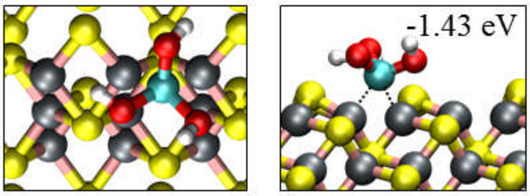

(c) Fe−As−Fe

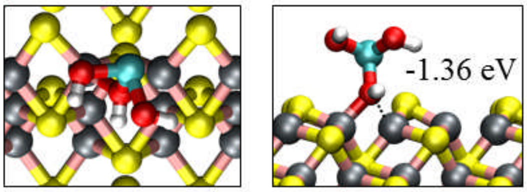

(d) Fe−O−Fe

FIGURE 5.12: Top (left) and side (right) views of the optimized adsorption complexes of $As(OH)_3$ on FeS(111) surface.

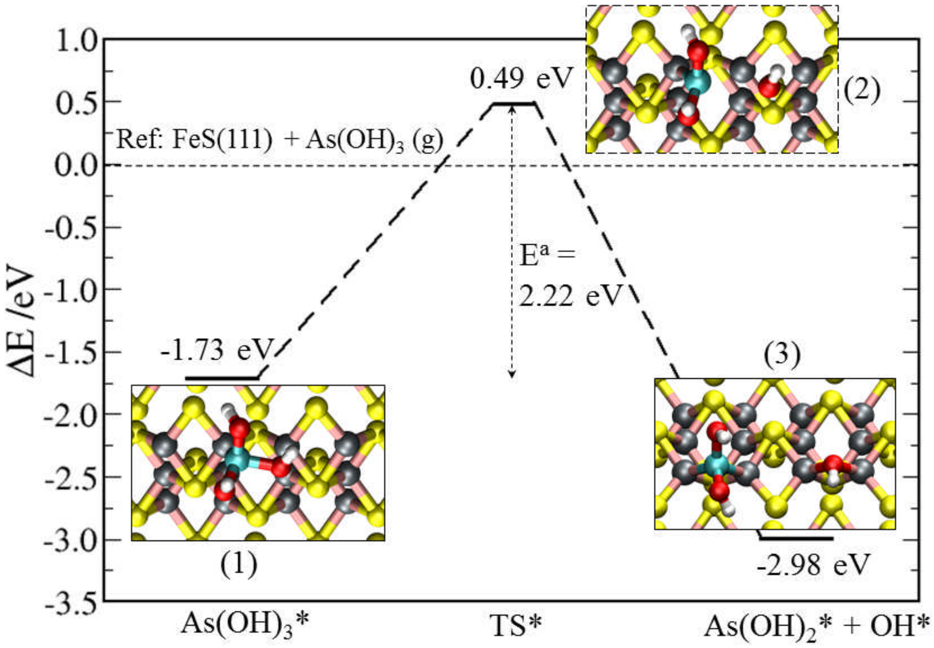

FIGURE 5.13: Reaction profile for the dissociation of $As(OH)_3$ surface-bound As–OH bond on FeS(111) surface. The insets show schematic representation of the steady states, numbered in accordance with the relevant stage in the overall reaction. The asterisks (*) denote the adsorbed species.

The monodentate adsorption complexes on the (111) surface shows preference for bridge site adsorption (Figure 5.12(c & d)) compared to the on-top Fe site adsorption calculated on the (011) and (100) surfaces. The bridging Fe−As−Fe adsorption complex (Figure 5.12c), released an adsorption energy of 1.49 eV, whereas the bridging Fe−O−Fe adsorption complex (Figure 5.12d) released an adsorption energy of 1.36 eV. The bridging As–Fe bond distances are calculated at 2.326 and 2.337 Å (the average value is reported in Table 5.5), and the closest As–S bond distance is calculated at 3.375 Å. For the bridging Fe−O−Fe complex, the bridging O–Fe bond distances are calculated at 2.214 Å and 2.110 Å (average value is reported in Table 5.5) and the closest As−S and As−Fe bond distances are calculated at 3.669 Å and 3.472 Å respectively.

Parameter	Fe−OO−Fe	Fe−AsO−Fe	Fe−As−Fe	Fe−O−Fe
E_{ads} /eV	–1.91	–1.73	–1.49	–1.36
$\sum q$ /e^-	0.18	0.08	0.05	0.03
d(As–O) /Å	1.839	1.912	1.812	1.941
	1.833	1.803	1.794	1.805
	1.813	1.798	1.794	1.775
d(O–H) /Å	0.994	0.982	0.979	0.989
	0.987	0.979	0.979	0.975
	0.975	0.979	0.980	0.970
d(O–Fe) /Å	2.102	2.075	–	2.162
d(As–Fe) /Å	3.031	2.215	2.332	3.472
d(As–S) /Å	3.752	3.324	3.375	3.669

TABLE 5.5: Adsorption energies (E_{ads}) and relevant bond distances of $As(OH)_3$ adsorbed on FeS (111) surface. $\sum q$ denotes the net charge gained by the $As(OH)_3$ molecule upon adsorption.

The isosurfaces of the electron density difference of the two lowest energy bidentate adsorption complexes as shown in Figure 5.14 give further insights into the bonding mechanism of $As(OH)_3$ on the FeS(111) surface. An inspection of the isosurfaces reveal charge depletion occurs from the molecules As and O atoms as well from the interacting surface Fe atoms (orange isosurfaces) but accumulate in the bonding regions between $As(OH)_3$ and the surface-bound atoms (green contours), which is consistent with the formation of chemical bonds. For the Fe−OO−Fe complex, we also see electron density accumulation between the hydrogen and sulfur atoms across the FeS layer, indicative of the hydrogen-bonded interaction between the two (the *z–x* plane view, Figure 5.14a). The hydrogen bonded interactions contribute to the stability of the $As(OH)_3$ molecule in Fe−OO−Fe complex, thus the stronger binding calculated for this adsorption complex. Compared to the Fe−OO−Fe complex, we observe no hydrogen bonding across the FeS layers in the Fe−AsO−Fe complex

(Figure 5.14b). The charge transferred from the interacting surfaces species to the $As(OH)_3$ molecule upon adsorption is found to be very small, 0.18 e^- in the Fe−OO−Fe complex and 0.08 e^- in the Fe−AsO−Fe complex (Table 5), which therefore suggest that the nature of the bonds is mainly physisorption.

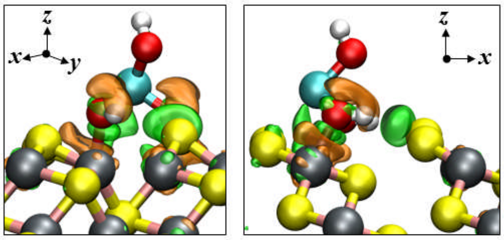

(a) Fe−OO−Fe

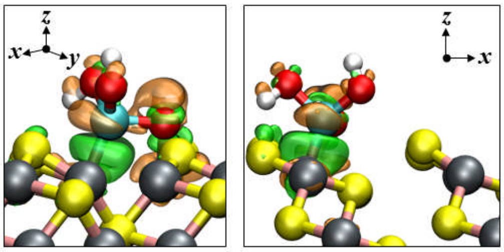

(b) Fe−AsO−Fe

FIGURE 5.14: Electron density difference plot relative to $As(OH)_3$ adsorbed in the (a) Fe−OO−Fe, and (b) Fe−OO−Fe configurations on FeS(111) surface, showing electron density rearrangement in the regions between the $As(OH)_3$ and the surface atoms upon adsorption. Green and orange contours respectively denote electron density increase and decrease by 0.02 electrons/Å^3.

The electronic density of states of the bidentate Fe−OO−Fe and Fe−AsO−Fe adsorption complexes projected on the As and O *p*-states and on the interacting surface Fe *d*-states reveal no significant mixing of the adsorbate and substrate states around the Fermi level (Figure 5.15). The interaction of the $As(OH)_3$ with the FeS surface occurs *via* mixing of the adsorbates *p*-orbitals and the surface Fe *d*-orbitals within the energy range of –3.5 eV to –6.5 eV dominated by the O *p*-orbitals and within the range of 1.0 eV to 4.0 eV dominated by the As *p*-orbitals.

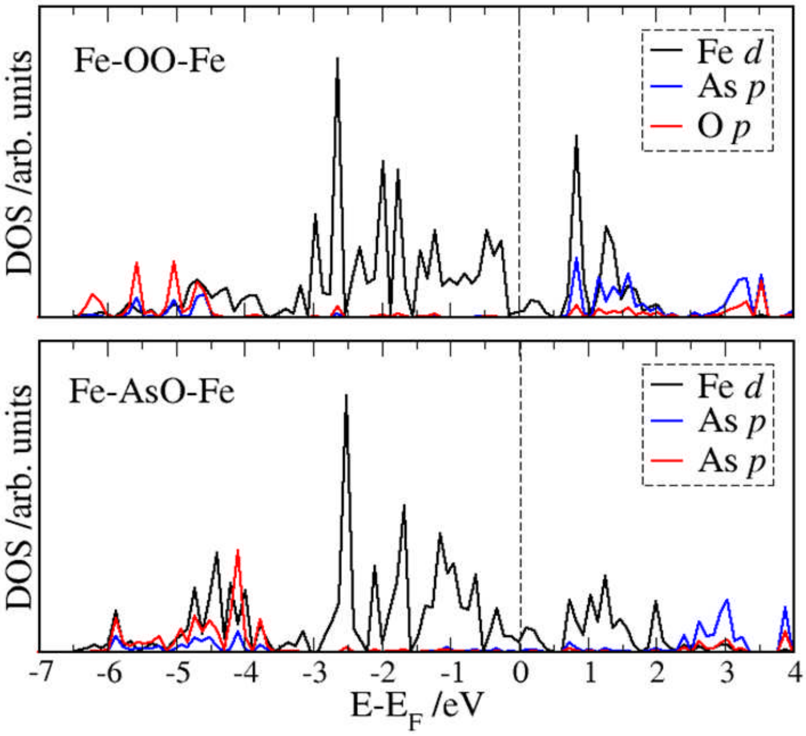

FIGURE 5.15: Electronic density of states for Fe−OO−Fe and Fe−AsO−Fe adsorption complexes on FeS(111) surface projected on the interacting surface Fe *d*-states and on the O and As *p*-states of $As(OH)_3$.

5.3.7 Vibrational properties

In order to propose an assignment for the As–O and O–H stretching vibrational modes of the adsorbed $As(OH)_3$, which can serve as a guide for future experimental identification of the different adsorption complexes of $As(OH)_3$ on mackinawite surfaces, we have computed the wavenumbers of the normal modes of all the different stable adsorption complexes on the (001), (011), (100), and (111) surfaces of mackinawite. To ensure that our assignments are of high accuracy, we first calculated the As–O and O–H stretching vibrational modes of the gas phase $As(OH)_3$ molecule (Table 5.6) and compared them with available experimental data of $As(OH)_3$ in aqueous solution (Loehr and Plane, 1968). The three As−O stretching vibrational modes for the gas phase $As(OH)_3$ molecule are calculated at 639.1, 632.3, and 674.8 cm^{-1}, which compares with the experimental values of (655.0, 655.0 and 710.0 cm^{-1}), (Loehr and Plane, 1968). The O–H stretching vibrational modes are calculated at 3743.5, 3715.3 and 3674.6 cm^{-1} which are similar to the O–H stretching modes of water (Shimanouchi, 1977).

Surface	Ads. complex	ν(As–O) /cm^{-1}			ν(O–H) /cm^{-1}		
$As(OH)_3$ (gas)	Experiment[a]	655.0	655.0	710.0	–	–	–
	Calculation	639.1	632.3	674.8	3743.5	3715.3	3674.6
(001)	As−down	621.8	608.3	625.2	3718.7	3708.4	3658.3
	As−up	629.8	612.3	629.2	3720.7	3710.4	3661.3
(011)	Fe−AsO−Fe	608.4	455.4	618.7	3684.6	3680.3	3677.9
	Fe−OO−Fe	584.6	555.6	611.3	3714.2	3667.8	3637.9
	Fe−As	621.8	600.3	629.2	3710.9	3705.4	3671.3
	Fe−O	618.9	572.9	662.6	3724.3	3697.9	3645.6
(100)	Fe−OO−Fe	592.9	626.0	665.6	3775.7	3520.0	3443.9
	Fe−AsO−Fe	549.8	586.9	645.1	3728.3	3711.6	3634.7
	Fe−As	589.3	610.3	631.3	3704.2	3698.5	3582.3
	Fe−O	554.3	620.0	658.7	3721.9	3700.7	3690.4
(111)	Fe−OO−Fe	591.8	557.7	616.4	3698.3	3670.5	3632.6
	Fe−AsO−Fe	607.7	459.6	617.3	3681.1	3678.5	3674.5
	Fe−As−Fe	620.9	582.9	630.6	3711.4	3703.5	3681.7
	Fe−O−Fe	609.6	458.4	619.7	3687.5	3679.4	3678.7

TABLE 5.6: As–O and O–H stretching vibrational frequencies of gas phase $As(OH)_3$ compared with adsorbed $As(OH)_3$ on the (001), (011), (100) and (111) surfaces of mackinawite. [a]Experimental data after Loehr & Plane, 1968.

The As–O and O–H stretching vibrational modes of the different adsorption complexes of $As(OH)_3$ on mackinawite surface are summarized in Table 5.6.

Compared to the gas phase As−O stretching modes, we noticed a reduction in the As−O stretching vibrational modes of the adsorbed $As(OH)_3$ species, in particular for the surface-bound As−O bonds, indicative of weakening of these bonds. This is consistent with the elongated As−O bonds calculated for the different $As(OH)_3$ adsorption complexes. For example the As−O stretching vibrational frequencies of the lowest energy adsorption complex on the (111) surface (Fe−OO−Fe) are assigned at 591.8, 557.7 and 616.4 cm^{-1}, all of which signifies reductions relative the free unperturbed gas phase As−O stretching vibrations of (639.1, 632.3, and 674.8 cm^{-1}). The O−H stretching vibrational modes of the adsorbed $As(OH)_3$ molecules show only small reduction relative the free molecules O−H stretching modes, suggestive of weak hydrogen interaction with the surface species.

5.4 Summary and conclusions

The adsorption complexes of $As(OH)_3$ on the low-index surfaces of mackinawite and between the internal layers of the bulk mineral under vacuum conditions were modelled using DFT calculations with a correction for long-range dispersion interactions (DFT-D2) within the Grimme's formalism. Segregation of $As(OH)_3$ with respect to the mackinawite surfaces is expected as our calculated adsorption energies show that it is energetically more favourable to adsorb $As(OH)_3$ at the mineral's surfaces (exothermic adsorption) rather than between the internal layers of the bulk mineral (endothermic adsorption). The strongest $As(OH)_3$–surface interactions was obtained on the FeS(111), whereas the weakest was obtained at the energetically most stable (001) surface. Molecular adsorption is found to energetically favoured over dissociative adsorption on the (011) and (100) surfaces, whereas the (111) favours dissociative adsorption. For the molecularly adsorbed complexes, the bidentate adsorption complexes (Fe−OO−Fe and Fe−AsO−Fe) are found to be generally energetically more favourable than the monodentate complexes (Fe−O and Fe−As). Within the most stable bidentate complexes, the calculated long As–Fe (3.031−3.314 Å) and As–S (3.397−3.752 Å) suggest an outer sphere complexation with respect to the As atoms, in agreement with the experimental observation of Farquhar *et al.*, 2002. Comparing the results obtained on the mackinawite surfaces to those obtained at pyrite (100) surface (Blanchard *et al.*, 2007), we found that $As(OH)_3$ interacts relatively more strongly with mackinawite surfaces than the pyrite surface. This result is in good agreement with the experimental works of Farquhar *et al.*, (2002), who demonstrated that mackinawite has higher As(III) removing efficiency from solution than pyrite.

Bibliography

- Amine N.; Kaneco S.; Kitagawa T.; Begum A.; Katsumata H.; Suzuki T.; and Ohta K.; *Industrial & Engineering Chemistry Research*, **45**, 8105 (2006)
- Ballantine J. M.; and Moore J. N.; *Geochim. Cosmochim. Acta* **52**, 475 (1988)
- Baroni S.; Giannozzi P.; and Testa A.; *Phys. Rev. Lett.*, **58**, 1861 (1987)
- Berner R. A.; *Science*, **137**, 669, (1962)
- Blanchard M.; Wright K.; Gale J. D.; and Catlow, C. R. A. *J. Phys. Chem. C,* **111**, 11390 (2007).
- Blanchard M.; Morin M.; Lazzeri M.; Balan E.; Dabo I.; *Geochimica et Cosmochimica Acta*, 86 182 (2012)
- Blöchl P. E.; *Phys. Rev. B*, **50**, 17953 (1994)
- Bostick B. C.; and Fendorf S.; *Geochim. Cosmochim.* Acta, **67**, 909 (2003)

- Catalano J. G.; Zhang Z.; Park C.; Fenter P.; Bedzyk M. J.; *Geochimica et Cosmochimica Acta,* **71**, 1883 (2007)
- Catalano J. G.; Park C.; Fenter P, Zhang Z.; *Geochimica et Cosmochimica Acta,* **72**, 1986 (2008)
- Devey A. J.; Grau-Crespo R.; de Leeuw N. H.; *J. Phys, Chem C,* **112**, 10960 (2008)
- Ding M.; de Jong B.H.W.S.; Roosendaal S.J.; Vredenberg A.; *Geochim. Cosmochim. Acta* **64**, 1209 (2000)
- Farquhar M. L.; Charnock J. M.; Livens F. R; and Vaughan D. J.; *Environ. Sci. Technol.,* **36**, 1757 (2002)
- Fendorf S.; Eick M.J.; Grossl P.; and Sparks D. L.; *Envir. Sci. Technol.* **31**, 315 (1997)
- Ferguson J. F.; and Gavis J.; *Water research,* **6**, 1259 (1972)
- Gallegos T. J.; Hyun S. P.; and Hayes K. F.; *Environ. Sci. Technol.,* **41**, 7781 (2007)
- Gallegos-Garcia M., Ramírez-Muñiz K. and Song S.; *Mineral Processing & Extractive Metall. Rev.,* **33**, 301 (2012)
- Grimme S.; *J Comput Chem,* **27**, 1787 (2006)
- Gulens J.; Champs D. R.; Jackson R. E.; *In: E.A. Jenne (Ed.), Chemical Modelling of Aqueous systems. A.C.S.,* **81** (1979)
- Henkelman G.; Arnaldsson A.; Jonsson H.; *Comput. Mater. Sci.* **36**, 354 (2006)
- Hiemstra T.; Van Riemsdijk W.H.; *J. Colloid Interf. Sci.* **210**, 182 (1999)
- Hughes M. F.; *Toxicology Letters,* **133**, 1 (2002)
- Kresse G.; and Furthmüller J.; *J. Comput. Mat. Sci.* **6**, 15 (1996)
- Kresse G.; and Hafner J.; *Phys. Rev. B.,* **47**, 558 (1993)
- Kresse G.; and Joubert D.; *Phys. Rev. B.* **59**, 1758 (1999)
- Livens F. R.; Jones M. J.; Hynes A. J.; Charnock J. M.; Mosselmans J. F.; Hennig C.; Steele H.; Collison D.; Vaughan D. J.; Pattrick R. A.; Reed W. A.; and Moyes L. N.; *J. Environ. Radioact.* **74**, 211 (2004)
- Lumsdon D. G.; Fraser A. R.; Russell J. D.; Livesey N. T. J.; *Soil Sci.* **35**, 381 (1984)

- Liu Z.; Shen J.; Carbrey J. M.; Mukhopadhyay R.; Agre P.; and Rosen B. P.; *Proc. Natl. Acad. Sci. U.S.A.*, **99**, 6053 (2002)
- Loehr T. M.; and Plane R. A.; *Inorg. Chem.* **7**, 1708 (1968)
- Manceau A.; *Geochim. Cosmochim. Acta*, **59**, 3647 (1995)
- Mills G.; Jónsson H.; and Schenter G. K.; *Surf. Sci.*, **324**, 305 (1995)
- Monkhorst H. J.; and Pack J. D.; *Phys. Rev. B.* **13**, 5188 (1976)
- Moore J. N.; Ficklin W. H.; and Johns C.; *Environ. Sci. Technol.* **22**, 432 (1988)
- Mullet M.; Boursiquot S.; and Ehrhardt J. J.; *Colloids and Surfaces A: Physicochem. Eng. Aspects* **244**, 77 (2004)
- Nordstrom D. K. *Science*, **296**, 2143 (2002)
- O'Day P. A.; Vlassopoulos D.; Root R.; and Rivera N.; *Proc. Natl. Acad. Sci. U.S.A.*, **101**, 13703 (2004)
- Ohfuji H.; and Rickard D.; *Earth Plan et Sci. Lett.* **241**, 227 (2006)
- Perdew J. P.; Chvary J. A.; Vosko S. H.; Jackson K. A.; Pederson M. R.; Siingh D. J.; and Fiolhais C.; Phys. Rev. B. **46**, 6671 (1992)
- Pierce M. L.; and Moore C. B.; *Water Res.* **16**, 1247 (1982)
- Ramirez-Solis A.; Mukopadhyay R.; Rosen B. P.; Stemmler T. L.; *Inorg. Chem.*, **43**, 2954 (2004)
- Ramirez-Solis A.; Hernandez-Cobos, J.; Vargas C.; *J. Phys. Chem. A*, **110**, 7637 (2006)
- Reich M.; and Becker U.; *Chemical Geology*, **225**, 278 (2006)
- Rickard D.; and Luther G. W.; *Chemical Reviews*, **107**, 514(2007)
- Sadiq M.; *Water, Air, Soil Pollut.* **93**, 117 (1997)
- Sanders O. I.; Rensing C.; Kuroda M.; Mitra B.; and Rosen B. P.; *J. Bacteriol.*, **179**, 3365 (1997)
- Scheinost A. C.; and Charlet L.; *Environ. Sci. Technol.* **42**, 1984 (2008)
- Sherman D. M.; Randall S. R.; *Geochimica et Cosmochimica Acta*, **67**, 22, 4223 (2003)
- Shimanouchi T.; *J. Phys. Chem.* **6**, 3. (1977)

- Smedley P. L.; and Kinniburgh D. G.; *Appl. Geochem.* **17**, 517 (2002)
- Swedlund P.J.; Webster J.G.; *Wat. Res.* **33**, 3413 (1999)
- Tasker P. W.; *J. Phys. C: Solid State Physics*, **12**, 4977 (1979)
- Tossell J. A.; *Geochim. Cosmochim. Acta*, **61**, 1613 (1997)
- U. S. Environmental Protection Agency; Special reports on ingested inorganic arsenic skin cancer: Nutritional essentiality. *Report EPA/625 3-87-13* (1999)
- Ulitsky A.; and Elber R.; *J. Chem. Phys*. **92**, 1510 (1990)
- Watson J. H. P.; Cressey B. A.; Roberts A. P.; Ellwood D. C.; Charnock J. M.; and Soper A. K.; J. Magn. Magn. Mater. 214, 13-30 (2000).
- Watson G. W.; Kelsey E. T.; de Leeuw N. H.; Harris D. J.; and. Parker S. C.; *J. Chem. Soc., Faraday Trans.,* **92**, 433 (1996)
- Waychunas G. A.; Rea B. A.; Fuller C. C.; Davis J. A.; *Geochim. Cosmochim. Acta*, **57**, 2251 (1993)
- Waychunas Davis J. A.; Fuller C. C.; *Geochim. Cosmochim. Acta*, **59**, 3655-3661 (1995)
- Waychunas G.A.; Fuller C.C.; Rea B.A.; Davis J. A.; *Geochim. Cosmochim. Acta*, **60**, 1765 (1996)
- Welch A. H.; Westjohn D. B.; Helsel D. R.; and Wanty R. B.; *Ground Water*, 38, 589 (2000)
- Williams P. M.; Price A. H.; Raab A.; Hossain S. A.; Feldmann J.; and Meharg A. A.; *Environ. Sci. Technol*., **39**, 5531 (2005)
- Wolthers M.; van der Gaast S. J; Rickard D.; *Am. Mineral*, **88**, 2007 (2003)
- Wolthers M.; Charlet L.; van Der Weijden C. H.; van der Linde P. R.; and Rickard D.; *Geochimica et Cosmochimica Acta*, **69**, 3483 (2005)

Chapter 6

Adsorption of methylamine on low-index FeS surfaces

Abstract

Dispersion corrected density functional theory calculations have been used to investigate the interactions of methylamine (CH_3NH_2) with the low-index surfaces of mackinawite (FeS). We show from energy minimization calculations that the CH_3NH_2 molecule interacts weakly (E_{ads} =0.18 eV) with the most stable FeS (001) surface, but adsorbs relatively strongly on the (011), (100) and (111) surfaces realising energies of 1.26 eV, 1.51 eV and 1.88 eV respectively. Analysis of the nature of the bonding reveals that the CH_3NH_2 molecule interacts with the mackinawite surfaces *via* the lone-pair of electrons located on the N atom. We have also proposed a kinetic model for the desorption process of methylamine yielding a simulated temperature programmed desorption with a relative desorption temperature of <140 K at the (011) surface, <170 K at (100) surface, and < 180 K at the (111) FeS surfaces.

6.1 Introduction

Today, nanoparticles have already become indispensable materials for many industrial applications due to their unique size dependent properties such as electrical, magnetic, mechanical, optical and chemical properties, which largely differ from those of their bulk materials (Jun *et al.,* 2005; Kimberly *et al*., 2002; Alivisatos *et al*., 1996; Ozin, 1992; Marignier *et al.*, 1985). Because nanoparticles have different surface structures and surface interactions compared to the sub-micron sized particles, they have an extremely high tendency of adhesion and aggregation (Tao *et al.*, 2008). It is therefore important to develop synthesis techniques to control the dispersion or aggregation phenomena of nanoparticles.

Considerable interests have developed in the synthesis and characterization of transition metal chalcogenide nanocrystals in recent times as they are being explored for potential applications in: solar cells (Lin *et al*., 2009; Puthussery *et al.,* 2011; Bi *et al*., 2011; Wu *et al*., 2011), solid state batteries (Yamaguchi *et al.*, 2010; Paolella *et al.,* 2011), biomedicine (Feng *et al.*, 2013; Lai *et al*., 2012), and heterogeneous catalysis (Cody, 2004). Various shaped transition metal chalcogenide nanocrystals can be synthesized by using various reducing agents, surface-capping agents, absorptive small molecules, or inorganic ions. Suitable capping agent such as long-chain amines and L-cysteine are often dissolved in the synthesis solution to prevent the aggregation of iron sulfide nanoparticles (He *et al.*, 2006; Wang *et al.,* 2010; Vanitha & O'Brien, 2008; Ramasamy *et al*., 2010). The surface capping agents help to stabilize and passivate the nanoparticle surfaces, thus improving the stability of the nanoparticles against temperature and possible oxidation that could result in their degradation (Nguyen, 2013).

The capping agents used in the synthesis of the iron sulfide nanocrystals however, need to be removed to produce the accessible active surface sites required for heterogeneous catalytic reactions. Nevertheless, complete removal of these capping agents is rarely achieved and the molecules on the surface often interfere in the catalytic reactions, with either negative or, less often, positive effects. The interplay between adequately protecting the surfaces during synthesis, but subsequently desorbing to allow catalytic reactions to take place, suggests that the capping agents should not bind too strongly to the surface, but not too weakly either.

The characterization of the interactions of the amine functional group with iron sulfide surfaces is therefore of practical interest. Methylamine (CH_3NH_2) is the simplest primary amine, and therefore well suited to address the interactions of the amine functional group with the different FeS surfaces. The interactions of methylamine with transition metal oxide surfaces have already been reported in the literature. For example, Borck *et al.* (2007), have carried out first-principles DFT calculations to analyse and compare the molecular adsorption of methylamine on the α-Al_2O_3(0001) and α-Cr_2O_3(0001) surfaces and showed that methylamine in both cases binds to the exposed surface cations *via* the N lone-pair orbital. There also exist extensive experimental information in the literature regarding the adsorption properties, including temperature-programmed reactions of methylamine on several low-index transition metal surfaces such as Ni(100) (Baca *et al.*, 1985; Che-Chen *et al.*, 1993), Ni(111) (Chorkendorff *et al.*, 1987; Gardin *et al.*, 1992), Cr(100), Cr(111) (Baca *et al.*, 1985), Cu(110) (Maseri *et al.*, 1990), Ru(001) (Johnson *et al.*, 1992), Rh(111) (Hwang *et al.*, 1989), Pd(111) (Chen *et al.*, 1995), W(100) (Pearlstine *et al.*, 1986), and Pt(100), Pt(111) (Thomas *et al.*, 1987; Hwang *et al.*, 1987; Bridge *et al.*, 1988). The desorption temperatures of multilayer methylamine was predicted to be below 150 K at Ni_3Al (111) and NiAl (110) surfaces (Borck et al., 2010), similar to the desorption temperatures reported on metallic Ni(111), Cu(110), Ru(001) and Pd(111) surfaces (Chorkendorff *et al.*, 1987; Maseri *et al.*, 1990; Chen *et al.*, 1995).

The work presented in this chapter is aimed at characterizing the adsorption and desorption properties of methylamine on the low-index surfaces of mackinawite (FeS), using *ab initio* density functional theory methods with a correction for the long-range interactions (DFT-D2). The lowest energy adsorption structures of methylamine, the binding strengths and mechanism of bonding on the different low-index FeS surfaces have been characterised. The desorption temperatures of methylamine from the FeS surfaces have been determined *via* temperature programmed desorption (TPD) simulations using kinetic models. The implications of the adsorption strengths for shape control of the FeS nanoparticles have also been discussed.

6.2 Computational details

Geometry optimizations were carried out using the Vienna Ab-initio Simulation Package (VASP) code (Kresse *et al*., 1993, 996) which employs a basis set of plane-waves to solve the Kohn-Sham (KS) equations of the density functional theory (DFT) in a periodic system. Dispersion forces were accounted for using the Grimme DFT-D2 method (Grimme, 2006) which is essential for the proper description of the adsorption systems. Total energy calculations were carried out with the Generalized Gradient Approximation (GGA), using the PW91 functional (Perdew *et al*., 1992). The interaction between the valence electrons and the core was described with the projected augmented wave (PAW) method (Blöchl, 1994) in the implementation of

Kresse and Joubert (1999). The KS valence states were expanded in a plane-wave basis set with a cut off at 400 eV, which is high enough to ensure that no Pulay stresses occurred within the cell during relaxations. An energy threshold defining self-consistency of the electron density was set to 10^{-5} eV and the interatomic forces are minimized up to 0.01 eV/Å for structural relaxations. A Monkhorst-pack grid of 5 x 5 x 1 (Monkhorst and Pack, 1976) were used to sample the reciprocal space of the substrate-adsorbate system, which ensures electronic and ionic convergence.

The methylamine adsorption calculations were carried out on a (2 x 2) supercell of the different FeS surfaces in such a way that the effective coverage was 0.25 ML, where a monolayer (ML) is defined as one methylamine molecule per surface cation. Symmetry constraints were not included in the geometry optimization calculations, and in particular, the adsorbate was free to move away laterally and vertically from the initial adsorption site or reorient itself at the surface to find the minimum energy adsorption structure. To characterize the strength of interaction of the methylamine molecule with the various surfaces, the adsorption energy is calculated using the following equation

$$E_{ads} = E_{surf+CH_3NH_2} - (E_{surf} + E_{CH_3NH_2}) \qquad (6.1)$$

where $E_{surf+CH_3NH_2}$ represents the total energy of the adsorbate-substrate system, E_{surf} represents the energy of a clean surface, and $E_{CH_3NH_2}$ represents the energy of the methylamine molecule in the gas phase. A negative adsorption energy indicates an exothermic and favourable adsorption.

6.3 Results and discussions

6.3.1 Methylamine structure

Prior to the adsorption of methylamine on the various FeS surfaces, we have performed geometry optimization of the free molecule using cubic cell of size 20 Å. The gas phase structural parameters were then calculated and compared with available experimental data to ensure that our calculations are accurately reproducing the known bond distance and angles. Methylamine has the C_s point group symmetry, possessing a mirror plane along the C−N bond that bisects the H−N−H plane as shown in Figure 6.1.

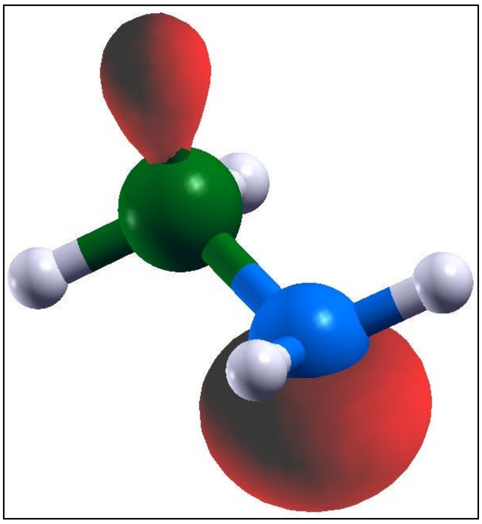

FIGURE 6.1: Relaxed structure of methylamine molecule showing the highest occupied molecular orbital (HOMO) dominated by the lone pair orbital of nitrogen.

The optimized structure shows the methylamine molecule has a staggered conformation with one methyl group hydrogen atom (H_{ip}) lying in the mirror plane at a distance of 1.106 Å from the C atom ($C{-}H_{ip}$), while the other two hydrogen atoms

(H_{op}) are out-of-plane at a distance of 1.098 Å from the C ($C{-}H_{op}$). The internal bond distances and the characteristic bond angles are accurately reproduced by the DFT−D2 method (Table 6.1), in excellent agreement with available experimental data (Iijima *et al.*, 1985). The highest occupied molecular orbital (HOMO) of methylamine is determined to be a non-bonding lone-pair orbital dominated by the 2*p* character of the nitrogen atom. The common expectation is that methylamine will bind to the FeS surfaces *via* this orbital.

Parameter	Experiment[a]	This work
$d(N{-}H)$ /Å	1.031	1.022
$d(C{-}N)$ /Å	1.472	1.470
$d(C{-}H_{ip})$ /Å	1.112	1.106
$d(C{-}H_{op})$ /Å	1.112	1.098
$\alpha(CNH)$ /°	111.5	110.1
$\alpha(HNH)$ /°	106.0	106.4
$\alpha(HCH)$ /°	108.4	107.9

TABLE 6.1: Comparison of calculated and experimental structural parameters of CH_3NH_2 molecule. [a]Experimental data taken from (Iijima *et al.*, 1985)

6.3.2 Adsorption of CH_3NH_2 on FeS(001) surface

Two stable adsorption structures of CH_3NH_2 have been calculated on the FeS(001) surface: (1) NH_2 group either pointing towards (denoted as N-down) or (2) away (denoted as N-up) from the surface atoms as shown Figure 6.2. In both configurations, the CH_3NH_2 molecule was only physisorbed giving a very weak interaction, and releasing an adsorption energy of 0.18 eV and 0.05 eV for the N-up and N-down configurations, respectively. During geometry optimization, the CH_3NH_2 molecule in the N-up configurations moved away perpendicularly from the S adsorption site until the distance between the carbon atom and the surface sulfur atom is 3.072Å and the closest S and H interatomic distance is calculated at 2.645 Å, an indication weak hydrogen bonded interaction between the $–CH_3$ tail and the terminating S atom. In the N-down configuration, the interatomic distance between the N atom and the closest terminating S atom is calculated at 3.115 Å and the shorted S and H interatomic distance is 2.887Å, which is slightly longer than that of the N-up configuration, indicative of even weaker hydrogen bonded interactions in the N-down configuration in agreement with the calculated weak binding energy.

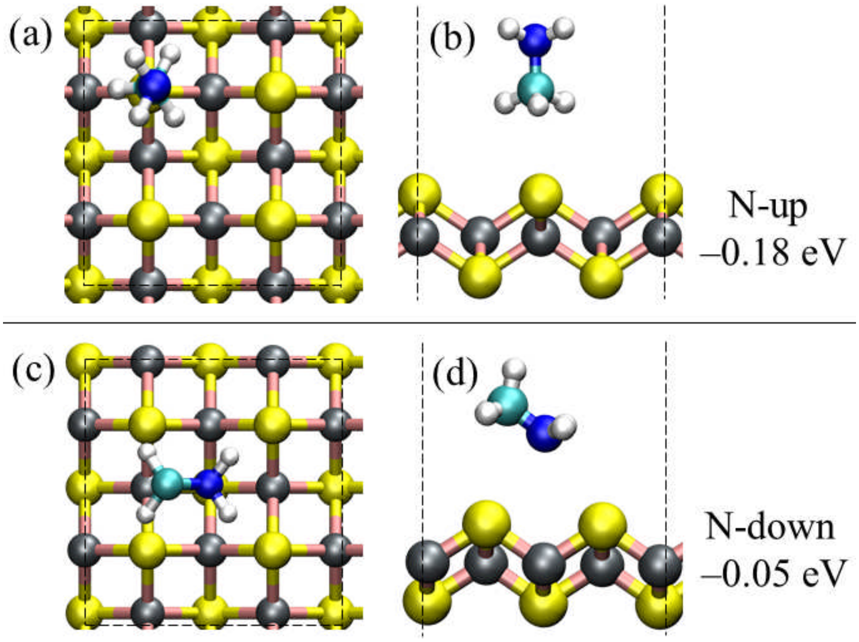

FIGURE 6.2: Top (left) and side (right) views of the relaxed adsorption structures of CH_3NH_2 on FeS (001) surface. (Colour scheme: Fe = grey, S = yellow, N = blue, C = green and H = white).

Consistent with the weak interaction, no significant structural changes were observed in the adsorbed methylamine molecule’s internal bond lengths and angles and no charge transfer occurs between the molecule and the (001) surface atoms (see Table 6.2). The weak interaction of the methylamine with the (001) can be attributed to the electrostatic repulsion between the methylamine molecule and the topmost sulfur atoms in the (001) surface.

Config.	E_{ads} /eV	d(H–S) /Å	$d_{\mathrm{(C-S)}}$/ Å	$d_{\mathrm{(N-S)}}$/ Å	$d_{\mathrm{(C-N)}}$/ Å	$d_{\mathrm{(C-Hip)}}$/ Å	$d_{\mathrm{(N-H)}}$ /Å	α(HNH) /°
N-up	–0.18	2.645	3.072	–	1.463	1.108	1.021	106.6
N-down	–0.05	2.887	–	3.115	1.470	1.106	1.022	106.3

TABLE 6.2: Calculated adsorption energies and selected parameters of methylamine adsorption on FeS(001) surface.

6.3.3 Adsorption of CH_3NH_2 on FeS(011) surface

Contrast to the physisorption obtained at the (001) surface, the CH_3NH_2 molecule is chemisorbed on the FeS(011) surface *via* the N atom with the C−N axis either oriented either along (denoted as M-AL) or across (denoted as M-AC) the FeS layer as shown schematically in Figure 6.3. The adsorption energy for the M-AL and M-AC configurations are respectively calculated to be −1.26 eV and −1.24 eV suggesting that the binding energy is not significantly dependent on the orientation of the molecule's C−N axis on the surface. The N–Fe bond distance in the M-AL and M-AC adsorption configurations are calculated at 2.107 Å and 2.109 Å respectively. In both configurations, there is no direct H-bond formation between the amine's hydrogen atoms and the surface atoms, the closest H–S and H–Fe interatomic bond distances are calculated respectively at (3.199 Å and 2.759 Å) for the M-AL structure and (3.172 Å and 2.679 Å) for the M-AC structure. The optimized internal bond distances of the adsorbed CH_3NH_2 molecule are reported in

Table 6.3. For the M-AL adsorption structure, the C−N, C−H$_{op}$, C−H$_{ip}$ and N−H bond distances are calculated at 1.481 Å, 1.101 Å, 1.100 Å and 1.023 Å respectively. Similar bond distances are calculated for the M-AC adsorption structure (see Table 6.3). An analysis of the surface structure after the methylamine adsorption reveals no significant adsorption-induced structural changes to the (011) surface. The surface Fe atom to which the N atom binds is only slightly displaced upwards in the *z*-direction by 0.07 Å relative to its position in the clean surface for both adsorption structures. The adsorption of CH_3NH_2 on the (011) was repeated on larger surface areas using a simulation made of (3 x 2) and (4 x 2) supercells. The adsorption energies at (3 x 2) and (4 x 2) surfaces are calculated to be −1.28 eV and −1.29 eV respectively, both of which are close to the adsorption energy calculated using the (2 x 2) simulation cell (−1.26 eV), indicating that adsorption energy of CH_3CNH_2 is also not significantly coverage dependent.

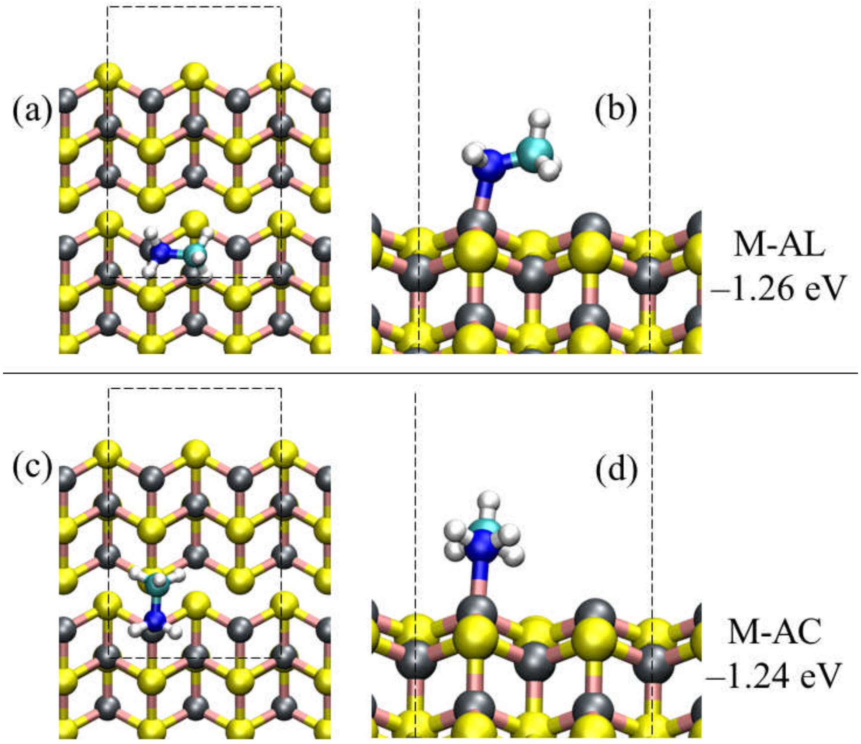

FIGURE 6.3: Top (left) and side (right) views of the relaxed adsorption structures of CH_3NH_2 along (M-AL) (top) and across (M-AC) (bottom) the FeS(011) surface.

Surface	FeS(011)		FeS(100)		FeS(111)	
Config.	M-AL	M-AC	M-AL	M-AC	M-AL	M-AC
E_{ads} /eV	–1.26	–1.24	–1.51	–1.28	–1.69	–1.88
d(N–Fe) /Å	2.107	2.109	2.094	2.137	2.082	2.057
d(C–N) /Å	1.481	1.488	1.479	1.481	1.482	1.486
d(C–Hip) /Å	1.101	1.102	1.104	1.100	1.101	1.100
d(C–Hop) /Å	1.100	1.097	1.097	1.096	1.095	1.099
d(N–H) /Å	1.023	1.024	1.025	1.026	1.028	1.027
α(HNH) /°	107.0	106.7	105.8	106.0	107.1	104.9
$\sum q$ /e^-	0.06	0.06	0.08	0.06	0.09	0.11

TABLE 6.3: Calculated adsorption energies and selected parameters of CH_3NH_2 adsorption on the (011), (100) and (111) surfaces of FeS. M-AL and M-AL denotes the orientation of C-N axis of methylamine along and across the FeS layer. $\sum q$ denotes charge transferred from the methylamine molecule unto the surface.

6.3.4 Adsorption of CH_3NH_2 on FeS(100) surface

The lowest energy adsorption structures of the CH_3NH_2 molecule on the FeS(100) surface are schematically shown in Figure 6.4. The energetically most favoured configuration is calculated to be the M-AL adsorption structure (Figure 6.4 (a & b)), in which an adsorption energy of 1.57 eV is released. When adsorbed in the M-AC configuration (Figure 6.4(c & d)), the adsorption is calculated at –1.28 eV, *i.e.*, 0.29 eV less than the binding energy calculated for the M-AL adsorption structure. The stronger interaction calculated for the M-AL configuration can be attributed to presence of hydrogen bonded interactions between the molecule's H and surface S atoms. In the M-AL adsorption structure, the CH_3NH_2 molecules is rotated through an angle of 30 ^{o} with respect the surface plane, such that one of the H atoms of the

–NH_2 head tilts towards the surface sulfur atom forming a weak hydrogen bond at S−H distance of 2.321 Å and the N−Fe bond distance is calculated at 2.094 Å.

The Fe atom to which CH_3NH_2 molecule is bound to displaces slightly upwards in the *z*-direction by 0.09 Å and 0.07 Å in the M-AL and M-AC configurations respectively. The internal C−N, C−H_{op}, C−H_{ip} and N−H bond distances of the adsorbed methylamine molecule in the M-AL configurations are respectively calculated 1.479 Å, 1.104 Å, 1.097 Å, and 1.025 Å. The internal bond distances of the adsorbed CH_3NH_2 show only a small deviation from the gas phase distances, suggesting there is no significant adsorption induced structural in the methylamine molecule upon adsorption.

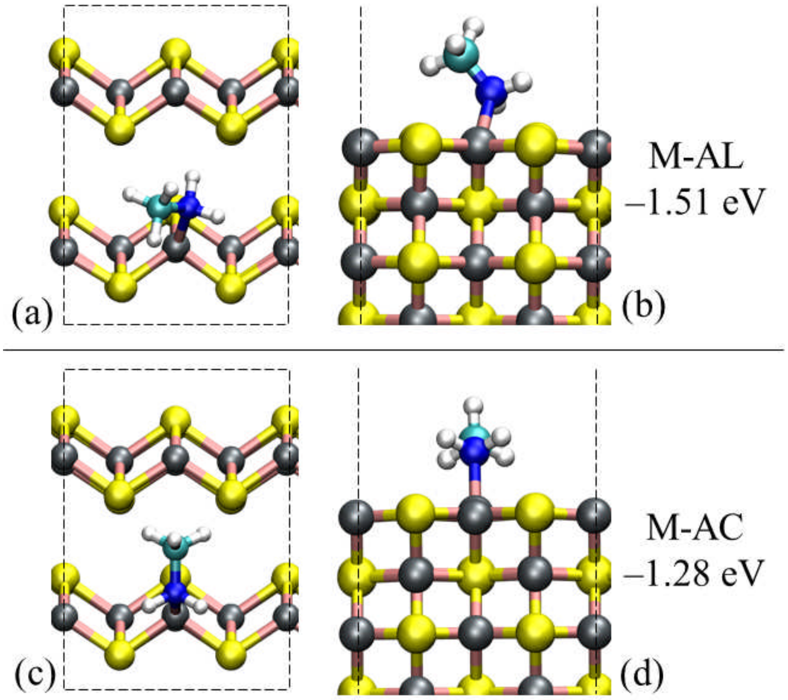

FIGURE 6.4: Top (left) and side (right) views of the relaxed adsorption structures of CH_3NH_2 along (M-AL) (top) and across (M-AC) (bottom) the FeS(100) surface.

In the M-AC adsorption structure, the N−Fe bond distance is calculated to be 2.137Å and the closet H–S bond distance is 2.626 Å, compared to the (2.321 Å) calculated in the M-AL configuration. The larger N−Fe bond distance (2.137Å) calculated for the M-AC configurations compared that of the M-AL configuration (2.094 Å) is consistent with the slightly stronger binding energy calculated for the M-AL configuration than the M-AC configuration. All the relevant structural parameters of the adsorbed CH_3NH_2 molecule in both configurations are summarized in Table 6.3.

6.3.5 Adsorption of CH_3NH_2 on FeS(111) surface

The geometries of the lowest energy adsorption structures obtained on the FeS(111) surface are shown in Figure 6.5. The CH_3NH_2 molecules is found to bind more strongly on the (111) surface than on the (001), (011) or (100) surfaces. The lowest energy adsorption structure on the FeS(111) surface is calculated to be the M-AC configuration (Figure 6.5a). The CH_3NH_2 molecule binds *via* the N atom with its C–N axis oriented across the FeS layer (M-AC) releasing an adsorption of 1.88 eV. This adsorption structure is characterized by the shortest N–Fe bond distance calculated at 2.057 Å and the interatomic distance between S and H atoms is calculated to be 2.501 Å. The optimized internal bond distances of the adsorbed molecule are summarized in Table 6.3, and show no significant deviation from the gas phase bond distances. The strong interaction *via* the N atom however, caused a reduction in the α(HNH) bond angle (from 106.6 ^{o} in the free state to 104.9 ^{o} in the adsorbed state).

When the CH_3NH_2 molecule is adsorbed on the (111) surface *via* the N atom such that its C–N axis is oriented along the FeS layer (M-AL), Figure 6.5b, it released an adsorption energy of 1.69 eV, *i.e.*, 0.19 eV less than the lowest energy (M-AC) structure but still energetically more favourable by 0.43 eV and 0.18 eV than the lowest adsorption structures obtained at the (011) and (100) surfaces respectively.

The N–Fe bond distance in the M-AL configuration on the (111) surface is calculated to be 2.082 Å, and the shortest distance between the closest H and S atoms is calculated at 2.587 Å. The internal C−N, C−H_{op}, C−H_{ip} and N−H bond distances of the adsorbed molecule in the M-AL configuration are calculated at 1.482 Å, 1.101 Å, 1.095 Å and 1.028 Å respectively, (Table 6.3).

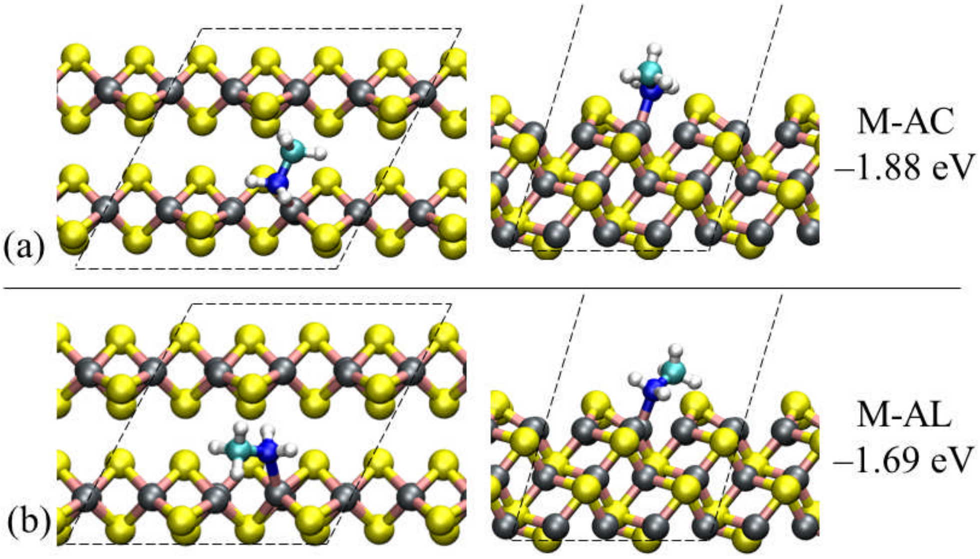

FIGURE 6.5: Top (left) and side (right) views of the relaxed adsorption structures of CH_3NH_2 across (M-AC) and along (M-AL) the FeS (111) surface layer.

6.3.6 Electronic structures

The highest occupied orbital of CH_3NH_2 is a lone pair orbital localized on the N atom as shown Figure 1.6. The common expectation is that CH_3NH_2 binds to FeS surfaces *via* this orbital. Insight on this issue can be gained from the electron density difference ($\Delta\rho$), obtained by subtracting from the electron density of the adsorbate system the sum of the electron densities of the clean surface and the molecule as in equation 6.2.

$$\Delta\rho = \rho_{CH_3NH_2/FeS(hkl)} - (\rho_{FeS(hkl)} + \rho_{CH_3NH_2}) \tag{6.2}$$

The atomic positions of the clean FeS surface and of the CH_3NH_2 layer are taken to be the same as those of the relaxed total adsorbate-substrate system. In this way, the presentation highlights electronic structure and bond formation. The isosurfaces of the electron density differences for the lowest energy adsorption structures of methylamine on the (011), (100) and (111) FeS surfaces are displayed in Figure 6.6.

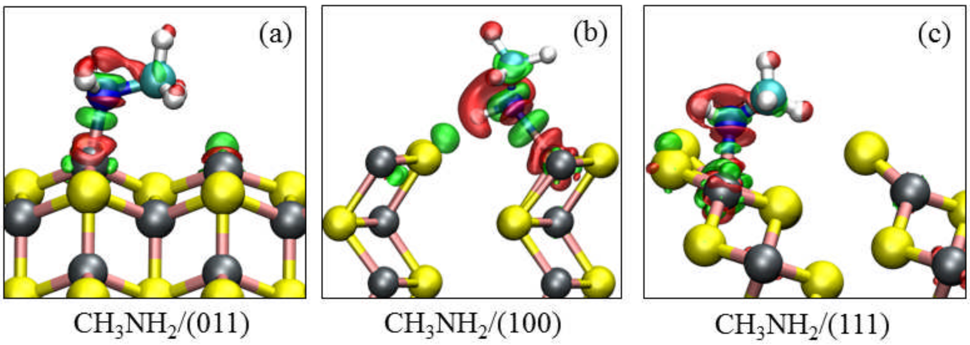

CH_3NH_2/(011) CH_3NH_2/(100) CH_3NH_2/(111)

FIGURE 6.6: Electron density difference plots relative to adsorbed CH_3NH_2 on FeS surfaces, showing electron rearrangement in the regions between the CH_3NH_2 and FeS surface atoms upon adsorption. Green and red contours respectively denote electron density increase and decrease by 0.02 electrons/Å^3.

There is an accumulation of electron density in the N–Fe bond regions, consistent with the formation of a chemical bond. The charge transfer between the adsorbate and the substrate, as estimated by using the space partitioning scheme of Bader (Bader, 1990), is small. Approximately 0.06 e^-, 0.08 e^-, and 0.11 e^- is transferred from the methylamine molecule in the lowest energy adsorption structures to the (011), (100), and (111) surfaces, indicating that the N–Fe bonds are dominated by physisorption characteristics. In Table 6.3, the charge transfers for the other identified stable adsorption structures are reported. There is also evidence of electron density accumulation between the hydrogens of either the NH_2 head or CH_3 tail and the surface species, indicative of hydrogen-bonded interactions between these species. For example, the strong hydrogen-bonded interactions on the (100) surface

(Figure 6.5b), caused the molecule in the M-AL configuration to rotate through an angle of 30 ° towards the surface sulfur atom in the next layer, giving rise to a shorter H–S distance calculated at 2.321 Å. Such hydrogen bonded interactions have also been reported at oxide surfaces (Sanders *et al.*, 1995; Oliva *et al.*, 2007). The electronic density of states projected on the N *p*-orbitals and the interacting Fe *d*-orbitals, which are shown for the strongest binding configurations in Figure 6.7, give further insight into the bonding mechanism methylamine on the (011), (100) and (100) FeS surfaces. The *p*-orbitals of the nitrogen are shown to hybridize with the *d*-orbitals of the interacting surface Fe atoms within the energy range of –4.0 eV to –6.0 eV, consistent with the formation of physisorbed bond between the two interacting species.

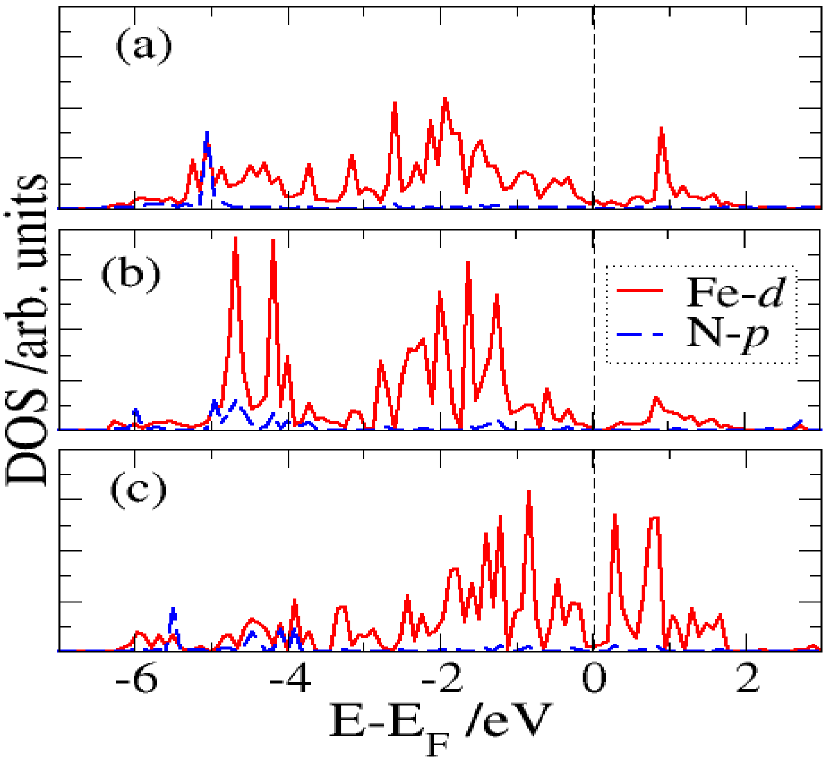

FIGURE 6.7: Electronic density of states of CH3NH$_2$ adsorbed on (a) (011), (b) (100), and (c) (111) surfaces of mackinawite, projected on the interacting surface Fe *d*-states and on the N *p*-states.

6.3.7 Vibrational properties

In order to propose an assignment for the vibrational modes of the adsorbed methylamine we have computed the wavenumbers of the normal modes at the (011) (100) and (111) surfaces. In Table 6.4, we present the calculated and the experimental data (in brackets) of the gas phase methylamine molecule (Shimanouchi, 1972), which agree well. The vibrational frequencies for the adsorbed methylamine at the FeS surface with their corresponding assigned vibrational modes are also summarized. On the (011), (100) and (111) surfaces, the NH_2 scissors frequencies are calculated at 1586 cm^{-1}, 1566 cm^{-1} and 1560 cm^{-1} respectively. The NH_2 symmetric and asymmetric stretching frequencies can be assigned at 3641cm^{-1} and 3576 cm^{-1} on the FeS(011) surface, 3401cm^{-1} and 3263 cm^{-1} on the FeS(100), and 3398 cm^{-1} and 3215 cm^{-1} on the FeS(111) surface. The normal modes within the regions of 2900-3100 cm^{-1} can be assigned to CH_3 deformation modes. The C−N stretching frequencies are assigned at 1006 cm^{-1}, 1011 cm^{-1}, and 1000 cm^{-1} on the (011), (100) and (111) surfaces respectively. The calculated C−N stretching frequencies show good agreement with earlier theoretical and experimental investigations of the vibrational frequencies of gas phase CH_3NH_2 (Wolff & Ludwig, 1972; Baca *et al.*, 1985; Gardin *et al.*, 1992). The normal modes around 1300 cm^{-1} can be assigned to the NH_2 twisting mode and the peak at 1100 cm^{-1} is assigned to the CH_3 rocking mode. It is to be noted that the NH_2 symmetric and asymmetric stretching modes are red-shifted relative to the gas-phase molecule at the (111) and (100) surface but blue shifted at the (011) surface (see Table 6.4) suggesting a stronger interactions between the methylamine with the (111), and (100) surfaces than the (011), which is in good agreement with the larger adsorption energies calculated at the (111) and (100) surfaces compared to the (011) surface.

Vibration No.	Free CH_3NH_2	M-AL/ FeS(011)	M-AL/ FeS(100)	M-AC/ FeS(111)	Assignments
υ_1	3450.2 (3427)	3640.9	3400.6	3398.4	NH_2 a-stretching
υ_2	3365.9 (3361)	3575.5	3262.9	3215.3	CH_3 s-stretching
υ_3	3033.1 (2985)	3021.9	3109.9	3100.2	CH_3 stretching
υ_4	2995.9 (2961)	3013.9	3037.1	3021.4	CH_3 stretching
υ_5	2932.6 (2820)	2959.5	2964.4	2899.7	CH_3 deformation
υ_6	1604.9 (1623)	1585.6	1565.8	1560.2	NH_2 scissors
υ_7	1463.2 (1473)	1474.1	1458.8	1451.3	CH_3 deformation
υ_8	1441.4 (1473)	1454.7	1453.5	1450.5	CH_3 deformation
υ_9	1401.9 (1430)	1403.5	1412.2	1401.6	CH_3 rocking
υ_{10}	1303.1 (1419)	1306.6	1300.1	1299.8	NH_2 twisting
υ_{11}	1126.1 (1130)	1179.0	1198.0	1183.0	CH_3 rocking
υ_{12}	937.0 (780)	985.6	1026.3	1030.1	NH_2 wagging
υ_{13}	1033.7 (1044)	1006.2	1011.3	1000.4	CN stretching
υ_{14}	792.9 (780)	951.4	978.3	980.8	NH_2 wagging

TABLE 6.4: Vibrational frequencies of methylamine adsorbed at FeS surfaces. The calculated and experimental values (given in brackets, Shimanouchi, 1972) of the gas phase methylamine are also given. (M = methylamine, a = asymmetric and s = symmetric stretching).

6.3.8 Temperature programmed desorption (TPD)

In order to simulate CH_3NH_2 temperature programmed desorption from the different FeS surfaces, we propose a kinetic model which suppresses the molecule adsorption process step to mimic an experimental batch reactor with a high pumping speed to avoid re-adsorption of the CH_3NH_2 molecule. The CH_3NH_2 pressure and coverage as a function of time are governed by the following differential equations:

$$\frac{dP_{CH_{3NH_2}}}{dt} = k_{des} \cdot \theta_{CH_3NH_2} = -\frac{d\theta_{CH_3NH_2}}{dt} \qquad (6.3)$$

Where $\theta_{CH_3NH_2}$ denotes the surface coverage of the methylamine in monolayers (ML), t the time and k_{des} is the rate of desorption. The desorption rate constant (k_{des}) is derived from conventional classical harmonic transition state theory of Evans-Polanyi-Eyring as in equation 6.4 (Laidler & King, 1983):

$$k_{des} = \left(\frac{k_B T}{h}\right)\left(\frac{q^{\#}}{q}\right)\exp\left(-\frac{E_{des}}{k_B T}\right) \tag{6.4}$$

where k_B is the Boltzmann constant, T is the temperature, h is the Planck constant, $q^{\#}$ is the partition function of the transition state, q is the partition function of the reactants, and E_{des} is the desorption activation energy. For the desorption process one assumes that the transition state is infinitely close to the desorbed state. In practice, this means using the partition functions of the free molecule for $q^{\#}$ in equation 6.4 but with two degrees of freedom in the translational partition function because the third is taken as the reaction coordinate for desorption.

The calculated desorption energy E_{des} of methylamine on the different FeS were corrected by the zero-point energy (ZPE). The TPD intensity which is equal to the desorption rate of the adsorbed molecule, were obtained by solving the set ordinary differential equations in 6.3, following standard recipes and different sets of initial conditions as implemented in the Maple software.

The TPD simulations started with a pre-adsorbed CH_3NH_2 on the (011), (100) and (111) surfaces with coverage $(\theta_{CH_3NH_2})$ between 0.1 and 0.9 ML, where we consider that a ML has been reached when all equivalent active sites are occupied. We have considered a temperature range between 100–400 K with an increment of 5 K/s, measuring the pressure every second. Raising the temperature leads to an increment of the CH_3NH_2 pressure as plotted and shown in Figure 6.8. The desorption processes of CH_3NH_2 show the maximum rate at 135 K, 165 K and 180 K on the (011), (100) and (111) surfaces respectively. The results indicate that methylamine is thermally more stable at the (111) surface compared to the (011) and (100) surfaces, and this is consistent with the calculated binding energies which show the strength of CH_3NH_2 adsorption on the different surfaces increase in the order: (011) < (100) < (111). Our calculated desorption temperatures for methylamine on the FeS surface compares to the desorption temperature of multilayer methylamine at $Ni_3Al(111)$ and NiAl(110) surfaces predicted to be 150 K (Borck *et al.*, 2010). Similar desorption temperatures have been reported for methylamine on Cu(110) (Maseri *et al.*, 1990) and Ru(001) (Johnson *et al.*, 1992). On Ni(100), Ni(111), Cr(100), and Cr(111) approximately one monolayer of surface species of methylamine was shown to be stable up to about 300 K (Chorkendorff *et al.*, 1987).

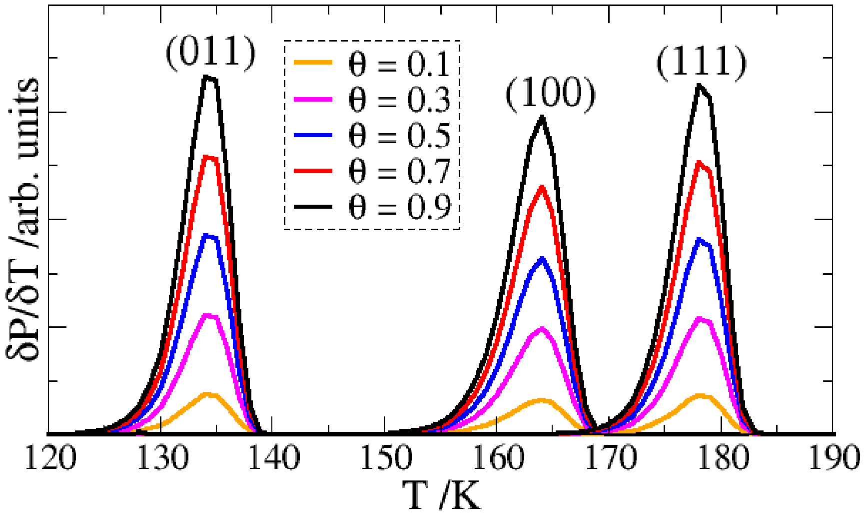

FIGURE 6.8: Simulated TPD curves of CH_3NH_2 on FeS (011), (100) and (111) surfaces for a reaction time of 1 m/s at different initial coverages.

6.4 Summary and conclusions

We have used Density Functional Theory calculations with a correction for the long-range interactions (DFT-D2) to unravel the adsorption and desorption behaviour of methylamine on the (001), (100), (011), and (111) surfaces of mackinawite. The methylamine molecule is shown to interact very weakly with the energetically most stable (001) surface, but adsorb relatively strongly on the (011), (100) and (111) surfaces, preferentially at Fe sites. Analysis of the nature of the bonding between adsorbate and the substrate reveals that methylamine interacts with the surface Fe atoms *via* the lone-pair of electrons located on the N atom. The adsorption process is shown to be characterized with only a small charge transfer from the methylamine to the interacting surface Fe atoms, indicating that the N–Fe bonds are mainly of physisorbed character. The stronger binding of methylamine to the (011), (100) and (111) surfaces rather than the (001) plane indicates that these surfaces should become more prominent in the crystal morphology in the presence of methylamine; crystal growth will be hindered on the (011), (100) and (111) surfaces compared to the (001) surface, which does not interact significantly with the capping agent. As such, the FeS moiety could grow much more rapidly perpendicular to the (001) surface, rather than extend the (001) surface horizontally and this surface is therefore expected to become less dominant in the morphology with respect to the other surfaces, as is found in many crystals grown in the presence of growth-modifying moieties (Cooper & de Leeuw, 2002, 2006). The greater prominence of the more reactive surfaces in the particle grown in the presence of methylamine or similar surfactants should also enhance the catalytic performance of the FeS nanoparticles.

From a macroscopic point of view, the simulated TPD process shows relatively low desorption temperatures, <140 K on (011), <170 K on (100) and <180 K on (111) FeS surfaces, which are comparable to experimental desorption temperatures predicted at metallic surfaces. These low temperatures of desorption imply that a small molecule such as methylamine is desorbed too easily to act as an effective capping agent under the kind of ambient conditions where other capping agents may work, for example a long chain amine such as oleylamine. However, this study shows the selectivity of the methylamine functional group towards capping different FeS surfaces in a range of temperatures, thereby favouring the expression of more reactive surfaces in the particle morphology. The low desorption temperature does of course mean that the molecule is removed easily to produce the accessible active surface sites required for heterogeneous catalytic reactions.

Bibliography

- Alivisatos P.; Science, **271**, 933 (1996)
- Bader R. F. W.; Atoms in Molecules—A Quantum Theory (Oxford: Oxford University Press) 1990
- Baca A. G.; Schulz M. A.; Shirley D. A.; *J. Chem. Phys*. **83**, 6001 (1985)
- Bi, Y.; Yuan Y.; Exstrom C. L.; Darveau S. A.; Huang J.; *Nano Lett*., **11**, 4953 (2011)
- Borck O.; Schroder E.; *Journal of Physics-Condensed Matter*, **18**, 10751 (2006)
- Borck Ø.; Svenum I. H.; Walle L. E.; Andersen T. H.; Schulte K.; Borg A.; *Journal of Physics-Condensed Matter*, **22**, 395004 (2010)
- Borck Ø.; Hyldgaard P.; Schroder E.; *Phys. Rev. B.*, **75**, 035403 (2007)

- Bridge M. E.; Somers J.; *Vacuum*, **38**, 317 (1988)
- Burda C.; Chen X.; Narayanan R.; El-Sayed M. A.; *Chem. Rev.*, **105**, 1025 (2005)
- Burton P. D.; Boyle T. J.; Datye A. K.; *J. Catal*. **280**, 145 (2011)
- Chen J. J.; Winograd N.; *Surf. Sci*. **326**, 285 (1995)
- Chen G.; Zen J. M.; Fan F. R.; Bard A. J.; *J. Phys. Chem*., **95**, 3682 (1991)
- Che-Chen C.; Cheng K.; Richard S.; *J. Vac. Sci. Technol. A*, **11**, 2122 (1993)
- Chen X.; Wang Z.; Wang X.; Wan J.; Liu J.; Qian Y.; *Inorg. Chem*., 44, 951 (2005)
- Chorkendorff I.; Russell J. N.; Yates J. T.; *J. Chem. Phys*. **86**, 4692 (1987)
- Cody G.; Boctor N.; Brandes J.; Filley T.; Hazen R.; Yoder H.; *Geochim. Cosmochim. Acta*, 68, 2185 (2004)
- Cooper T.G.; de Leeuw N.H.; *Mol. Simul*. **28**, 539 (2002)
- Cooper T.G.; de Leeuw N.H.; *J. Cryst. Growth*, **294**, 137 (2006)
- Coppens P.; X-Ray Charge Densities and Chemical Bonding, Oxford University Press, USA, (1997)
- Ennaoui A.; Fiechter S.; Jaegermann W.; and Tributsch H.; *J. Electrochem. Soc.* **133**, 97 (1986)
- Feng W. H.; Liang Z.; Weidong S.; Shuyan S.; Yonngqian L.; Song W.; Hongjie Z.; *Dalton Trans.*, 9246 (2009)
- Feng M.; Lu Y.; Yang Y.; Zhang M.; Xu Y.-J.; Gao H.-L.; Dong L.; Xu W.-P.; Yu S.-H.; *Scientific Reports* **3**, 2994, (2013)
- Gardin D. E.; Somorjai G. A.; *J. Phys. Chem*. **96**, 9424 (1992)
- He Z.; Yu S. H.; Zhou X.; Li X.; Qu J.; *Adv. Funct. Mater*., **16**, 1105 (2006)
- Hu J.; Odom T. W.; Lieber C. M.; *Acc. Chem. Res*., 32, 435 (1999)
- Hwang S. Y.; Seebauer E. G.; Schmidt L. D.; *Surf. Sci.* **188**, 219 (1987)

- Hwang S. Y.; Kong A. C. F.; Schmidt L. D.; *J. Phys. Chem.* **93**, 8327 (1989)
- Iijima T.; Jimbo H.; Taguchi M.; *J. Mol. Struct.* **144**, 381 (1986)
- Johnson D. F.; Wang Y. Q.; Parmeter J. E.; Hills M. M.; Weinberg W. H.; *J. Am. Chem. Soc.* **114**, 4279 (1992)
- Joo J.; Na H. B.; Yu T., Yu J. H.; Kim Y. W.; Wu F.; Zhang J. Z.; and Hyeon T.; *J. Am. Chem. Soc*. **125**, 11100 (2003)
- Jun Y. W.; Huh Y. M.; Choi J. S.; Lee J.–H.; Song H-T.; Kim S.; Yoon S.; Kim K.–S.; Shin J.S.; Cheon J.; *J. Am. Chem. Soc*., **127**, 5732 ((2005)
- Kimberly D.; Dhanasekaran T.; Zhang Z.; Meisel D.; *J. Am. Chem. Soc*., **124**, 2312 (2002)
- Kim C.; Kim S. S.; Yang S.; Han J. W.; Lee H.; *Chemical Communications*, **48**, 6396 (2012)
- Kim Y. Y., Walsh D.; *Nanoscale*, **2**, 240 (2010)
- Kirkeminde A.; Scott R.; Ren S.; *Nanoscale*, **4**, 7649 (2012)
- Kora A.; Beedu S.; Jayaraman A.; *Organic and Medicinal Chemistry Letters*, **2**, 17 (2012)
- Lai C.-H.; Lu M.-Y.; Chen L.-J.; *J. Mater. Chem*., **22**, 19 (2012)
- Laidler K. J.; King M. C.; *J. Phys. Chem.* 87, 2657 (1983)
- Lin Y.-Y.; Wang D.-Y.; Yen H.-C.; Chen H.-L.; Chen C.-C.; Chen C.-M.; Tang C.-Y.; Chen C.-W.; *Nanotechnology*, **20**, 405207 (2009)
- Maseri F.; Peremans A.; Darville J.; Gilles J. M.; *J. Electron Spectrosc. Relat. Phenom.* **54**, 1059 (1990)
- Marignier J. L.; Belloni J.; Delcourt M. O.; Chevalier J. P.; *Nature*, **317**, 344 (1985)
- Nath M.; Choudhury A.; Kundu A.; Rao C. N. R.; *Adv. Mater*., **15**, 2098 (2003)
- Nguyen T-D; *Nanoscale*, 5, 9455 (2013)

- Ozin G. A.; *Adv. Mater*., **4**, 612 (1992)
- Oliva C.; van den Berg C.; Niemantsverdriet M. H.; Curulla-Ferre D.; *J. Catal.* **248**, 38 (2007)
- Paolella A.; George C.; Povia M.; Zhang Y.; Krahne R.; Gich M.; Genovese A.; Falqui A.; Longobardi M.; Guardia P.; Pellegrino T.; Manna L.; *Chem. Mater.* **23**, 3762 (2011)
- Pearlstine K. A.; Friend C. M.; *J. Am. Chem. Soc.* **108**, 5842 (1986)
- Puthussery J.; Seefeld S.; Berry N.; Gibbs M.; Law M.; *J. Am. Chem. Soc*., **133**, 716 (2011)
- Quintanilla A.; Butselaar-Orthlieb V. C. L.; Kwakernaak C.; Sloof W. G.; Kreutzer M. T.; Kapteijn F.; *J. Catal*. **271**, 104 (2010)
- Ramasamy K.; Malik M. A.; Helliwell M.; Tuna F.; O'Brien P.; *Inorg. Chem*., 49, 8495 (2010)
- Roldan A.; Novell G.; Ricart J. M.; Illas F.; *J. Phys. Chem. C* 114, 5101 (2010)
- Sanders H. E.; Gardner P.; King D. A.; *Surf. Sci*. **331**, 1496 (1995)
- Sperling R. A.; Parak W. J.*; Phil. Trans. R. Soc. A*, **368**, 1333 (2010)
- Stankus D. P.; Lohse S. E.; Hutchison J. E.; Nason J. A.; *Environmental Science & Technology* **45**, 3238 (2011)
- Steinhagen C.; Harvey T. B.; Stolle C. J.; Harris J.; Korgel B. A.; *J. Phys. Chem. Lett.*, 3, 2352 (2012)
- Tao A. R.; Habas S.; Yang P.; *small*, **4**, 310 (2008)
- Thimmaiah S.; Rajamathi M.; Singh N.; Bera P.; Meldrum F. C.; Chandrasekhar N.; Seshadri R.; *J. Mater. Chem*. **11**, 3215 (2001)
- Thomas P. A.; Masel R. I.; *J. Vac. Sci. Technol. A*, **5**, 1106 (1987)
- Trentler T. J.; Denler T. E.; Bertone J. F.; Agrawal A.; Colvin V. L.; *J. Am. Chem. Soc.* **121**, 1613 (1999)
- Vanitha P. V.; O'Brien P.; *J. Am. Chem. Soc*., 130, 17256 (2008)

- Wang A. W.; Wang Q. H.; Wang T. M.; *CrystEngComm*, **12**, 755 (2010)
- Wolff H.; Ludwig H.; *J. Chem. Phys.* **56**, 5278 (1972)
- Wu B.; Song H.; Zhou J.; Chen X.; *Chem. Commun.*, **47**, 8653 (2011)
- Xia Y.; Yang P.; *Adv. Mater*., **15**, 351 (2003)
- Yamaguchi Y.; Takeuchi T.; Sakaebe H.; Kageyama H.; Senoh H.; Sakai T.; Tatsumi K.; *J. Electrochem. Soc*, **157**, A630 (2010)

Chapter 7

Adsorption and dissociation of NO_x on low-index FeS surfaces

Abstract

Dispersion corrected density functional theory (DFT-D2) calculations have been used to study the adsorption and dissociation reactions of NO_x gases (nitrogen monoxide (NO) and nitrogen dioxide (NO_2)) on the low-index mackinawite surfaces. We show from our calculations that these environmentally important molecules interact very weakly with the energetically most stable (001) surface, but adsorb relatively strongly on the (011), (100) and (111) mackinawite surfaces, preferentially at Fe sites *via* charge donation from these surface species. The NO_x species exhibit a variety of adsorption geometries, with the most favourable for NO being the monodentate Fe−NO configuration, whereas NO_2 is calculated to form a bidentate Fe−NOO−Fe configuration. The calculated thermochemical and activation energy barriers for the direct dissociation of NO and NO_2 on the FeS surfaces show that NO prefers molecular adsorption, while dissociative adsorption (*i.e.*, $NO_2{}^* \rightarrow NO^* + O^*$) is preferred over molecular adsorption for NO_2 on the mackinawite surfaces. The high activation barriers calculated for further dissociation of the second N–O bond to produce either (N^* and $2O^*$) or (N^* and $O_2{}^*$) however, suggest that complete dissociation of NO_2 is unlikely to occur on the mackinawite surfaces.

7.1 Introduction

The removal of nitrogen oxides (NO_x) from lean exhaust streams remains one of the major challenges in environmental catalysis and a topic of extensive research (Liu and Gao, 2011; Breedon *et al.*, 2009; Hellman *et al.*, 2008; Brown & King, 2000; Rodriguez *et at.*, 2001, Liu & Woo, 2006). Atmospheric nitrogen oxides play important roles in the formation of photochemical smog and acid rain, and the destruction of ozone in the stratosphere, whereas they are also possible greenhouse gases exacerbating climate change (Liu & Woo, 2006). Short term or small level of NO_x exposures can cause irritation of the eyes and throat, tightness of the chest, nausea, headache, and gradual loss of strength (Strand *et al.*, 1996; Folinsbee, 1992). Prolonged exposure to NO and NO_2 can cause violent coughing, difficulty in breathing, and cyanosis; it could be fatal (Blomberg *et al*., 1999; Atkinson *et. al*, 2011). NO_2 decomposes on contact with water to produce acid rain in the form of nitrous acid (HNO_2) and nitric acid (HNO_3), which are highly corrosive (EPA-456/F-99-006R, 1999). Acid rain is destructive to anything it contacts, including plants, trees, and man-made structures like buildings, bridges, and the like.

$$2NO_2 + H_2O \rightarrow HNO_2 + HNO_3 \tag{7.1}$$

It is obviously important that the concentration of NO_x gases in the atmosphere is stabilized, but as the populations have grown and industrial activities have increased, the rate of NO_x emission from automobile exhausts and stationary sources has also increased dramatically over the years. All internal combustion engines emit pollutants; carbon monoxide (CO), hydrocarbons (HC), oxides of nitrogen (NO_x), and small particulate matter in the exhaust gas. In order to abate NO_x released into the environment, there is a need to develop novel catalysts with high efficiency towards the removal or destruction of NO_x (deNO_x processes). The adsorption and activation processes of NO_x over the active sites of a catalyst are a crucial part of the selective catalytic reduction (SCR) reactions of nitrogen oxides (Liu & Woo, 2006).

Earlier investigations of the adsorption and dissociation of NO_x molecules over catalysts surfaces have focused on transition metal oxides including TiO_2, BaO, ZnO and α-Al_2O_3 surfaces (Sorescu *et al.*, 2000; Rodriguez *et al.*, 2001; Branda *et al.*, 2004; Breedon *et al.*, 2009; Liu *et al.*, 2010). The adsorption and decomposition of NO_x molecules have also been investigated extensively using techniques such as temperature programmed desorption (TPD), low-energy electron diffraction (LEED), electron energy loss spectroscopy (EELS) and X-ray photoelectron spectroscopy (XPS) on pure metallic surfaces, such as, Pt(111) (Segner *et al.*, 1982; Dahlgren and Hemminger, 1982; Bartram *et al.*, 1987, 1987), Ru(001) (Schwalke *et al.*, 1986a,1986b), Rh(111) (Jirsak *et al.*, 1999), Ag(111) (Bare *et al.*, 1995; Polzonetti *et al.*, 1990; Brown *et al.*, 1995), Pd(111) (Banse *et al.*, 1990; Wickham *et al.*, 1991), Au(111) (Bartram and Koel, 1989; Wang *et al.*, 1998a, 1998b; Beckendorf *et al.*, 1993), and polycrystalline Au (Wickham *et al.*, 1990). These studies have demonstrated that NO_2 adsorbs dissociatively on Rh(111), Pd(111), Pt(111), Ru(001), and Ag(111) surfaces at low temperature but adsorbs molecularly onto Au(111) and polycrystalline Au.

Transition metal sulfide nanocrystals are also attracting attention for potential applications in heterogeneous catalysis owing to their unique and interesting physical, electronic, magnetic and chemical properties (Cody *et al.*, 2000, 2004; Geng *et al*., 2007; Akhtar *et al.*, 2011; Abdelhady *et al*., 2012; Joo *et al*., 2003). Iron sulfides are suggested catalysts in the iron-sulfur hypothesis for the origin of life (Wächtershäuser, 1992; Blöchl *et al.*, 1992). Nørskov and co-workers have also reported the extraordinary catalytic properties of MoS_2 surfaces and MoS nanoparticles (Moses *et al.*, 2009; Hinnemann *et al.*, 2005). For example, in petrochemical processes, sulfur-containing molecules are removed from the feedstream by adsorption on transition metal sulfides, mainly MoS_2 (Hinnemann *et al.*, 2005; Moses *et al.*, 2007; Lauritse *et al.*, 2007). A spectroscopy, microscopy and theoretical study of NO adsorption on MoS_2 and Co–Mo–S hydrotreating catalysts have been reported recently in the literature (Topsøe *et al.*, 2011). More recently, the interactions of NO_x molecules with the (100) surface of iron sulfide pyrite (FeS_2) has been reported using DFT calculations (Sacchi *et al.*, 2012). The NO_x species were shown to interact strongly with the pyrite (100) surface but the calculated high activation barriers for their dissociation suggest that the NO_x species will remain molecularly chemisorbed on pyrite surfaces even at high temperature. However, the diversity of naturally occurring iron sulfides, with iron existing in multiple oxidation states provides alternative iron sulfide systems for consideration as materials for the adsorption and decomposition of NO_x.

In the present study, we have investigated the catalytic properties of mackinawite (tetragonal FeS) towards NO and NO_2 adsorption and activation using DFT-D2 calculations, where we consider the nature of binding of the NO_x species to the FeS surfaces and their dissociation reaction mechanisms. The NO_x species are shown to adsorb relatively strongly on the different low-index FeS surfaces, preferentially at Fe sites *via* charge donation from these surface species. Upon adsorption, the N−O bonds are significantly activated as they are elongated compared to gas phase molecular distances and this is confirmed *via* vibrational frequency calculations.

7.2 Computational details

The methods used here are similar to those used in the earlier chapters. The systems have been modelled using the plane-wave pseudopotential method at the DFT level using the Vienna Ab-initio Simulation Package (Kresse *et al.*, 1993, 1994, 1996). Dispersion forces were accounted for using the DFT-D2 method of Grimme, which is essential for the proper description of the adsorption systems (Grimme, 2006). Total energy calculations were carried out with the Generalized Gradient Approximation (GGA)-PW91 functional (Perdew *et al.*, 1992). The interaction between the valence electrons and the core was described with the projected augmented wave (PAW) method in the implementation of Kresse and Joubert (Blöchl, 1994; Kresse & Joubert, 1999). The KS valence states were expanded in a plane-wave basis set with a cut off at 400 eV, which is high enough to ensure that no Pulay stresses occurred within the cell during relaxations. An energy threshold defining self-consistency of the electron density was set to 10^{-5} eV and the interatomic forces. A 5 x 5 x 1 Monkhorst-pack grid was used to sample the reciprocal space of the substrate-adsorbate system respectively, which ensures electronic and ionic convergence.

In order to accommodate a greater range of adsorption geometries and allow a better isolation of the NO_x molecules from their lateral periodic images, the NO_x adsorption and dissociation calculations were carried out on (4 x 2) supercells of the different low-index surface studied (Figure 7.1). These surface simulation cells are large enough to ensure that the minimum distance between the NO_x molecules and their images in the neighbouring cells is more than 10 Å in the *x*-direction and more than 6 Å in the *y*-direction, thereby avoiding any lateral interactions between the adsorbates in periodic cells along and across the FeS layers. This set up thus provide reliable adsorption energies for the isolated NO_x molecules. The isolated NO_x molecules were modelled in cubic box of lattice constants of 15 Å, sampling only the Γ-point of the Brillouin zone. To determine the lowest energy adsorption structures, the atoms of the adsorbate and the topmost three atomic layers of the slab were allowed to relax without constrains until the residual forces on each atom reached 0.01 eV/Å. In particular, the NO_x molecules were free to move away laterally or vertically from the initial site or re-orient themselves to find the minimum energy adsorption structure. The adsorption energy of the NO_x species was calculated using the expression:

$$E_{ads} = E_{surface+NO_x} - (E_{surface} + E_{NO_x}) \tag{7.2}$$

where $E_{surf+NO_x}$ and $E_{surface}$ represent the total energy of the adsorbate-substrate system and the clean surface respectively. E_{NO_x} represents the energy of the NO_x molecule in the gas phase. A negative adsorption energy indicates exothermic and favourable adsorption.

Bader charge analysis was carried out for all the adsorbate-substrate systems (Bader, 1990), using the Henkelman algorithm (Henkelman *et al.*, 2006) in order to quantify the charge transfer between the FeS surfaces and NO_x species. The climbing image nudged elastic band (CI-NEB) method was used to locate the transition state and reaction activation energy barriers of the NO_x dissociation process (Mills *et al.*, 1995). Transition states were further confirmed through frequency calculations, in which only one imaginary frequency is obtained corresponding to the reaction coordinate. The reaction energy (ΔE) is calculated as the total energy difference between the final state and the initial state and the activation barrier (E_a) is defined as the total energy differences between the initial state and the saddle point.

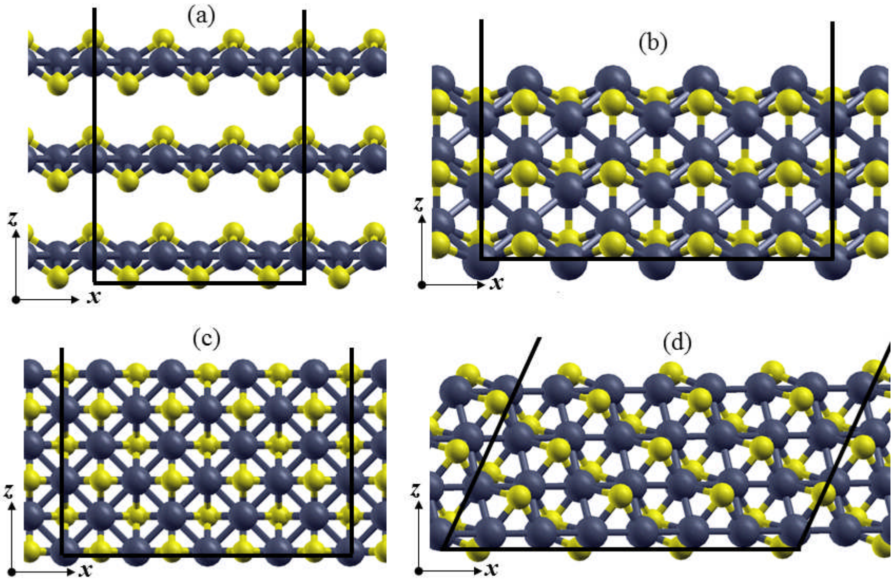

FIGURE 7.1: FeS surface terminations and simulation cells used for NO_x adsorption calculations: (a) (001)−3 x 3; (b) (011)−4 x 2; (c) (100)−4 x 2; and (d) (111)−4x2. (Colour scheme: Fe = grey, S = yellow).

7.3 Results and discussions

7.3.1 Gas phase NO and NO_2 molecules

Prior to the adsorption of the NO and NO_2 molecules on the low-index FeS surfaces, the structural parameters (bond distances and angles) in the gas phase were calculated and compared with available experimental data and earlier theoretical predictions. The calculated bond distances and angles in the gas phase can be directly compared to those in the adsorbed states, in order to determine their extent of activation. In Tables 7.1 and 7.2, the calculated bond distances, angles and the N−O stretching vibrational modes of NO and NO_2 in the gas phase are respectively reported. The calculated results for NO are d(N−O) = 1.160 Å and υ(N−O) = 1898 cm^{-1}, which agree with the experimental values of 1.170 Å and 1903 cm^{-1} (Lide, 2007), as well as to other DFT results (Breedon *et al.*, 2009). The d(N−O) and α(ONO) angle of NO_2 are respectively calculated to be 1.213 Å and 133.8 °, and the symmetric and asymmetric stretching vibrational modes are calculated at 1331 and 1665 cm^{-1} (Tables 7.2), all of which show good agreement with experimental data (Lide, 2007) and theoretical values predicted by Breedon *et al.*, 2009.

7.3.2 Adsorption of NO on FeS(001) surface

In order to identify the optimized adsorption structures of NO with the minimum energy on the (001), (011), (100) and (111) surfaces, the NO molecule was introduced to the surfaces in three different initial orientations: (1) oxygen pointing either towards (X–ON) or (2) away (X–NO) from the surface, and (3) NO adsorbed parallel to the surface plane (X–(NO)), where X denotes the interacting surface atom.

The optimized low-energy NO adsorption structures on the (001) surface are shown in Figure 7.2 (a–c) while the adsorption energies and relevant bond distances are summarized in Table 7.1. When adsorbed through the oxygen atom at an Fe site (Figure 7.2a), the NO molecule was only physisorbed, releasing an adsorption energy of 0.15 eV, and it moved away from the surface Fe binding site during geometry optimization until the distance between the oxygen atom and the surface iron atom is 4.040 Å. When the NO was adsorb *via* the nitrogen atom at an Fe site (Fe–NO), a positive adsorption energy of +0.12 eV was calculated, which suggests an unfavourable adsorption process. The Fe atom to which the NO is bound is pulled up by 1.201 Å from its initial surface position (see Figure 7.2b), causing significant distortion of the surface structure around the Fe adsorption site, hence the unfavourable adsorption.

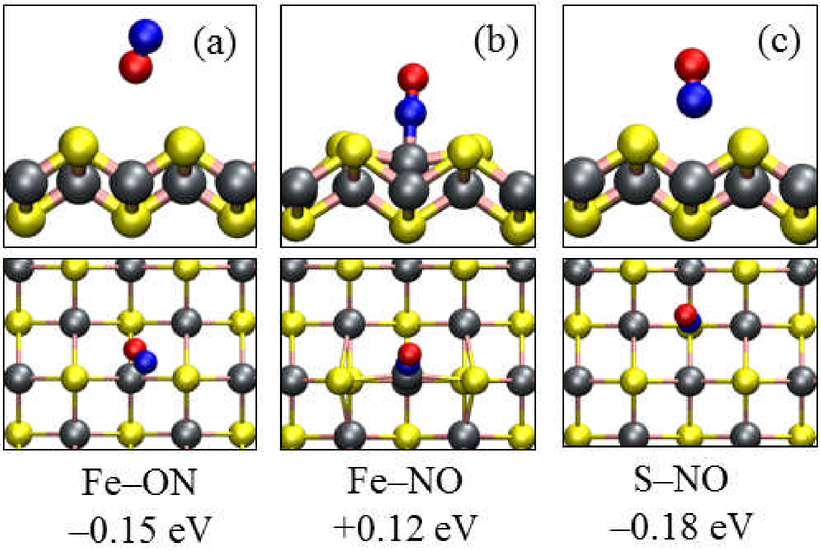

FIGURE 7.2: Side (top) and top (bottom) views of the optimized adsorption structures of NO on the (001) FeS surface. (Colour scheme: Fe = grey, S = yellow, N = blue and O = red).

The S–NO configurations (Figure 7.2c) gave a very weak interaction; the NO molecule moved away from the interacting sulfur atom until the S–N distance is 3.068 Å, releasing an adsorption energy of 0.18 eV. The relaxed structure of the S–ON configuration converges to the Fe–ON configuration, giving the same binding energy ($E_{ads} = -0.15$ eV). As expected, no charge transfer occurred from the surface to the NO molecule except in the Fe–NO configuration where a small charge (0.06 e^-) is transferred from the surface. The calculated N–O stretching vibrational frequencies reported in Table 7.1 confirm no significant softening of the N–O bonds as they remained virtually unchanged compared to the isolated NO bond length. The weak interaction of the NO molecule with the (001) surface can be attributed to the steric repulsion the NO molecule feels from the S atoms terminating the surface.

Surface	Configuration	E_{ads} /eV	*d*(Fe−N) /Å	*d*(Fe−O) /Å	*d*(N−O) /Å	*υ*(N−O) /cm^{-1}	∑q /e^{-}
	NO (gas)	–	–	–	1.160 (1.170)[a]	1898 (1903)[a]	–
(001)	Fe–ON	–0.15	–	4.040	1.166	1845	0.00
	Fe–NO	+0.12	1.643	–	1.179	1793	0.06
	S–NO	–0.18	–	–	1.161	1839	0.00
(011)	Fe–NO	–2. 87	1.664	–	1.199	1766	0.45
	Fe–ON	–1.32	–	1.790	1.187	1616	0.39
	Fe–NO–Fe	–2.74	1.688	2.130	1.245	1375	0.70
(100)	Fe–NO	–2.91	1.656	–	1.197	1773	0.45
	Fe–ON	–1.33	–	1.792	1.186	1656	0.36
(111)	Fe–NO	–3.21	1.790	–	1.259	1575	0.64
	Fe–ON	–1.48	–	1.981	1.219	1568	0.45

TABLE 7.1: Adsorption energies and relevant bond distances of NO adsorbed on the (001), (011), (100) and (111) FeS surfaces. ∑q denotes the net charge gained by NO and υ(N−O) is the stretching vibrational frequency. The experimental gas phase N−O bond distance and stretching frequency are reported in bracket, ([a]Lide, 2007).

7.3.4 Adsorption of NO on FeS(011) surface

In contrast to the weak interactions of NO with the (001) surface, the NO molecule adsorbs quite strongly at the (011) surface, preferentially at top–Fe site. The sulfur sites are basically unreactive towards NO adsorption. The relaxed NO adsorption structures on the (011) surface are shown in Figure 7.3 (a–c). The lowest energy configuration was calculated to be the Fe–NO configuration (Figure 7.3a), with the NO molecule binding perpendicularly to a top–Fe atom releasing an adsorption of 2.87 eV. The interacting Fe−N bond distance and the N−O bond length are calculated at 1.199 Å and 1.664 Å respectively. The Fe–ON configuration (Figure 7.3b), is found to be up to 1.55 eV less favourable, relative to the Fe–NO configuration, and its N−O and Fe−O bond distances are calculated at 1.187 Å and 1.790 Å respectively. The stronger binding energy calculated for Fe−NO configuration at the FeS(011) surface is similar to the results reported on pyrite (100) surface, where the Fe–NO configuration was calculated to be 1.14 eV energetically more favourable than the Fe–ON configuration (Sacchi *et al.*, 2012). Our calculated adsorption energies for NO at the FeS(011) surface compares with those calculated on metallic Fe (111) surface by Chen *et al.*, 2010, (–1.11 to –2.77 eV) using DFT VASP calculations.

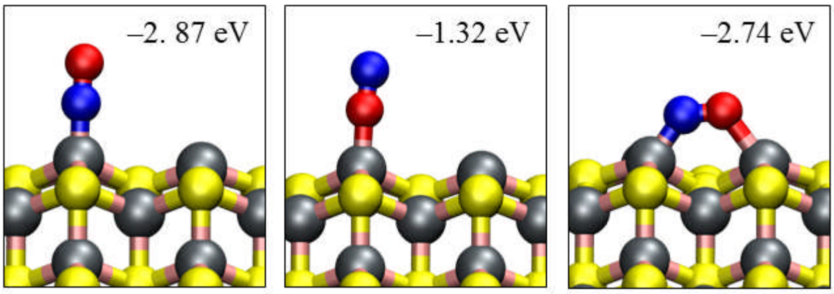

(a) Fe–NO (b) Fe–ON (c) Fe–NO–Fe

FIGURE 7.3: Side views of the optimized adsorption structures of NO on the (011) FeS surface.

We have also identified a stable side-on configuration where the NO binds parallel at the bridge site between two adjacent Fe atoms on the (011) surface *via* the N and O atoms (denoted by Fe–NO–Fe as shown in Figure 7.3c). This configuration is found to be only 0.13 eV less favourable than the most stable Fe–NO configuration and the N−O, N−Fe and O−Fe bond distances are calculated to be 1.245 Å, 1.688 Å and 2.130 Å respectively. In Table 7.1, a summary of the adsorption energies and the relevant bond distances for NO adsorbed on the (011) surface are presented. The stretched N−O bonds, particularly in the side-on Fe–NO–Fe configuration, suggest that NO might dissociate from this geometry but an attempt to cleave the N−O bond found this to be overall an endothermic process (ΔE= +0.60 eV) with an activation energy barrier of 1.16 eV. Another reaction path for NO dissociation was investigated, considering the most stable Fe–NO configuration as the starting point, but this dissociation reaction was also calculated to be endothermic (ΔE= +0.73 eV) overall and it has a very high activation energy barrier (4.12 eV), suggesting that NO will remain adsorbed molecularly on the (011) surface. The transition state for the dissociation of NO from the Fe–NO configuration on the pyrite (100) surface was found to possess a similarly high activation barrier of 5.44 eV (Sacchi *et al.*, 2012). The schematic illustration of the initial (IS), transition (TS) and final states (FS) of the dissociation of NO from the side-on Fe–NO–Fe configuration on the FeS(011) surface are shown in Figure 7.4

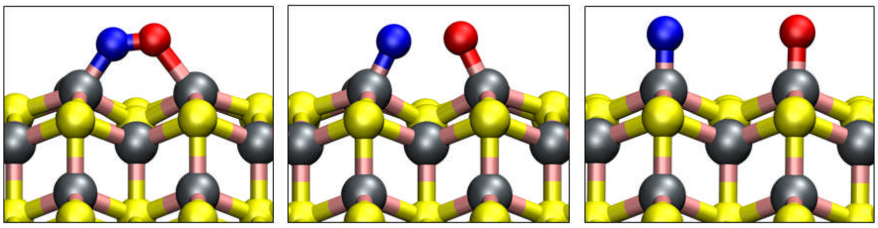
IS: E = 0.00 eV TS: E = 1.16 eV FS: E = 0.60 eV

FIGURE 7.4: The structures of the initial (IS), transition (IS), and final (FS) states of NO dissociation on FeS(111) surface. Energies are given relative to the IS state.

In agreement with the strong interaction of NO with the (011) surface, Bader population analysis on the adsorbed NO/FeS(011) systems reveal that the NO molecule draws significant charge from the interacting surface Fe atoms upon adsorption. When adsorbed in the Fe–NO, Fe–ON and Fe–NO–Fe configurations, the NO draws 0.45 e^-, 0.39 e^- and 0.70 e^- respectively, which causes elongation of the N–O bonds, as confirmed by calculated N–O stretching vibrational frequencies presented in Table 7.1. Further insight into local charge rearrangement within the NO/FeS(011) system was gained from the electron density difference iso-surfaces, obtained by subtracting from the charge density of the total adsorbate system the sum of the charge densities of the molecule and the clean surface (equation 7.3), calculated using the same geometry as the adsorbate system.

$$\Delta\rho = \rho FeS / NO_{(ads)} - (\rho FeS + \rho NO_{(gas)}) \tag{7.3}$$

The iso-surfaces of the electron density differences due to the adsorption of NO for the Fe–NO, Fe–ON, and Fe–NO–Fe configurations are displayed in Figure 7.5 (a–c).

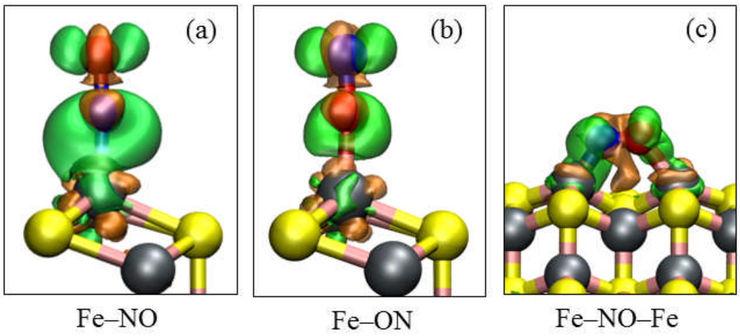

FIGURE 7.5: The electron density difference plots relative to the adsorbed NO, showing charge transfer in the regions between the NO and the surface Fe atoms upon adsorption on FeS(011). Green contours indicate electron density increase by 0.02 electrons/Å^3 and orange contours indicate electron density decrease by 0.02 electrons/Å^3.

From an inspection of the isosurface of charge density difference, it is clear that electron densities are depleted from Fe *d*–states and the NO internuclear axis region, but accumulate in the bonding region between NO and the surface Fe atoms, and on the NO molecule. The depletion of electron density from both the NO molecule and the surface Fe atoms shows that the interaction between NO and the surface corresponds to a donation and back-donation process (Blyholder, 1964), wherein the NO donate electron into the empty Fe *d*-orbitals and filled Fe *d*-orbitals back-donate into the 2pπ* orbitals of NO. The net charge accumulated on the adsorbed NO molecule as calculated from the Bader population analysis discussed above, however, suggests a stronger back-donation from filled Fe *d*-bands than the forward donation from the NO molecule.

7.3.5 Adsorption of NO on FeS(100) surface

The relaxed adsorption structures of NO on the (100) surface are shown in Figure 7.6 (a & b). No stable side-on configuration was found as the NO molecule flips back to the energetically most favoured Fe–NO configuration during geometry optimization. Similar to the (011) surface, the sulfur sites on the (100) surface remain unreactive towards NO adsorption compared to the Fe sites that are very reactive. The Fe–NO configuration is found to release an adsorption energy of –2.91 eV, whereas the Fe–ON configuration released an adsorption energy of 1.33 eV. In contrast to the perpendicularly adsorbed NO at the top–Fe sites on the (011) surface, the NO molecule is adsorbed in a tilted orientation on the (100) surface with the N−O bond forming an angle of ~60 ^{o} and ~41 ^{o} respectively with the surface normal in the Fe–NO and Fe–ON configurations.

Upon adsorption, the NO molecule draws charges of 0.45 e^{-} and 0.36 e^{-} from the interacting surface species in the Fe–NO and Fe–ON configurations respectively, which causes an elongation of the N–O bonds calculated at 1.197 Å for the Fe–NO configuration and 1.186 Å for the Fe–ON configuration, compared with the free unperturbed bond length of 1.160 Å. All the relevant interatomic bond distances and the stretching N–O vibrational frequencies for NO adsorption on the (100) surface are reported in Table 7.1. The dissociation of NO from the most stable Fe–NO configuration on the (100) surface was found to be both thermodynamically ($\Delta E = +0.71$ eV) and kinetically (energy barrier, $E_a = 4.02$ eV) unfavourable, which indicates that NO will remain molecularly chemisorbed on the (100) surface even at high temperatures.

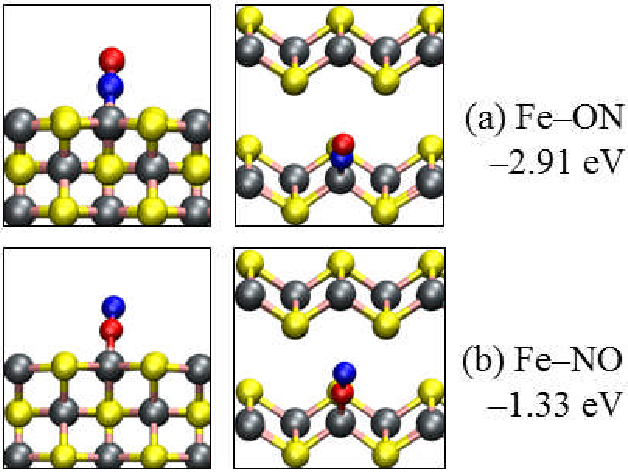

FIGURE 7.6: Side (left) and top (right) views of the optimized adsorption structures of NO on the (100) FeS surface.

7.3.6 Adsorption of NO on FeS(111) surface

The strongest surface–NO interaction was found on the (111) surface, which is the least stable surface among the four surfaces investigated. The lowest energy structure was calculated to be the Fe_2–NO configuration with the N atom bridging between adjacent Fe atoms as shown in Figure 7.7a, releasing an adsorption energy of 3.21 eV, *i.e.*, ~0.30 eV more favourable than the lowest energy structures on the (011) and (100) surfaces. The two Fe–N and N–O bond distances are calculated at 1.795 Å, 1.791 Å, and 1.209 Å respectively. When adsorbed *via* the oxygen atom, also preferentially at bridging Fe sites as shown in Figure 7.7b, the adsorption energy is calculated at –1.48 eV, *i.e.* 1.73 eV less stable than the most favoured Fe_2–NO structure. No stable side-on configuration was found on the (111) surface as the NO molecule flips back to the energetically most favoured Fe_2–NO configuration during geometry optimization.

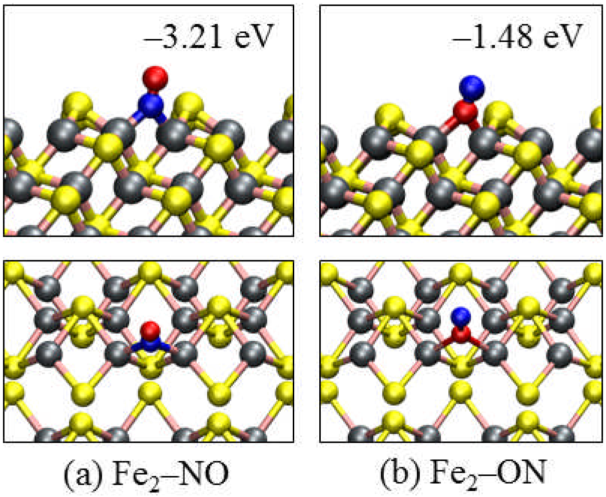

FIGURE 7.7: Side (top) and top (bottom) views of the optimized adsorption structures of NO on the (111) FeS surface.

The dissociation of NO from the most stable energy configuration (Fe_2–NO), leaves the N and O atoms adsorbed at bridge sites between two Fe atoms but, unlike on the (011) and (100) surfaces, the NO dissociation reaction on the (111) is exothermic ($\Delta E = -1.56$ eV). The calculated high activation energy barrier of 3.96 eV however, suggests that the dissociation might only occur at high temperatures. The structures of the initial, transition, and final states of the NO dissociation on the FeS(111) surface are shown in Figure 7.8.

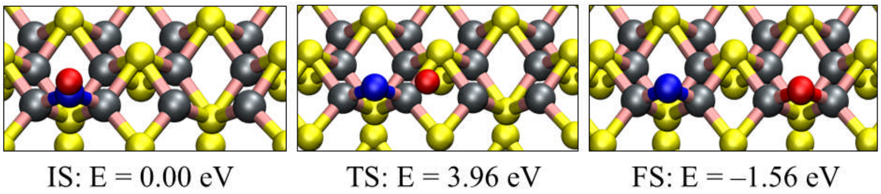

FIGURE 7.8: The structures of the initial (IS), transition (IS), and final (FS) states of NO dissociation on FeS(111) surface. Energies are given relative to the IS state.

The adsorption of the NO molecule on the (111) surface is characterized by significant charge transfer from the interacting surface species; the NO draws 0.64 e^{-} and 0.45 e^{-} from the surface when adsorbed in the Fe_2–NO and Fe_2–ON configurations respectively, consistent with covalent bonding. This effect causes an elongation of the N–O bonds as shown in Table 7.1, along with the stretching N–O vibrational frequencies. To gain further insight into the nature of bonding of NO with the (111) surface, we have plotted the electronic DOS of the lowest energy adsorption structure (Fe_2−NO), projected on the projected on orbitals of nitrogen and oxygen species and of the interacting surface Fe atoms (Figure 7.9). A comparison between the DOS of NO in the non-interacting state (Figure 7.9a) to the adsorbed state (Figure 7.7.b), reveal the disappearance of the NO–2π states at the Fermi level upon adsorption, which suggests a strong interaction between the adsorbate and the substrate Fe *d*-orbitals *via* mixing of this orbital.

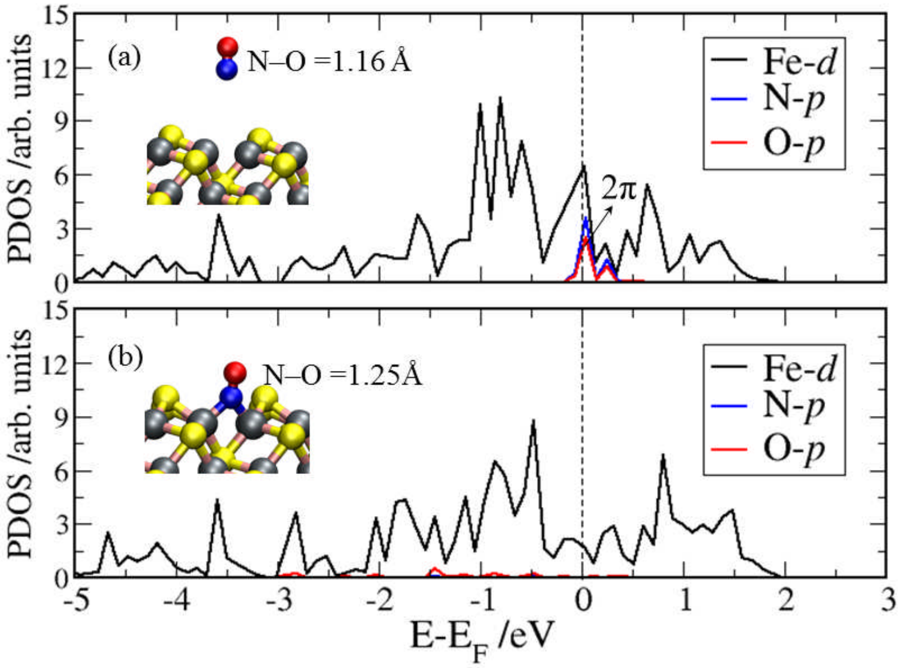

FIGURE 7.9: Projected density of states (PDOS) for NO adsorbed on FeS(111): (a) before interaction and (b) Fe_2−NO adsorption structure. The dashed line represents the Fermi level.

7.3.7 Adsorption and dissociation of NO_2

The optimized NO_2 adsorption structures with minimum energy on the (001), (011) and (100) and (111) FeS surfaces were calculated by considering four different initial adsorption configurations: *i.e.*, two bidentate configurations where the NO_2 binds *via* either two Fe−O bonds (denoted as Fe–ONO–Fe) or *via* one Fe−O bond and one Fe−N bonds (denoted as Fe–NOO–Fe) and two monodentate configurations in which the NO_2 binds to the surface *via* a single Fe−N bond (Fe–NO_2) or single Fe−O bond (Fe–ONO). We have also attempted adsorbing the NO_2 molecule at sulfur sites but found no stable chemisorbed S–NO_2 adsorption structure; the molecule always moves to a reactive Fe site during geometry optimization.

7.3.8 Adsorption of NO_2 on FeS(001) surface

Similar to the NO adsorption, the NO_2 molecule is found to undergo physisorption on the (001) surface, giving a weak interaction. The NO_2 molecule moved away from the different surface binding sites during geometry optimizations from all initial orientations. The optimized NO_2 adsorption geometries on the (001) surface are shown in Figure 7.10 (a–c), while the adsorption energies and relevant interatomic bond distances and angles are summarized in Table 7.2. The Fe–NO_2, Fe–ONO–Fe, and Fe–ONO configurations released adsorption energies of 0.23 eV, 0.26 eV, and 0.17 eV respectively. When we attempted to adsorb the NO_2 at a sulfur site (*i.e.*, S–NO_2), it relaxed to the Fe–NOO–Fe structure giving the same binding energy. Consistent with physisorption, we observed no charge transfers between the (001) surface and the NO_2 molecule upon adsorption and the N–O bond distances remained relatively unaffected.

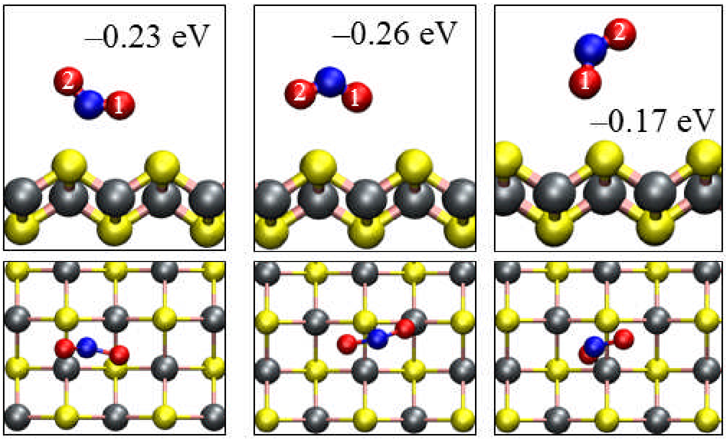

(a) Fe–NO$_2$ (c) Fe–ONO–Fe (c) Fe–ONO

FIGURE 7.10: Side (top) and top (bottom) views of the optimized adsorption structures of NO$_2$ on FeS(001) surface.

7.3.9 Adsorption and dissociation OF NO$_2$ on FeS(011)

Compared to the (001) surface, the NO$_2$ molecule is chemisorbed strongly on the (011) surface. The optimized NO$_2$ adsorption structures on the (011) surface are shown in Figure 7.11 (a–c) and their corresponding isosurfaces of the electron density difference are displayed in Figure 7.12 (d–f). The lowest energy structure is calculated to be the bidentate Fe−NOO−Fe structure (Figure 7.11a), releasing an adsorption energy of 2.67 eV, with calculated Fe–N and Fe–O bond distances of 1.927 Å and 1.953 Å respectively (Table 7.2). Bader population analysis indicates that the NO$_2$ molecule draws a charge 0.78 e$^-$ from the (011) surface upon adsorption, causing an elongation of the N−O bond distances calculated at 1.349 Å and 1.229 Å, compared with the free unperturbed bond length of 1.213 Å. Consistent with the elongated N–O bonds, we observe a significant reduction in the N–O stretching frequencies (Table 7.2) of the adsorbed NO$_2$ molecule compared to the gas phase NO$_2$ molecule.

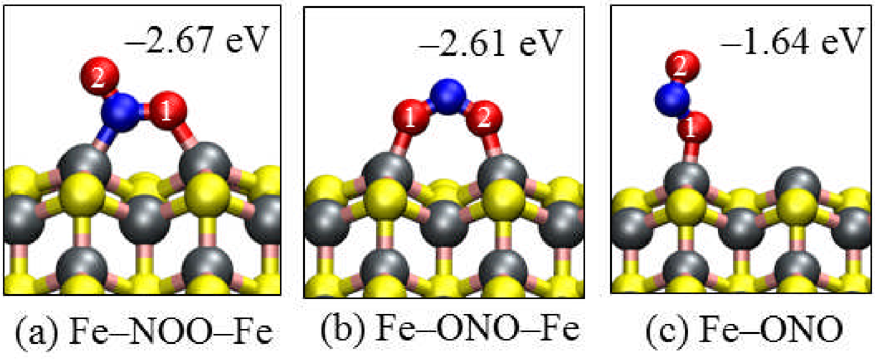

FIGURE 7.11: Side views of the optimized adsorption structures of NO_2 on the FeS(011) surface.

When the NO_2 molecule adsorbs *via* both oxygen atoms (*i.e.*, the bidentate Fe−ONO−Fe configuration as shown in Figure 7.11b, the adsorption energy is calculated to be –2.61 eV, *i.e.*, only 0.05 eV less than in the most favourable Fe−NOO−Fe structure. Bader population analysis indicates that a charge transfer of 0.71 e^- occurs from the surface to the NO_2 molecule, which causes structural changes in the molecule; the α(ONO) bond angle reduces from 133.8 ^{o} to 119.4 ^{o} and the two N−O bond distances are calculated at 1.289 Å and 1.286 Å, both suggesting an elongation of the N−O bonds relative to that of the free NO_2 molecule. The distances between the two oxygen atoms and the interacting surface Fe atoms (Fe–O) are 1.879 Å and 1.899 Å (the average value is reported in Table 7.2). The least stable configuration was calculated to be the monodentate oxygen (Fe−ONO) configuration (Figure 7.11c), which released an adsorption energy of 1.64 eV with an Fe–O bond distance of 1.874 Å. A charge of 0.51 e^- is transferred from the surface to the adsorbed NO_2 in this configuration which results in elongation of the N–O bonds calculated at 1.351 Å and 1.208 Å. No stable Fe−NO_2 configuration was obtained, as during energy minimization, it relaxes to the lowest energy structure (Fe−NOO−Fe).

Surface	Configuration	E_{ads} /eV	*d*(Fe−N) /Å	*d*(Fe−O) /Å	*d*(N−O_1) /Å	*d*(N−O_2) /Å	*α*(ONO) /^{o}	∑q /e^-	$υ_s$ /cm^{-1}	$υ_{as}$ /cm^{-1}	$υ_b$ /cm^{-1}
	NO_2 (g)	–	–	–	1.213	1.213	133.8^o	0.00	1331	1665	730
(001)	Fe–NOO–Fe	–0.23	3.707	3.853	1.224	1.221	130.7	0.00	1291	1606	721
	Fe–ONO–Fe	–0.26	–	3.827	1.226	1.226	131.5	0.00	1289	1618	718
	Fe–ONO	–0.17	–	3.901	1.225	1.218	131.3	0.00	1221	1616	722
(011)	Fe–NOO–Fe	–2.67	1.927	1.953	1.349	1.229	116.6	0.78	845	1455	716
	Fe–ONO–Fe	–2.61	–	1.889	1.289	1.286	119.4	0.71	1066	1088	713
	Fe–ONO	–1.64	–	1.874	1.351	1.208	113.8	0.51	798	1594	611
(100)	Fe–NOO–Fe	–2.73	1.924	1.950	1.362	1.228	116.7	0.80	847	1452	712
	Fe–ONO–Fe	–2.64	–	1.857	1.294	1.292	119.3	0.78	1050	1064	724
	Fe–ONO	–1.65	–	1.825	1.415	1.201	111.9	0.52	792	1591	604
(111)	Fe–NOO–Fe	–2.91	1.870	1.957	1.386	1.229	119.7	0.90	839	1398	719
	Fe–ONO–Fe	–2.69	–	1.978	1.271	1.270	116.0	0. 87	1048	1052	727
	Fe–ONO	–1.70	–	1.825	1.465	1.212	112.3	0.56	790	1588	612

TABLE 7.2: Adsorption energies and relevant bond distance and angles of NO_2 adsorbed on the (001), (011), (100) and (111) FeS surfaces. ∑q denotes the net charge gained by the NO_2 molecule upon adsorption. The experimental N−O bond distance and α(ONO) bond angel were reported at 1.197 Å and 134.1o respectively, and the symmetric stretch ($υ_s$), asymmetric stretch ($υ_{as}$) and the bending ($υ_b$) frequencies are reported at 1318, 1610, and 750 cm-1 respectively, (Lide, 2007).

An inspection of the iso-surfaces of NO_2 on the (011) surface in Figure 7.12 (a–c) shows significant charge redistribution within the NO_2–surface systems, which results in a net charge accumulation on the NO_2 molecule and in the bonding regions between NO_2 and the surface Fe atoms, and it is consistent with the formation of chemical bonds. The iso-surfaces reveal that some charge depletion occurs from Fe *d*–states and the adsorbed NO_2 molecule, which suggests donation of electrons from the NO_2 into the empty Fe *d*-orbital and a back-donation from the filled Fe *d*-orbitals into the empty antibonding orbitals of NO_2. The calculated net charge accumulation on the adsorbed NO_2 molecule as estimated from our Bader population analysis indicates stronger back-donation from the interacting surface Fe *d*-orbitals to the NO_2 than the forward donation from the NO_2 to the surface.

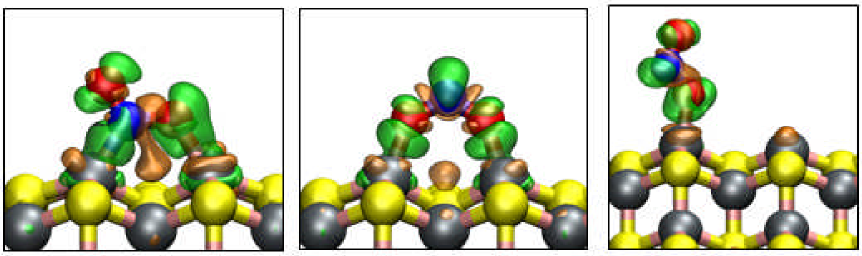
(a) Fe–NOO–Fe (b) Fe–ONO–Fe (c) Fe–ONO

FIGURE 7.12: The electron density difference plots relative to the adsorbed NO, showing charge transfer in the regions between the NO_2 and the surface Fe atoms upon adsorption on the FeS(011). Green contours indicate electron density increase by 0.02 electrons/Å^3 and orange contours indicate electron density decrease by 0.02 electrons/Å^3.

The reaction profile for NO_2 dissociation on the (011) surface starting from the most stable bidentate Fe−NOO−Fe configuration is shown in Figure 7.13. The complete dissociation proceeds in two steps: step 1 represents the cleavage of the first N–O bond to produce NO and O fragments adsorbed at adjacent top–Fe sites (R1), and step 2 represents a further dissociation of the second N–O bond to produce either

(N* and O_2*), denoted R2–A, or adsorbed atomic species (*i.e.*, N* and two O*), denoted R2–B. The cleavage of the first N–O bond (R1) was found to be exothermic (ΔE= –0.76 eV) and has a low activation energy barrier of 0.32 eV, which suggests that NO_2 will readily dissociate into NO* and O* species on the (011) surface. Further dissociation of the second N–O bond *via* reactions R2–A and R2–B is, however, found to be both thermodynamically and kinetically unfavourable. Reactions R2–A and R2–B are respectively endothermic by 2.63 eV and 0.93 eV, and have high activation energy barriers calculated at 5.12 eV and 4.22 eV respectively, which suggests that complete dissociation of NO_2 on the (011) surface is unlikely to occur even at high temperatures.

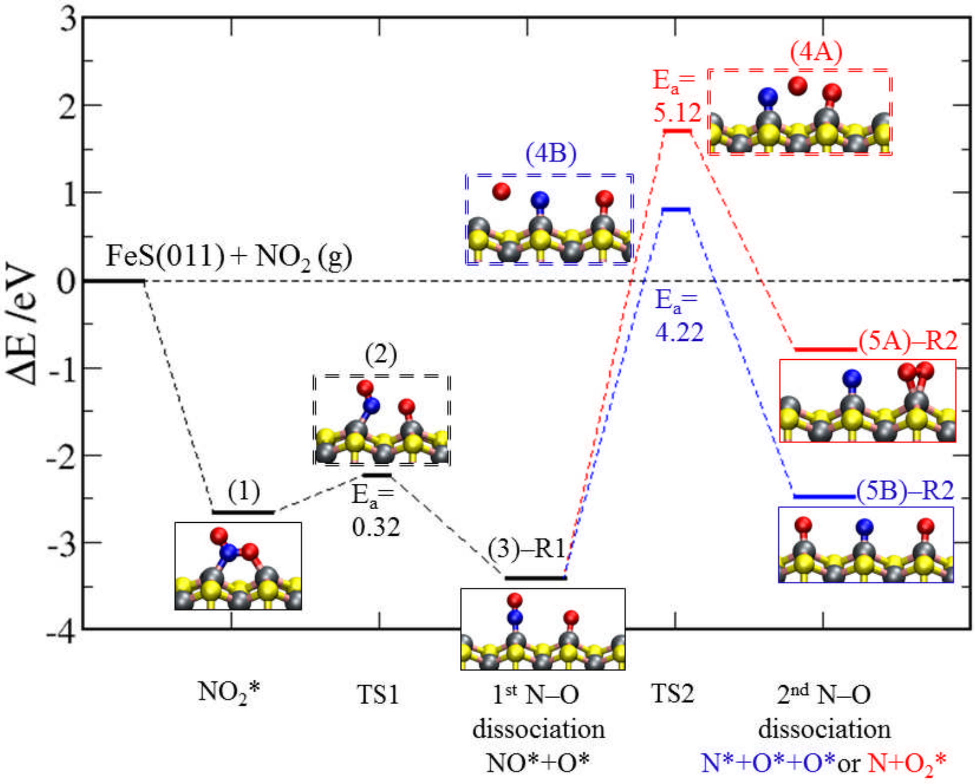

FIGURE 7.13: Reaction profile for NO_2 dissociation on FeS(011) surface. The insets show schematic representation of the steady states, numbered in accordance with the relevant stage in the overall reaction. (Colour scheme: Fe = grey, S = yellow, N = blue and O = red). Note the transition states are framed in dashed lines and the asterisks (*) denote the adsorbed species.

7.3.10 Adsorption and dissociation of NO_2 on FeS(100)

The relaxed NO_2 adsorption structures on the (100) surface are shown in Figure 7.14 (a & b). As on the (011) surface, the lowest energy configuration on the (100) surface was calculated to be a bidentate Fe−NOO−Fe (Figure 7.14a), which released an adsorption energy of 2.73 eV, *i.e.*, only 0.06 eV more favourable than the lowest energy structure on the (011) surface. Bader population analysis indicates that the NO_2 molecule draws 0.80 e^- from the surface, which causes an elongation of the two N−O bonds (1.362 Å, 1.228 Å) and a reduction in the α(ONO) bond angle (133.8 ^{o} → 116.7 ^{o}) as shown in Table 7.2. The other bidentate configuration with two Fe−O bonds (Fe−ONO−Fe), Figure 7.14b, is only 0.09 eV less favourable than the most stable bidentate Fe−NOO−Fe configuration, while the monodentate Fe−ONO configurations is less favourable by up to 1.03 eV relative to the lowest energy bidentate Fe−NOO−Fe configuration.

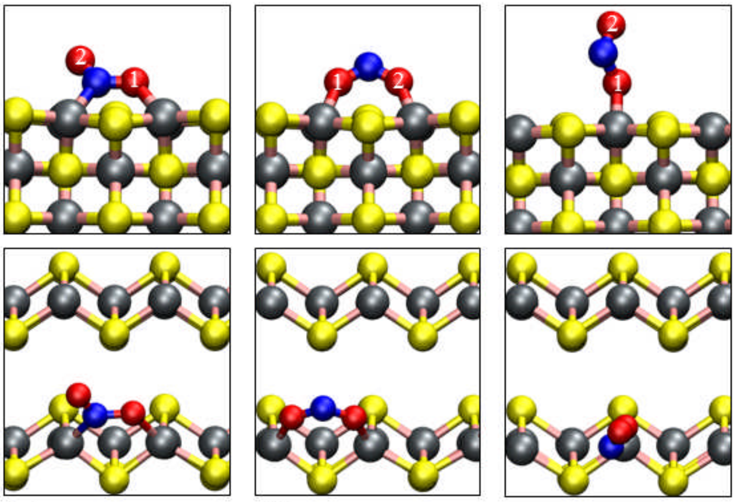

(a) Fe–NOO–Fe
–2.73 eV

(b) Fe–ONO–Fe
–2.64 eV

(c) Fe–ONO
–1.65 eV

FIGURE 7.14: Side (top) and top (bottom) views of the optimized adsorption structures of NO_2 on the FeS(100) surfaces.

The close comparison between the binding energies of NO_2 on the (100) and (011) surfaces is consistent with the small difference in their calculated surface energies; 1.04 J m^{-2} for the (100) and 0.95 J m^{-2} for the (011) surfaces and suggest that both surfaces have similar reactivity toward NO_2 activation. The reaction profile for the dissociation of NO_2 from the most stable bidentate Fe−NOO−Fe configuration on the (100) surface is shown Figure 7.15. The dissociation of the first N–O bond produces NO and O that are adsorbed at adjacent top–Fe sites and the reaction is exothermic (ΔE = –0.75 eV) with low activation barrier of 0.30 eV, which is close to the barrier for the dissociation of the first N–O on the (011) surface (0.32 eV), and therefore suggests that NO_2 will also readily dissociate into NO* and O* fragments on the (100) surface.

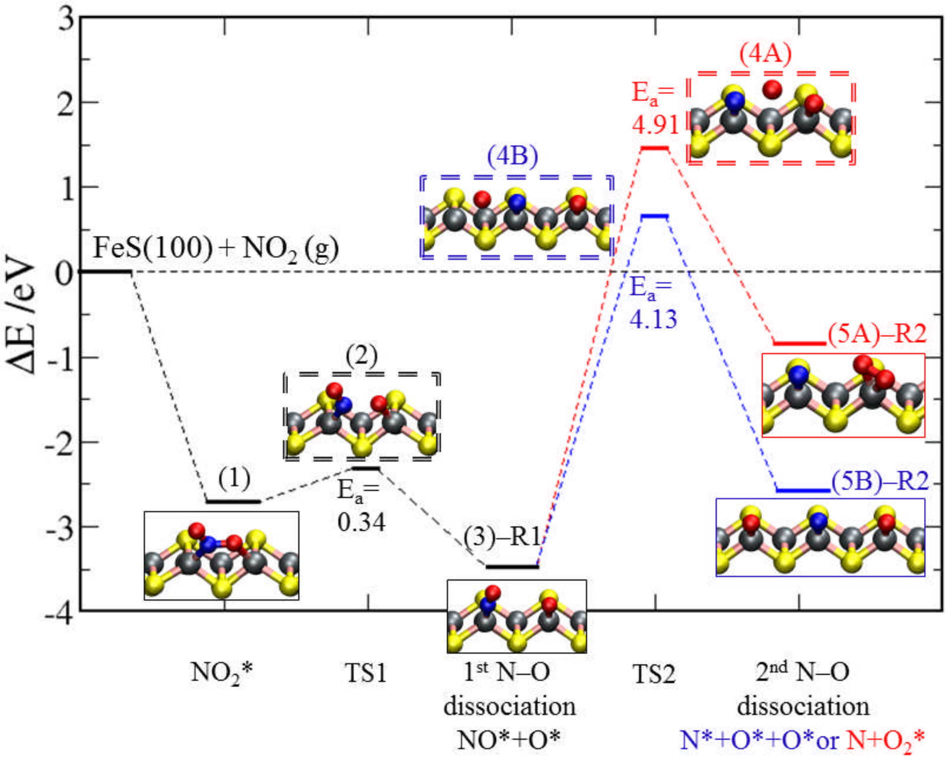

FIGURE 7.15: Reaction profile for NO_2 dissociation on FeS(100) surface. The insets show schematic representation of the steady states, numbered in accordance with the relevant stage in the overall reaction. (Colour scheme: Fe = grey, S = yellow, N = blue and O = red). Note the transition states are framed in dashed lines and the asterisks (*) denote the adsorbed species.

Further dissociation of the second N–O bond to *via* reactions R2–A or R2–B is found to be endothermic relative to the relaxed structure of the first N–O bond cleavage with high activation energy barriers. The (ΔE, E_a) for reactions R2–A and R2–B are (2.61 eV, 4.91 eV) and (0.89 eV, 4.13 eV) respectively, which again suggests that complete dissociation of NO_2 on the (100) surface is unlikely to occur even at high temperatures.

7.3.11 Adsorption and dissociation of NO_2 on FeS(111)

The strongest NO_2–FeS interaction was observed on the (111) surface, similar to the NO adsorption. The lowest energy structure (Fe−NOO−Fe), shown in Figure 7.16a, released an adsorption energy of 2.91 eV with the Fe–N and Fe–O bond distances calculated at 1.870 Å and 1.957 Å. The highest charge transfer (0.90 e^-) from FeS surface to the adsorbed NO_2 molecule is found in this configuration, which causes an elongation of the N−O bond distances calculated at 1.386 Å and 1.229 Å, compared with the free unperturbed bond length of 1.213 Å (Table 7.2). The α(ONO) bond angle is also reduced to 119.7 ^{o} compared to the free NO_2 bond angle of 133.8 ^{o}. The other bidentate configuration with two Fe−O bonds (Fe−ONO−Fe), Figure 7.16b, released an adsorption energy of 2.69 eV, *i.e.*, 0.22 eV less favourable than the most stable Fe−NOO−Fe configuration.

The least stable adsorption structure on the (111) was calculated to be a monodentate Fe–O configuration (*i.e.*, Fe−ONO, Figure 7.16c), which released an adsorption energy of 1.70 eV. Bader population analysis indicates that a charge transfer of 0.87 e^- and 0.56 e^- occurs from the surface to the NO_2 molecule when adsorbed in the bidentate Fe−ONO−Fe and monodentate Fe−ONO configurations respectively.

The charge gained by the NO_2 molecule causes weakening of its N–O bonds as they are elongated relative to the free N–O bonds distances (Table 7.2).

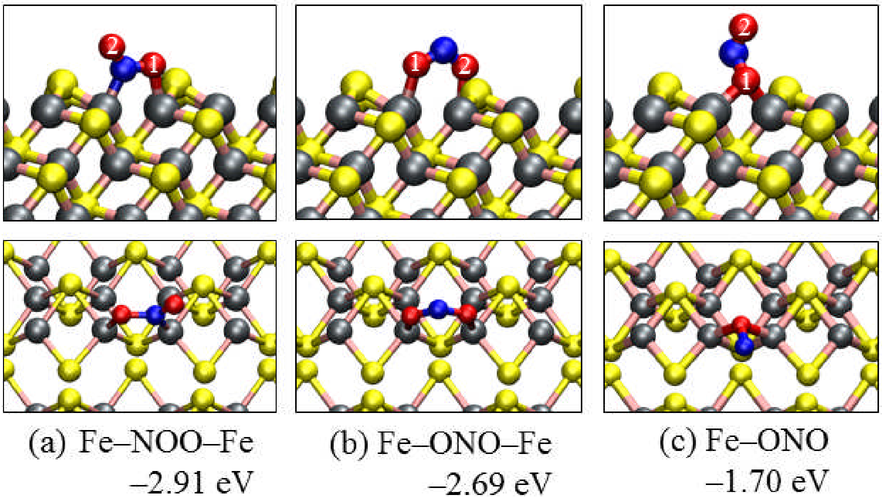

(a) Fe–NOO–Fe –2.91 eV (b) Fe–ONO–Fe –2.69 eV (c) Fe–ONO –1.70 eV

FIGURE 7.16: Side (top) and top (bottom) views of the optimized adsorption structures of NO_2 on the FeS(111) FeS surface.

To gain further insight into the strong interaction of the NO_2 with the FeS(111) surfaces, we have plotted the electronic DOS of the strongest surface–NO_2 system, projected on orbitals of nitrogen and oxygen species and of the interacting surface Fe substrate. Before the adsorption of NO_2 (Figure 7.17a), the projection on the N and O atoms and on the surface Fe atoms show states at the Fermi level, which suggests that electron transfer can occur between the surface atoms Fe atoms and the NO_2 molecule. Upon adsorption (Figure 7.17b), the strong hybridization between the O and N *p*-orbitals and the surface Fe *d*-orbitals causes the abrupt disappearance of the molecule's states at the Fermi level, which is consistent with the strong interactions and significant calculated charge transfer. We also note broadening of the N and O *p*–states at 1.0 eV upon adsorption, again suggesting their strong interaction with the surface Fe *d*–orbitals.

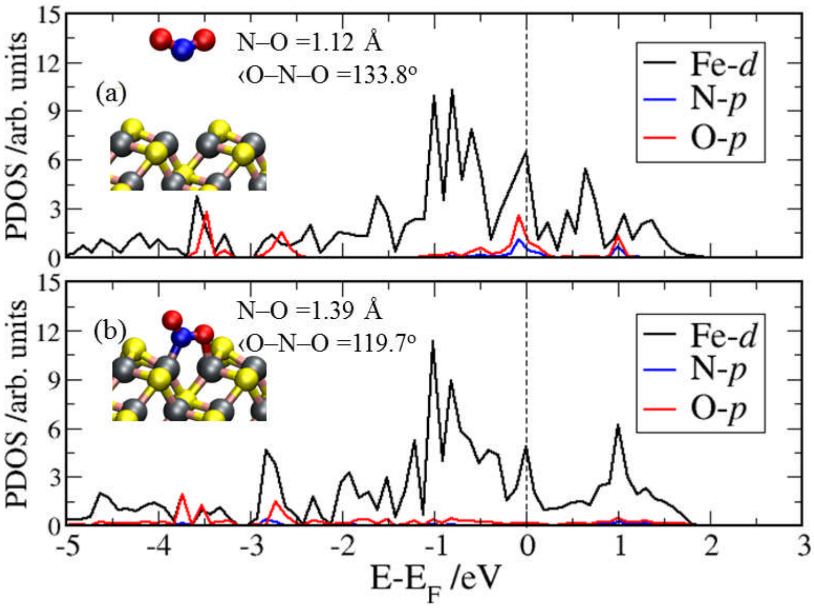

FIGURE 7.17: Projected density of states (PDOS) for NO_2 adsorbed on FeS(111): (a) before interaction and (b) Fe−NOO−Fe adsorption structure. The dashed line represents the Fermi level.

The reaction profile for the dissociation of NO_2 from the most stable Fe−NOO−Fe configuration on the (111) surface is shown in Figure 7.18. The dissociation of the first N–O bond leaves the NO and O fragments adsorbed at bridge sites between two Fe atoms and the reaction is found to be highly exothermic (ΔE = −3.54 eV), but the total reaction barrier was calculated at 1.96 eV. The higher activation barrier for the dissociation of the first N−O bond on the (111) compared to the (011) and (100) surfaces can be attributed to the additional energy required to move the dissociated products from the top–Fe site to the most stable bridging–Fe sites.

Dissociation of the second N−O bond towards the production of N* and two O* was also found to be exothermic (ΔE = –1.45 eV) with an activation energy barrier of 3.80 eV, while the alternative path to produce N* and O_2* was found to be endothermic (ΔE = +2.78 eV) with a higher activation energy barrier of 4.35 eV. Although the thermodynamics favour the formation N* and two O*, the calculated high activation energy barrier suggests that this might only be attainable at higher temperatures. The unfavourable thermodynamics and kinetics for the production of N* and O_2*, however, indicates that this reaction is unlikely to occur at all.

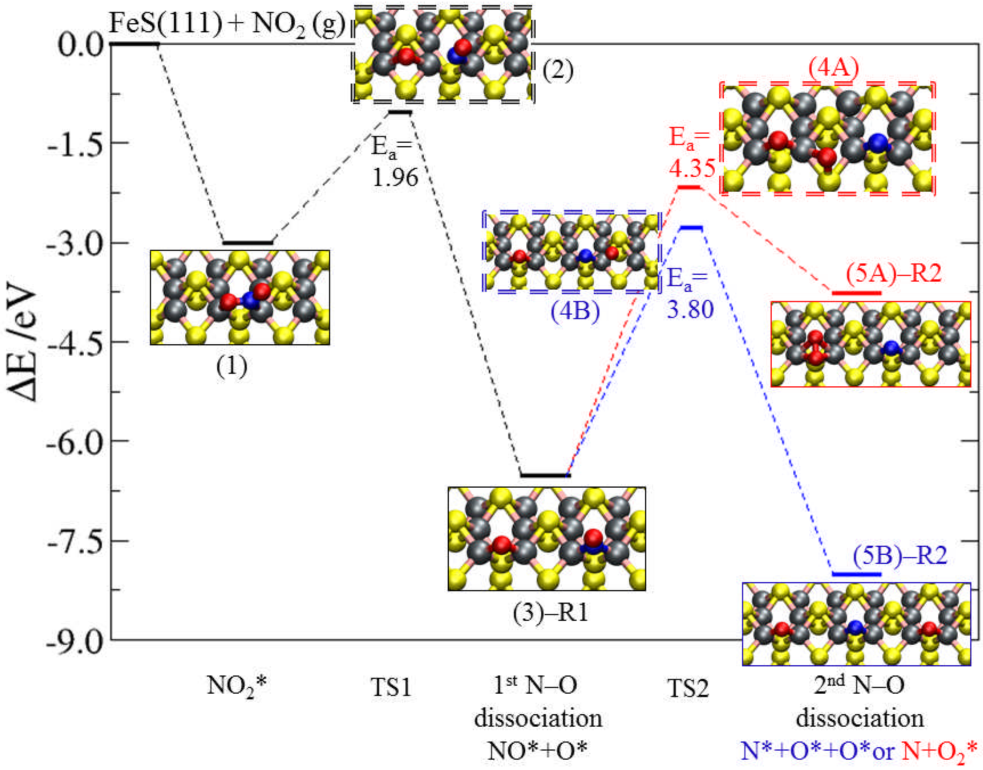

FIGURE 7.18: Reaction profile for NO_2 dissociation on FeS (111) surface. The insets show schematic representation of the steady states, numbered in accordance with the relevant stage in the overall reaction. (Colour scheme: Fe = grey, S = yellow, N = blue and O = red). Note the transition states are framed in dashed lines and the asterisks (*) denote the adsorbed species.

7.4 Summary and conclusions

In this chapter, we have modelled the adsorption and dissociation reactions of NO and NO_2 on the (001), (011), (100) and (111) surfaces of mackinawite using DFT-D2 calculations. The energetically most stable (001) was found to show the least reactivity towards the NO_x molecules, as only weak interactions occur at any of the surface sites. Compared to the (001), the NO_x gases adsorb relatively strongly on the less stable (011), (100) and (111) surfaces, preferentially at Fe sites, exhibiting a variety of adsorption geometries, with the most favourable for NO being the monodentate Fe−NO configuration, whereas NO_2 is calculated to form a bidentate Fe−NOO−Fe configuration. The strong interactions of the NO_x species on these is characterised by significant electron transfer from the interacting surface species to adsorbates, which causes weakening of the N–O bonds particularly the surface-bound N–O bonds in the case of NO_2 as they are elongated relative to the free unperturbed NO_x bond lengths. Stretching N−O vibrational frequencies of the adsorbed NO_x molecules show significant reduction relative to that of the gas phase molecules, confirming the N−O bonds are significantly activated upon adsorption.

Comparing the results obtained on the mackinawite surfaces to those obtained at the pyrite (100) surface (Sacchi *et al.*, 2012), it is obvious that the NO_x species interact more strongly with mackinawite surfaces than the pyrite (100) surface, which indicates that mackinawite surfaces are more reactive towards NO_x adsorption and activation than the pyrite (100) surface. The stronger interaction of the NO_x species with the mackinawite surfaces compared to the pyrite (100) surface can be rationalized by considering the shorter Fe–N and Fe–O bond distances calculated on the mackinawite surfaces compared to the pyrite surfaces. The magnitude of our calculated adsorption energies and interatomic Fe–N and Fe–O bond distances for the NO_x species on the mackinawite surfaces however, compares with those reported on the metallic Fe(111) surface (Chen *et al.*, 2010). Similar to the adsorption characteristics calculated on the mackinawite surfaces, adsorption of the NO_x species on the Fe (111) surface was shown to be characterized with significant charge transfer from the interacting Fe atom to the NO_x species (0.72 to 1.19 e^- for NO_2), which gave rise to the stronger binding and larger distortion in the N−O bonds distances observed.

The calculated reaction profiles for the dissociation of NO_2 show that the (011), (100) and the (111) surfaces exhibit considerable catalytic activity toward the cleavage of the first N–O bond to produce NO* and O* fragments, with favourable thermodynamics and kinetics. The calculated high activation energy barriers for further dissociation of the second N–O bond to produce either (N* and O_2*) or (N* and two O*), however, suggest that complete dissociate NO_2 is not likely to occur on (011) and (100) surface but could occur on (111) mackinawite surface at high temperatures and pressures. This information about the reaction mechanism, the catalytic activity of the major surfaces, and the importance of the surface structure would otherwise be difficult to obtain with experimental measurements, indicating that periodic DFT calculations might play a vital role in the rational design of improved catalytic FeS surfaces for the adsorption and dissociation of environmentally important NO_x molecules.

Bibliography

- Abdelhady A. L.; Malik M. A.; O’Brien P.; Tuna F.; *J. Phys. Chem. C*, **116**, 2253 (2012)
- Akhtar M.; Akhter J.; Malik M. A.; O’Brien P.; Tuna F.; Raftery J.; Helliwell M.; *J. Mater. Chem.*, **21**, 9737 (2011)
- Bader R.F.W.; *Atoms in Molecules –A quantum theory, Oxford University Press, New York*, **1990**
- Banse B. A.; Koel B. E.; *Surf. Sci.*, **232**, 275 (1990)

- Bare S. R.; Griffiths K.; Lennard W. N.; Tang H. T.; *Surf. Sci.*, **342**, 185 (1995)
- Beckendorf M.; Katter U. J.; Schlienz H.; Freund H. J.; *J. Phys. Chem.*, **5**, 5471 (1993)
- Bi Y.; Yuan Y.; Exstrom C. L.; Darveau S. A.; Huang J.; *Nano Lett.*, **11**, 4953 (2011)
- Blöchl E.; Keller M.; Wächtershäuser G.; Stetter K. O.; *Proc. Natl. Acad. Sci. U.S.A.*, **89**, 8117 (1992)
- Blöchl P. E.; *Phys. Rev. B*, **50**, 17953 (1994)
- Blyholder G.; *J. Phys. Chem.*, **68**, 2772 (1964)
- Bartram M. E.; Koel B. E., *Surf. Sci.*, **213**, 137 (1989)
- Bartram M. E.; Windham R. G.; Koel B. E.; *Surf. Sci.*, **184**, 57 (1987)
- Bartram M. E.; Windham R. G.; Koel B. E.; *Langmuir*, **4**, 240 (1988)
- Branda M. M.; Valentin C. D.; Pacchioni G.; *J. Phys. Chem. B*, **108**, 4752 (2004)
- Breedon M.; Spencer M. J. S.; Yarovsky I.; *Surface Science*, **603**, 3389 2009)
- Brown W. A.; Gardner P.; King D. A.; *Surf. Sci.*, **330**, 41 (1995)
- Brown W. A.; King D. A.; *J. Phys. Chem. B*, **104**, 2578 (2000)
- Burch R.; Breen J. P.; Meunier F. C.; *Applied Catalysis B: Environmental*, **39**, 283-303 (2002)
- Chen H. L.; Wu S. Y.; Chen H. T.; Chang J. G.; Ju S. P.; Tsai C.; Hsu L. C.; *Langmuir*, **26**, 7157 (2010)
- Cody G. D.; Boctor N. Z.; Filley T. R.; Hazen R. M.; Scott J. H.; A. Sharma and H. S. Yoder Jr., *Science*, **289**, 1337 (2000)
- D.R. Lide, *Physical Constants of Organic Compounds, CRC Handbook of Chemistry and Physics, Taylor and Francis, Boca Raton, FL*, (2007)
- Dahlgren D.; Hemminger J. C.; *Surf. Sci.* **123**, 739 (1982)

- Ennaoui A.; Fiechter S.; Jaegermann W.; Tributsch H.; *J. Electrochem. Soc.* **133**, 97 (1986)
- Epling W. S.; Campbell L. E.; Yezerets A.; Currier N. W.; Parks J. E.; *Catal.Rev. Sci. Eng*., **46**, 163 (2004)
- Geng B.; Liu X.; Ma J.; Du Q.; *Mater. Sci. Eng., B*, **145**, 17 (2007)
- Grimme S.; *Journal of Computational Chemistry*, **27**, 1787 (2006)
- Haneda M.; Kintaichi Y.; Hamada H.; *Appl. Catal. B*, **31**, 251 (2001)
- He H.; Yu Y.; *Catal. Today*, **100**, 37 (2005)
- Hellman A.; Panas I.; Grönbeck H.; *J. Chem. Phys*., **128**, 104704 (2008)
- Henkelman G.; Arnaldsson A.; Jonsson H., *Comput. Mater. Sci*., **36**, 354 (2006).
- Hinnemann B.; Moses P. G.; Bonde J.; Jorgensen K. P.; Nielsen J. H.; Horch S.; Chorkendorff I.; Norskov J. K.; *J. Am. Chem. Soc.*, **127**, 5308 (2005)
- Jirsak T.; Dvorak J.; Rodriguez J. A.; *Surf. Sci*., **436**, L683 (1999)
- Joo J.; Na H. B.; Yu T.; Yu J. H.; Kim Y. W.; Wu F.; Zhang J. Z.; Hyeon T.; *J. Am. Chem. Soc*., **125**, 11100 (2003)
- Kresse G.; and Hafner J.; *Phys. Rev. B*, **48**, 13115 (1993)
- Kresse G.; Hafner J.; *J. Phys. Condens. Matter*, **6**, 8245 (1994)
- Kresse G.; Furthmuller J.; *Phys. Rev. B*, **54**, 11169 (1996)
- Kresse G.; Joubert D.; *Phys. Rev. B.*, **59**, 1758 (1999)
- Lauritse J. V.; Kibsgaard J.; Olesen G. H.; Moses P. G.; Hinnemann B.; Helveg S.; Nørskov J. K.; Clausenc B. S.; Topsøe H.; Besenbacher E. L. F.; *Journal of Catalysis*, , **249**, 220 (2007)
- Liu G.; Gao P-X.; *Catal. Sci. Technol.*, **1**, 552 (2011)
- Liu Z. M.; Woo S. I.; *Catal. Rev*., **48**, 43 (2006)
- Liu Z. M.; Hao J. M.; Fu L. X.; Zhu T. L.; Li J. H.; Cui X. Y.; *Appl. Catal. B*, **48**, 37 (2004)

- Liu Z.; Ma L.; Junaid A. S. M.; *J. Phys. Chem. C*, **114**, 10 (2010)
- Liu Z. M.; Oh K. S.; Woo S. I.; *Catal. Lett.*, **106**, 35 (2006)
- Mills G.; Jónsson H.; Schenter G. K.; *Surf. Sci.*, **324**, 305 (1995)
- Moses P. G.; Mortensen J. J.; Lundqvist B. I.; Nørskov J. K.; *J. Chem. Phys.*, **130**, 104709 (2009)
- Moses P. G.; Hinnemann B.; Topsøe H.; Nørskov J. K.; *Journal of Catalysis,* **248**, 188 (2007)
- Perdew J. P.; Chevary J. A.; Vosko S. H.; Jackson K. A.; Pederson M. R.; Singh D. J.; Fiolhais C.; *Phys. Rev. B*, **46**, 6671 (1992)
- Polzonetti G.; Alnot P.; Brundle C. R.; *Surf. Sci*., **238**, 226 (1990)
- Puthussery J.; Seefeld S.; Berry N.; Gibbs M.; Law M.*; J. Am. Chem. Soc.*, **133**, 716 (2011)
- Rodriguez J. A.; Jirsak T.; Liu G.; J. Hrbek, J. Dvorak and A. Maiti, *J. Am. Chem. Soc.*, **123**, 9597 (2001)
- Sacchi M.; Galbraith M. C. E.; Jenkins S. J.; *Phys. Chem. Chem. Phys*., **14**, 3627 (2012)
- Segner J.; Vielhaber W.; Ertl G. Isr.; *J. Chem.* **22**, 375 (1982)
- Schwalke U.; Parmeter J. E.; Weinberg W. H.; *J. Chem. Phys*., **84**, 4036 (1986a)
- Schwalke U.; Parmeter J. E.; Weinberg W. H.; *Surf. Sci.*, **178**, 625 (1986b)
- Sorescu D. C.; Rusu C. N.; Jr.Yates J. T.; *J. Phys. Chem. B*, **104**, 4408 (2000)
- Topsøe N-Y.; Tuxen A.;, Besenbacher F.;, Topsøe H.;, *Journal of Catalysis* **279** 337 (2011)
- U. S. Environmental Protection Agency. Nitrogen Oxides (NO_x), Why and How They Are Controlled*.* *Report EPA-456/F-99-006R*, (1999)
- Wächtershäuser G.; *Biophys. Molec. Biol*., **58**, 85 (1992)

- Wang J.; Koel B. E.; *J. Phys. Chem. A*, **102**, 8573 (1998)
- Wang J.; Voss M. R.; Busse H.; Koel B. E.; *J. Phys. Chem. B*, **102**, 4693 (1998)
- Westerberg B.; Fridell E. J.; *Mol. Catal. A Chem*., 165, 249 (2001)
- Wickham D. T.; Banse B. A.; Koel B. E.; *Surf. Sci*., **243**, 83 (1991)
- Wickham D. T.; Banse B. A.; Koel B. E.; *Catal. Lett*., **6**, 163 (1990)
- Wolthers M.; van der Gaast S. J; Rickard D.; *Am. Mineral*, **88**, 2007 (2003)
- Wu B.; Song H.; Zhou J; Chen X.; *Chem. Commun*., **47**, 8653 (2011)

Chapter 8

Summary, conclusions and future works

In this thesis, we have presented a comprehensive computational study of the bulk and surface structures of hematite (α-Fe_2O_3) and mackinawite (tetragonal FeS), and subsequent adsorption mechanisms of benzene on hematite; arsenious acid, methylamine and nitrogen oxides on mackinawite low-index surfaces, using a state-of-the-art methodology based on the density functional theory techniques.

In the first part of the thesis, we have modelled the interactions of a single benzene molecule with the (0001) and $(01\bar{1}2)$ surfaces of hematite under vacuum conditions using the Hubbard corrected density functional theory (DFT–GGA+U) calculations. Hematite is correctly described as a charge-transfer insulator, in agreement with the spectroscopic evidence when the optimized value for the U = 5 eV is employed. Without the inclusion of the U correction term, the positions of the iron 3*d*-orbitals in relation to the oxygen 2*p* states was incorrectly predicted, characterizing the α-Fe_2O_3 as a *d-d* Mott-Hubbard insulator. Energy minimization calculations of the benzene-hematite surface adsorption complexes show that the benzene molecule interacts more strongly with the $(01\bar{1}2)$ surface than the (0001), preferentially with its molecular plane parallel to the surface planes. The nature of benzene interactions with the hematite surfaces is characterized mainly by cation-π interactions between the π-electrons of benzene ring and d-orbitals, and van der Waals interactions are found to play important role in stabilizing the benzene molecule at the surface. The calculated binding energies in the range of 0.28−1.52 eV is significant, indicating that the hematite surfaces play an important role in the retention of aromatic hydrocarbons in soils and sediments. Although these results provides fundamental insight into the interactions of a single benzene molecule with hematite surfaces under vacuum conditions, further investigations which includes the effects of water on the sorption behaviour is needed to provide a complete description and an improve our understanding of the mechanisms of aromatic hydrocarbons by hematite. Under aqueous conditions, the benzene molecule will have to compete with water molecules for the active binding sites on the mineral surface and this may significantly affect the energetics and sorption geometries. Our calculated interatomic distances for the adsorption of isolated benzene molecule on the hematite surface under vacuum conditions in this thesis could, however, serve towards the development of reliable forcefields that can be employed in classical MD simulations to simulate complex systems, including single and poly-aromatic hydrocarbons and the effect of water, which will provide a more realistic description of the hematite-water-benzene system.

The second part of the thesis which spans chapters 4−7, presents the results of the characterization of the bulk properties, structures, stabilities and reactivity of the low-index surface mackinawite (FeS) using dispersion corrected density functional theory within the scheme proposed by the Grimme (DFT-D2). We demonstrate that the inclusion of van der Waals dispersive interaction sensibly improves the prediction of interlayer separation distance in FeS, in good agreement with experimental data. The effect of interstitial impurity atoms in the interlayer sites on the structure and properties of FeS is also investigated, and it is found that these contribute considerably to the mechanical stability of the FeS structure by replacing the weak dispersive forces between layers with chemically bonded interactions between the interstitial metal dopants and the S and Fe_{net} atoms.

We show from geometry relaxation calculations on the low- index FeS surfaces that, the (001) surface terminated by sulfur atoms is by far the most energetically stable surface of mackinawite, in agreement with selected areas electron diffraction (SAED) analyses results on FeS nanocrystals (both freeze-dried and precipitated mackinawite), (Ohfuji & Rickard, 2006). The simulated crystal morphology of FeS which is based on the calculated surface energies also shows excellent agreement with the crystals grown by Ohfuji and Rickard (2006), who described thin and tabular crystals from their high resolution transmission electron microscope (HRTEM) examination of FeS aggregates. The large area of the (001) surface reflections and the well-define corner and edges of the FeS crystal suggests potential high reactivity of mackinawite.

As an extension the surface study, the sorption mechanism of arsenious acid ($As(OH)_3$) on the low-index surfaces of mackinawite have been studied. The structures of $As(OH)_3$ adsorption complexes on mackinawite surfaces have characterized, where bidentate adsorption complexes (Fe−OO−Fe and Fe−AsO−Fe) are generally found to be energetically more favourable than the monodentate complexes (Fe−O and Fe−As). The strongest $As(OH)_3$-surface interaction was obtained at the (111) surface, where the molecule interacts with the surface *via* two O–Fe bonds (Fe−OO−Fe complex). The calculated long As–Fe (3.031−3.314 Å) and

As–S (3.397−3.752 Å) interatomic distances for the most stable bidentate adsorption complexes clearly suggest an outer-sphere complexation with respect to the As atom at the mackinawite surfaces, in agreement with the experimental observation. Although the results presented here already show a good agreement with experimental observations, future theoretical extension to this work could incorporate the effect of water and surface defects in order to provide a complete understanding of the mechanisms of arsenic retention by iron sulfides.

Next, the growth modifying properties of methylamine, an amine capping agent used in the synthesis of iron sulfides have been modelled by its direct adsorption of the low-index FeS surfaces. The methylamine molecule is shown to interact very weakly with the energetically most stable (001) surface but adsorb relatively strongly on the less stable (011), (100) and (111) surfaces preferentially at Fe sites *via* its lone-pair of electrons located on the N atom. The differences in the strengths of interactions of methylamine with the various surfaces indicate the selectivity of the methylamine functional group towards capping the different FeS surfaces. The stronger binding of methylamine to the (011), (100) and (111) surfaces rather than the (001) plane suggest that these surfaces should become more prominent in the crystal morphology in the presence of methylamine. From a macroscopic point of view, the simulated TPD process shows relatively low desorption temperatures, <140 K at the (011) surface, <170 K at the (100), and <180 K at the (111) FeS surfaces, which are comparable to experimental desorption temperatures predicted at metallic surfaces. These low temperatures of desorption imply that a small molecule such as methylamine is desorbed too easily to act as an effective capping agent under the kind of ambient conditions where other capping agents may work, for example a long chain amine such as oleylamine. The low desorption temperature does of course mean that the molecule is removed easily to produce the accessible surfaces required for heterogeneous catalytic reactions. In future works, the interactions of longer chain amines with extended FeS surfaces could be investigated in order to evaluate the effects of the amine chain length on binding strengths and FeS shape modulation.

Finally, the catalytic properties of mackinawite nanocatalyst for the adsorption, activation and decomposition of environmentally important NO_x gases have been explored. The FeS surfaces show strong catalytic activity towards the activation of NO_x molecules as they are adsorbed relatively strongly on the (011), (100) and (111) surfaces, preferentially at Fe sites *via* charge donation from these surface species. While NO is found to adsorb molecularly at the FeS surfaces, dissociative adsorption (*i.e.*, $NO_2^* \rightarrow NO^* + O^*$) is preferred over molecular adsorption for NO_2 on the reactive FeS surfaces. In light of the strong catalytic activity of FeS towards the NO_x molecules, further research into the adsorption, activation and dissociation processes of other environmental important gases such as CO and CO_2 can be undertaken, which will help improve our understanding of the catalytic roles iron sulfides play in the origin life iron-sulfur world hypothesis theory. The adsorption and dissociation reactions of H_2O to form H and OH, and their possible chemical reactions with CO and CO_2 on mackinawite surfaces are also worth investigating in future studies.

Finally, the strong reactivity and the interesting catalytic activities of FeS towards the molecules investigated in this work should stimulate experimental efforts to synthesize FeS nanocrystals and in particular explore its chemical activity for potential applications in environmental catalysis.